



**FRIEDRICH-SCHILLER-
UNIVERSITÄT
JENA**

Methods and Instrumentation For Raman Characterization Of Bladder Cancer Tumor

Kumulative Dissertation

zur Erlangung des akademischen Grades *Doktor-Ingenieurin (Dr.-Ing.)*

vorgelegt dem Rat der Chemisch-Geowissenschaftlichen Fakultät der
Friedrich-Schiller-Universität Jena von

M.Sc. Eliana Fernanda Cordero Bautista

geboren am 15.04.1989 in Cucuta, Kolumbien

Gutachter

1. Gutachter: Prof. Dr. Rainer Heintzmann, Leibniz-IPHT, Jena
2. Gutachter: Prof. Dr. Jürgen Popp, Leibniz-IPHT, Jena

Tag der öffentlichen Verteidigung: 01.07.2020

Contents

Contents	i
Motivation	iv
Abbreviations	vi
1 Introduction	1
1.1 Fundamentals of Raman spectroscopy	1
1.2 Instrumentation and Raman fiber probes	5
1.3 Clinical applications of Raman spectroscopy in oncology	8
2 State Of The Art On Bladder Cancer Diagnosis	10
2.1 Definition of bladder pathology and current diagnosis	10
2.2 Main constitutional components of bladder	13
2.3 Instrumentation employed in previous studies	14
2.3.1 Raman system	15
2.3.2 Raman probes	15
2.4 Evaluation of Raman spectra	17
3 Selected Work and Results	21
3.1 Evaluation of shifted excitation Raman difference spectroscopy (SERDS) and comparison to computational background correction approaches for biochemical Raman spectral analysis	22
3.2 Clinical study for the characterization of bladder tissue using a compact Raman spectroscopy imaging system	29
3.3 <i>Ex vivo</i> Combination of Raman-imaging spectroscopy and piezo-tube based optical coherence tomography for bladder tissue diagnostics	34

4	Summary	41
5	Zusammenfassung	47
6	Bibliography	53
7	Publications	66
7.1	Evaluation of Shifted Excitation Raman Difference Spectroscopy and Comparison to Computational Background Correction Methods Applied to Biochemical Raman Spectra	67
7.2	Bladder Tissue Characterization Using Probe-Based Raman Spectroscopy: Evaluation of Tissue Heterogeneity and Influence on The Model Prediction .	85
7.3	Morpho-molecular ex vivo characterization and grading of non-muscle-invasive bladder cancer biopsies using forward imaging probe based multimodal optical coherence tomography and Raman spectroscopy	100
7.4	In-vivo Raman spectroscopy: from basics to applications	113
8	Erklärungen	138
	Conferences	i
	Workshops	ii
9	Acknowledgments	iii

Motivation

Worldwide, 549,393 newly diagnosed cases of bladder cancer were reported last year with nearly 200,000 deaths.^{1,2} Bladder cancer accounts for 3 % of all cancer worldwide and remains one of the most expensive cancers to treat in oncology in the western world.³⁻⁵ The main reasons of the high average lifetime treatment costs include the requirement of regular hospitalization, an intensive follow-up period and further disease monitoring.⁶⁻⁸ The improvement of diagnostic practices enables earlier oncoming of effective treatment which can reduce the recurrence rate and consequently decrease the follow-up procedures, resulting in a significant lowering of associated public health costs.

Among the diagnostic procedures, the gold standard approaches are cystoscopy,⁹ and histopathology.¹⁰ The transurethral resection of bladder tumor (TURBT) is performed under local anesthetic, but may result in distress and discomfort to the patient.¹¹ This also can increase the risk of tissue and organ function damage,^{12,13} reducing the recurrence rates in a year for early diagnosed patients.^{14,15} Histology results still produce false positives by labeling small papillary and flat lesions as cancer or false negatives due to sampling errors.¹⁶

In recent years, significant effort went into the development of optical imaging and spectroscopic approaches to assist the standard techniques by providing real-time detection of macroscopic and microscopic biomedical information.^{17,18} In particular, the combination of such modalities can provide clinically relevant biomarkers along with chemical and morphological properties of the bladder tissue. Optical imaging and spectroscopy have been applied to identify anomalies in tissue based on the analysis of its composition and structure at the microscopic level. Compact implementation of the modalities, rapid acquisition of the data and high specificity for the multiclass discrimination of diseases is demanded for clinical translation. The development of a multimodal optical imaging system that satisfies the mentioned conditions can potentially support point-of-care decisions and facilitate earlier oncoming diagnosis and treatment.

Raman Spectroscopy (RS) and Optical coherence tomography (OCT) are established

non-invasive optical imaging techniques for biomolecular^{19–22} and morphological^{23–26} characterization of human tissue, respectively. RS and OCT are emerging in clinical investigations, as techniques that can assist the diagnosis of tumor diseases. RS providing the molecular changes to detect tumors and OCT imaging the morphological features to detect the stage of the tumor.²⁷ The combination of both modalities can provide on-site assistance during cystoscopy to avoid the unnecessary rejection of tissue and to enhance accuracy during diagnosis. This thesis focuses mainly on the implementation and the clinical studies for grading diagnosis by using Raman spectroscopy.

Concretely, Raman spectroscopy has been widely used to observe molecular activity in humans in a non-invasive manner. RS detects vibrational modes in tissues and generates fingerprint spectra attributed to specific molecules and their surroundings, supporting thereby the identification of tissue anomalies. Numerous clinical studies of RS at the academic level have been reported. For instance, the diagnosis of cardiovascular diseases, in oncology and the molecular characterization of human cells and organs. RS utilizes the relation between proteins, lipids and nucleic acid content to discriminate tumors in different organs, e.g., brain, neck, lungs and breast tissues, as well as several studies in colon, cervical, prostate and bladder cancer.

RS oncological investigations target to identify malignant tumors, detect cancer in early stages, decrease the amount of redundant biopsies and assist surgery for adequate tumor resection.²⁸ Despite promising results, most of the applications approached in scientific studies are still far from clinical approval and commercialization.^{29,30} The research results reported in this dissertation address the identified technical and analytical constraints that still need to be further investigated in order to allow the transition of Raman imaging based spectroscopic solutions to routine medical diagnosis and surgical procedure of bladder cancer.

List of Abbreviations

ALS	Asymmetric least squares
CA	Clustering analysis
CCD	Charge coupled device
CIS	Carcinoma in situ
CLE	Confocal laser endomicroscopy
CV	Cross-validation
EMSC	Extended multiplicative signal correction
FOV	Field of view
HGPUC	High grade papillary urothelial carcinoma
ISUP	International society of urology
LDA	Linear discriminant analysis
LG	Low grade
LGPUC	Low grade papillary urothelial carcinoma
MCR	Multivariate curve resolution
MIBC	Muscular invasive bladder cancer
ML1	Model level 1
ML2	Model level 2
NA	Numerical aperture
NBI	Narrow band imaging
NMIBC	Non-muscle invasive bladder cancer
NT	High grade
NT	Non-tumor
OCT	Optical coherence tomography
OPA	Orthogonal projection approach
PCA	Principal component analysis
PDD	Photodynamic diagnosis

PLS	Partial least squares
PUNLMP	Papillary urothelial neoplasm of low malignant potential
QE	Quantum efficiency
ROI	Region of interest
RS	Raman spectroscopy
SERDS	Shifted-excitation Raman difference spectroscopy
SNIP	Sensitive nonlinear iterative peak clipping
SNR	Signal to noise ratio
SVM	Support vector machine
TURBT	Transurethral resection of bladder tumor
UPUNLMP	Urothelial proliferation of uncertain malignant potential
WHO	World health organization
WLC	White light cystoscopy

1

Introduction

1.1 Fundamentals of Raman spectroscopy

Raman spectroscopy (RS) is a nondestructive optical vibrational spectroscopic technique that provides molecular information based on the inelastic scattering of electromagnetic radiation, where energy is transferred between photons and molecular vibrations.³¹ This light scattering phenomenon is named Raman Effect and was first reported by Chandrasekhara Venkata Raman in 1928.³² The Raman Effect results from the interaction between electromagnetic waves (incident light from a laser) with matter (solid, liquid or gas). This phenomenon is exhibited as the scattering of light resulting from the periodical perturbation of the constituent molecules. The oscillation of the electron cloud within the molecules leads to a periodic separation of charge, known as induced dipole moment.

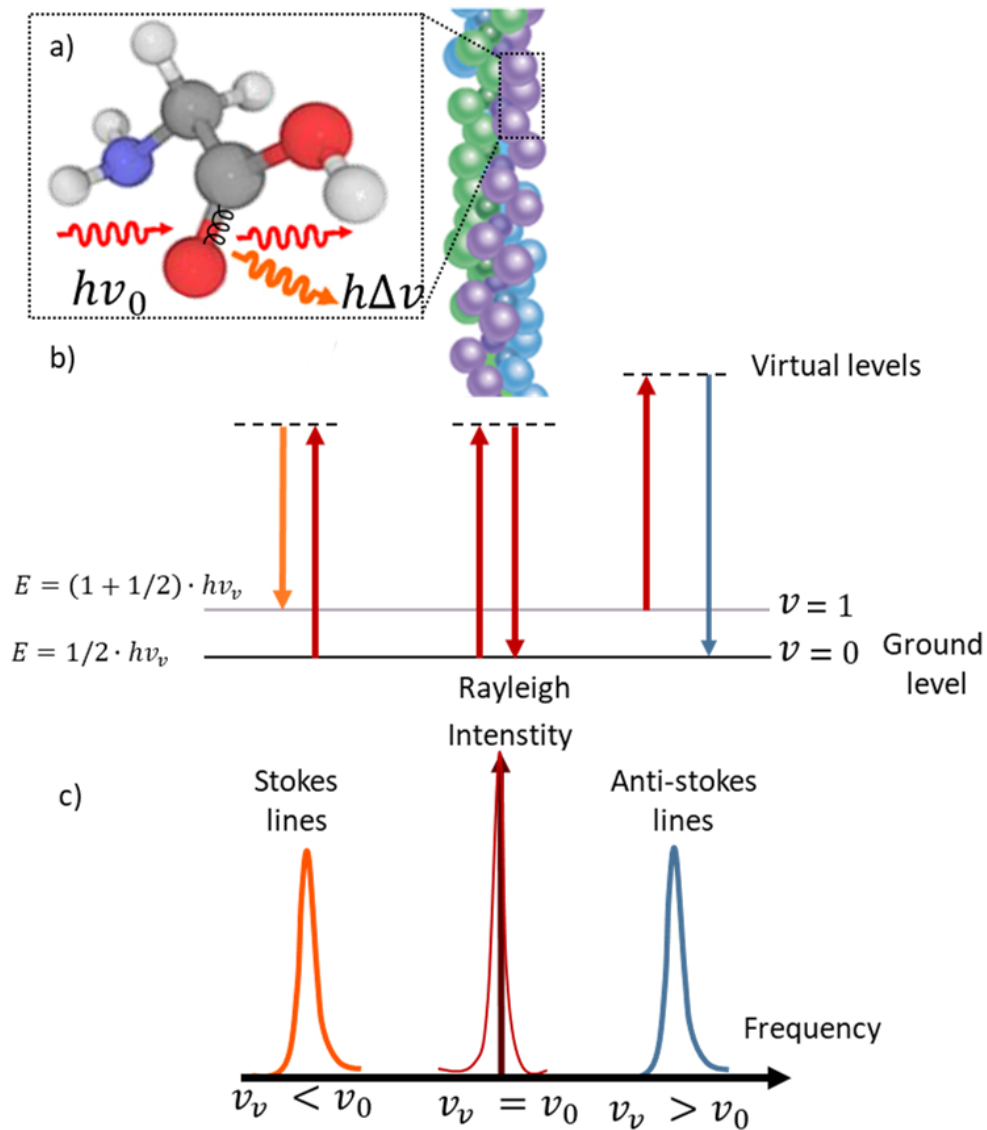


Figure 1.1: Raman scattering process: a) light scattering due to an electromagnetic incident wave (glycine molecule of collagen), b) quantum theory of Raman scattering, h is Plank's constant ν_ν is the molecular vibration frequency, E is the energy level; c) the strong Rayleigh scattering line at the excitation frequency and the weak, red and blue shifted Raman scattering bands, Stokes and anti-stokes respectively. b) and c) adapted from.³¹

If the incident electromagnetic waves interact with the molecules in a way that energy is either lost or gained, the scattered electromagnetic waves are shifted in frequency, this effect is known as inelastic scattering. Raman scattering is one form of inelastic scattering, where change of the induced polarizability and its frequency is characteristic of the molecule with a unique vibrational mode. The strength of the induced electromagnetic dipole moment of

an excited molecule is expressed by:

$$p = \alpha E_0 \cos(2\pi\nu_0 t) \quad (1.1)$$

Where ν_0 is the frequency of the incident electromagnetic field ($E_0 \cos(2\pi\nu_0 t)$), E_0 is the amplitude of the electromagnetic wave at t time and α is the polarizability. The polarizability is a tensor, which depends on dimension and shape of the chemical bond and therefore on the vibration of the molecule.³¹ This relationship can be expressed as a Taylor series, which is expanded around the equilibrium nuclear geometry $Q = 0$:

$$\alpha = \alpha_0 + \sum_k \frac{\partial \alpha}{\partial Q_k} \cdot Q_k + \frac{1}{2} \sum_{k,l} \frac{\partial^2 \alpha}{\partial Q_k \partial Q_l} \cdot Q_k \cdot Q_l + \dots \quad (1.2)$$

The normal coordinates Q_k and Q_l correspond to the k^{th} and l^{th} normal vibration of the molecule, related with the frequencies ν_k and ν_l . The normal coordinate oscillation can be approximated by a harmonic oscillator, namely

$$Q_k = Q_{v0} \cdot \cos(2\pi \cdot \nu_v \cdot t + \varphi_v) \quad (1.3)$$

Where φ_v denotes a phase angle and Q_{v0} the amplitude of the normal vibration. Considering vibrations totally independent, the v^{th} normal vibration can be represented by

$$\alpha_v = \alpha_0 + \alpha'_v \cdot Q_v \quad (1.4)$$

With α_v the polarizability, substituting equations:

$$\alpha_v = \alpha_0 + \alpha'_v \cdot \cos(2\pi \cdot \nu_v \cdot t + \varphi_v) \quad (1.5)$$

If the first two terms of the Taylor series are considered, it can be assume that the polarizability tensor behaves as a harmonic oscillator, with a frequency ν_v that is equivalent to the vibrational frequency of the normal coordinate of the molecule. If the equations are replaced in the definition of the dipole moment, it becomes

$$p = \alpha_0 \cdot E_0 \cos(2\pi\nu_0 t) + \alpha'_v \cdot E_0 \cdot Q_{v0} \cdot \cos(2\pi\nu_0 t) \cdot \cos(2\pi \cdot \nu_v \cdot t + \varphi_v) \quad (1.6)$$

Which can be rewritten as

$$\begin{aligned} p &= \alpha_0 \cdot E_0 \cos(2\pi\nu_0 t) \\ &+ \frac{1}{2} \cdot \alpha'_v E_0 \cdot Q_{v0} \cdot \cos[2\pi \cdot (\nu_0 + \nu_v) \cdot t + \varphi_v] \\ &+ \frac{1}{2} \cdot \alpha'_v E_0 \cdot Q_{v0} \cdot \cos[2\pi \cdot (\nu_0 - \nu_v) \cdot t - \varphi_v] \end{aligned}$$

As a result, the induced dipole moment is a function of the vibrational frequencies of the molecule (ν_v) and of the incident radiation (ν_0). In the equation, the first term corresponds to the elastic scattering of the electromagnetic radiation, also known as Rayleigh scattering. The second and third term in the formula represents the inelastic scattering, Raman scattering, where the second term corresponds to higher frequency of scattered radiation also named anti-Stokes scattering, while the last term is related to the reduction of frequency (Stokes scattering), this is shown in Figure 1.1 c). The variation of polarizability with the molecular vibration produces Raman scattering. Therefore, the vibrational mode of the molecules is only Raman active when the polarizability changes with vibrational displacement between the molecules. Maximum compression and elongation between molecules will result in high negative and positive change in the polarizability, representing the vibrational pattern of the molecule. This is the classical framework for describing Raman scattering.

The definition of Raman scattering in terms of discrete vibrational energy states is also relevant to understand the quantum mechanical framework, which is illustrated in Figure 1.1 b). Considering a vibrational energy well where each discrete vibrational state corresponds to a vibrational quantum number, neighbor energy levels differ as

$$\Delta E_{vib} = h\nu_{vib} \tag{1.7}$$

A given fraction of molecules will exist in each vibrational state following the Boltzmann distribution, where each vibrational quantum level can be interpreted as the probability function of the instantaneous displacement. Hence, Raman scattering can also be interpreted as a shift in vibrational energy state resulting from the interaction of an incident photon. Once the incident electromagnetic wave induces an oscillating dipole moment, it puts the molecular system into a virtual energy state, which is several times greater than the vibrational quanta and is generally different to any particular electronic state. During the interaction with the incident photon, energy equivalent to the vibrational mode is provided to the molecule. As a result, photon energy is changed. Stokes scattering is the most common Raman scattering process because it is more likely that the molecular system is found in the ground vibrational

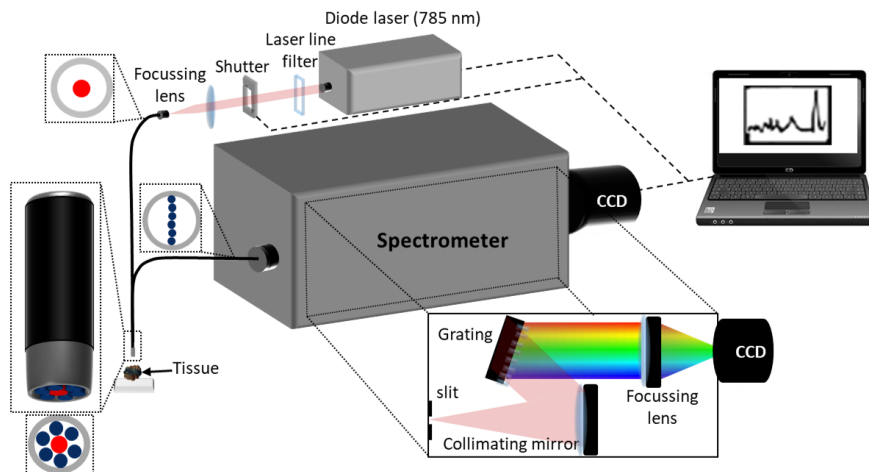


Figure 1.2: Raman fiber probe setup: The excitation source is filtered and focussed to be guided by the excitation fiber of the Raman probe to the sample and the scattered signal is collected by the collection fibers (blue), which transmit the signal to the spectrometer. The CCD camera detects and digitize the signal as a function of wavelength.

state, while for the anti-stokes scattering, the molecule must originally be in an excited vibrational state.

1.2 Instrumentation and Raman fiber probes

Successful implementations of Raman spectroscopy depends mainly to its instrumentation and the selected parameters. A careful selection is necessary in order to facilitate the measurement of the weak signals, which are often overlapped with background signals. The Figure 1.2 illustrates a Raman setup and Raman fiber probe, used for tissue characterization. The excitation source typically employed is an intense, collimated monochromatic laser which is filtered and focused before to excite the sample. Raman scattering signal is around 10^6 times weaker than the Rayleigh signal in solid materials.³³ Spectrometers are employed to take the signal and disperse it into spectral components and merge the signal on the CCD camera, where the signal is digitized as function of the wavelength. The large mismatch in scattering intensity enables the elastically scattered signal to dominate over the Raman signal. Therefore, notch filters are used to reject the elastically scattered light before it enters the spectrometer.³⁴ In the course of this dissertation a review was prepared to present an update of the *in vivo* clinical applications of Raman spectroscopy, shown in [EC4]. Section two describes in more detail the main challenges and instrumental approaches when

implementing compact Raman systems in clinics.

The generated Raman signal is not only depending on the power of excitation but also on the wavelength, which varies inversely with the fourth power of the excitation wavelength. A shorter laser wavelength increases the Raman scattering probability. However, laser wavelengths in the shorter visible and UV also lead to fluorescence, which may interfere with the Raman signals. Tissue and cells contain several fluorescent constituents therefore, background correction strategies need to be applied to deal with the high fluorescence.³¹

A key component of a Raman system is the detector, in most cases a charged couple device (CCD) is used. For the selection of the CCD important technical parameters, for instance the noise level and the quantum efficiency (QE) are considered. To collect very low intensity Raman signal, it is crucial that the quantum efficiency is high. High performance CCD cameras have usually above 90 % QE for a region between 800 and 910 nm range³⁵ which allows an efficient detection of the generated photons in the low wavelength region for a 785 nm excitation. Two main sources of noise are present in CCD cameras, read and dark noise. Read noise occurs during the read-out process of the charges from the chip and depends on the acquisition speed and the analog-to-digital conversion, for the CCD selection this feature is very important to ensure the highest achievable signal to noise ratio (SNR). Dark noise is caused by thermally generated electrons in the silicon structure of the CCD, which make this noise temperature dependent. The technical solution to this type of noise is the employment of thermoelectric cooling, which reduces the noise. This is crucial when considering the integration time of the measurements and number of fibers needed in a probe for the collection efficiency, which can also increase the noise considerably.^{36,37} The [EC4] presents a more detailed description of the instrumental requirements for clinical Raman applications. Raman imaging applications usually employ translational stages with submicrometer step-size resolution to scan the samples and obtain a spectral image that can provide a spectrum per pixel; normally this signal can be collected by a Raman probe, which will define the resolution and quality of the obtained Raman image.³⁸

An endoscopic Raman probe integrates many functions into specially arranged fibers, for the light excitation and sample signal collection. They can be classified according to their applications, according to the filtering methods, optical components or amount of fibers they possess. According to the number of fibers, there are single and multi-fiber Raman probes.³⁹ An overview of recently applied Raman probe design is presented in [EC4]. The single Raman probes are usually made with one fiber and some optical components, such as filters and focusing lens. Single Raman probes possess great efficiency due to the complete overlap of excitation and collection light at all distances from the fiber end facet. Their production

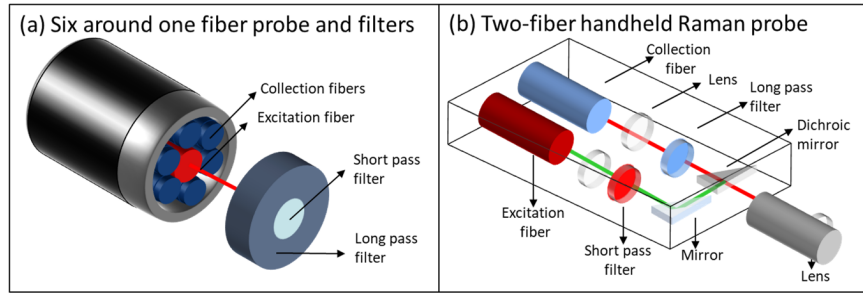


Figure 1.3: Common designs of fiber-based Raman probes: a) six around one fiber probe, the micro-filters are located at the fiber tip; b) handheld Raman probe.

cost is much lower in comparison with the multi-fiber probes. However, one of the major drawbacks is the multiplexing of excitation and scattered radiation at one end of the fiber and the very large Raman scattering from the fiber material itself.⁴⁰

Multifiber Raman probes can be arranged from two fibers to more-around-one fiber probes. The basic two fiber probes have three typical configurations. For instance, a two fiber probe can be made up of two parallel fibers with flat tips, as illustrated in Figure 1.3 a); this is not efficient due to the large dead volume. Another typical configuration is a non-coaxial fiber Raman probe, which has better collection efficiency but probes of this kind are often too large for clinical applications that need to be performed in internal organs. It is also possible to configure two fibers with an angle between them to enhance the overlap of excitation and collection light. The selection of any configuration depends mainly on the application, the instrumentation, the measuring environment and the needs in terms of signal.⁴¹

The six-around-one probe has the excitation fiber at the center and the collection fibers around the centered fiber. They can be arranged at different geometries, can be parallel with flat tips and possess a large dead volume. Any arrangement can be applied to enhance collection efficiency,⁴² Figure 1.3 a) illustrate a typical design with the filters placed at the fiber tips.

In a typical more-around-one fiber probe, the excitation fiber located in the center is filtered with a short-pass filter that reflects the silica based Raman background and the collection signal can be filtered from Rayleigh scattering with a long pass filter, which suppresses the backscattered laser light from re-entering the collection fibers. Filters are located at the distal end of each fiber. This can be observed in more detail in Figure 1.3 a) and b). The clinical studies performed within this doctoral dissertation employed handheld Raman probes with the previously described configurations illustrated in Figure 1.3.

1.3 Clinical applications of Raman spectroscopy in oncology

The potential of Raman spectroscopy for the detection of cancer in different organs has been studied for the past two decades. Most of the investigations have focused on early diagnosis aimed to improve diagnosis and treatment of cancer, where oncological needs can be fulfilled by Raman spectroscopy by providing guidance during intra-operative resection of tumor margins and assisting the early detection of pre-malignant tissue.⁴³ Early diagnosis of breast cancer has been reported by Saha et al.⁴⁴ They performed an *ex vivo* study by using a multi-fibre Raman probe to detect microcalcifications in breast tissue, achieving a specificity of 97 % and thereby proving the potential of Raman spectroscopy being employed as a real-time tool for radiologist.⁴⁴

Further *ex vivo* and *in vivo* studies in skin cancer detection demonstrated the capability of RS to detect and discriminate benign, malignant and pre-malignant skin tumors.^{45–49} Skin and breast are easy to access; it is also of special interest to prove that RS instrumentation is so well developed that internal organs can also be accessed for further analysis. One of the first studies that proved the technical feasibility of measuring *in vivo* lungs lesions employing a multi-fiber RS probe was performed in 2008.⁵⁰ RS applied to the diagnosis of gastric lesions have also been reported by Huang’s group, where a multi-fiber Raman probe has been employed to diagnose gastric cancer *in vivo* with an accuracy of 85.6 %.^{51–53} Clinical studies in colon specimens were also conducted *ex vivo*^{54–56} and *in vivo*^{57,58} where Raman probes were employed to detect anomalies, as hyperplastic polyps and adenocarcinomas, malignant and non-malignant groups were classified and anatomically differences of colon anomalies were also studied. Similarly, investigations in cervical cancer were conducted using fiber optic probes, reporting the diagnosis of cervical dysplasia,^{59,60} grading of squamous intraepithelial lesions and the *in vivo* feasibility real time discrimination of cervical lesions.^{61,62} The section “medical *in vivo*” applications of [EC4] presents an overview of the latest clinical studies and applications of Raman spectroscopy as a potential tool for medical diagnosis and intra-operative assistance.

Although Raman spectroscopy has demonstrated being a sophisticated technique with the ability to accurately discriminate tumor changes in different organs, there are still many practical limitations. Further developments in the improvement of multivariate classification algorithms and the diagnostic models are required. Optimized design and construction approaches of Raman probes are needed to enhance signal to noise ratios and to ensure system robustness to withstand day-to-day usage by clinical staff, including decontamination and

disinfection processes. More clinical studies are required in order to allow a clinical transition of the systems where medical standard and evaluations need to be further implemented. This research work aims to contribute in the design and performance of new clinical studies and development of new strategies for robustness in multivariable statistical modelling for oncologic diagnostic in bladder.

2

State Of The Art On Bladder Cancer Diagnosis

2.1 Definition of bladder pathology and current diagnosis

The human urinary bladder is an elastic pelvic organ which possess the functions to expand (when filled ovoid-formed) and to contract (when empty tetrahedral-formed).^{63,64} Its water-tight characteristic is determined by the urothelium (epithelium) layer, which also offers a barrier between urine and underlying tissues. The different types of urothelial cells provide a well-organized protein barrier with tight junctions limiting solute and water movements across the barrier. In this layer there is a higher presence of proteins and lipids. Another important layer is the connective tissue or lamina propria and it is mainly composed of collagen. This layer connects the urothelium with the muscle layer, which consists mainly of actin. The muscle of the bladder wall is protected by a mucosa that consists of a tight transitional epithelium, which is made up basal cell, intermediate and superficial layer.⁶⁵ Bladder cancer is a heterogeneous superficial lesion of the urothelium, which includes flat or papillary anomalies as well as invasive disease. The non-invasive urothelium carcinoma restricts the

malignant cells into the urothelial layer. If the tumor cells reach the basement membrane and invade connective tissue and underlying muscle, the neoplasm becomes invasive.⁶⁶ Several grading systems for bladder cancer have been established but the most commonly employed grading scheme is adopted by the World Health Organization International Society of Urological Pathology (WHO/ISUP), which divides papillary carcinomas into low-grade and high grade. Most of the diagnosed bladder cancer is of urothelial type, however, many subtypes also exists within urothelial neoplasia and lamina propria.⁶⁷

Bladder tumor lesions can be distinguished in two main groups: papillary (rounded) lesions and flat lesions. Among papillary, the urothelial papilloma is a benign tumor composed of separate fibrovascular cores, which are lined with retained cellular organization, preserving the umbrella cell layer of the urothelium (<7 cell thickness). Low malignancy is presented if the thickness of the papilloma increases thickening of the urothelium and is known as papillary urothelial neoplasm of low malignant potential (PUNLMP), the flat counterpart is known as urothelial proliferation of uncertain malignant potential (UPUMP). Neoplasm or tumor occurs by nuclei enlargement and structural abnormality in nucleus and architecture of the urothelial cells, commonly named low grade papillary urothelial carcinoma (LGPUC), where the nuclei enlargement is less than five times of a white blood cell. A similar representation of the low grade papillary in a flat lesion is known as urothelial dysplasia. High grade carcinoma occurs when extremely nuclear abnormally, variability in size, form and cell disorganization is exhibited. Contrary to low grade neoplasm, high grade papillary urothelial carcinoma (HGPUC) nuclei enlargement measures more than five times of a white blood cell. A flat duplicate of the high grade carcinoma, compassed within the flat lesions, is the urothelial carcinoma *in situ* (CIS), which possess identical cellular and architectural characteristics of HGPUC without having the fibrovascular cores, normally grows along the bladder mucosa. High grade carcinoma cells are fragmented, showing loss of polarity and disorganization respect to the basement membrane.^{10,66,67}

The described non-muscle invasive bladder cancer (NMIBC) lesions are typically diagnosed identifying the extension of the local tumor and spread to upper urinary track and other organs. The clinical evaluation of the tumor invasion is provided by cystoscopy.⁶⁸ Clinical suspicion is confirmed by differentiating between NMIBC and muscular invasive malignancy (MIBC) during first biopsy. In case that NMIBC is identified, a follow procedure is the transurethral resection of the bladder, which aims to entirely remove all visible malignancies. When MIBC is diagnosed tumor grade and stage need to be determined.⁶⁹ TURB is in any case necessary and it is desired to reduce recurrence and follow-up procedures. Molecular, microscopic and macroscopic imaging techniques can potentially facilitate the tumor detec-

tion during biopsy offering real-time visualization of cancer cells.

The macroscopic imaging techniques are more established techniques, generally with a wide field of view, millimeter resolution and mucosal depth. A new improvement of the standard, white light cystoscopy (WLC) is narrow band imaging (NBI),¹⁶ which enhanced contrast between glucose and blood vessels, improving tumor visualization and detection.⁷⁰ A well established imaging technique is the Photodynamic Diagnosis (PDD), which increases visual contrast between benign and malignant tissue by selective fluorophores. Multiple studies validated its ability to distinguish malignant and flat tumors, allowing a more complete tumor resection and reducing overall cost of bladder cancer care.⁷¹ However, PDD has also shown high false positive diagnosed lesions, which may results from its macroscopic nature.⁷²

Microscopic imaging approaches encompass for instance confocal laser endomicroscopy (CLE), which is in early experimental stage and not commercially available. CLE uses a fiber optic probe inserted into an operating cystoscope and a fluorescent agent to obtain real-time microscopic images of the tissue, helping to achieve detailed images of tissue structure and evaluate appearance of individual cells, which allow distinguishing high from low grade neoplasm.⁷³ A wider depth between 1 to 3 mm, is achieved by optical coherence tomography (OCT), without the need for a contrast agent and providing real-time cross-sectional images of superficial tissues using near infrared light reflection from tissue. OCT can differentiate between normal and abnormal urothelium and is commercially available.⁷⁴ However OCT does not differentiate tumor grades and requires improvements in tissue contrast.⁷⁵

The incorporation of high definition and multiple chip cameras allows WLC to obtain optimal endoscopic images. Despite the achieved optical quality, the detection of small papillary bladder tumors and flat urothelial carcinoma *in situ* needs improvement.⁷⁶⁻⁷⁸ Reported macroscopic and microscopic imaging technologies propose the chance to enhance detection and staging of malignant tumors. To date, photodynamic diagnosis has the more evidence-based data, encompassing reduction in disease recurrence, where the high false positive detection rate is one of the major limitation.⁷⁹ Here, Raman spectroscopy can play an important role, complementing the information that recent technologies actually provide, enabling objective biochemical assessment of biopsied tissue samples. This section focusses mainly on the investigations performed on bladder tissue using Raman spectroscopic systems and presents a brief overview of the achievements and the main constraints of recent Raman spectroscopic developments.

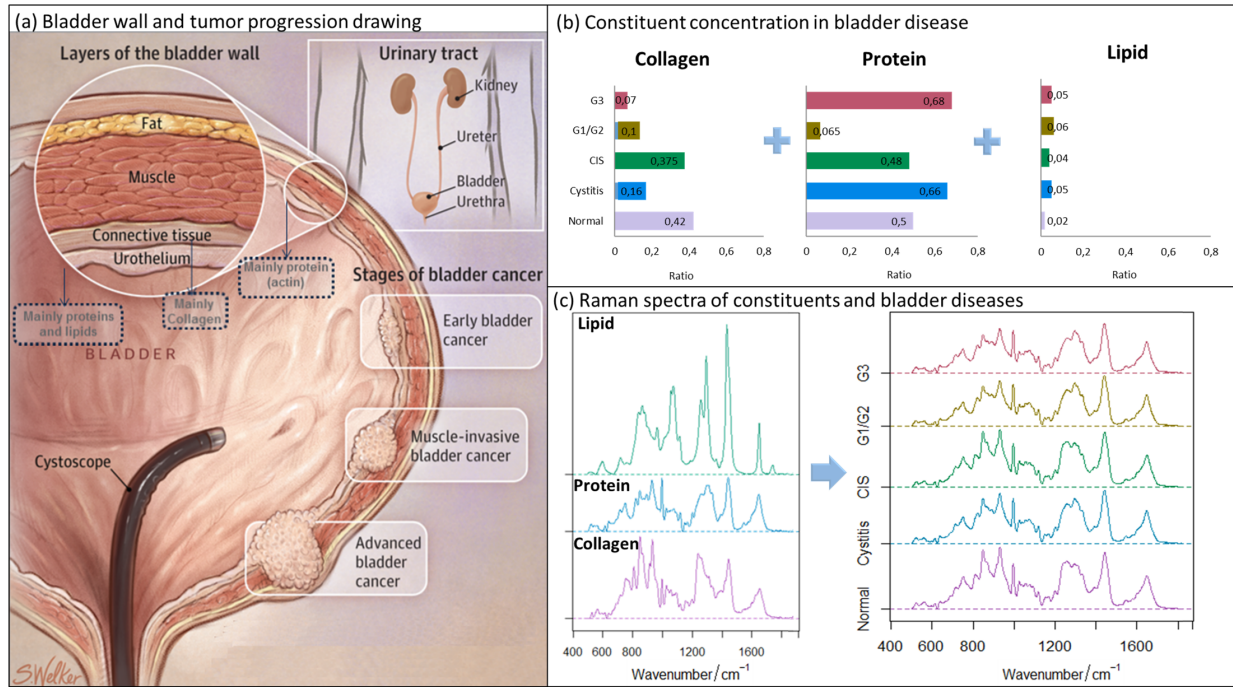


Figure 2.1: Bladder constitution and tumor progression: a) drawing of the bladder wall layers and the tumor progression from early to advanced bladder cancer (drawing used from Razmaria et. al⁸¹); b) concentration of collagen, protein and lipid for each bladder disease (normal-lila, cystitis-blue, CIS-green, low grade/G1/G2-orange and high grade/G3-red), concentrations obtained from Stone et. al;⁸² c) measured and reconstructed Raman spectra: Left panel measured Raman spectra of lipid (green), protein (blue), collagen (lila), and right panel Raman spectra of bladder diseases. The Raman spectra for the bladder diseases was constructed using lipid, collagen and protein measured spectra and the concentrations provided by the least square algorithm presented in.⁸²

2.2 Main constitutional components of bladder

The urothelium is the lining epithelium of the bladder with a thickness that varies from three to seven cell layers, where each layer is mainly formed by tightly packed urothelial cells. Urothelium lies upon an extracellular matrix which is mostly constituted by collagen I and III⁸⁰ and is also known as the basal lamina. The second extracellular matrix that follows the lamina propria is formed by an elastic fiber network of muscle bundles.⁸¹ This is visualized in Figure 2.1 a). Molecular changes with tumor progression are strong related with changes in protein matrix. Tumor degrades the cellular matrix and invades the basement membrane by actions of protease families, encoding thymidine phosphorylase, which promotes the production of matrix metalloproteinase (MMP). MMP is a large group of enzymes with various

proteins of the extracellular matrix, which play a role in tissue remodeling and inflammatory conditions.⁸³ Non-muscle invasive tumors can be associated with increment of nuclear activity of thymide phosphorylase.^{84,85} In the same way NMIBC can also be associated with loss of collagen VII, where cell migration in normal urothelial cells is restricted, causing the loss of polarity and subsequently loss of collagen VII.⁸⁶

An investigation on the main constituents of bladder tissue and its tumor progression is reported by Stone et al.,⁸² where the Raman spectra of bladder tissue constituents were measured to find the quantity and its change through disease progression, the concentrations obtained for lipids, collagen and lipids are represented in Figure 2.1 b). Among the selected constituents, DNA was measured as representative component of the cell nucleus. Actin was also considered, as being present in cell cytoplasm, collagen as representative constituent of the lamina propria, and oleic acid as abundant in urothelium. In the same way pure constituents associated with malignancy were considered, as lycopene and choline reported to be abundant in malignant tissue. Ordinary least squares fitting was applied to obtain the relative concentrations of the measured constituents in healthy bladder tissue, as well as in each tumor malignancy measured. Pure spectra of protein, lipid and collagen were measured from chicken meat (see left panel of Figure 2.1 c). The relative concentrations and the pure spectra were employed to reconstruct Raman bladder spectra for healthy state and for bladder tumor diseases (right panel Figure 2.1 c). The reconstructed bladder spectra provide an overview of the expected relevant Raman bands that are associated to the presence of lipids, proteins and collagen in bladder tissue and its cancerous diseases.

The Raman spectra and the concentrations presented in Figure 2.1 b) and c) show that low and high grade tumors present an increment of protein content and a decrease in collagen. An important observation to differentiate low and high grade is given between the increment of collagen and decrease of protein in low grade. For carcinoma *in situ* the collagen concentration increases, which can be related to damages in the connective tissue.

2.3 Instrumentation employed in previous studies

Numerous *ex vivo* studies on bladder biopsies have been reported, where different instrumentation has been employed. Most of the studies aim to use very compact Raman systems, however, this is only feasible by using a hand held Raman probe. This section review briefly the instrumentation developments reported in the past years.

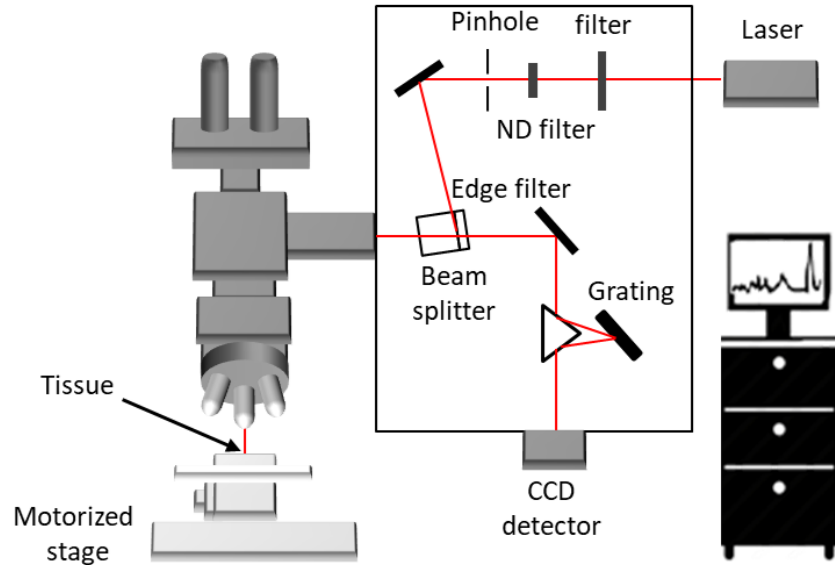


Figure 2.2: Typical Micro-spectrometer Raman setup with a near-infrared laser attached to a microscope, image adapted from.⁹⁰

2.3.1 Raman system

Raman mapping is performed employing a computer controller motorized stage and a Raman microspectrometer, as the Figure 2.2 illustrates. The laser light is coupled into the microscope via a single mode optical fiber and short pass filter, usually an objective is used to focus the laser light onto the sample. Additional optical elements are employed, filters to suppress the laser light that is scattered back and to transmit the wavelength range required for the system. Laser light is focused to the sample and the light collection is performed by an objective and optical elements that redirect the signal to the spectrometer and to the CCD camera. Among the variety of Raman microspectrometers available in the market, many studies have employed Renishaw and Kaiser Raman systems (Renishaw system 100/1000 and HoloSpec).^{82, 87–90}

2.3.2 Raman probes

The Visionex Gaser 10 forward viewing fiber optic probe^{87, 91} was the first employed Raman fiber probe *in vivo* and was used in guinea pigs bladder. The measurements were performed with a laser power of 170 mW and a laser wavelength of 830 nm. The Raman probe was formed by a central excitation fiber of 400 μm core diameter and NA of 0.22 with 6 sur-

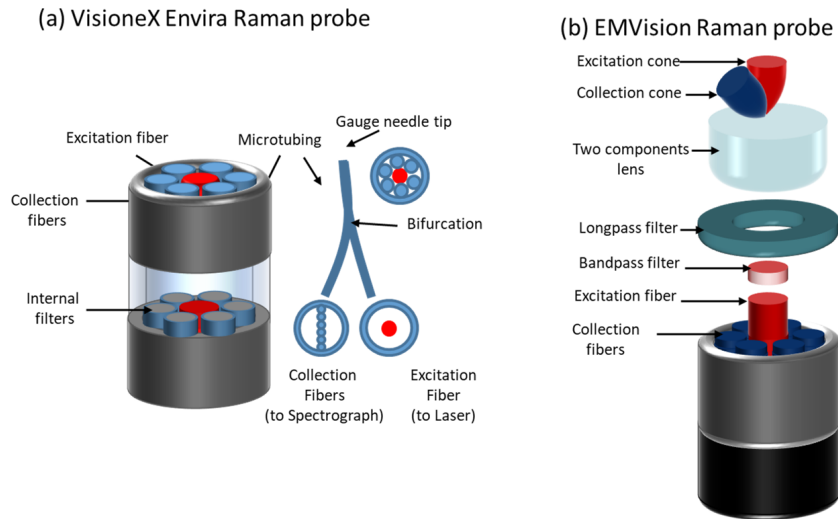


Figure 2.3: Fiber Raman probes employed in previous clinical studies on bladder: a) VisioneX Envira Raman probe;⁹⁶ b) EMVision Raman probe.⁹⁴

rounding collecting fibers (300 μm core diameter), the fibers were covered by a metal case and the probe diameter was approximately 2.5 mm. The filters were placed onto the core of the fibers and 2.5 cm spaced from the probe tip. A Visionex Envira Raman probe with a very similar design, was also used for the first *ex vivo* study on bladder tissue, the probe could penetrate the sample with a depth of 500 μm in a volume of 1 mm^3 .⁹²

In 2009 Grimbergen et al.⁹³ reported a clinical study in bladder biopsies employing an EMVision Raman probe during TURBT. The EmVision probe has a central excitation fiber and 7 surrounding collection fibers, the collection volume of this fiber is around 1 cm^3 and the filters are located at the tip of the fiber, this probe was also used in the first *in vivo* study on human bladder reported by Draga et al.⁹⁴ Barman et al.⁹⁰ measured *ex vivo* biopsies utilizing a bifurcated optical fiber Raman probe, where the excitation light fiber had a 200 μm core diameter and NA of 0.1, for this design 15 collection fibers with a 200 μm core diameter surrounded the delivery fiber. The short pass filter in this design was located at the tip of the excitation fiber and the long pass filter was placed at the tips of the collection fibers. Recently a low resolution Raman probe with a 7-around-1 design was employed to measure fresh bladder tissue and was built with low-OH fibers (core diameter of 300 μm and a 0.2 NA), the centered fiber had a band-pass filter glued at the distal end and the collection fibers tips were connected to a ring formed long-pass filter.⁹⁵ Many designs has been reported and the review [EC4] presents a detailed description of the influence of the probe design in the Raman signal.

2.4 Evaluation of Raman spectra

The evaluation of Raman spectra plays an essential role in Raman spectroscopy-based clinical applications. Each step in the data processing workflow is crucial to achieve reliable and accurate diagnosis. A branch of study employed since 1972, known as chemometrics, is an essential area of investigation and contributes substantially to the statistical modeling in Raman spectroscopy.⁹⁷ Reported studies on bladder cancer have been applying different approaches to train and validate the statistical and multivariate models, this section briefly reviews the typically employed approaches in the clinical studies applied to bladder cancer diagnosis.

The pretreatment of Raman spectra reported to date has very similar workflows, where mainly one of the first steps involves is the wavenumber and intensity calibration. Wavelength calibration is usually performed by measuring standard samples, such as polystyrene or paracetamol; known spectral peaks of these samples are used as reference to correct the changes or shift that may occur due to setup and environmental conditions. The intensity calibration is performed by using a standardized white lamp, where the lamp spectrum is measured and compared to the standard spectrum. by using the measured and reference lamp spectra a transfer function is computed and applied to correct the spectra.

Right after calibration it is also a common procedure to correct spectrum of possible cosmic spikes, dark and shot noise, where special algorithms can be applied to treat these technical issues. The fluorescence background is typically removed by using polynomial fit techniques, like least squares or extended multiplicative signal correction. Normalization in the intensity axis is applied to correct band intensity values of each spectrum to achieve a common scale. Once the raw spectra is preprocessed, the corrected set of Raman spectra are employed for statistical modeling to translate spectral signals into high-level information like tumor grading. For instance, principal components analysis (PCA) and partial least squares (PLS) has been extensively used to extract and select relevant spectral features and translate this into disease classes. Statistical modelling is further developed by applying clustering, classification or regression. Multivariate approaches, such as, linear discriminant analysis (LDA), clustering analysis (CA), support vector machine (SVM) and artificial neuronal networks (ANN) have been employed.

- **Principal component analysis (PCA)** reduces the number of variables within a data set by transforming the spectral set into a group of variables denominated principal components (PC); here all principal components are orthogonal to each other and represent most of the variance of the data set. Statistically, the covariance matrix of

the data set is determined and the eigenvectors of this matrix are calculated in order to find the PCs.⁹⁸

- **Partial least squares (PLS)** is an extension of PCA in which the information in the original data set is estimated onto a small number of underlying (latent) variables to ensure that the first components are the ones most relevant for predicting the response variables.⁹⁹
- **Linear discriminant analysis (LDA)** optimizes class categorization by computing the direction that provides the best separation for two or more groups of data. LDA finds a linear combination of vectors that optimize the ratio between-group variance and within-group variance.¹⁰⁰
- **Clustering analysis (CA)** organizes the spectra into clusters, which share similar spectral features. CA is based on finding distances between and within each cluster and an average spectrum is normally used to represent each cluster. Supervised classification generally utilizes LDA to define the group membership. On the other hand unsupervised classification, where the class membership is unknown, utilizes hierarchical cluster analysis (HCA) or K-means clustering.¹⁰¹
- **Support vector machine (SVM)** uses a null space matrix to transform a non-linear separation problem into a linear separation problem. SVM sets a boundary between groups of data that fall into different classes.¹⁰²
- **Artificial neuronal networks (ANN)** organize layers which are elaborated on a number of interconnected nodes with an activation function. The input layer contains the input data of the network and is connected to the called “hidden layers” where the processing is performed through a system of weighted connections. ANNs are built with a learning rule which changes the weights of the connections in relation to input patterns.¹⁰³

The performance of the statistical model is evaluated by the cross validation, where a validation set of data is used to estimate the accuracy of the multivariate algorithm. This step is also crucial for reliable diagnosis. There are several approaches to evaluate the performance of the model and the selected classifier. The validation method should be clearly defined, a commonly used approach is leave-one-out, which uses a single spectrum for the validation.

The approaches to select the training and testing set to create and validate the model variate, for instance, k -folds selection, blind selection, random selection of data. It is, however,

recommended to define the approach in close relation to the measured data and the provided true data, sampling and size of the data in order to avoid miss classification. A summary of the clinical studies performed on bladder tissue for cancer diagnosis is displayed in Table 2.1. It can be observed that new optimized diagnosis approaches and instrumentation improvements have been reported to date. New reported clinical studies have demonstrated that diagnosis accuracy is improving. Regardless of the methods applied, high noise and fluorescence background, tissue heterogeneity, overfitting in statistical modeling, remain as unresolved issues which need further optimization.

Year	Tissue type	Equipment	Samples	Statistical modeling	Results
2002 ¹⁰⁴	Snap-frozen bladder biopsies	micro-spectrometer	12 samples and patients	PCA-LDA (Normal, CIS, LG, MG, HG)	Sensitivities 93 %, 96 % and 98 % Specificities 99 %, 96 % and 96 %
2005 ⁹²	Snap-frozen bladder biopsies	Fiber-optic Raman system	24 patients	PCA (Benign and malignant tumor)	Accuracy 84 % Sensitivity 89 % Specificity 79 %
2006 ¹⁰⁵	Snap-frozen bladder biopsies	Raman micro-spectrometer	15 patients	Cluster analysis and LDA (Tumor and non-tumor)	Sensitivity 94 % Specificity 92 %
2006 ⁸²	Snap-frozen bladder biopsies	Raman micro-spectrometer	15 patients	Ordinary least squares	Concentration of constituents in relation with bladder disease
2009 ⁸⁹	Snap-frozen bladder biopsies	Raman micro-spectrometer	73 patients	PCA/LDA (With and without ALA group differentiation)	Sensitivity 75.4 % Specificity 88.7 %

2010 ⁹⁴	Bladder locations during TURBT (<i>in vivo</i>)	Multi-fiber Raman probe with a portable Raman system. Handheld Emvision fiber-optic Raman probe	21 patients	PCA/LDA (Bladder tumor and normal tissue)	Sensitivity 85 % Specificity 79 %
2010 ¹⁰⁶	Bladder paraffin treated bladder tissue and cells	Raman microspectrometer	172 patients	PCA (Non-tumor, low grade and high grade)	Low grade corrected assigned 74 % High grade corrected assigned 98.5 %
2012 ⁹⁰	Bladder paraffin treated bladder tissue and cells	Confocal Raman spectroscope with Raman probe	28 biopsies from 14 patients	PCA (Cancer and normal)	Accuracy 92 % Sensitivity 85.7 % Specificity 85.7 %
2018 ¹⁰⁷	Snap-frozen biopsies	Portable fiber optic Raman system with handheld Emvision fiber-optic Raman probe	32 biopsies from 10 patients	PCA/ANN (Normal, low grade and high grade)	Accuracy 93.1 % Normal sens. 88.5 % spec. 95.1 % Low grade sens. 90.3 % spec. 98 %
2018 ¹⁰⁸	Fresh biopsies after TURBT	Raman microspectrometer	12 biopsies from 8 patients	PCA (Normal, low grade and high grade)	Accuracy 93 % Sensitivity 99 % Specificity 87 %

Table 2.1: Summary of the clinical studies performed on bladder tissue

3

Selected Work and Results

This section presents an overview of the investigations, clinical studies and approaches applied to deal with the main open research questions when applying Raman spectroscopy as a diagnostic tool for bladder cancer tumor grading and general Raman Spectroscopy-based oncological clinical studies, as described in the last section. The related research topics are outlined as follows:

- Fluorescence background correction for biological Raman spectra can be performed using technical and computational methods, an overview of the main issues when applying different approaches is introduced and a carefully evaluation through experiments and simulations is presented in order to define the main advantages when applying a specific background correction approach and the parameters that require optimization when employing any technique in biological applications.
- Model creation and evaluation are strongly influencing the diagnostic capabilities of Raman spectroscopy in oncological clinical applications; the goal is to achieve a systematic model development that avoids over-fitting, training error and estimation errors. The influence of heterogeneity in the model performance is evaluated and a robust cross validation approach is proposed.

- During cystoscopy suspicious tumors are detected through white light endoscopy, where suspicious tumor tissue is resected and further examined by histopathology. Just after resection, the pathologist provides information about the differentiation of the cells and the depth penetration of the tumor in the tissue, known as grading and staging of tumor respectively. Information about tumor grading and staging during cystoscopy will assist onsite diagnosis and reduce significantly the amount of unnecessary biopsy. In this study we present an *ex vivo* study, where optical coherence tomography (OCT) and Raman spectroscopy (RS) are combined to visualize morphological changes of tissue in depth and biomolecular features respectively. The OCT-RS compact system performs automatically, and statistical modeling algorithms are developed to provide onsite prediction of the detected lesions.

3.1 Evaluation of shifted excitation Raman difference spectroscopy (SERDS) and comparison to computational background correction approaches for biochemical Raman spectral analysis

Biological tissue is generally constituted by collagen, elastin, protein and lipid cells, which are also considered key sources of autofluorescence.¹⁰⁹ In tissues, the extracellular matrix generally plays an important role in the autofluorescence emission, even more than cells, because elastin and collagen, within all the endogenous fluorophores, exhibits high quantum yields.¹¹⁰ The autofluorescence contributions in tissue are undesired when measuring Raman signals, because the fluorescence obscure relevant Raman bands. Therefore, it is necessary to apply background correction removal prior to statistical modeling in order to further analyze the Raman spectra.

An overview of instrumental and computational techniques is presented in Table 3.1, it is however relevant to evaluate the performance of the most applied approaches under high fluorescence conditions and to determine theoretically and experimentally the most effective method to correct background present in bladder tissue. An evaluation and comparison of Shifted Excitation Raman Difference Spectroscopy (SERDS) and Extended Multiplicative Signal Correction (EMSC) is reported in [EC1].

The investigation presented in this subsection focuses in evaluating both SERDS and EMSC for lipid, protein, collagen and simulated fluorescence spectra, where the optimal shift

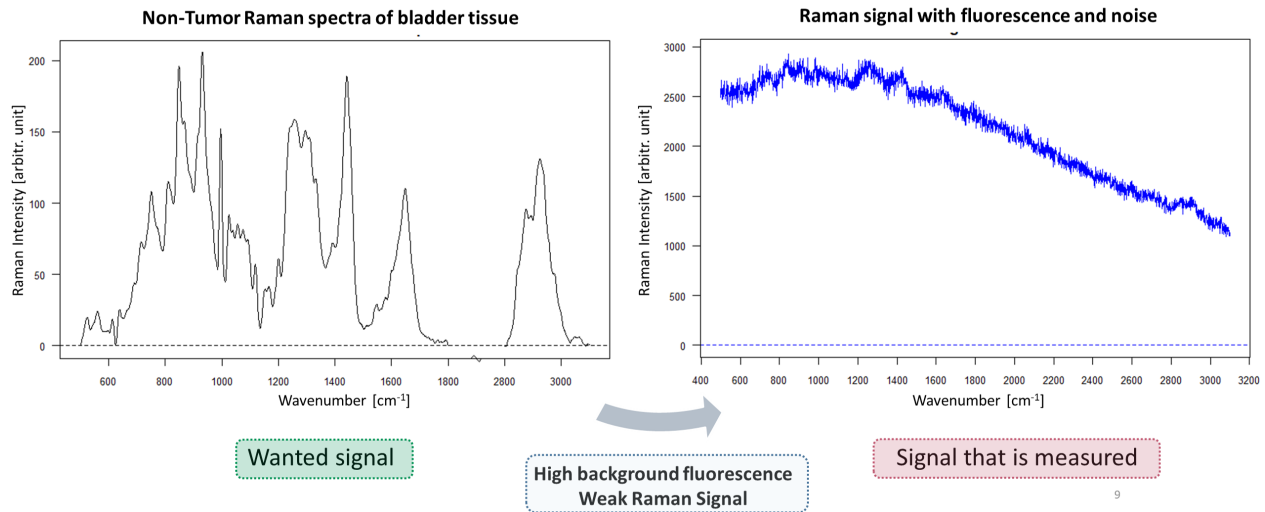


Figure 3.1: Measured and background corrected Raman spectrum. Left panel shows the desired Raman spectrum for bladder tissue in healthy state and right panel shows the real measured Raman spectrum with noise and fluorescence, where clearly the fluorescence and the noise obscure the Raman bands of the bladder tissue

and the signal to noise ratio is evaluated.

Separation of fluorescence is possible through modulation, where fluorescence occurs independently from the excitation frequency always from the first level of the ground state of the fluorophore. Here shifted excitation Raman difference spectroscopy plays a role, where two Raman spectra are recorded at two minimally different excitation wavelengths. In theory, the two measured Raman spectra are composed of identical fluorescence but shifted Raman peaks. Therefore, the fluorescence can be subtracted from the difference spectrum of the two recorded Raman spectra. However, high fluorescence spectra is very noisy and the signal to noise ratio (SNR) increases in the difference spectrum. In addition, the resulted difference spectrum can be very difficult to interpret. Therefore, it is necessary to evaluate which optimal shift can be applied in order to achieve high SNR and interpretable difference Raman spectrum.

The evaluation of optimal shift was performed using Raman spectra of lipid, collagen and protein sections of low fluorescent chicken meat measured on a commercial Raman microscope setup (Holoprobe, Kaiser optical system). Simulation of fluorescence, noise and SNR was performed previous to calculate the optimal shift evaluation.

The spectra were acquired at 1 second integration time and excited with 785 nm laser wavelength. The set of fluorescence spectra from real measurements were fitted, multiplied by a constant factor and added to the Raman spectra.

Methods	Description	Advantages	Disadvantages
Shifted excitation Raman difference spectroscopy ¹¹¹¹¹²¹¹³	Small changes in excitation wavelength gives a shifted Raman spectrum, fluorescence contributions does not change with the shift and can be subtracted.	Fluorescence can be effectively removed in samples with spectral bands of similar spectral widths, e.g crystalline proteins.	A lot of noise is added when subtracting high fluorescent signal.
Photobleaching ¹¹⁴	Sample irradiation for a long period of time, where a photolytic decomposition of the fluorescent molecules is induced.	Overall fluorescence background can be reduced.	Changes of relative peak heights occurring due to photobleaching process can produce physical and chemical changes in sample constituents.
Time-gating Raman spectroscopy ¹¹⁵	Ultrashort laser pulses driving a Kerr shutter to gather early-arriving Raman photons, while blocking later-arriving fluorescence.	The use of pulse energies below the damage threshold improve SNR for the fluorescence removal process at reasonable integration times.	Low signal to noise ratio, highly complex and costly.
Modulated Excitation wavelength shifting ¹¹⁶	Raman signal measured at two closely spaced excitation wavelengths and the two shifted Raman signals are treated with a low-frequency modulator to reconstruct Raman spectrum.	Effective background rejection based on the fluorescence lifetime is achieved.	Need of lock-in detection, wavelength variable and fast lasers are required, is costly and fast read-out camera is needed for efficient signal correction.

Extended Multiplicative Scatter Correction ¹¹⁷	Based on least square fitting of pre-defined background and the pure components.	SNR is not reduced, special equipment is not required and it does not affect spectral interpretation.	The removal of complex and unknown background is very challenging.
Polynomial Fitting ¹¹⁸	Relies on user-selected spectral locations where the zero baseline will be fit and on iterative polynomial ability.	Simple and effective method to eliminate background.	It is time consuming due to subject intervention, is challenging to identify non-Raman active frequencies and the high noise circumstances is a crucial limiting factor.
Least Squares Methods ¹¹⁹	are based on fitting of linear combinations of reference data to the measured spectra, here the sum of the squared differences between observed and fitting values is minimized.	Reasonable mathematical correction of fluorescence background can be achieved under the right selection of parameters.	Method susceptible to variability and high noise circumstances is a crucial limiting factor.

Table 3.1: Summary of the instrumental and computational background correction methods applied to Raman spectra

The noise was determined by applying a Poisson distribution function on the square root of the fluorescence intensity. The generated background and noise is added to the original spectra, the section 2.1 "Theoretical approach" of [EC1] describe in more detail the mentioned steps. The shift simulation of different laser excitation wavelength is performed by generating a set of shifted spectra by multiple wavelength steps between 1 nm and 4 nm. The signal to noise ratio (SNR) was estimated under the shot noise-limited definition, where the shot noise is considered as the only noise source and is determined as the square root of the signal intensity. Each spectral pixel was employed to calculate the SNR, therefore as a result a wave-number dependent SNR spectrum was obtained, where the regions with

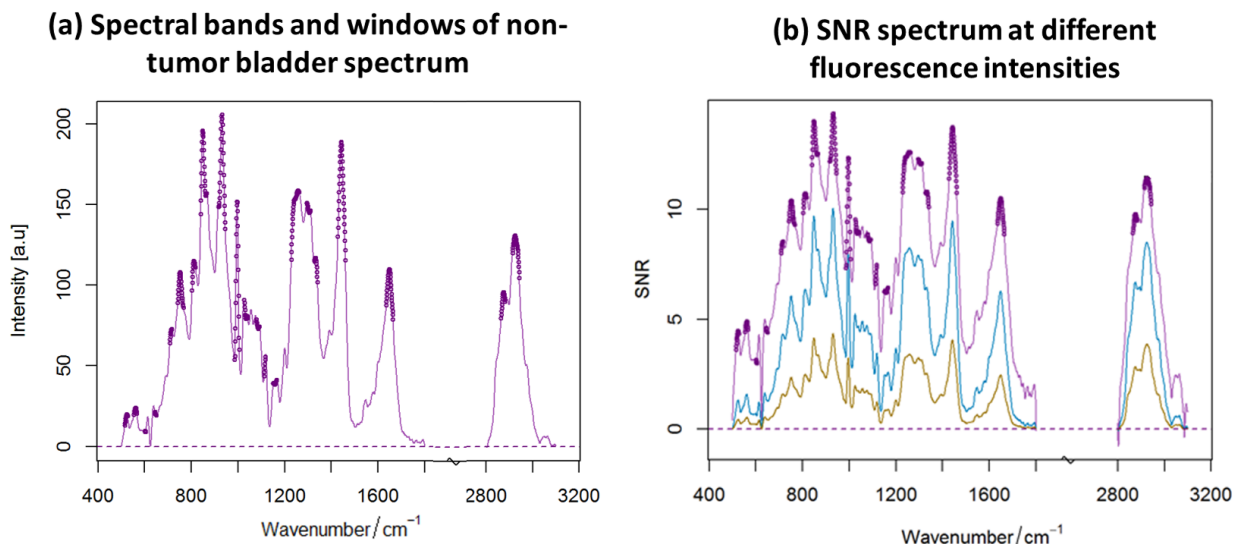


Figure 3.2: SNR spectra at different fluorescence intensities: a) spectral bands of the measured spectrum. The points (purple colored) in the spectrum are the maxima and the windows estimated bands; b) SNR spectrum with fluorescence, the spectrum is SNR without fluorescence (purple colored), the blue with fluorescence 5 times the maximal band of the spectral signal and the yellow spectrum is the SNR with fluorescence factor 10 of the normal signal

not relevant Raman bands were not considered. The single value of SNR was calculated by employing a band finder function with the second derivative of the SNR spectrum, where the maximum bands were considered to average each SNR detected peak intensity.

High intensity of the fluorescence signal, not just obscures Raman spectra but also add noise level, which increases with the fluorescence intensity following the square root of the total signal intensity, as showed in Figure 3.2. The definition of SNR allows evaluating the performance of SERDS, by simulating the shift, the noise and fluorescence on the measured spectra.

The optimal shift is usually defined as the wavelength difference, which is equivalent to the half-width of a Raman band.¹²⁰ This definition just applies when the spectrum has bands with similar bandwidths, which is not the situation of Raman spectra of most biological samples. In this investigation a new approach to determine the optimal shift by applying the autocorrelation function is proposed; the autocorrelation determines the level of similarity of a spectrum when it is shifted. When two spectra are completely overlapped there is a perfect autocorrelation ($acf=1$), which means that the difference spectrum of the full overlapped functions will be equivalent to zero, meaning that there is no signal in the difference spectrum.

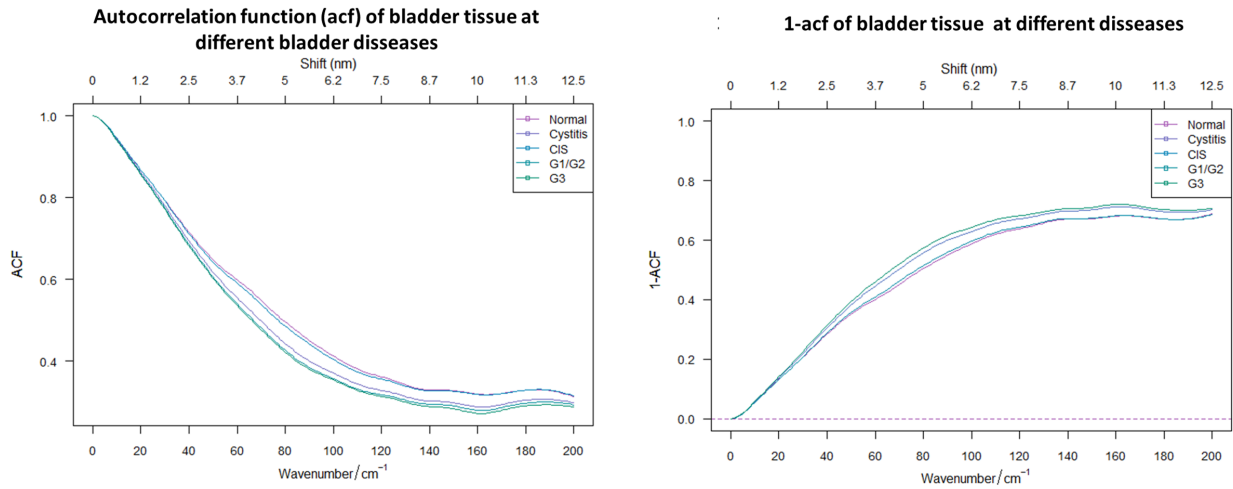


Figure 3.3: Optimal shift estimation by using the autocorrelation function (left) and by using the 1-autocorrelation function (right) of reconstructed bladder tissue spectra

If the correlation is low or nearly zero, the low self-similarity is an indicator of high intensity signals for the difference spectrum between the two spectra. Therefore, the value obtained by normalizing is used as reference of high signal in the difference spectrum. The autocorrelation and the value “1-afc” for the measured spectra of the pure components was calculated, this is illustrated in the Figure 3.3. The region employed to analyze the optimal shift was selected under the technical implementation limitation (shifts under 13 nm). Therefore, a range between 0 and 12.6 nm was selected for the acf calculations. The highest intensities in the difference spectra of a typical lipid, protein and collagen spectrum were observed at shifts of 5 nm and 7 nm respectively, see Figure 2 a) and b) of [EC1]. Figure 3.3 shows that higher shifts results in a reduction of the 1-afc intensity which indicates a reduction of signal for the difference spectrum. Shortly, high shifts result in higher SNR and low correlation between the shifted spectra serves as indicator of higher signal in its different spectra.

This study evaluates the performance of SERDS and EMSC for simulated Raman spectra at different fluorescence intensities, and each measured constituent, i.e. lipid, collagen, and protein. To illustrate in more detail the performance of the correction provided by the mentioned approaches, the reconstructed bladder spectra with a fluorescence 4 times the spectral signal intensity is shown in the Figure 3.4.

One can observe that the EMSC corrected spectra is comparable to the original spectra with noise, indicating that the computational background correction manages to maintain the original spectra and the intensity of the signal is not reduced during the background correction process. On the other hand, the difference spectrum based on SERDS correction

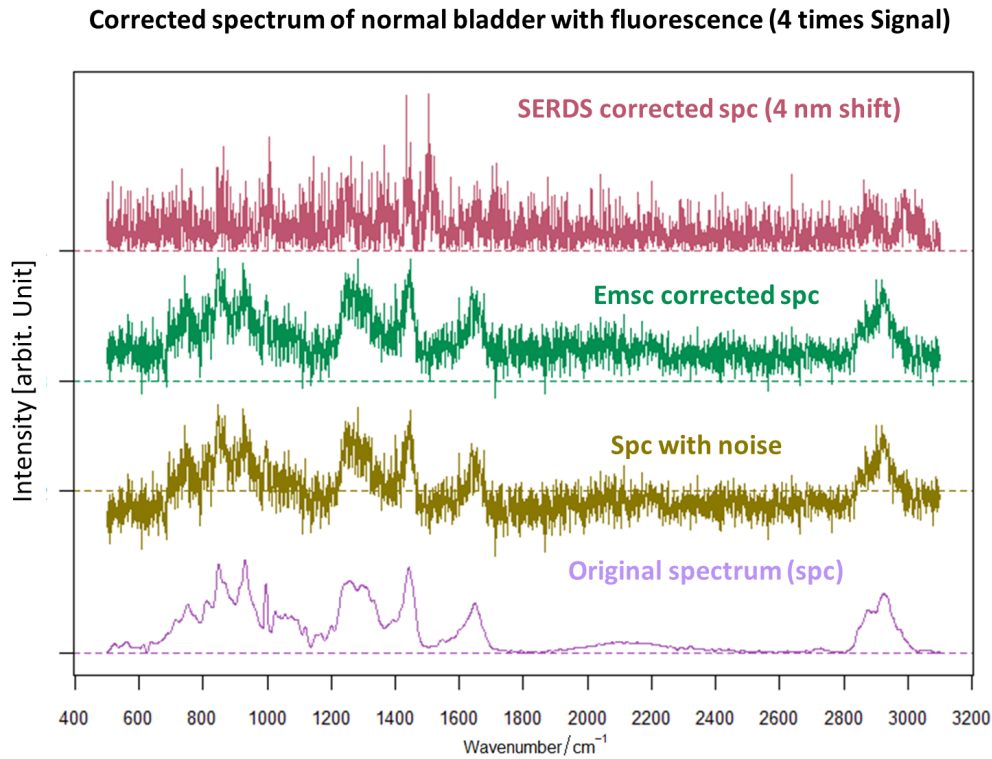


Figure 3.4: EMSC (red) and SERDS (green) corrected spectra of reconstructed bladder tissue. Previous to correction the simulated Raman spectrum with a fluorescence 4 times the spectral signal intensity. Comparing corrected spectra to the original spectrum (purple) and the spectrum with added noise (blue). SERDS correction was applied with a 4 nm shift

loses signal during the correction process due to the shot noise effect. During the SERDS correction the spectral intensities are subtracted but the noise is added due to its random nature. As a result the SNR decreases, being very low at high fluorescence intensities. The SNR decreases inversely proportional to the square root of the fluorescence background in a Raman spectrum.

A relation between SNR and fluorescence is introduced and expressed mathematically in [EC1]. Despite that both, EMSC and SERDS have showed to serve as practical solutions to eliminate the fluorescence background, each technique offers different advantages and can be applied according to the experimental needs. If Raman spectra of high autofluorescent tissue are measured, EMSC is a very suitable solution because despite the high noise levels expected in tissue like bladder the SNR is preserved, which is not the case that SERDS can offer. If very complex background needs to be removed like unknown light signal in Operation Theater, EMSC is challenging but SERDS can be useful to remove such kind of background.

This study demonstrated EMSC feasibility when correcting background in bladder tissue.

3.2 Clinical study for the characterization of bladder tissue using a compact Raman spectroscopy imaging system

Clinical histology is a well established medical procedure to diagnose bladder cancer, however, depends on invasive and time-consuming procedures, which can result in increased health risk for the patient and makes the today's cancer diagnosis and treatment of bladder cancer one of the most expensive medical practices.³

In the past decade, Raman spectroscopy has proved to be a potential technique to enable the detection of label-free chemical information at tissue level for medical diagnosis of cancer tumors, helping to improve the diagnostic precision, as described in the previous chapter.¹²¹

One specific problem with current Raman imaging systems is that they are large and require significant space, which is frequently very limited in a clinical environment. In addition, there are a variety of not well understood effects on the performance of tissue classification using Raman spectroscopy. In [EC2], a clinical study for the characterization of bladder tissue using a compact Raman spectroscopy imaging system is reported.

For this study 67 biopsies were obtained during TURBT from healthy bladder wall and from bladder tumor of 28 patients. The patients were informed and written consent was conferred under approved clinical study protocol (No: H-17015549). Data from 19 biopsies were excluded from the data analysis for one of the following reasons: instrumental failure, insufficient signal-to-noise ratio or excessive fluorescence signal that obscured the Raman spectra. The data consisted of wide field images, multiple Raman spectra and histopathological grading. Each sample was divided in two pieces and one piece was frozen (-80°C) for pathological analysis. 5 % of the samples were frozen and 95 % of the biopsies were fresh. The fresh biopsies were handled with a fresh needle and placed on top of a CaF_2 slide.

Conventional Raman-imaging systems are large (approx. 3 m^3) and not compact enough for clinical investigations, where space in or close to an operation theater is highly limited. To achieve a compact optical setup a handheld Raman probe was employed. Most common probes can readily achieve a focal spot size of $100\ \mu\text{m}$, and offer a collection NA of 0.35. The compact system we employed is integrated by an imaging spectrometer (princeton instruments, IsoPlane 160) with a CCD camera (pixis 400), an 785 nm wavelength laser (toptica, XTRA), a Raman probe (InPhotonics) and motorized x-y platform (thorlabs, MLS203), all

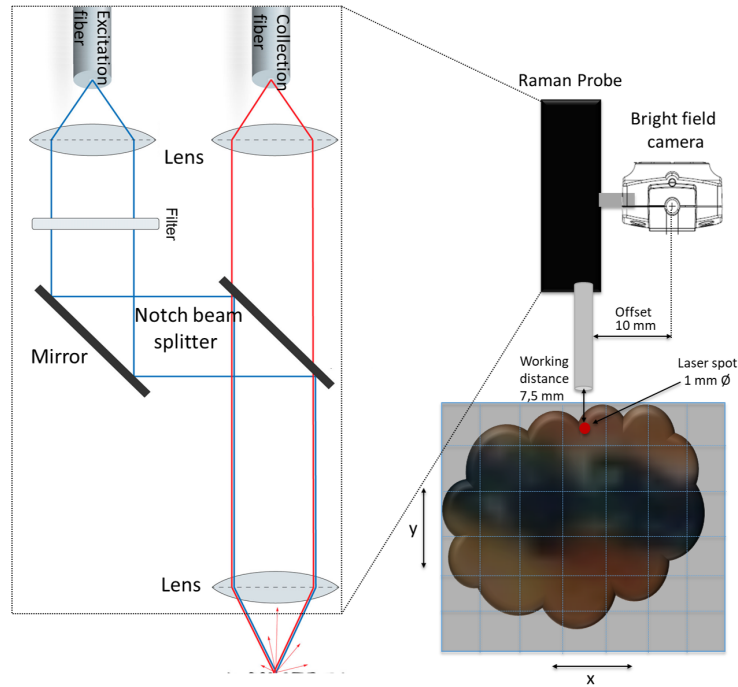


Figure 3.5: Workflow of the scanning system and inphotonics Raman fiber probe.

the setup is detailed as described in [EC2].

The handheld Raman probe is fiber-coupled by a 785 nm excitation laser, see Figure 3.5. The beam is collimated, filtered, and reflected by a mirror and a dichroic mirror. The excitation light is further focused by a lens to a spot size of $100 \mu\text{m}$. The generated Raman signal is collected by the same lens, and after passing the dichroic filter the light is filtered and focused onto a collection fiber with an NA of 0.22 and a diameter of $200 \mu\text{m}$, which is then coupled to a spectrometer. The system scans and acquires the Raman signal pixel-wise within a selected area, as illustrated in Figure 3.5.

One of the main challenges is the high background, due to the high autofluorescence from the tissue that obscures the Raman signal. In addition, there is some background from the fiber and optic components of the probe. Initially, it is necessary to evaluate the best approach to remove the background and it is crucial to know how the created model can deal with biopsy heterogeneity. In order to address the background problem, the acquired Raman spectra was pre-treated. As first step, wavenumber calibration was applied by employing the relative peak positions of acetaminophen (Sigma-Aldrich) and the intensity calibration was done by utilizing the reference spectrum of the Kaiser HCA calibration lamp. Following intensity calibration and cosmic spike correction, further treatment involved noise filtering by

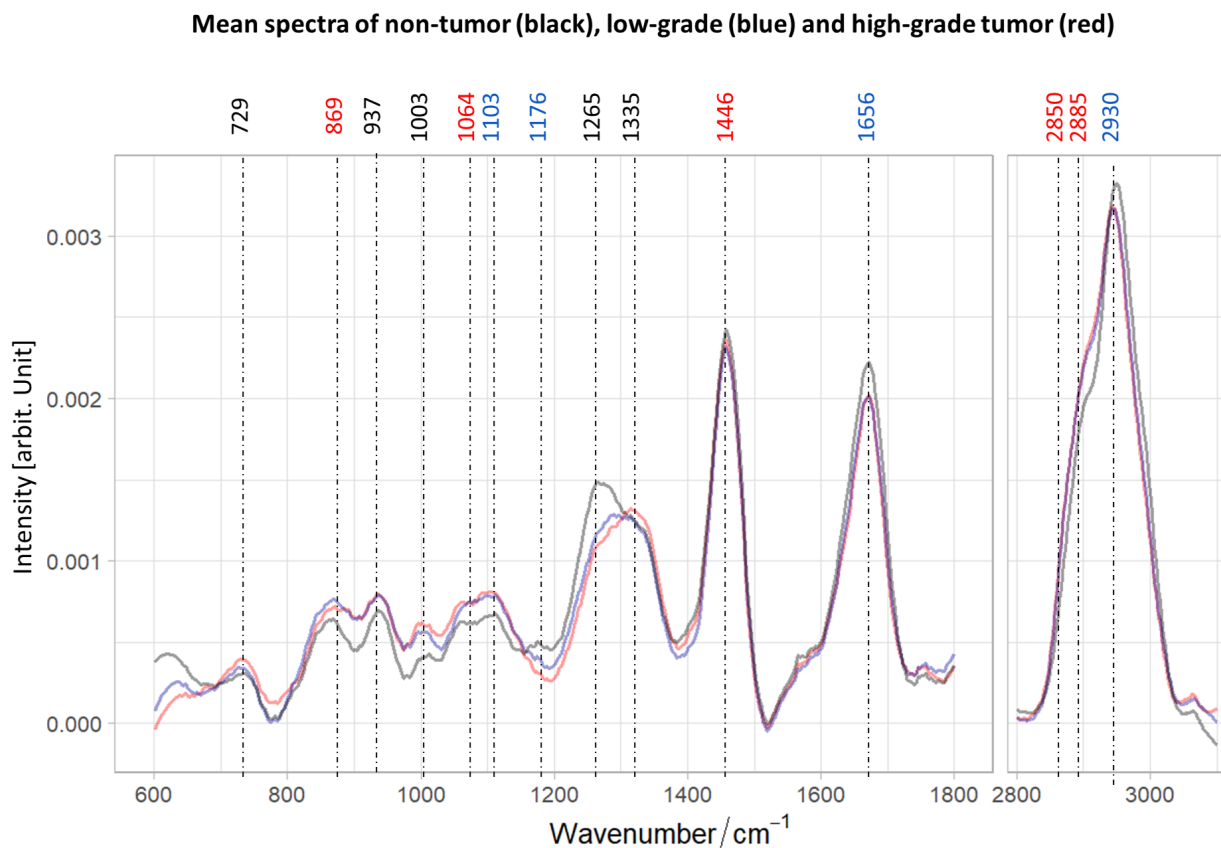


Figure 3.6: Mean spectra of non-tumor (black), low-grade (blue) and high-grade tumor (red). The main Raman bands are also assigned, where the black correspond to collagen bands, blue to protein and red to lipid bands.

applying PCA using the `prcomp` function of `stats` package and the Savitsky-Golay filter. To correct the fluorescence background extended multiplicative signal correction was performed (EMSC) and the spectra were then max normalized to unity, a detailed description of the pretreatment workflow is reported in [EC2].

The band assignments are displayed in Figure 3.6. Spectral contributions of lipids are observed at 869, 1064, 1646 cm^{-1} , where an increment of bands intensities in tumor spectra in comparison with the non-tumor spectrum is seen. The increment in lipid content can be associated to tumor tissue. Relevant lipid bands are resolved at the CH_2 bending mode in lipids. On the other hand, CH_2 symmetric stretching of protein and lipids are displayed at 1446, 2850, 2885 and 2930 cm^{-1} , band assignment was elaborated with the support of,^{122, 123, 124} reference database.

The statistical modeling was executed combining partial least squares regression (PLS) to

reduce dataset dimension and the linear discriminant analysis (LDA) to separate the classes: non-tumor, low-grade and high-grade tumor. This combination is known as PLS-LDA. The supplementary information of [EC2] shows the performance of other classifiers, such as support vector machine, Quadrant discriminant analysis and logistic regression.

The cross-validation procedure was performed following the steps:

1. Randomly selection of spectra from 1 to 80 per biopsy creating a dataset per selection.
2. Mean spectrum of the random selection per biopsy is calculated.
3. As CV, k -fold partition of mean spectra into random 5 subsets is applied.
4. Each of the selected random groups will form a training set of 5 mean spectra and a testing dataset of left mean spectra.
5. The training set creates the models level 1 (ML1) and the testing set validates the model with 10 iterations, in total 5000 models are generated. ML1 differentiate tumor and non-tumor spectra.
6. Randomly 10 % of the created ML1 predictions are used to compute the mean of predictions per single spectrum. As a result a mean prediction per single spectrum in each biopsy dataset is originated, producing a mapping of prediction values to classify tumor and non-tumor.
7. The spectra predicted as tumor by ML1 is employed to create and validate the second level models (ML2) which classify the tumor as low and high grade tumor.
8. A mean tumor spectrum is calculated per biopsy.
9. A random k -fold partition into 5 subsets is applied to divide the set into training and testing set.
10. The training set creates the ML2 and the testing set validates the model, this process is repeated 10 times per biopsy and subset. In total 160 models and predictions are obtained.

The Figure 3.7 a) and b) show two typical heterogeneous biopsies, the prediction of the models for the indicated number of spectra is also presented in Figure 3.7 c) and d), which clearly show that if the amount of random spectra selected to build the models level 1 is

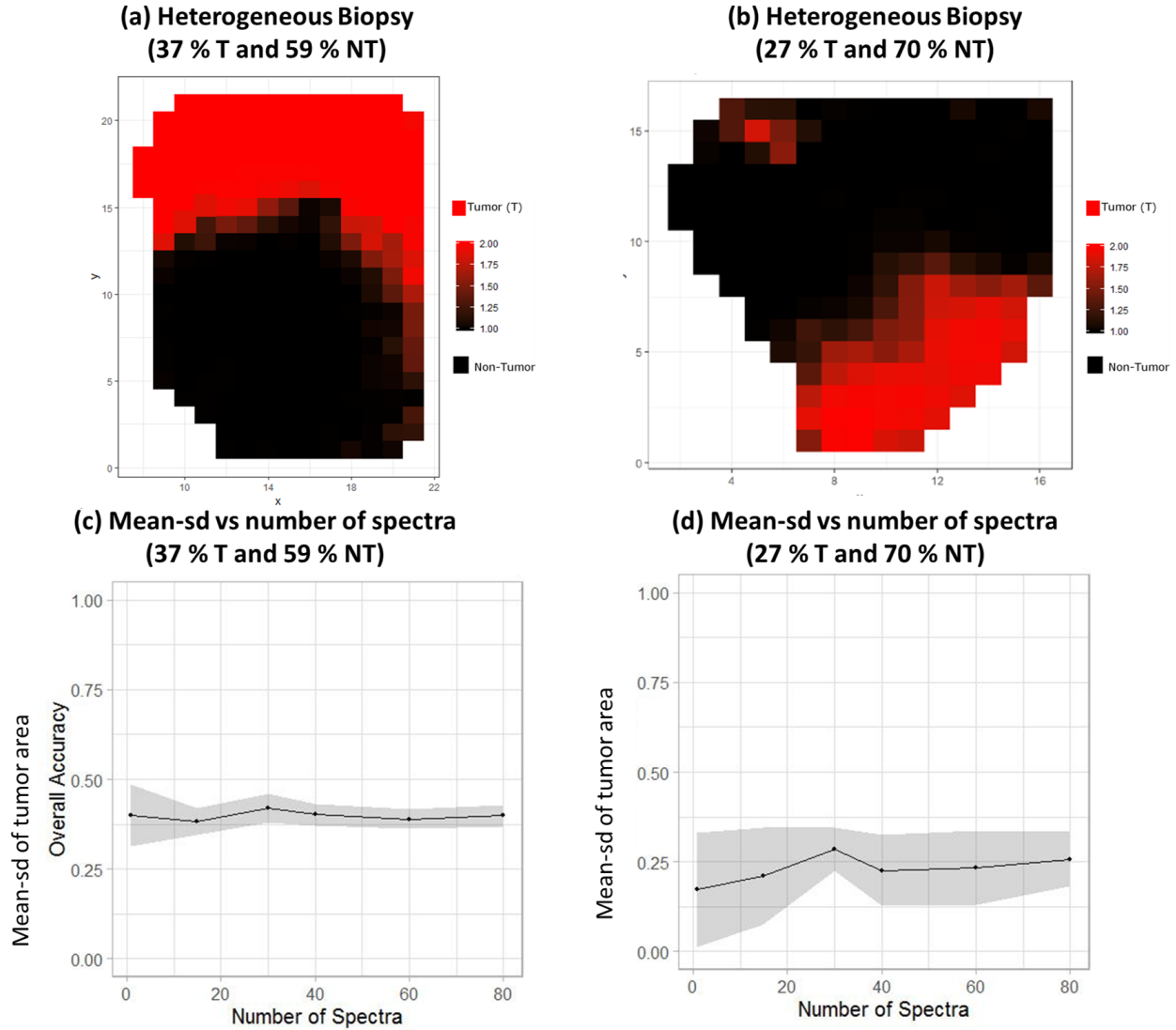


Figure 3.7: Mean prediction map for tumor and non-tumor regions of heterogeneous biopsies and Means-sd of tumor area against the number of spectra randomly selected to build the models: a) mean prediction map of test biopsy with 37 % of tumor area and 59 % of non-tumor area; b) mean prediction map of test biopsy with 27 % of tumor area and 70 % of non-tumor area; c) mean-sd of tumor area of test biopsy with 37 % of tumor area and 59 % of non-tumor area and d) mean-sd of tumor area of test biopsy with 27 % of tumor area and 70 % of non-tumor area.

high, the prediction becomes more stable in comparison of low amount of random spectra. The predictions for the tumor area displayed in Figure 3.7 c) and d) serve as indicator of the number of spectra required to build the model in order to achieve a robust prediction. In order to ensure that just spectra from tumor areas are entering the subsequent modeling phase, the predictions achieved per single spectrum as displayed in Figure 3.7 a) and b) were averaged and respective spectrum was considered as “tumor” at a mean prediction above 1.5 and as “non-tumor” for mean predictions below to 1.5. The obtained prediction maps serve to understand the model behavior when the biopsy is heterogeneous and adapt the ML2 construction and validation to the first level predictions obtained in ML1.

As a result, the ML1 classify non-tumor and tumor biopsies with a sensitivity of 92 % and a specificity of 93 % and ML2 differentiate low and high grade tumor achieving a predictive performance of 84 % accuracy with a sensitivity of 85 % and a specificity of 83 %, more details of the models performance and a comparison of different CV approaches is reported in [EC2]. In addition, the obtained Raman images were analyzed to learn about the heterogeneity of non-tumor and tumor bladder tissue at the bulk level, where mapping the Raman intensity of specific bands on the biopsies was useful to observe the distribution of tissue constituents as collagen and lipids on the scanned biopsy. Mapping observations indicated that lipid contributions are more dominant in tumor biopsies in comparison to the non-tumor biopsies. The constituent maps are illustrated in [EC2].

Bladder tumor grading was achieved and the relevant alterations in molecular constituents were correlated to evaluate the tissue heterogeneity. The study presented in this subsection reports a novel approach to use the validation and prediction of the model to characterize the tissue heterogeneity, providing more reliable results for tumor grading in non homogeneous bladder biopsies with non-tumor and tumor sections. The developed Raman system can complement the well-established methods, such as cystoscopy, to differentiate and detect tumor areas and different tumor grade on the bladder tissue.

3.3 *Ex vivo* Combination of Raman-imaging spectroscopy and piezo-tube based optical coherence tomography for bladder tissue diagnostics

Onsite real time assistance during cystoscopy can be accomplished by applying the combination of optical modalities to acquire more information about the tissue. In this study we implemented a system that combines optical coherence tomography (OCT) and Raman

spectroscopy (RS). OCT for tumor staging and RS for tumor grading in bladder tissue. OCT has the potential to identify the invasion and depth of the tumor by taking cross-sectional images of the bladder wall. Raman spectroscopy, on the other hand, can obtain information about the grade by assessing the biochemical composition on the tissue's surface, allowing the identification of tumor grade on the analyzed surface, in [EC3] the *ex vivo* combination of RS and OCT imaging for bladder tissue diagnoses is investigated.

The multimodal combination was employed in a clinical study to measure 119 fresh biopsies obtained during TURBT. The study has the approval of the local ethical committee and the Danish national board of medicine and the examinations were performed under written consent of patients. A summary of the disease of the measured biopsies is presented in Table 1 and Table 2 of [EC3]. Three biopsies were not considered for analysis due to its nature of papillary urothelial neoplasm of low malignant potential (PUNLMP), which is not a cancerous lesion but can increase the probability of tumor progression. Right after reception the biopsies were humidified with a sodium-chloride solution and delivered to the OCT-RS system within 15 minutes. For the biopsies that were not measured in a period below 20 minutes, samples were frozen to -80°C . During examinations with the OCT-RS system, the biopsies were placed on CaF_2 slides with the urothelium facing the system probes, measurements were performed in approximately 15 minutes, once the measurements were finished, the biopsies were stored in a formalin solution for pathological examination. The measurements were done sequentially at the same location through the biopsy. To acquire different information, molecular and morphologic, at the same sample locations two fiber probes were used and mounted on a holder with a known offset.

The Raman and OCT probes are mounted above an automated translation stage (MLS203), see Figure 3.8. Raman and OCT systems are communicated by a trigger-based Arduino communication (Board model UNO/R3) and all the system was controlled by a in-house developed LabView human machine interface (HMI), which set the coordinates, acquire the images and communicate between both imaging systems. The measurement workflow starts with a bright field image, which is obtained with a CMOS camera (DCC1645C). Once the image is acquired the user selects a region of interest (ROI) and the LabView HMI estimates the scanning coordinates for the Raman and OCT probes. The OCT system was acquiring nine images in 1 minute and the Raman system 30x30 spectral pixels in 13 minutes. For the Raman system a similar setup as the one described in [EC2] was employed. The RS spectrometer, a laser and CCD camera were integrated in a Acton series LS785 Princeton system, detailed information is described in the material and methods section of [EC3]. The in-house developed Raman probe was connected to the system as it is shown in the left panel

of Figure 3.8. The presented Raman probe reported in [EC3] performs better than the In-Photonics Raman probe employed in [EC2], the SNR is higher and the fiber background is properly filtered which allows analyzing in more detail the fingerprint region without obscuring relevant collagen and protein bands. Inside the Raman probe, the fiber transmitted excitation light is focussed by a standard lens, it passes a narrow-band clean-up filter and a dichroic- long-pass filter, then light is focussed by an objective lens to a spot size of 100 μm , the same objective collects the Raman signal and after passing the dichroic filter an additional long-pass filter transmits the acquired signal and focused it to the collection fiber (200 μm diameter). The OCT system utilizes an akinetic swept source laser with a central wavelength of 1304 nm and a swept frequency of approximately 173 kHz, optical OCT system is based on a Mach-Zehnder interferometer configuration. The OCT probe is a piezo-tube based fiber endoscope with a diameter of 3 mm and a length of 15.6 mm, its optical components are arranged in a Fourier-plane configuration which permit a telecentric scanning across the tissue plane, the OCT probe is illustrated in the right side of Figure 3.8. The field of view (FOV) of the OCT probe is adjusted to 1 to 1.4 mm scanning diameter and the piezo tube is driven to a frequency of 510 Hz and is attached to a scanning fiber, which follows a spiral scanning pattern. The OCT acquisition system utilizes a position sensitive device (PSD, SpotOn Analog, Duma Optronics Ltd.) to reconstruct volumetric OCT-stacks of the spirilized scan pattern within 2 seconds. The FOV of the OCT probe is not large enough to scan a biopsy with a single scan, therefore subsequent scans ware performed in a rasterized scan pattern. The acquired OCT images are then stitched together in a post-processing step to obtain an image of the whole biopsy.

Data analysis of Raman acquired spectra follows previously described workflow for pre-treatment, reported in [EC2] and [EC3]. One additional step is added for the background correction, were before to apply EMSC for fluorescence correction, the corrected spectra was baselined applying asymmetric least squares (ALS). Statistical modeling was performed by applying PLS-LDA classification to initially differentiate tumor and non-tumor spectra, and further classify the tumor spectra into low and high-grade tumor. Classification and cross-validation is detailed described in [EC2] and [EC3]. As a result two models are created: model level 1 (ML1) and model level 2 (ML2), were the predictions of the models created in ML1 are utilized to train, validate and test ML2. Tumor and non-tumor biopsies are differentiated with an accuracy of 92 %, one can see clearly in Figure 3.9 a) how the test dataset is separated into tumor and non-tumor, where the beeswarm plot displays the linear discriminant coefficients. In particular, the negative coefficients belong to the predicted non-tumor class (black points) and positive coefficients are related to spectra predicted as tumor,

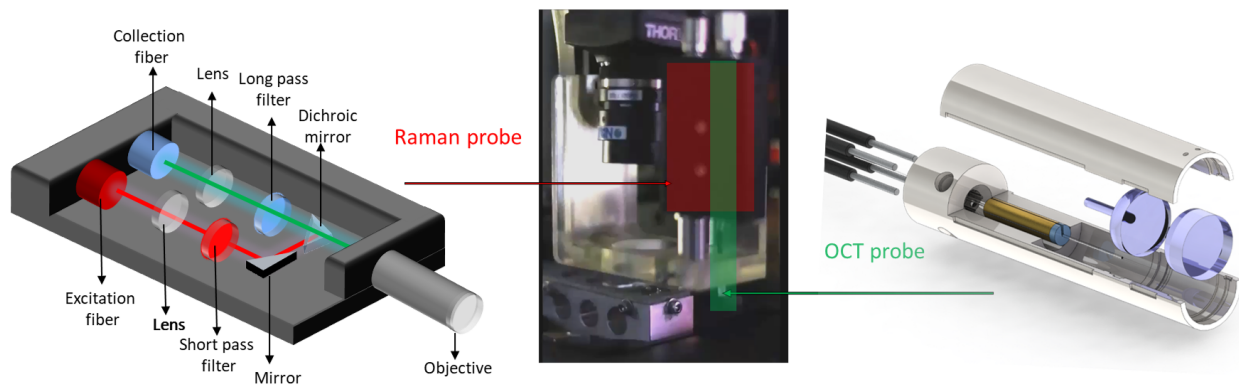
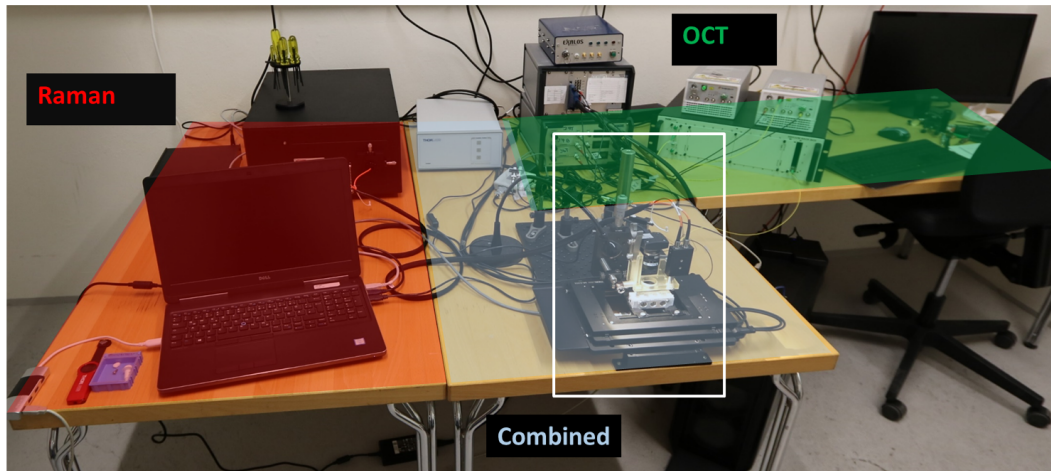


Figure 3.8: Combined multimodal imaging system and fiber Raman and OCT probes. The Raman system and Raman probe are highlighted in red and consists of a translate platform, a PC and a black box, which contains a single mode laser, a spectrometer and the CCD camera. Besides a bright field camera (located between the probes in the white highlighted area), the Arduino Board is connected to the Raman-PC. The OCT setup is highlighted in green and it includes a laser source, the interferometric optical setup including the photodiodes, driving electronics for the endoscope and a PC. An internal visualization of the Raman probe is displayed at the bottom left panel; in the same way also the internal components of the OCT probe are visualized at the bottom right panel.

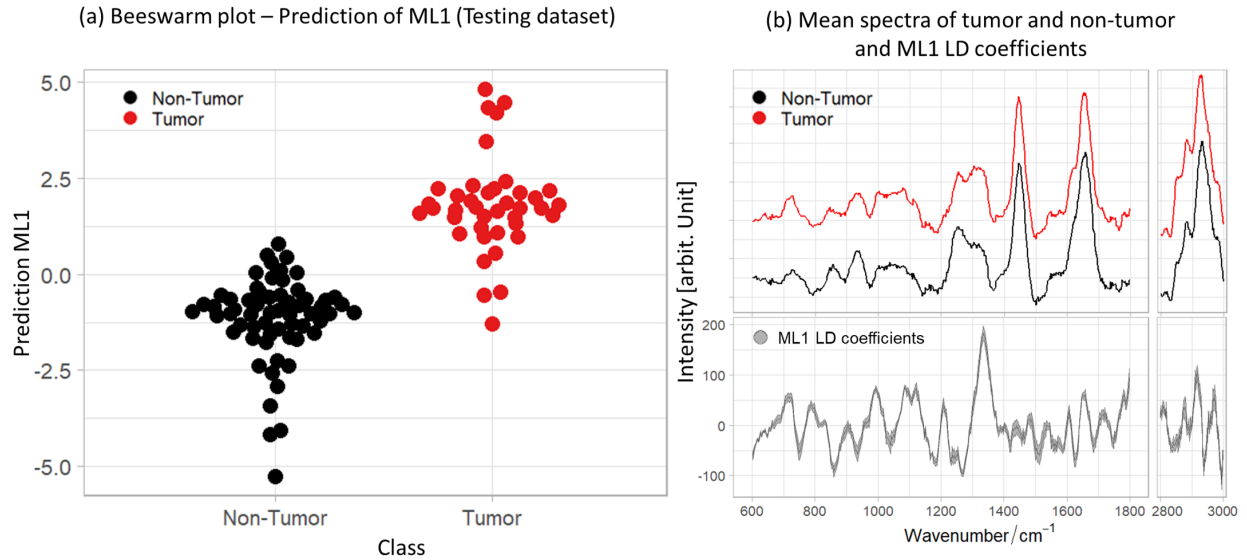


Figure 3.9: Linear discriminant coefficients and mean spectra of tumor (red) and non-tumor (black) biopsies: a) beeswarm plot of the predicted classes after testing the first model (ML1); b) mean spectra of tumor and non-tumor stacked with the mean-sd linear discriminant coefficients of the predicted model after validating the first model (ML1) with the testing dataset.

this is well related to the mean spectra of tumor and non-tumor biopsies and the linear discriminant coefficients per wavelength displayed in Figure 3.9 b). The negative peaks observed between the bands 856 , 937 and 1265 cm^{-1} ,¹²⁴ mostly collagen bands, show high intensity peaks in the non-tumor mean spectrum. On the other hand, the lipid bands are well related to positive peaks between the bands $1299/1300$, 1656 and 2885 cm^{-1} , which are associated to the CH_2 deformation, twist vibration and $C = C$ symmetric stretching of lipids.¹²⁵ The grading classification performance of ML2 achieved an accuracy of 77 % for the low and high-grade differentiation, where true positives (LG) can be easier identified than false negatives (HG), achieving a sensitivity of 81 % and specificity of 68 % to differentiate low-grade from high-grade tumor. A relevant fact related to the low specificity lies in the small variations between LG and HG spectra and the small number of HG spectra measured in this study (11 biopsies). In addition to the statistical modeling a multivariate curve resolution (MCR) algorithm was applied to estimate the collagen distribution in the imaged bladder tissue, the algorithm provides an estimation of the concentration of the extracted pure components in the biopsy Raman image providing a visualization of relevant tissue constituents through the sample.¹²⁶ The estimation of pure components initiates with an orthogonal projection approach (OPA), which performs an initial estimation of the pure

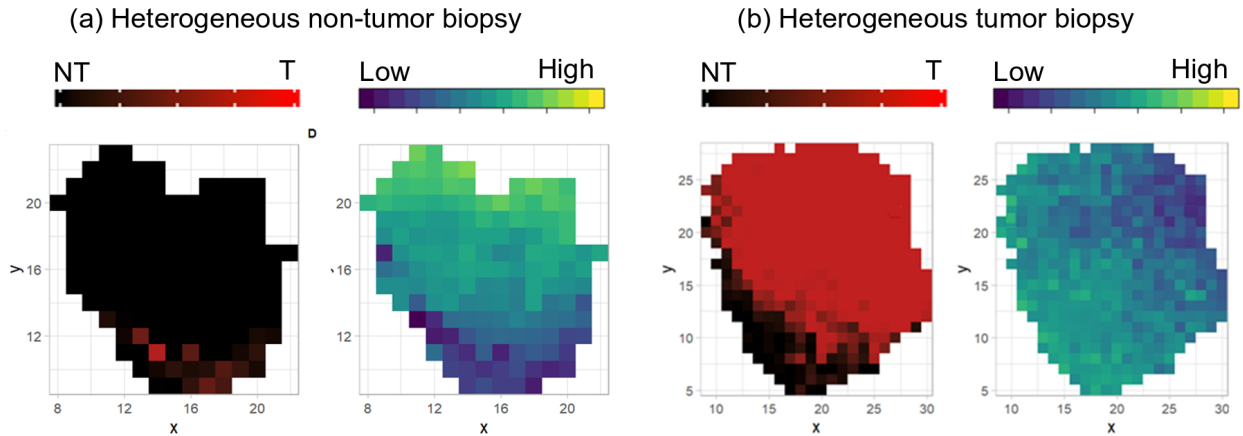


Figure 3.10: Mapping of ML1 predictions (left) and collagen distribution (right) for: a) heterogeneous non-tumor; b) heterogeneous tumor. The minimum collagen concentration value is 0.043 and the maximum value is 0.052.

components based on their dissimilarity. The initial guesses of pure components are then compared to literature in order to associate them to pure components, most of the extracted components in non-tumor biopsies were meeting main relevant bands of pure collagen spectra previously reported.⁸² The mean standard deviation of the extracted OPA components is used to calculate the MCR pure components and concentrations; here ALS complements the MCR algorithm serving as fitting function, the materials and method section of [EC3] describes comprehensively the methodology employed to obtain the mapping of collagen distribution on the biopsies.

The results of the statistical modeling are consistent with the relation between collagen dominant presence in non-tumor spectra. Accordingly, collagen distribution can be related to the mean predictions of model level 1 (ML1), which classifies tumor and non-tumor spectra. The prediction maps are illustrated next to the collagen distribution maps of each heterogeneous biopsy. Figure 3.10 shows clearly this relation. Two heterogeneous biopsies are compared, where a biopsy diagnosed as non-tumor, 3.10 a), has areas which present also lower collagen content and can be related to tumor presence. In the biopsy diagnosed as tumor, Figure 3.10 b), there are areas that were predicted as non-tumor and present a brighter area in the collagen distribution map, indicating more presence of collagen in non-tumor areas as in the neoplastic areas. The darker mapped areas are indicating lower collagen content.

OCT images are classified by applying texture analysis,¹²⁷ where the texture reflections are examined, associated and correlated to histopathological images in order to correlate

the changes in texture to any malignancy. Once the changes are detected the classification was performed applying a Gaussian support vector machine (SVM) function using a holdout validation with 20 % of the data, more details of how this approach is applied is described in [EC3]. Tumor areas are detected with an accuracy of 73.4 %, a sensitivity of 78 % and a specificity of 69 %.

The endoscopic combination of OCT and Raman can provide visual information to assist the diagnosis of bladder staging and grading during cytology. Raman spectroscopy demonstrated distinct spectral differences in the biochemical composition of non-tumor, low- and high-grade tumor in bladder tissue *ex vivo*, particularly in the Raman bands associated to lipids and collagen. The biochemical statistical modeling using Raman spectra of the bladder biopsies and the MCR concentrations of extracted collagen component in the bulk samples demonstrated that the presence of collagen is reduced in tumor tissue in comparison to the non-tumor tissue. The obtained MCR maps could be used to chemically visualize the constituent distinction of non-tumor and tumor biopsies.

4

Summary

Raman spectroscopy systems and chemometric data analysis have been demonstrated to be capable to assist disease diagnosis in oncology. Employing new instrumental implementations, data handling and diagnostic classification algorithms, it was possible to show the feasibility of Raman spectroscopic systems in the characterization of cancerous tumors in different organs. Although Raman spectroscopy has been extensively studied in diverse oncological applications, there are open challenges that need to be tackled when implementing compact fiber-based Raman systems, introduced in [EC2]. For one, more attention needs to be paid to the pre-treatment of data, especially when correcting the background signal coming from the sample (autofluorescence) and the setup (fiber, filters and optical elements). In addition, it is required to explore in detail the evaluation of tissue heterogeneity and its impact on the development, validation and robustness of classification models. Furthermore, the biochemical information provided by Raman spectroscopy is limited to the sample surface and its biochemical constituents, missing morphological cross-sectional features which are relevant to early tumor staging. Therefore, the combination of modalities plays an important role in achieving a more comprehensive interpretation of the detected cancerous tumor. The aforementioned challenges were addressed in this thesis. The investigations reported were related to three main themes: pre-treatment workflow and background correction, hierarchical

modeling and validation on heterogeneous samples and combination of Raman spectroscopy with modalities that complement morphological and biochemical data.

In the first study, experimental and computational methods to subtract fluorescence and fiber background in biological samples were evaluated from theoretical and practical viewpoints [EC1]. The theoretical evaluation of SERDS (instrumental technique) and EMSC (computational method) on lipid, protein and collagen samples was performed on simulated data sets with artificial fluorescence and noise levels. SERDS is simulated by an in-house algorithm that mimics recorded spectra at different wavelengths by shifting the spectra and computing the difference between the shifted spectra. In addition, the algorithm simulates the different noise and fluorescence intensities and correlates the shifted spectra to evaluate the optimal shift. Computational background correction was performed by using an EMSC function (available in R). Before applying EMSC, an in-house algorithm simulates computationally the fluorescence background using a polynomial approach. The background correction is performed at different background and noise intensities. EMSC was selected after comparing its performance with other background correction approaches such as the modified polynomial fitting, asymmetric least squares, iterative least squares and fill peaks algorithms, this is presented in more detail in [EC2]. The performance of the instrumental and computational approach was compared by evaluating the signal to noise ratio (SNR) of the corrected spectra. It was demonstrated that to obtain good background correction by SERDS the spectra first must be smoothed and baseline corrected in order to compensate signal intensity fluctuations and an additional computational background correction is required to achieve background-free difference spectra. The study also showed that a large shift allows retaining more signal intensity in a spectrum after subtraction, where optimal shifts of 7 to 11 nm were computed for different biological constituents. The presented optimal wavelength shifts are larger than expected, but in practice large shifts can lead to the excitation of different fluorophores resulting in diverse fluorescence profiles. SERDS spectra are also challenging for further analysis. Even though specialized reconstruction algorithms are available, it is still complicated to get an adequate determination of the exact band positions. Nevertheless, SERDS can be a potential solution to subtract unknown background since it does not need previous knowledge of the background to perform a correction. The background correction provided by EMSC for the simulated and experimental data yields promising results, achieving higher SNR than SERDS in the corrected spectra. On the other hand, complex samples and backgrounds can be challenging to correct because there is a need to compute approximations of pure spectra and fluorescence background components. Concisely, EMSC and SERDS are powerful tools for fluorescence background correction. For

the situation in which background type is known and can be reliably estimated, EMSC surpasses SERDS, since it does not modify the Raman spectrum and does not need additional equipment to perform the correction. Nevertheless, when the background is unknown and cannot be estimated, SERDS could potentially be a good choice to suppress the background.

The second investigation presents a study in which fiber-based Raman spectroscopy is used to differentiate bladder cancer from healthy tissue, especially giving attention to the influence of heterogeneity in the measured samples observed when performing Raman mapping of the tissues, see [EC2]. This study was focused on, firstly, proving that fiber-based Raman spectroscopy imaging can be applied to effectively assist bladder cancer diagnosis mimicking *in vivo* conditions by providing tumor differentiation and grading. Secondly, presenting a data pre-processing workflow which automatically corrects fiber and autofluorescence background signal. Thirdly, introducing a robust chemometric scheme, capable to extract comprehensive information from the biopsies and effectively classify non-tumor, low- and high-grade tumor bladder tissue. Lastly, the impact of heterogeneity on the model performance was evaluated using the prediction of first level model and the biochemical band information distribution to compute the tumor/non-tumor relation with the dominant constituents of bladder tissue. The optimal workflow to pre-treat the acquired data was also based in an evaluation of effective computational methods. Within the available background correction methods in this study, asymmetric least squares (ALS), the polynomial fitting, statistics-sensitive non-linear iterative peak-clipping algorithm (SNIP) correction and EMSC were tested. In [EC2] it is shown that ALS leads to over-fitting in the low and high-wavenumber region and background from fiber and substrate is not suppressed. Similar observations were made when correcting with polynomial fitting. On the one hand, SNIP correction could remove fiber background as EMSC does; on the other hand it requires higher computational effort taking longer than EMSC to compute the correction and shows higher standard deviation. Therefore, EMSC was selected to automatically correct the background of all measured biopsies. Four classifiers were tested to accomplish robust classification. Before applying the classifier, data reduction was performed by the partial least square (PLS) method. Among the tested classifiers LDA demonstrated the best performance compared to quadrant discriminant analysis (QDA), support vector machine (SVM) and linear progression (LP), the results of the performance are shown in [EC2]. The LDA classifier achieved the highest sensitivity and accuracy and demonstrated being less prone to over-fitting in comparison to QDA. Nevertheless, a good classifier is not enough in order to achieve the best performance, considering that the data set contains heterogeneous sets of spectra. We proposed in this study a new approach to build and validate the model, by applying a hierarchical workflow, where ini-

tially tumor and non-tumor spectra are classified by employing k -fold cross validation. The first level models ML1 differentiate between tumor and non-tumor achieving 92 % accuracy and only tumor regions from tumor biopsies were sent to the second level models ML2 for the high-grade/low-grade classifications. In [EC2] it was also demonstrated that the new classification strategy achieved better scores when discriminating tumor grade than the classical one level model classification procedure, despite that tumor grading differentiation has been very challenging due to the data size, the designed classification scheme proved to be efficient compared to classical methods. This clinical study, as preliminary step to precede performing *in vivo* tests, is evidence that fiber-based Raman spectroscopy can serve as a very useful modality to effectively discriminate healthy and tumor tissue as well as tumor grades during TURBT. Tissue heterogeneity was tackled with the predictions achieved with ML1, where the mean predictions of each pixel were mapped to display tumor and non-tumor sections of each biopsy, the results were discussed in more detail in [EC2]. Collagen and lipid band intensities were also mapped, and the band intensity distribution was correlated with the ML1 mean prediction to show the relation between collagen and lipid content in healthy and cancerous tissue. Collagen rich regions are observed for healthy tissue in comparison to cancerous tissue which is lipid rich. These findings demonstrate that the fiber-based Raman system is capable to complement cystoscopy during TURBT conditions in order to obtain immediate tumor and cancer grading discrimination.

The combination of modalities was investigated in study three [EC3], where Raman spectroscopy (RS) and optical coherence tomography (OCT) were implemented in a fiber-based setup *ex vivo*. The investigation focuses on demonstrating that the fiber-based implementations, which can be integrated into endoscopes, can assess tumor in-situ and providing grading of the bladder wall. As initial stage to achieve optimal *in vivo* performance, [EC3] reports the development of a combined OCT-RS system which provides tumor staging and grading of bladder biopsies. The system is designed for *in vivo* performance by employing fiber probes for each modality in order to obtain operation benchmarks for the best expected scheme. In total, 119 biopsies were measured by imaging the top surface of the biopsy mimicking *in vivo* circumstances. To image the biopsy a motorized X-Y platform was employed for the scanning and OCT stacks and Raman spectra were collected from the same locations. Approximately 9 OCT stacks and 300 Raman spectra were acquired per biopsy and the same biopsy surface was also sent for histopathological analysis. The OCT images were analyzed by applying texture analysis to classify the OCT images automatically, which effectively allowed the successful differentiation of different tumor stages. In addition, the OCT stacks were further treated to acquire equally sized fragments excluding the border areas of the field

of view to avoid high texture features. The Raman spectra were pre-processed as described in materials and methods section of [EC2], following a specific workflow to pre-treat Raman spectra such as calibration, denoising, EMSC background correction and area normalization. Statistical modeling of the Raman data was performed by applying hierarchical classification as reported in [EC2] and [EC3], where dimension reduction by PLS and classification by LDA were conducted. The cross validation of the model was done by applying k -folds and the validation of the models was performed by a hierarchical scheme which created two model levels (ML1 and ML2) to classify firstly tumor/non-tumor and secondly low-/high-grade cancer tissue. The first classification layer (ML1) predictions were employed to input the tumor areas to the second classification layer (ML2). In addition, Raman prediction maps and multivariate curve resolution (MCR) were applied to map the collagen distribution on biopsies, as it is one of the main constituents employed to differentiate cancerous tumor from normal bladder tissue. The diagnostic evaluation of OCT achieved 78 % sensitivity and 69 % specificity for early stage cancer differentiation. RS achieved in ML2 a sensitivity of 81 % and specificity of 61 % for low- and high-grade tissue discrimination and to distinguish non-tumor tissue the ML1 provided a sensitivity of 95 % and a specificity of 88 %. Relevant observations that link the LDA coefficients and constituent bands were also reported, where tumor related negative coefficients were associated with lipid bands and LDA positive coefficients with collagen bands. OCT and RS information was also correlated by overlapping the OCT stacks and the RS prediction maps in order to visualize the tumor sections predicted by RS with the OCT staging to detect tumor areas on the biopsy. Clinically relevant information about tumor stage and grade was provided by the developed OCT-RS system, where both modalities provided comprehensive diagnostic evidence about tissue staging and grading to complement in-situ assessment of the bladder wall. The reported findings open the path for further development of multimodal endoscopic probes which facilitate OCT and RS to deliver the surgeons relevant clinical data in real-time. In-situ tumor discrimination enables better biopsy handling and minimizes tissue resection by providing accurate assessment.

In conclusion, this thesis is an advance towards resolving most of the open concerns of Raman spectroscopic fiber-based implementation for real-time cancer diagnosis of bladder tissue. The presented work provides: (1) Evaluation and comparison of background correction strategies of Raman spectra in highly fluorescent biological samples; (2) Assessment of bladder tumor grading through an automated fiber-based Raman imaging system as an initial stage for *in vivo* diagnosis; (3) Multimodal combination of OCT and RS employing endoscopic probes to diagnosis bladder tissue grading and staging mimicking *in vivo* conditions. All these contributions are substantial and highly beneficial to further drive the clinical

translation of Raman spectroscopy towards the bladder oncological field.

5

Zusammenfassung

Es wurde gezeigt, dass Ramanspektroskopische Systeme und chemometrische Datenanalysen die Diagnose von Krankheiten in der Onkologie unterstützen können. Mithilfe neuer instrumenteller Implementierungen, Datenhandhabungs- und diagnostischer Klassifizierungsalgorithmen konnte die Machbarkeit von Raman-spektroskopischen Systemen bei der Charakterisierung von Krebstumoren in verschiedenen Organen gezeigt werden. Obwohl die Raman-Spektroskopie in verschiedenen onkologischen Anwendungen eingehend untersucht wurde, gibt es einige offene Herausforderungen, die bei der Implementierung der in [EC2] eingeführten kompakten faserbasierten Raman-Systemen angegangen werden müssen. Zum einen muss der Vorbehandlung von Daten mehr Aufmerksamkeit gewidmet werden, insbesondere bei der Korrektur des Hintergrundsignals der Probe (Fluoreszenz) und des Aufbaus (Faser, Filter und optische Elemente). Darüber hinaus müssen die Bewertung der Gewebheterogenität und ihre Auswirkungen auf die Entwicklung und Validierung von Klassifizierungsmodellen eingehend untersucht werden. Beispielsweise müssen alternative Ansätze getestet werden, um eine robuste Modellierung aufzubauen. Darüber hinaus ist die biochemische Information, die durch Raman-Spektroskopie bereitgestellt wird, auf die Probenoberfläche und ihre biochemischen Bestandteile beschränkt, wobei morphologische Querschnittsmerkmale fehlen, die für das frühe Staging von Tumoren relevant sind. Daher spielt die Kombination der Modalitäten

eine wichtige Rolle für eine umfassendere Interpretation des erkannten Krebstumors. Auf diese genannten Herausforderungen wurden in der vorliegenden Arbeit eingegangen. Die Untersuchungen bezogen sich auf drei Hauptthemen: Vorbehandlung und Hintergrundkorrektur der Raman-Daten, hierarchische Modellierung und Validierung heterogener Proben und Kombination von Modalitäten, sodass sich morphologische und biochemische Daten ergänzen.

In der ersten Studie wurden experimentelle und rechnerische Methoden zur Subtraktion von Fluoreszenz und Faserhintergrund in biologischen Proben unter theoretischen und praktischen Gesichtspunkten bewertet [EC1]. Die theoretische Bewertung von SERDS (Instrumentaltechnik) und EMSC (Berechnungsmethode) an Lipid-, Protein- und Kollagenproben wurde an simulierten Datensätzen mit künstlicher Fluoreszenz und Rauschpegeln durchgeführt. SERDS wird durch einen hausinternen Algorithmus simuliert, der aufgezeichnete Spektren bei verschiedenen Wellenlängen nachahmt, indem die Spektren verschoben und die Differenz zwischen den verschobenen Spektren berechnet werden. Zusätzlich simuliert der Algorithmus die verschiedenen Rausch- und Fluoreszenzintensitäten und korreliert die verschobenen Spektren, um die optimale Verschiebung der Anregungswellenlänge zu berechnen. Die rechnergestützte Hintergrundkorrektur wurde mit einer EMSC-Funktion (verfügbar in R) durchgeführt. Vor der Anwendung von EMSC simuliert ein hausinterner Algorithmus den Fluoreszenzhintergrund mithilfe eines Polynomansatzes. Die Hintergrundkorrektur wird bei unterschiedlichen Hintergrund- und Rauschintensitäten durchgeführt. EMSC wurde ausgewählt, nachdem seine Leistung mit anderen Ansätzen zur Hintergrundkorrektur verglichen wurde, wie der modifizierten Polynomannäherung, den Algorithmen für asymmetrische kleinste Quadrate, iterative kleinste Quadrate und Fill Peaks. Dies wird in [EC2] ausführlicher dargestellt. Die Leistung des instrumentellen und rechnerischen Ansatzes wurde durch Auswertung des Signal-Rausch-Verhältnisses (SNR) der korrigierten Spektren verglichen. Es wurde gezeigt, dass zur Erzielung einer guten Hintergrundkorrektur durch SERDS die Spektren zuerst geglättet und die Basislinie korrigiert werden müssen, um Signalintensitätsschwankungen auszugleichen, und eine zusätzliche rechnerische Hintergrundkorrektur erforderlich ist, um hintergrundfreie Differenzspektren zu erzielen. Die Studie zeigte auch, dass eine große Verschiebung es ermöglicht, mehr Signalintensität in einem Spektrum nach der Subtraktion beizubehalten, wobei optimale Verschiebungen von 7 bis 11 nm für verschiedene biologische Bestandteile berechnet wurden. Die dargestellten optimalen Wellenlängenverschiebungen sind größer als erwartet, aber in der Praxis können große Verschiebungen zur Anregung verschiedener Fluorophore führen, was zu verschiedenen Fluoreszenzprofilen führt. SERDS-Spektren sind auch eine Herausforderung für die weitere Analyse. Obwohl spezial-

isierte Rekonstruktionsalgorithmen zur Verfügung stehen, ist es immer noch schwierig, die genauen Bandpositionen angemessen zu bestimmen. Dennoch kann SERDS eine mögliche Lösung sein, um unbekanntem Hintergrund zu subtrahieren, da keine Vorkenntnisse erforderlich sind, um eine Korrektur durchzuführen. Die von der EMSC bereitgestellte Hintergrundkorrektur für die simulierten und experimentellen Daten liefert vielversprechende Ergebnisse und erzielt in den korrigierten Spektren ein höheres SNR als SERDS. Allerdings können komplexe Proben und Hintergründe schwierig zu korrigieren sein, da Näherungen von unbehandelten Spektren und Fluoreszenzhintergrundkomponenten berechnet werden müssen. Zusammenfassend, EMSC und SERDS sind leistungsstarke Methoden für die Hintergrundkorrektur von Fluoreszenz. Für die Situation, in der der Hintergrundtyp bekannt ist und zuverlässig geschätzt werden kann, übertrifft EMSC SERDS, da es das Raman-Spektrum nicht modifiziert und keine zusätzliche Ausrüstung benötigt, um ein höheres SNR zu erreichen. Wenn der Hintergrund unbekannt ist und nicht geschätzt werden kann, ist SERDS möglicherweise eine gute Wahl, um den Hintergrund zu unterdrücken.

Die zweite Untersuchung präsentiert eine Studie, in der faserbasierte Raman-Spektroskopie verwendet wird, um Blasenkrebsgewebe von gesundem Gewebe zu unterscheiden, wobei insbesondere der Einfluss der Heterogenität in den gemessenen Proben berücksichtigt wird, die bei der Raman-Abbildung der Gewebe beobachtet wurden, siehe [EC2]. Diese Studie konzentrierte sich zum einen auf den Nachweis, dass die faserbasierte Raman-Spektroskopie angewendet werden kann, um die Blasenkrebsdiagnose effektiv zu unterstützen und in-vivo-Zustände zu simulieren. Dies geschieht indem Tumor-Differenzierung und Grading bereitgestellt werden. Zum anderen wird eine Datenvorbehandlung vorgestellt, die automatisch das Hintergrundsignal von Fasern und Autofluoreszenz korrigiert. Ebenfalls wird eine robuste, chemometrische Methode präsentiert, mit der umfassende Informationen aus den Biopsien extrahiert und Gewebe, das keine Tumore enthält, sowie niedrig- und hochgradiges Tumorgewebe effektiv klassifiziert werden können. Abschließend wird der Einfluss der Heterogenität auf die Modellleistung unter Verwendung der Vorhersage des First-Level-Modells und der Verteilung der biochemischen Bandeninformationen bewertet, um die Tumor/Nicht-Tumor-Beziehung mit den dominierenden Bestandteilen des Blasengewebes zu berechnen. Der optimale Workflow zur Vorbehandlung der erfassten Daten basierte auch auf einer Bewertung effektiver Berechnungsmethoden. Im Rahmen der verfügbaren Hintergrundkorrekturmethode in dieser Studie wurden asymmetrische kleinste Quadrate (ALS), die Polynom-Anpassung, statistik-sensitive nichtlineare iterative Peak-Clipping-Algorithmus (SNIP) - Korrektur und EMSC getestet. In [EC2] wird gezeigt, dass ALS zu einer Überanpassung im Bereich niedriger und hoher Wellenzahlen führt und der Hintergrund von Fasern und

Substraten nicht unterdrückt wird. Ähnliche Beobachtungen wurden bei der Korrektur mit Polynomannpassung gemacht. Einerseits könnte die SNIP-Korrektur den Faserhintergrund ebenso wie die EMSC entfernen, andererseits erfordert sie einen höheren Rechenaufwand als die EMSC, und zeigt eine höhere Standardabweichung. Daher wurde EMSC ausgewählt, um den Hintergrund aller gemessenen Biopsien automatisch zu korrigieren.

Vier Klassifikatoren wurden getestet, um eine robuste Klassifizierung zu erreichen. Vor der Anwendung des Klassifikators wurde die Datenreduktion durch Partial Least Square (PLS) durchgeführt. Unter den getesteten Klassifikatoren zeigte LDA die beste Leistung im Vergleich zu Quadrantendiskriminanzanalyse (QDA), Support Vector Machine (SVM) und linearer Progression (LP). Die Ergebnisse der Leistungsfähigkeit sind in [EC2] angegeben. Der LDA-Klassifikator erzielte die höchste Empfindlichkeit und Genauigkeit und zeigte, dass er im Vergleich zu QDA weniger anfällig für Überanpassung ist. Trotzdem reicht ein guter Klassifikator nicht aus, um die beste Leistung zu erzielen, wenn man bedenkt, dass der Datensatz heterogene Datensätze von Spektren enthält. Wir schlugen in dieser Studie einen neuen Ansatz zur Erstellung und Validierung des Modells durch Anwendung eines hierarchischen Workflows vor, bei dem zunächst Tumor- und Nicht-Tumor-Spektren mithilfe einer k -fachen Kreuzvalidierung klassifiziert werden. Die Modelle der ersten Ebene ML1 unterscheiden zwischen Tumor und Nicht-Tumor mit einer Genauigkeit von 92%, woraufhin nur Tumorregionen aus Tumorbiopsien für die hochgradigen/niedriggradigen Klassifikationen an die Modelle der zweiten Ebene ML2 weitergegeben wurden. In [EC2] wurde auch gezeigt, dass die neue Klassifizierungsstrategie bei der Unterscheidung des Tumorgrades bessere Ergebnisse erzielt als das klassische einstufige Modellklassifizierungsverfahren. Obwohl die Unterscheidung des Tumorgrades aufgrund der Datengröße des entworfenen Klassifizierungsschemas sehr schwierig war, erwies sich das zweistufige Verfahren im Vergleich zu klassischen Methoden als effizient. Diese klinische Studie als vorbereitender Schritt für die Durchführung von *in vivo* Tests ist ein Beweis dafür, dass die faserbasierte Raman-Spektroskopie eine sehr vielversprechende Methode zur wirksamen Unterscheidung von gesundem und tumorartigen Gewebe sowie Tumorgraden während der TURBT darstellt. Die Gewebheterogenität wurde mit den mit ML1 erzielten Vorhersagen untersucht, wobei die gemittelte Vorhersage jedes Pixels so abgebildet wurden, dass Tumor- und Nicht-Tumor-Schnitte jeder Biopsie angezeigt wurden. Die Ergebnisse wurden detailliert in [EC2] diskutiert. Kollagen- und Lipidbandenintensitäten wurden ebenfalls visualisiert, und die Bandenintensitätsverteilung mit der mittleren ML1-Vorhersage korreliert, um die Beziehung zwischen Kollagen- und Lipidgehalt in gesundem und krebsartigem Gewebe zu zeigen. Kollagenreiche Regionen werden für gesundes Gewebe im Vergleich zu krebsartigem Gewebe beobachtet, das im Gegensatz dazu lipidhaltig ist. Diese Ergebnisse

zeigen, dass das faserbasierte Raman-System die Zystoskopie unter TURBT-Bedingungen ergänzen kann, um eine sofortige Einstufung von Tumor und Krebs zu erreichen.

Die Kombination von verschiedenen Modalitäten wurde in der dritten Studie [EC3] untersucht, in der Raman-Spektroskopie (RS) und optische Kohärenztomographie (OCT) in einem faserbasierten Aufbau *ex vivo* implementiert wurden. Die Untersuchung konzentriert sich auf den Nachweis, dass fasergestützte Implementierungen, die in Endoskope integriert werden können, Tumore *in situ* bewerten und eine Einstufung der Blasenwand ermöglichen. [EC3] berichtet über die Entwicklung eines kombinierten OCT-RS-Systems, das die Tumorabstufung und Einstufung von Blasenbiopsien ermöglicht, um eine optimale *in vivo* Leistungsfähigkeit zu erzielen. Das System ist für *in vivo* Anwendungen ausgelegt, indem für jede Modalität Fasersonden verwendet werden, um Indikatoren zur Handhabung für das am besten zu erwartende Schema zu erhalten. Insgesamt wurden 119 Biopsien durch Vermessung der Oberfläche gemessen, wobei die *in vivo* Bedingungen nachgeahmt wurden. Um die Biopsie bildgebend zu messen, wurde ein motorisierter X-Y-Tisch für das Scannen verwendet und OCT-Volumen und Raman-Spektren wurden an denselben Orten gesammelt. Pro Biopsie wurden ungefähr 9 OCT-Volumen und 300 Raman-Spektren aufgenommen, und die gleiche Biopsie wurde auch zur histopathologischen Analyse gesendet. Die OCT-Bilder wurden analysiert, indem eine Texturanalyse angewendet wurde, um die OCT-Bilder automatisch zu klassifizieren, was die erfolgreiche Differenzierung des Tumors effektiv ermöglichte. Zusätzlich wurden die OCT-Volumen weiter behandelt, um Fragmente gleicher Größe zu erhalten, mit Ausnahme der Randbereiche des Sichtfelds um hohe Texturmerkmale zu vermeiden. Die Raman-Spektren wurden wie im Abschnitt [EC2] "Materialien und Methoden" beschrieben vorbehandelt, um Raman-Spektren wie Kalibrierung, Rauschunterdrückung, EMSC-Hintergrundkorrektur und Flächennormalisierung vorzubereiten. Die statistische Modellierung der Raman-Daten wurde durchgeführt, indem eine hierarchische Klassifizierung angewendet wurde, wie in [EC2] und [EC3] angegeben, wobei eine Dimensionsreduzierung durch PLS und eine Klassifizierung durch LDA durchgeführt wurden. Eine k -fache Kreuzvalidierung des Modells und die Validierung der Modelle erfolgte durch ein hierarchisches Schema mit zwei Modellebenen (ML1 und ML2). Zuerst wird Tumor / Nicht-Tumor und als zweites niedrig- / hochwertiges Krebsgewebe klassifiziert. Die Vorhersagen der ersten Klassifizierungsschicht (ML1) wurden verwendet, um die Tumorgebiete in die zweite Klassifizierungsschicht (ML2) einzugeben. Darüber hinaus wurden Raman-Vorhersage-Abbildungen und multivariate Kurvenauflösungen (MCR) angewendet, um die Kollagenverteilung auf Biopsien abzubilden, da dies einer der Hauptbestandteile ist, die zur Unterscheidung von Krebstumor und normalem Blasengewebe eingesetzt werden. Die

diagnostische Bewertung durch OCT ergab eine Sensitivität von 78% und eine Spezifität von 69% für die Krebsdifferenzierung im Frühstadium. ML2 durch RS erreichte eine Sensitivität von 81% und eine Spezifität von 61% für die Unterscheidung von geringem und hohem Tumorgrad. Zur Unterscheidung von Nicht-Tumorgewebe lieferte das ML1 eine Sensitivität von 95% und eine Spezifität von 88%. Relevante Beobachtungen, die die LDA-Koeffizienten und die konstituierenden Banden verknüpfen, wurden ebenfalls berichtet, wobei mit Tumor assoziierte negative Koeffizienten mit Lipidbanden und positive LDA-Koeffizienten mit Kollagenbanden assoziiert wurden. OCT- und RS-Informationen wurden auch durch Überlappen der OCT-Volumen und der RS-Vorhersage-Abbildungen korreliert, um die Tumovorhersage von RS mit dem OCT-Staging zur Erkennung von Tumorgebieten auf der Biopsie zu visualisieren. Klinisch relevante Informationen zu Tumoreinstufung und -grad lieferte das entwickelte OCT-RS-System, bei dem beide Modalitäten umfassende diagnostische Belege für die Gewebestufe und -klassifizierung ermöglichte, um die *in situ* Beurteilung der Blasenwand zu ergänzen. Die präsentierten Ergebnisse öffnen den Weg für weitere Entwicklungen multimodaler endoskopischer OCT und RS Sonden, die es ermöglichen, den Chirurgen relevante klinische Daten in Echtzeit zu liefern. *In situ* Tumordiskriminierung ermöglicht eine bessere Handhabung der Biopsie und eine Minimierung der Gewebsresektion.

Zusammenfassend ist die vorliegende Arbeit ein Fortschritt bei der Lösung der meisten offenen Herausforderungen der Implementierung von Raman-spektroskopischen Fasern für die Echtzeit-Krebsdiagnose von Blasengewebe. Die vorgestellte Arbeit bietet: (1) Bewertung und Vergleich von Hintergrundkorrekturstrategien von Raman-Spektren in stark fluoreszierenden biologischen Proben; (2) Bewertung der Blasen-Tumor-Einstufung durch ein automatisiertes, fasergestütztes Raman-Bildgebungssystem als ein Anfangsstadium für die *in vivo* Diagnose; (3) Multimodale Kombination von OCT und RS unter Verwendung von endoskopischen Sonden zur Diagnose der Blasengewebsklassifizierung und zur Durchführung unter *in vivo*-ähnlichen Bedingungen. Alle diese Beiträge sind substanziell und von großem Nutzen, um die klinische Translation der Raman-Spektroskopie im Bereich der Blasenonkologie voranzutreiben.

6

Bibliography

- [1] Freddie Bray, Jacques Ferlay, Isabelle Soerjomataram, Rebecca L. Siegel, Lindsey A. Torre, and Ahmedin Jemal. Global cancer statistics 2018: GLOBOCAN estimates of incidence and mortality worldwide for 36 cancers in 185 countries. 68(6):394–424.
- [2] Sebastien Antoni, Jacques Ferlay, Isabelle Soerjomataram, Ariana Znaor, Ahmedin Jemal, and Freddie Bray. Bladder cancer incidence and mortality: A global overview and recent trends. 71(1):96–108.
- [3] K. D. Sievert, B. Amend, U. Nagele, D. Schilling, J. Bedke, M. Horstmann, J. Hennenlotter, S. Kruck, and A. Stenzl. Economic aspects of bladder cancer: what are the benefits and costs? 27(3):295–300.
- [4] Robert S. Svatek, Brent K. Hollenbeck, Sten Holmäng, Richard Lee, Simon P. Kim, Arnulf Stenzl, and Yair Lotan. The economics of bladder cancer: Costs and considerations of caring for this disease. 66(2):253–262.
- [5] Frank A. Sloan, Arseniy P. Yashkin, Igor Akushevich, and Brant A. Inman. The cost to medicare of bladder cancer care.

- [6] Olivier Traxer, Federico Pasqui, Bernard Gattegno, and Margaret S. Pearle. Technique and complications of transurethral surgery for bladder tumours. 94(4):492–496.
- [7] Richard J. Sylvester, Adrian P.M. van der Meijden, Willem Oosterlinck, J. Alfred Witjes, Christian Bouffoux, Louis Denis, Donald W.W. Newling, and Karlheinz Kurth. Predicting recurrence and progression in individual patients with stage ta t1 bladder cancer using EORTC risk tables: A combined analysis of 2596 patients from seven EORTC trials. 49(3):466–477.
- [8] Grace Cheung, Arun Sahai, Michele Billia, Prokar Dasgupta, and Muhammad S Khan. Recent advances in the diagnosis and treatment of bladder cancer. 11:13.
- [9] Madelon N. M. van der Aa, Ewout W. Steyerberg, Chris Bangma, Bas W. G. van Rhijn, Ellen C. Zwarthoff, and Theo H. van der Kwast. Cystoscopy revisited as the gold standard for detecting bladder cancer recurrence: diagnostic review bias in the randomized, prospective CEFUB trial. 183(1):76–80.
- [10] Marko Babjuk. Trends in bladder cancer incidence and mortality: Success or disappointment? 71(1):109–110.
- [11] Viktor Soukup, Marko Babjuk, Joaquim Bellmunt, Guido Dalbagni, Gianluca Giannarini, Oliver W. Hakenberg, Harry Herr, Eric Lechevallier, and Maria J. Ribal. Follow-up after surgical treatment of bladder cancer: A critical analysis of the literature. 62(2):290–302.
- [12] Joshua S. Engelskjerd and Christopher M. Deibert. Cystoscopy. In *StatPearls*. StatPearls Publishing.
- [13] Timothy C. Chang, Gautier Marcq, Bernhard Kiss, Dharati R. Trivedi, Kathleen E. Mach, and Joseph C. Liao. Image-guided transurethral resection of bladder tumors – current practice and future outlooks. 3(3):149–159.
- [14] Christopher J. Down, Rajesh Nair, and Ramesh Thurairaja. Bladder cancer. 34(10):532–539.
- [15] Tina Schubert, Steffen Rausch, Omar Fahmy, Georgios Gakis, and Arnulf Stenzl. Optical improvements in the diagnosis of bladder cancer: implications for clinical practice. 9(11):251–260.

- [16] Zhangqun Ye, Jia Hu, Xiaodong Song, Fan Li, Xuetao Zhao, Shan Chen, Xiaofeng Wang, Dalin He, Jinhai Fan, Dingwei Ye, Jinchun Xing, Tiejun Pan, and Dongwen Wang. A comparison of NBI and WLI cystoscopy in detecting non-muscle-invasive bladder cancer: A prospective, randomized and multi-center study. 5(1).
- [17] Jen-Jane Liu, Michael J. Droller, and Joseph C. Liao. New optical imaging technologies for bladder cancer: Considerations and perspectives. 188(2):361–368.
- [18] Beata Brozek-Pluska, Jacek Musial, Radzislaw Kordek, Elena Bailo, Thomas Dieing, and Halina Abramczyk. Raman spectroscopy and imaging: applications in human breast cancer diagnosis. 137(16):3773.
- [19] Pavel Matousek, Edward R. C. Draper, Allen E. Goodship, Ian P. Clark, Kate L. Ronayne, and Anthony W. Parker. Noninvasive raman spectroscopy of human tissue in vivo. 60(7):758–763.
- [20] F. Bonnier, A. Mehmood, P. Knief, A. D. Meade, W. Hornebeck, H. Lambkin, K. Flynn, V. McDonagh, C. Healy, T. C. Lee, F. M. Lyng, and H. J. Byrne. In vitro analysis of immersed human tissues by raman microspectroscopy. 42(5):888–896.
- [21] Christoph Krafft and Jürgen Popp. The many facets of raman spectroscopy for biomedical analysis. 407(3):699–717.
- [22] James F. Brennan, Yang Wang, Ramachandra R. Dasari, and Michael S. Feld. Near-infrared raman spectrometer systems for human tissue studies. 51(2):201–208.
- [23] Mette Mogensen, Hanan A. Morsy, Lars Thrane, and Gregor B.E. Jemec. Morphology and epidermal thickness of normal skin imaged by optical coherence tomography. 217(1):14–20.
- [24] P. Beatriz Garcia-Allende, Iakovos Amygdalos, Hiruni Dhanapala, Robert D. Goldin, George B. Hanna, and Daniel S. Elson. Morphological analysis of optical coherence tomography images for automated classification of gastrointestinal tissues. 2(10):2821.
- [25] Adolf Friedrich Fercher. Optical coherence tomography – development, principles, applications. 20(4):251–276.
- [26] Hui Wang, Caroline Magnain, Sava Sakadžić, Bruce Fischl, and David A. Boas. Characterizing the optical properties of human brain tissue with high numerical aperture optical coherence tomography. 8(12):5617–5636.

- [27] Wei Luo, Freddy T. Nguyen, Adam M. Zysk, Tyler S. Ralston, John Brockenbrough, Daniel L. Marks, Amy L. Oldenburg, and Stephen A. Boppart. Optical biopsy of lymph node morphology using optical coherence tomography. 4(5):539–547.
- [28] Gregory W. Auner, S. Kiran Koya, Changhe Huang, Brandy Broadbent, Micaela Trexler, Zachary Auner, Angela Elias, Katlyn Curtin Mehne, and Michelle A. Brusatori. Applications of raman spectroscopy in cancer diagnosis. 37(4):691–717.
- [29] Inês P. Santos, Elisa M. Barroso, Tom C. Bakker Schut, Peter J. Caspers, Cornelia G. F. van Lanschot, Da-Hye Choi, Martine F. van der Kamp, Roeland W. H. Smits, Remco van Doorn, Rob M. Verdijk, Vincent Noordhoek Hegt, Jan H. von der Thüsen, Carolien H. M. van Deurzen, Linetta B. Koppert, Geert J. L. H. van Leenders, Patricia C. Ewing-Graham, Helena C. van Doorn, Clemens M. F. Dirven, Martijn B. Busstra, Jose Hardillo, Aniel Sewnaik, Ivo ten Hove, Hetty Mast, Dominiek A. Monserez, Cees Meeuwis, Tamar Nijsten, Eppo B. Wolvius, Robert J. Baatenburg de Jong, Gerwin J. Puppels, and Senada Koljenović. Raman spectroscopy for cancer detection and cancer surgery guidance: translation to the clinics. 142(17):3025–3047.
- [30] Matthew J. Baker, Hugh J. Byrne, John Chalmers, Peter Gardner, Royston Goodacre, Alex Henderson, Sergei G. Kazarian, Francis L. Martin, Julian Moger, Nick Stone, and Josep Sulé-Suso. Clinical applications of infrared and raman spectroscopy: state of play and future challenges. 143(8):1735–1757.
- [31] Practical raman spectroscopy. OCLC: 246612753.
- [32] C. V. Raman and K. S. Krishnan. A new type of secondary radiation. 121(3048):501.
- [33] Bret C. Windom and David W. Hahn. Raman spectroscopy. In Q. Jane Wang and Yip-Wah Chung, editors, *Encyclopedia of Tribology*, pages 2742–2747. Springer US.
- [34] *Spectroscopic instrumentation: fundamentals and guidelines for astronomers*. Springer.
- [35] Princenton Instruments. *Datasheet PIXIS 1300*, 4 2013. Rev. 2.1.
- [36] Zhiyun Li, M. Jamal Deen, Shiva Kumar, and Ponnambalam Ravi Selvaganapathy. Raman spectroscopy for in-line water quality monitoring — instrumentation and potential. In *Sensors*.
- [37] Steve Howell. Basics of charge coupled devices. page 27.

- [38] Eliana Cordero, Ines Latka, Christian Matthäus, Iwan Schie, and Jürgen Popp. In-vivo raman spectroscopy: from basics to applications. 23(7):1–23.
- [39] Ines Latka, Sebastian Dochow, Christoph Krafft, Benjamin Dietzek, and Jürgen Popp. Fiber optic probes for linear and nonlinear raman applications - current trends and future development: Fiber optic raman probes. 7(5):698–731.
- [40] Luís F. Santos, Rolf Wolthuis, S. Koljenović, Rui M. Almeida, and Gerwin J. Puppels. Fiber-optic probes for in vivo raman spectroscopy in the high-wavenumber region. 77(20):6747–6752.
- [41] Oliver Stevens, Ingeborg E. Iping Petterson, John C. C. Day, and Nick Stone. Developing fibre optic raman probes for applications in clinical spectroscopy. 45(7):1919–1934.
- [42] Jason T. Motz, Martin Hunter, Luis H. Galindo, Joseph A. Gardecki, John R. Kramer, Ramachandra R. Dasari, and Michael S. Feld. Optical fiber probe for biomedical raman spectroscopy. 43(3):542.
- [43] Nicholas Stone, Catherine Kendall, Jenny Smith, Paul Crow, and Hugh Barr. Raman spectroscopy for identification of epithelial cancers. 126:141.
- [44] A. Saha, I. Barman, N. C. Dingari, S. McGee, Z. Volynskaya, L. H. Galindo, W. Liu, D. Plecha, N. Klein, R. R. Dasari, and M. Fitzmaurice. Raman spectroscopy: a real-time tool for identifying microcalcifications during stereotactic breast core needle biopsies. *Biomed. Opt. Express*, 2(10):2792–2803, Oct 2011.
- [45] P. J. Caspers, G. W. Lucassen, R. Wolthuis, H. A. Bruining, and G. J. Puppels. In vitro and in vivo Raman spectroscopy of human skin. *BIOSPECTROSCOPY-NEW YORK-*, 4:S31–S40, 1998.
- [46] H. Lui, J. Zhao, D. McLean, and H. Zeng. Real-time Raman Spectroscopy for In Vivo Skin Cancer Diagnosis. *Cancer Research*, 72(10):2491–2500, May 2012.
- [47] Nikolaos Kourkoumelis, Ioannis Balatsoukas, Violetta Moulia, Aspasia Elka, Georgios Gaitanis, and Ioannis Bassukas. Advances in the in vivo raman spectroscopy of malignant skin tumors using portable instrumentation. 16(7):14554–14570.
- [48] C. Fink and HA. Haenssle. Non-invasive tools for the diagnosis of cutaneous melanoma. *Skin Res Technol.*, 23(3):261–71, 2017.

- [49] Xu Feng, Austin J Moy, Hieu T. M. Nguyen, Jason Zhang, Matthew C. Fox, Katherine R. Sebastian, Jason S. Reichenberg, Mia K. Markey, and James W. Tunnell. Raman active components of skin cancer. *Biomedical Optics Express*, 8(6):2835–2850, May 2017.
- [50] Michael A. Short, Stephen Lam, Annette McWilliams, Jianhua Zhao, Harvey Lui, and Haishan Zeng. Development and preliminary results of an endoscopic raman probe for potential in vivo diagnosis of lung cancers. 33(7):711–713.
- [51] Zhiwei Huang, Seng Khoon Teh, Wei Zheng, Kan Lin, Khek Yu Ho, Ming Teh, and Khay Guan Yeoh. In vivo detection of epithelial neoplasia in the stomach using image-guided Raman endoscopy. *Biosensors and Bioelectronics*, 26(2):383–389, October 2010.
- [52] Zhiwei Huang, Mads Sylvest Bergholt, Wei Zheng, Kan Lin, Khek Yu Ho, Ming Teh, and Khay Guan Yeoh. In vivo early diagnosis of gastric dysplasia using narrow-band image-guided raman endoscopy. 15(3):037017.
- [53] Zhiwei Huang, Annette McWilliams, Harvey Lui, David I. McLean, Stephen Lam, and Haishan Zeng. Near-infrared raman spectroscopy for optical diagnosis of lung cancer. 107(6):1047–1052.
- [54] Andrea Molckovsky, Louis-Michel Wong Kee Song, Martin G. Shim, Norman E. Marcon, and Brian C. Wilson. Diagnostic potential of near-infrared raman spectroscopy in the colon: Differentiating adenomatous from hyperplastic polyps. 57(3):396–402.
- [55] A. Beljebbar, O. Bouché, M.D. Diébold, P.J. Guillou, J.P. Palot, D. Eudes, and M. Manfait. Identification of raman spectroscopic markers for the characterization of normal and adenocarcinomatous colonic tissues. 72(3):255–264.
- [56] Michael A. Short, Isabella T. Tai, David Owen, and Haishan Zeng. Using high frequency Raman spectra for colonic neoplasia detection. *Optics Express*, 21(4):5025–5034, February 2013.
- [57] Mads Sylvest Bergholt, Wei Zheng, Kan Lin, Khek Yu Ho, Ming Teh, Khay Guan Yeoh, Jimmy Bok Yan So, and Zhiwei Huang. Combining near-infrared-excited autofluorescence and raman spectroscopy improves in vivo diagnosis of gastric cancer. 26(10):4104–4110.

- [58] Michael A. Short, Wenbo Wang, Isabella T. Tai, and Haishan Zeng. Development and *in vivo* testing of a high frequency endoscopic raman spectroscopy system for potential applications in the detection of early colonic neoplasia. 9(1):44–48.
- [59] L Rotter, P Rotterová, I Kinkorová Luňáčková, Jana kašpírková, M Michal, and Robert Hudecek. Dysplasia and cervical cancer: Current diagnostic possibilities. *Ceska gynekologie / Ceska lekarska spolecnost J. Ev. Purkyne*, 79:314–320, November 2014.
- [60] Jianhua Mo, Wei Zheng, Jeffrey J. H. Low, Joseph Ng, A. Ilancheran, and Zhiwei Huang. High wavenumber raman spectroscopy for in vivo detection of cervical dysplasia. 81(21):8908–8915.
- [61] Shiyamala Duraipandian, Wei Zheng, Joseph Ng, Jeffrey J. H. Low, A. Ilancheran, and Zhiwei Huang. In vivo diagnosis of cervical precancer using Raman spectroscopy and genetic algorithm techniques. *The Analyst*, 136(20):4328, 2011.
- [62] Shiyamala Duraipandian, Wei Zheng, Joseph Ng, Jeffrey J. H. Low, A. Ilancheran, and Zhiwei Huang. Effect of hormonal variation on in vivo high wavenumber Raman spectra improves cervical precancer detection. page 82140A, February 2012.
- [63] J Delancey, J Gosling, K Creed, J Dixon, V Delmas, D Landon, and P Norton. Gross anatomy and cell biology of the lower urinary tract. page 66.
- [64] DUANE R. HICKLING, TUNG-TIEN SUN, and XUE-RU WU. Anatomy and physiology of the urinary tract: Relation to host defense and microbial infection. 3(4).
- [65] Christopher H. Fry and Bahareh Vahabi. The role of the mucosa in normal and abnormal bladder function. 119:57–62.
- [66] Donna E. Hansel. *Precision molecular pathology of bladder cancer*. Springer Science+Business Media.
- [67] David MacVicar. Carcinoma of the bladder. page 204.
- [68] Marko Babjuk, Maximilian Burger, Richard Zigeuner, Shahrokh F. Shariat, Bas W. G. van Rhijn, Eva Compérat, Richard J. Sylvester, Eero Kaasinen, Andreas Böhle, Joan Palou Redorta, Morgan Roupřet, and European Association of Urology. EAU guidelines on non-muscle-invasive urothelial carcinoma of the bladder: update 2013. 64(4):639–653.
- [69] Invasive bladder cancer. OCLC: ocm67375397.

- [70] Richard T. Bryan, Lucinda J. Billingham, and D. Michael A. Wallace. Narrow-band imaging flexible cystoscopy in the detection of recurrent urothelial cancer of the bladder. 101(6):702–706.
- [71] Maximilian Burger, Dirk Zaak, Christian G. Stief, Thomas Filbeck, Wolf-Ferdinand Wieland, Wolfgang Roessler, and Stefan Denzinger. Photodynamic diagnostics and noninvasive bladder cancer: Is it cost-effective in long-term application? a germany-based cost analysis. 52(1):142–147.
- [72] Arnulf Stenzl, Maximilian Burger, Yves Fradet, Lance A. Mynderse, Mark S. Soloway, J. Alfred Witjes, Martin Kriegmair, Alexander Karl, Yu Shen, and H. Barton Grossman. Hexaminolevulinate guided fluorescence cystoscopy reduces recurrence in patients with nonmuscle invasive bladder cancer. 184(5):1907–1914.
- [73] Shailendra S. Chauhan, Barham K. Abu Dayyeh, Yasser M. Bhat, Klaus T. Gottlieb, Joo Ha Hwang, Sri Komanduri, Vani Konda, Simon K. Lo, Michael A. Manfredi, John T. Maple, Faris M. Murad, Uzma D. Siddiqui, Subhas Banerjee, and Michael B. Wallace. Confocal laser endomicroscopy. 80(6):928–938.
- [74] J. A. Izatt, M. R. Hee, E. A. Swanson, C. P. Lin, D. Huang, J. S. Schuman, C. A. Puliafito, and J. G. Fujimoto. Micrometer-scale resolution imaging of the anterior eye in vivo with optical coherence tomography. 112(12):1584–1589.
- [75] Hsing-Wen Wang and Yu Chen. Clinical applications of optical coherence tomography in urology. 3(1).
- [76] Patrice Jichlinski and Hans-Jurg Leisinger. Fluorescence cystoscopy in the management of bladder cancer: A help for the urologist! 74(2):97–101.
- [77] C.C. Cauberg Evelyne, Jean J.M.C.H. de la Rosette, and Theo M. de Reijke. Emerging optical techniques in advanced cystoscopy for bladder cancer diagnosis: A review of the current literature. 27(2):245–251.
- [78] Aristeo Lopez and Joseph C. Liao. Emerging endoscopic imaging technologies for bladder cancer detection. 15(5):406.
- [79] Tomoaki Takai, Teruo Inamoto, Kazumasa Komura, Yuki Yoshikawa, Taizo Uchi-moto, Kenkichi Saitô, Naoki Tanda, Junko Kouno, Koichiro Minami, Hirofumi Uehara, Kiyoshi Takahara, Hajime Hirano, Hayahito Nomi, Satoshi Kiyama, and Haruhito

- Azuma. Feasibility of photodynamic diagnosis for challenging TUR- bt cases including muscle invasive bladder cancer, BCG failure or 2nd-TUR. 16(6):2297–2301.
- [80] Gerard Apodaca. The uroepithelium: Not just a passive barrier. 5(3):117–128.
- [81] Aria A. Razmaria. Bladder cancer. 314(17):1886–1886.
- [82] Nicholas Stone, Maria Consuelo Hart Prieto, Paul Crow, Jeremy Uff, and Alistair William Ritchie. The use of raman spectroscopy to provide an estimation of the gross biochemistry associated with urological pathologies. 387(5):1657–1668.
- [83] Tim O’Brien, David Cranston, Susan Fuggle, Roy Bicknell, and Adrian L Harris. Different angiogenic pathways characterize superficial and invasive bladder cancer. page 5.
- [84] Shigeyuki Aoki, Yoshiaki Yamada, Kogenta Nakamura, Tomohiro Taki, Motoi Tobiume, and Nobuaki Honda. Thymidine phosphorylase expression as a prognostic marker for predicting recurrence in primary superficial bladder cancer.
- [85] Norio Nonomura, Yasutomo Nakai, Masashi Nakayama, Hitoshi Inoue, Kazuo Nishimura, Eijirou Hatanaka, Ryouichi Arima, Tomomi Kishimoto, Tsuneharu Miki, Hideya Kuroda, and Akihiko Okuyama. The expression of thymidine phosphorylase is a prognostic predictor for the intravesical recurrence of superficial bladder cancer. 11(4):297–302.
- [86] M. Liebert, R. Washington, G. Wedemeyer, T. E. Carey, and H. B. Grossman. Loss of co-localization of alpha 6 beta 4 integrin and collagen VII in bladder cancer. 144(4):787–795.
- [87] B. W. D. De Jong, TC Bakker Schut, K. P. Wolffenbuttel, J. M. Nijman, D. J. Kok, and G. J. Puppels. Identification of bladder wall layers by raman spectroscopy. 168(4):1771–1778.
- [88] B.W.D. de Jong, T.C.Bakker Schut, J. Coppens, K.P. Wolffenbuttel, D.J. Kok, and G.J. Puppels. Raman spectroscopic detection of changes in molecular composition of bladder muscle tissue caused by outlet obstruction. 32(1):57–65.
- [89] M. C. M. Grimbergen, C. F. P. van Swol, R. O. P. Draga, P. van Diest, R. M. Verdaasdonk, N. Stone, and J. H. L. R. Bosch. Bladder cancer diagnosis during cystoscopy using raman spectroscopy. page 716114.

- [90] Ishan Barman, Narahara Chari Dingari, Gajendra Pratap Singh, Rajesh Kumar, Stephen Lang, and Ghulam Nabi. Selective sampling using confocal raman spectroscopy provides enhanced specificity for urinary bladder cancer diagnosis. 404(10):3091–3099.
- [91] Martin G. Shim, Brian C. Wilson, Eric Marple, and Michael Wach. Study of fiber-optic probes for in vivo medical raman spectroscopy. 53(6):619–627.
- [92] P. Crow, A. Molckovsky, N. Stone, J. Uff, B. Wilson, and L.-M. WongKeeSong. Assessment of fiberoptic near-infrared raman spectroscopy for diagnosis of bladder and prostate cancer. 65(6):1126–1130.
- [93] M.C.M. Grimbergen, C.F.P. van Swol, R.J.A. van Moorselaar, J. Uff, A. Mahadevan-Jansen, and N. Stone. Raman spectroscopy of bladder tissue in the presence of 5-aminolevulinic acid. 95(3):170–176.
- [94] Ronald O. P. Draga, Matthijs C. M. Grimbergen, Peter L. M. Vijverberg, Christiaan F. P. van Swol, Trudy G. N. Jonges, J. Alain Kummer, and J. L. H. Ruud Bosch. In vivo bladder cancer diagnosis by high-volume raman spectroscopy. 82(14):5993–5999.
- [95] Pu Chen, Aiguo Shen, Wei Zhao, Seong-Joon Baek, Hua Yuan, and Jiming Hu. Raman signature from brain hippocampus could aid alzheimer’s disease diagnosis. 48(24):4743–4748.
- [96] Michael Pinto, Kevin C. Zorn, Jean-Philippe Tremblay, Joannie Desroches, Frédéric Dallaire, Kelly Aubertin, Eric T. Marple, Chris Kent, Frederic Leblond, Dominique Trudel, and Frederic Lesage. Integration of a raman spectroscopy system to a robotic-assisted surgical system for real-time tissue characterization during radical prostatectomy procedures. 24(2):025001.
- [97] Svante Wold. Chemometrics; what do we mean with it, and what do we want from it? 30(1):109–115.
- [98] Jonathon Shlens. A tutorial on principal component analysis. page 13.
- [99] Paul Geladi and Bruce R. Kowalski. Partial least-squares regression: a tutorial. 185:1–17.
- [100] Alaa Tharwat, Tarek Gaber, Abdelhameed Ibrahim, and Aboul Ella Hassanien. Linear discriminant analysis: A detailed tutorial. 30(2):169–190.
- [101] Encyclopedia of analytical chemistry: applications, theory, and instrumentation.

- [102] Yun Xu, Simeone Zomer, and Richard G. Brereton. Support vector machines: A recent method for classification in chemometrics. 36(3):177–188.
- [103] F. Marini, R. Bucci, A.L. Magrì, and A.D. Magrì. Artificial neural networks in chemometrics: History, examples and perspectives. 88(2):178–185.
- [104] Nicholas Stone, Catherine Kendall, Neil Shepherd, Paul Crow, and Hugh Barr. Near-infrared raman spectroscopy for the classification of epithelial pre-cancers and cancers. 33(7):564–573.
- [105] Bas W. D. de Jong, Tom C. Bakker Schut, Kees Maquelin, Theo van der Kwast, Chris H. Bangma, Dirk-Jan Kok, and Gerwin J. Puppels. Discrimination between nontumor bladder tissue and tumor by raman spectroscopy. 78(22):7761–7769.
- [106] Amos Shapiro, Ofer. N. Gofrit, Galina Pizov, Jeffrey Kirk Cohen, and John Maier. Raman molecular imaging: A novel spectroscopic technique for diagnosis of bladder cancer in urine specimens. 59(1):106–112.
- [107] Hao Chen, Xin Li, Neil Broderick, Yüewen Liu, Yajun Zhou, Jianda Han, and Weiliang Xu. Identification and characterization of bladder cancer by low-resolution fiber-optic raman spectroscopy. 11(9):e201800016.
- [108] Daniela Bovenkamp, Ryan Sentosa, Elisabet Rank, Mikael Erkkilä, Fabian Placzek, Jeremias Püls, Wolfgang Drexler, Rainer Leitgeb, Nathalie Garstka, Shahrokh Shariat, Clara Stiebing, Iwan Schie, Jürgen Popp, Marco Andreana, and Angelika Unterhuber. Combination of high-resolution optical coherence tomography and raman spectroscopy for improved staging and grading in bladder cancer. 8(12):2371.
- [109] A. Sally Davis, Anke Richter, Steven Becker, Jenna E. Moyer, Aline Sandouk, Jeff Skinner, and Jeffery K. Taubenberger. Characterizing and diminishing autofluorescence in formalin-fixed paraffin-embedded human respiratory tissue. 62(6):405–423.
- [110] Monica Monici. Cell and tissue autofluorescence research and diagnostic applications. In *Biotechnology Annual Review*, volume 11, pages 227–256. Elsevier.
- [111] Sebastian Dochow, Norbert Bergner, Christoph Krafft, Joachim Clement, Michael Mazilu, Bavishna B. Praveen, Praveen C. Ashok, Rob Marchington, Kishan Dholakia, and Jürgen Popp. Classification of raman spectra of single cells with autofluorescence suppression by wavelength modulated excitation. 5(18):4608–4614.

- [112] Michael Mazilu, Anna Chiara De Luca, Andrew Riches, C. Simon Herrington, and Kishan Dholakia. Optimal algorithm for fluorescence suppression of modulated raman spectroscopy. 18(11):11382.
- [113] Shuxia Guo, Olga Chernavskaia, Jürgen Popp, and Thomas Bocklitz. Spectral reconstruction for shifted-excitation raman difference spectroscopy (SERDS). 186:372–380.
- [114] A. M. Macdonald and P. Wyeth. On the use of photobleaching to reduce fluorescence background in raman spectroscopy to improve the reliability of pigment identification on painted textiles. 37(8):830–835.
- [115] Florian Knorr, Zachary J. Smith, and Sebastian Wachsmann-Hogiu. Development of a time-gated system for raman spectroscopy of biological samples. 18(19):20049–20058.
- [116] John DiBenedetto, Gene A. Capelle, and Mary O’Neill. Time-resolved hyperspectral fluorescence spectroscopy using frequency-modulated excitation. 112(1):013109.
- [117] Nils Kristian Afseth and Achim Kohler. Extended multiplicative signal correction in vibrational spectroscopy, a tutorial. 117:92–99.
- [118] Chad A. Lieber and Anita Mahadevan-Jansen. Automated method for subtraction of fluorescence from biological raman spectra. 57(11):1363–1367.
- [119] Bruce Slutsky. Handbook of Chemometrics and Qualimetrics. *Journal of Chemical Information and Computer Sciences*, 38(6):1254–1254, November 1998.
- [120] Jun Zhao, Mike M. Carrabba, and Fritz S. Allen. Automated fluorescence rejection using shifted excitation raman difference spectroscopy. 56(7):834–845.
- [121] F. Siebert and Peter Hildebrandt. *Vibrational spectroscopy in life science*. Tutorials in biophysics. Wiley-VCH. OCLC: ocn181420638.
- [122] Zanyar Movasaghi, Shazza Rehman, and Ihtesham U. Rehman. Raman spectroscopy of biological tissues. 42(5):493–541.
- [123] K. Czamara, K. Majzner, M. Z. Pacia, K. Kochan, A. Kaczor, and M. Baranska. Raman spectroscopy of lipids: a review: Raman spectroscopy of lipids. 46(1):4–20.
- [124] Joke De Gelder, Kris De Gussem, Peter Vandenabeele, and Luc Moens. Reference database of raman spectra of biological molecules.

- [125] Halina Abramczyk, Jakub Surmacki, Monika Kopec, Alicja Klaudia Olejnik, Katarzyna Lubecka-Pietruszewska, and Krystyna Fabianowska-Majewska. The role of lipid droplets and adipocytes in cancer. raman imaging of cell cultures: MCF10a, MCF7, and MDA-MB-231 compared to adipocytes in cancerous human breast tissue. 140(7):2224–2235.
- [126] L. Duponchel, W. Elmi-Rayaleh, C. Ruckebusch, and J. P. Huvenne. Multivariate curve resolution methods in imaging spectroscopy: Influence of extraction methods and instrumental perturbations. 43(6):2057–2067.
- [127] Kirk W. Gossage, Tomasz S. Tkaczyk, Jeffrey J Rodriguez, and Jennifer K Barton. Texture analysis of optical coherence tomography images: Feasibility for tissue classification. *Journal of Biomedical Optics*, 8(3):570–575, 7 2003.

7

Publications

In the present section the reprints of the publications which are included in the frame of the theses are shown. All details regarding the copyright are indicated on each title page.

[EC1] Evaluation of Shifted Excitation Raman Difference Spectroscopy and Comparison to Computational Background Correction Methods Applied to Biochemical Raman Spectra

Eliana Cordero*, Florian Korinth*, Clara stiebing, Christoph Krafft, Iwan W. Schie, and Jürgen Popp, *Sensors*, 2017, 17(8):1724, DOI: 10.3390/s17081724.

[EC2] Bladder Tissue Characterization Using Probe-Based Raman Spectroscopy: Evaluation of Tissue Heterogeneity and Influence on The Model Prediction

Eliana Cordero, Jan Rürger, Dominik Marti, Abdullah S. Mondol, Thomas Hasselager, Karin Mogensen, Gregers G. Hermann, Jürgen Popp, and Iwan W. Schie, *Journal of Biophotonics*, 2019.

[EC3] Morpho-molecular ex vivo characterization and grading of non-muscle-invasive bladder cancer biopsies using forward imaging probe based multi-modal optical coherence tomography and Raman spectroscopy

Fabian Placzek*, Eliana Cordero B.*, Simon Kretschmer, Lara M. Wurster, Florian

Knorr, Gerardo González-Cerdas, Mikael T. Erkkilä, Çağlar Ataman, Gregers G. Hermann, Karin Mogensen, Thomas Hasselager, Peter E. Andersen, Hans Zappe, Jürgen Popp, f, Wolfgang Drexler, Rainer A. Leitgeb, and Iwan W. Schie, submitted to the Analyst, 2019.

[EC4] In-vivo Raman spectroscopy: from basics to applications

Eliana Cordero*, Ines Latka*, Christian Matthäu, Iwan W. Schie, and Jürgen Popp, Journal of Biomedical Optics, 2018, 23(7):1-23, doi: 10.1117/1.JBO.23.7.071210.

* Equally contributed author

7.1 Evaluation of Shifted Excitation Raman Difference Spectroscopy and Comparison to Computational Background Correction Methods Applied to Biochemical Raman Spectra

Eliana Cordero*, Florian Korinth*, Clara stiebing, Christoph Krafft, Iwan W. Schie, and Jürgen Popp, Sensors, 2017, 17(8):1724, DOI: 10.3390/s17081724

Der Nachdruck der folgende Publikation erscheint mit freundlicher Genehmigung von Sensors (Basel). Reprinted with kind permission from Sensors (Basel).

Erklärung zu den Eigenantenteilen der Promovendin sowie der weiteren Doktoranden/Doktorandinnen als Co-Autoren an der Publikation

Doktoranden	Eliana Cordero	Florian Korinth
Konzeption des Forschungsansatzes	x	x
Planung der Untersuchungen	x	x
Datenerhebung	x	x
Datenanalyse und -interpretation	x	x
Theoretischer Teil	x	
Experimenteller Teil		x
Schreiben des Manuskripts	x	x
Vorschlag Anrechnung Publikationsäquivalente	1,0	

Article

Evaluation of Shifted Excitation Raman Difference Spectroscopy and Comparison to Computational Background Correction Methods Applied to Biochemical Raman Spectra

Eliana Cordero ^{1,†}, Florian Korinth ^{1,†}, Clara Stiebing ¹, Christoph Krafft ¹, Iwan W. Schie ^{1,*} and Jürgen Popp ^{1,2}

¹ Leibniz Institute of Photonic Technology (IPHT), Albert-Einstein-Straße 9, Jena 07743, Germany; eliana.cordero@leibniz-ipht.de (E.C.); florian.korinth@leibniz-ipht.de (F.K.); clara.stiebing@leibniz-ipht.de (C.S.); christoph.krafft@ipht-jena.de (C.K.); juergen.popp@leibniz-ipht.de (J.P.)

² Institute of Physical Chemistry and Abbe Center of Photonics, Friedrich Schiller University Jena, Helmholtzweg 4, Jena 07743, Germany

* Correspondence: iwan.schie@leibniz-ipht.de

† These authors contributed equally to this work.

Received: 26 June 2017; Accepted: 20 July 2017; Published: 27 July 2017

Abstract: Raman spectroscopy provides label-free biochemical information from tissue samples without complicated sample preparation. The clinical capability of Raman spectroscopy has been demonstrated in a wide range of in vitro and in vivo applications. However, a challenge for in vivo applications is the simultaneous excitation of auto-fluorescence in the majority of tissues of interest, such as liver, bladder, brain, and others. Raman bands are then superimposed on a fluorescence background, which can be several orders of magnitude larger than the Raman signal. To eliminate the disturbing fluorescence background, several approaches are available. Among instrumental methods shifted excitation Raman difference spectroscopy (SERDS) has been widely applied and studied. Similarly, computational techniques, for instance extended multiplicative scatter correction (EMSC), have also been employed to remove undesired background contributions. Here, we present a theoretical and experimental evaluation and comparison of fluorescence background removal approaches for Raman spectra based on SERDS and EMSC.

Keywords: Raman spectroscopy; SERDS; EMSC; background correction; signal to noise ratio

1. Introduction

There is a significant requirement for rapid and minimally to non-invasive tools for cancer diagnosis. The ability to obtain specific biochemical information from biological samples without the need for labeling makes Raman spectroscopy attractive for many diagnostic applications in medicine [1,2]. For instance, Raman spectroscopy has been used to accurately identify and grade transitional cell carcinoma (TCC) in vitro and has shown promising results as an auxiliary method for pathological identification of bladder tissue [3–6]. The development of optical fiber Raman probes with high efficiency and throughput provided the opportunity to perform in vivo measurements of skin, brain, esophagus, and bladder, demonstrating that data acquisition, analysis and diagnostics can be performed at the patient in real time [7–10].

Human tissue is mainly composed of proteins, lipids, nucleic acids, and carbohydrates [11]. One of the main challenges for the implementation of Raman spectroscopy in the clinic is the excitation of auto-fluorescence in tissue. Biological tissues can show significant auto-fluorescence [12], which depends on the excited fluorophores, the excitation wavelength, and is several magnitudes stronger

than the Raman signal, leading to high shot noise. A considerable number of instrumental [13–16] and computational methods have been proposed to reduce or subtract the fluorescence background contribution in Raman spectra [17–20].

Computational methods include, for example, polynomial fitting [21], different least squares methods [22] and extended multiplicative scatter correction (EMSC) [23]. Polynomial fitting approximates the broad fluorescence background as an n -order polynomial function, fitting the polynomial function to spectral areas without Raman bands. Next to manually deciding which areas should be used, automatic methods for curve fitting in chromatographic analysis have been proposed under high noise circumstances, which is a limiting factor for this method [24]. Least squares methods rely on fitting of linear combinations of reference data to the measured spectra, where the sum of the squared differences between the observed values and the fitted values is minimized [25]. Different least squares approaches have previously been implemented, such as for instance iterative least squares or weighted least squares [26,27]. One very promising framework for model-based background correction in Raman spectroscopy is EMSC [28]. It is also based on a least squares fitting of pre-defined background spectra, but also including the fitting of pure components spectra [23]. Further computational techniques used to separate the fluorescence background from Raman spectra are principal component analysis [29], and wavelets analysis [30]. Wavelets analysis decomposes the spectrum into different frequency components and the background is suppressed by setting the very low frequency components to zero. Furthermore, by setting the high frequency components to zero as well, noise contributions can be removed. However, the transformation of the signal into frequency bands may result in distortion in some spectral areas [19,31].

As a methodical approach photobleaching has been suggested to remove fluorescence. By irradiating the sample with an excitation laser for a long period of time, a photolytic decomposition of the fluorescent interfering molecules is induced [14,15,32]. Another technique that addresses the reduction of the fluorescence background, as well as low signal to noise ratio (SNR) problems, is time-gating Raman spectroscopy. It employs ultra-short laser pulses that drive an all-optical Kerr shutter to gate early-arriving Raman photons, while blocking the later-arriving fluorescence photons. However, the systems are highly complex, costly, and challenging to modify [33]. Modulated excitation wavelength shifting is an instrumental method, where Raman measurements are performed at two closely spaced excitation wavelengths to obtain two shifted Raman spectra. By introducing a low-frequency modulator, a Raman spectrum is reconstructed. The main limitation is the need of lock-in detection [34]. Modulated Raman spectroscopy was introduced with a frequency-modulated excitation laser, continuous acquisition of Raman spectra, and without lock-in detection [35]. A popular instrumental method that has been widely applied is shifted excitation Raman difference spectroscopy (SERDS) [16,36–39]. SERDS is based on the principle that small changes in the excitation wavelength result in a spectral shift of the Raman spectrum, while the fluorescence contribution does not change spectrally. By calculating the difference between closely shifted Raman spectra all wavelength-independent contributions are removed. It was shown that not only fluorescence can be effectively removed by this method, but also ambient light, etaloning, and any other non-varying source [40–42]. Since the positions of the Raman bands are used for the interpretation of Raman spectra, it was previously suggested that the optimal shift in excitation wavelength should correspond to the full width at half maximum of a relevant Raman band [43,44]. Applying this shift results in a difference spectrum where the band position corresponds to the inflection point between the minimum and maximum of the respective band. This assumption is valid for samples, which have spectral bands with similar spectral widths, such as powders or crystalline proteins, and are acquired at very high spectral resolution. Since the Raman bandwidth of specific biological components vary within one spectrum, this theoretical optimal shift for the reconstruction of band positions cannot be applied for complex biological Raman spectra. Moreover, for biomedical applications there is not just one single Raman band, which is important for the differentiation between, e.g., tumor and non-tumor tissues.

Previous studies have evaluated the capability of SERDS to subtract strong fluorescence background exceeding the Raman signal up to a ratio of 200:1 [36,44–48]. A main topic in these studies is the necessary processing of SERDS spectra, using computational methods in order to acquire typical Raman spectra [37,49–51]. However, there are no studies where SERDS is evaluated and compared directly to computational background correction methods.

In this study, theoretical and experimental results for SERDS spectra of biological components, such as lipids and proteins, are evaluated. SNRs are determined based on different fluorescent background estimations. Additionally the concept of an optimal shift for SERDS is discussed theoretically and experimentally. Different algorithms for optimizing the spectral quality of the difference spectra are tested and compared to EMSC as a conventional computational background correction method.

2. Materials and Methods

2.1. Theoretical Approach

Raman spectra of lipid and protein components of chicken meat with a low fluorescence background were recorded, using a commercial Raman microscope setup (Holoprobe, Kaiser Optical System, Ann Arbor, MI, USA) with an excitation wavelength of 785 nm and an integration time of 1 s, see Figure 1a,b. These spectra were used as a basis for the theoretical analysis on the influence of fluorescent background contributions and noise levels on the recovery of informational content.

Data analysis of the Raman spectra and spectral simulations were performed in R [52], using the packages *hyperSpec*, *Ramancal*, *baseline*, and *pracma* [53–56]. The recorded Raman spectra were wavelength calibrated, during which all spectra were corrected to the same wavenumber axis relative to 785 nm. Furthermore, the spectra were background corrected by using support points determined from a convex hull of the spectrum and smoothed by applying a local polynomial regression fitting. The processed spectra were shifted by multiple wavelength steps between 1 nm and 4 nm to simulate Raman spectra recorded at different excitation wavelengths. The optimal shift was evaluated using the autocorrelation function from the *forecast* package [57,58]. The computational background correction was performed on the measured Raman spectra at 785 nm excitation, using the *emsc* function available in the *cbmodels* package [59]. For the simulations of different auto-fluorescence contributions, fluorescence spectra were measured on the commercial Raman setup and fitted by a polynomial function. The different fluorescence intensity levels were simulated by the multiplication of a constant factor and added to the Raman spectra of lipids and proteins. The noise contribution was estimated by applying a Poisson distribution function on the square root of the intensity, see Figure 1c,d.

SNRs were determined under the shot noise-limited definition [60], where the noise is calculated as the square root of the signal intensity. The SNR was calculated for each pixel of the spectrum, leading to a wavenumber-dependent SNR spectrum. Regions without relevant bands were removed. To determine a single SNR value for each spectrum, the second derivative of the spectrum without noise was calculated and the maxima including surrounding points of a certain wavenumber window were detected. A threshold was used to determine spectral locations to calculate the SNRs of importance, see Figure 1e,f. Those selected SNRs were averaged to obtain a mean SNR for the entire spectrum. The second derivative and smoothing of the preprocessed spectrum were performed by using the polynomial filtering method of Savitzky and Golay [55].

2.2. Experimental Approach

Raman measurements were performed using a tunable diode laser DL Pro (Toptica Photonics AG, Gräfelfing, Germany) enabling a tuning range from 765 to 805 nm. To achieve a higher output power the laser was coupled, using a single mode fiber, into a laser amplifier (BoosTA, Toptica Photonics AG). The output laser power at 785 nm after the amplifier was adjusted to 200 mW. The laser power at 785 nm after the objective was 95 mW. No damage to the tissue was observed.

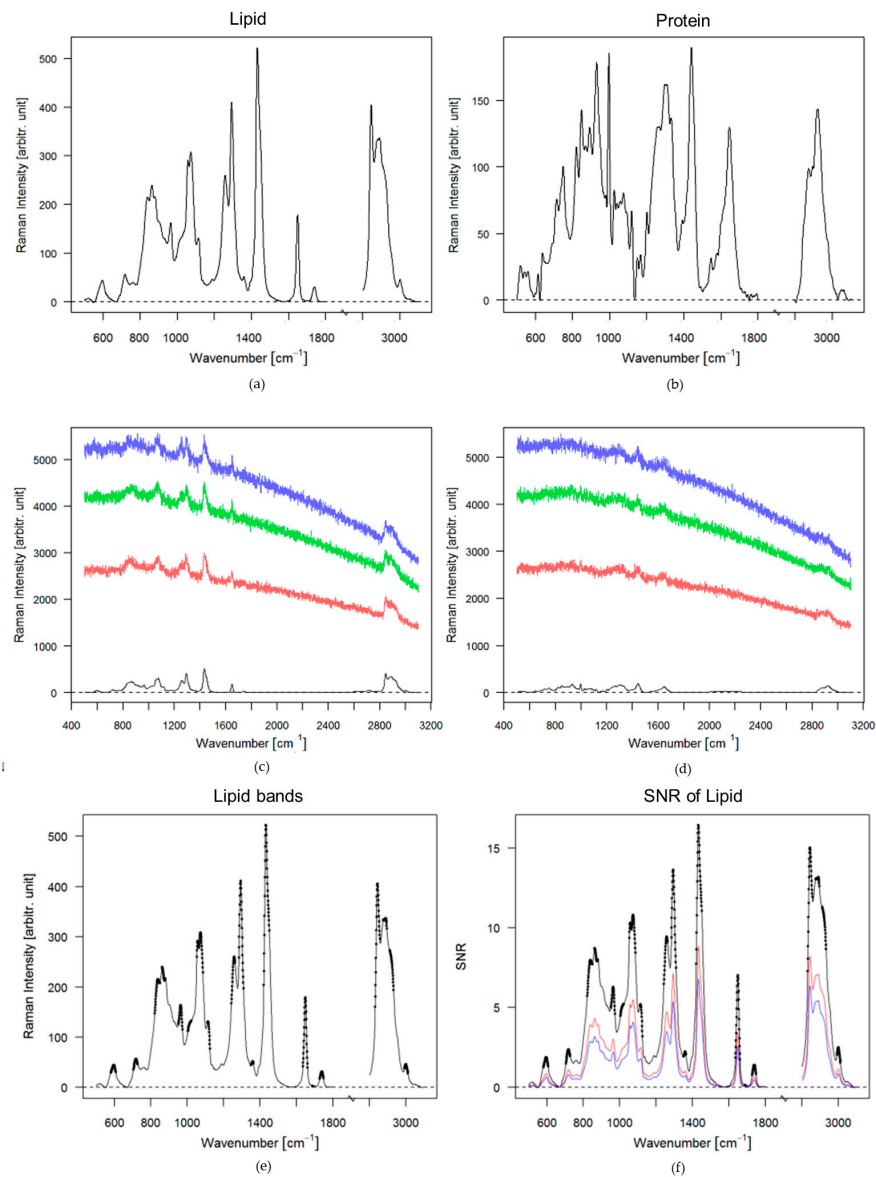


Figure 1. Baseline corrected spectra and spectra with simulated fluorescence backgrounds and shot noise levels: (a) Baseline corrected spectrum of lipids; (b) Baseline corrected spectrum of proteins; (c) Lipid spectra with added fluorescence intensities, i.e., 10 (blue), 8 (green) and 5 (red) times the maximal band of the lipid signal, including corresponding noise levels. The black spectrum is the lipid spectrum without fluorescence; (d) Protein spectra with added fluorescence intensities, i.e., 10 (blue), 8 (green) and 5 (red) times the maximal band of the lipid signal, including corresponding noise levels. The black spectrum is the protein spectrum without fluorescence; (e) Spectral bands and windows of the measured lipid spectrum, the black points are the maxima and the windows estimated by the Savitzky and Golay function; (f) SNR of the lipid spectra with fluorescence, the black spectrum is the SNR of the lipid spectrum, the red spectrum correspond to the SNR of the lipid spectrum with fluorescence 5 times the maximal band of the lipid signal, the blue spectrum is the SNR of the lipid spectrum with fluorescence factor 10 of the lipid signal.

Excitation wavelengths between 784 and 786 nm were chosen. Wavelengths below and higher than this range experienced high losses due to filter parameters, resulting in reduced excitation power.

and lower Raman signals. The laser was guided into a home-built microscope setup with a 40× magnification, NA = 0.55 objective lens. The setup has been previously described [61]. The sample was placed on a holder, which is mounted on two motorized x-y translational stages (CONEX MFA-Series; Newport, Irvine, CA, USA). To allow a sample translation in z-direction the motorized x-y translational stages were mounted on an automated z-positioning stage (MTS25-Z8, Thorlabs, Newton, NJ, USA). The generated Raman signal was collected by the same objective lens and separated from the excitation light by a dichroic notch filter (785 nm, bandwidth 89 nm; Semrock, Rochester, NY, USA). An additional notch filter (785 nm ± 19 nm; Laser Components, Olching, Germany) was used for a reliable suppression of the excitation light. An achromatic doublet (100 mm; Thorlabs) focuses the Raman signal onto a multimode fiber (105 μm core, Thorlabs). The signal was then fiber-coupled into a spectrometer (IsoPlane160, Princeton Instruments, Acton, MA, USA) that is equipped with a grating with 400 grooves/mm, blazed at 750 nm, and allows a spectral resolution of 9 cm⁻¹. The signal is dispersed onto a charge-coupled device (CCD) (PIXIS-400BR-eXcelon; Princeton Instruments) with a nominal quantum efficiency of up to 98% at 800 nm. The setup is controlled by in-house written data-acquisition software in LabView (National Instruments, Austin, TX, USA). The data acquisition was designed such that at each spatial location in the sample five Raman spectra at different excitation wavelengths, ranging between 784 nm to 786 nm with an interval of 0.5 nm, were measured consecutively. After all measurements for one spatial location were performed, the next location was measured.

Raman images were acquired of meat samples, providing typical biological spectra of fibrous protein from muscle tissue and tendons, non-fibrous proteins, lipids, and bone. Images were acquired of 10 mm by 10 mm areas with a step size of 0.5 mm, and an integration time of 1 s. Data analyses were performed in R [52]. All spectra were cleared from cosmic spikes [62,63]. To generate background corrected Raman spectra, the spectra measured at 785.0 nm were baseline corrected by EMSC. Seven components, i.e., constant offset, a linear function, and multiple fluorescence functions were used as background estimates; and Raman spectra of collagen, protein, lipid spectrum and bone were used for pure component spectra. The components were fitted to the measured Raman spectra. The determined coefficients multiplied with the background component spectra were subtracted from the raw spectra. The corrected spectra were area normalized and grouped into four clusters by hierarchical cluster analysis (HCA).

Difference spectra were obtained by subtracting the Raman spectra acquired at different excitation wavelengths from the Raman spectrum measured at the excitation wavelength of 786 nm of the same spatial location in the tissue sample. Thereby, four SERDS spectra per image point with different wavelength shifts, i.e., 0.5 nm, 1.0 nm, 1.5 nm, 2.0 nm, were obtained, which can be represented in four SERDS images containing 400 Raman difference spectra. Before calculating the differences spectra, the cosmic spike-corrected spectra were normalized or optimized. Three different types of processing methods were tested:

$$\text{area normalization : } S_{an}(\tilde{\nu}_i) = \frac{S(\tilde{\nu}_i)}{\sum_{i=1}^n S(\tilde{\nu}_i)} \quad (1)$$

z-score normalization/standard normal variate [64]:

$$S_{zn}(\tilde{\nu}_i) = \frac{S(\tilde{\nu}_i) - \text{mean}(S)}{SD(S)} \quad (2)$$

$$\text{subtraction optimization : } \text{minimization of } AUC (|S_1 - (x \cdot S_2)|) \quad (3)$$

with S —signal; $\tilde{\nu}$ —relative wavenumber; SD —standard deviation; AUC —area under the curve.

For the subtraction optimization a random value x is multiplied to the spectrum, which is being subtracted, and the area under the curve (AUC) of the absolute values of the difference spectrum is calculated. The value x is then iteratively adjusted, so that the AUC is minimized.

3. Results

3.1. Theoretical Approach

Ideally, Raman spectra show defined bands, as seen in Figure 1a for lipids and Figure 1b for proteins. However, due to the high auto-fluorescence background in biological tissue, Raman bands are superimposed with an auto-fluorescence background and as well as accompanying shot noise, shown in Figure 1c,d.

Even small amounts of fluorescent molecules in a sample can cause high background intensities. The fluorescence scattering cross-section is usually several orders of magnitude higher than the Raman scattering cross-section [65,66].

After adding the simulated fluorescence background and shot noise to the Raman signal, as shown in Figure 1, the Raman bands can barely be distinguished, because the noise level is increasing with the intensity of the fluorescence signal, following the square root of the total signal intensity. Therefore, at higher fluorescence contributions the SNR is lower for a constant Raman signal intensity, as shown in Figure 1f. An estimated average SNR value of the main bands for each spectrum was calculated based on the described algorithm in the materials and method Section 2.1. The average SNR for the lipid spectrum without fluorescence is approximately 6.8 (Figure 1f, black spectrum). If the lipid spectrum has a fluorescence intensity five times higher than the maximal band intensity of the lipid spectrum the average SNR decreases to 3.4 (Figure 1f, red spectrum). For a fluorescence intensity 10 times higher than the maximal band intensity of the lipid spectrum the average SNR is only 2.5.

In order to evaluate different methods to correct auto-fluorescence background contributions a set of fluorescence intensities was created to simulate fluorescence contributions at different intensities and hence, different SNRs for a Raman signal with constant signal intensity. SERDS simulations were then performed on the set of created noise and background affected spectra. Before the evaluation of SERDS for background correction, an optimal laser wavelength shift had to be determined. The optimal shift distance has often been defined as the wavelength difference, which corresponds to the half-width of a Raman band [43]. However, this is only valid when bands with similar bandwidth are present within a spectrum, which is not the case in Raman spectra of most biological samples as discussed in the introduction. Therefore, the optimal wavelength shift was defined as the shift, which retains most of the signal information in the difference spectrum. Autocorrelation of pure Raman spectra were performed to determine the optimal shift. The autocorrelation function of lipid (black) and protein (red) is shown in Figure 2a.

A complete overlap between the spectrum and itself results in a perfect autocorrelation ($acf = 1$), seen in Figure 2a. Meaning, if two signals are fully overlapped the difference spectrum of those signals will have zero informational content. A very low autocorrelation coefficient indicates a low self-similarity of the signal and will result in high signal intensities in the difference spectra. Hence, high $1-acf$ values will result in higher signal of difference spectra. This approach was used as an indicator for the optimal shift for pure spectra of lipid and protein. Shifts were analyzed in a region between 0 to 12.6 nm because a higher shift might result in effects on the fluorescence spectrum and are technically very challenging to implement. The highest intensities retained in the difference spectra were for a shift of 7 nm for lipid, and 10 nm for protein, corresponding to 110 and 160 cm^{-1} , respectively (see Figure 2b). These values are much higher than commonly reported [37,67,68]. It is also visible in Figure 2b that when the shift in wavelength for lipid is higher than 7 nm the $1-acf$ decreases, resulting in a reduction of signal. The influence of the shift on the retained signal intensity can be best visualized by plotting the corresponding difference Raman spectra for lipids with and without noise, as seen in Figure 2c,d. For a shift of 1 nm (green) there is 47% of the signal retained, for a shift of 2 nm (black) 54% of the signal is retained and by shifting 4 nm (blue) a considerable part of the signal is retained (68%).

To compare SERDS and EMSC the simulated Raman spectra with fluorescence and noise from Figure 1c,d, with a fluorescence intensity level of five times the maximal band of the lipid signal,

were chosen. A Raman shift of 4 nm was used and after applying SERDS the absolute values of the difference lipid and protein spectra were calculated (see Figure 3a,b, blue spectra).

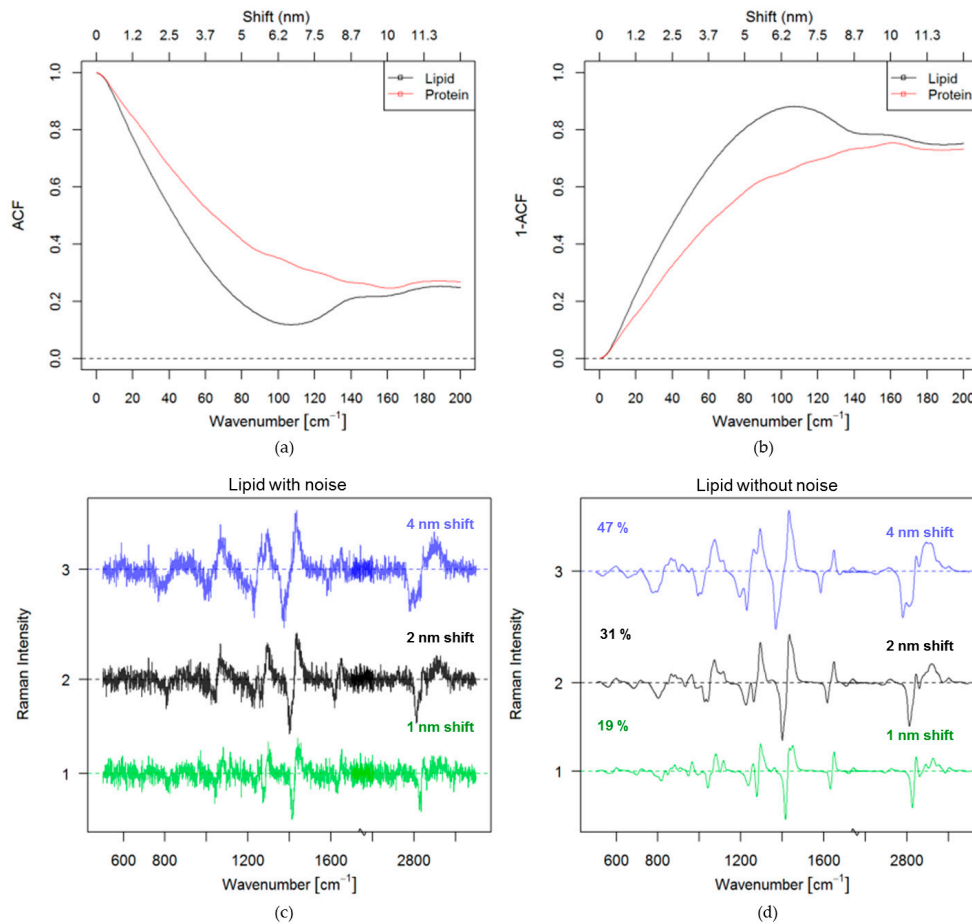


Figure 2. Optimal shift: (a) Estimation by using the autocorrelation function of lipid and protein spectra (b) Estimation by using the 1-autocorrelation function of lipid and protein spectra; (c) Simulation of the difference spectra of lipid at 1 nm shift (green), 2 nm shift (black) and 4 nm shift (blue) with noise, the values are the percentage values of the retained signal; (d) Simulation of the difference spectra of lipid at 1 nm shift (green), 2 nm shift (black) and 4 nm shift (blue) without noise.

The absolute values of the difference spectra are illustrated in order to indicate how much signal is retained in the difference spectra. The same plot also shows the EMSC corrected spectra (green), and the original Raman spectra with and without noise, colored red and black, respectively. The processed SERDS signal (blue) has lower intensity than the EMSC corrected spectra (green). When comparing the EMSC corrected spectra (green) with the original spectra with noise (red) in Figure 3, one can see that it resembles the original spectra with noise quite well. The intensity of the signal is not reduced as in the case of the difference spectrum based on SERDS (blue). The reader should keep in mind that the acquisition time for SERDS is twice as long, as for a normal spectrum, because two spectra are acquired. Hence, the intensity of the Raman signal for the background corrected case should actually be twice as high.

In a shot noise limited measurement the SNR of a Raman signal is inversely proportional to the square root of the sum of the Raman signal and the fluorescence (Equation (4)). Consequently, the SNR will be very low at very high fluorescence intensities. For SERDS a further problem occurs, which is

that while the signal intensity is subtractive, the noise contribution is additive, Equation (5). Hence, one disadvantage in SERDS is the reduction of the overall SNR in the difference spectra. It is possible to express the SNR of SERDS measurements in terms of the SNR of Raman measurements for identical acquisition conditions, i.e., the acquisition time of a Raman spectrum has to match the acquisition time of two SERDS spectra.

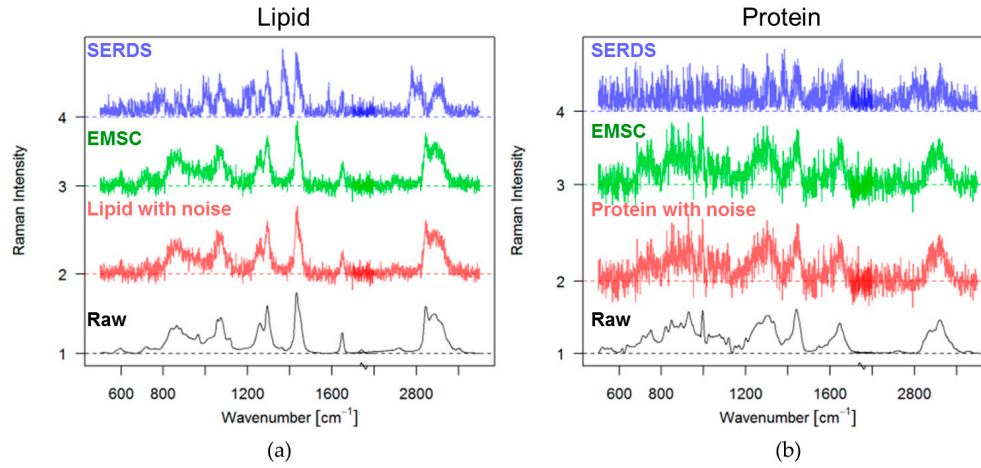


Figure 3. EMSC and SERDS spectra for lipid and protein: (a) Lipid spectrum without background (black); lipid spectrum with noise added (red, noise corresponds to the poison distribution of original spectrum and the added fluorescence five times the maximal band of the lipid signal); EMSC corrected lipid spectrum after adding a fluorescence background five times the maximal band of the lipid signal (green); absolute values of SERDS difference spectrum of lipid after shifting 4 nm (blue); (b) Protein spectrum without background (black); protein spectrum with noise added (red, this noise corresponds to the poison distribution of original spectrum and the added fluorescence five times the maximal band of the protein signal); EMSC corrected protein spectrum after having fluorescence background five times the maximal band of the protein signal (green); absolute values of SERDS difference spectrum of protein after shifting 4 nm (blue).

Equation (9) shows that for S_2 smaller than S_1 the SNR_{SERDS} will be smaller or equal to half of the SNR_{RAMAN} ; for $S_2 = S_1$ SNR_{SERDS} is 0; and for $S_2 \geq 2S_1$ $SNR_{SERDS} \geq SNR_{RAMAN}/2$. The last term indicates that the SERDS difference spectrum can locally have a higher SNR as a Raman spectrum. However, in general the total spectral SNR is of importance and the local SNR is not always meaningful. The summation in Equation (10) allows assessing the SNR over the entire measurable spectral region or a region of interest. Because the autocorrelation function for any reasonable shift is non-zero (see also Figure 2a), the total SNR of SERDS is always smaller than the SNR of Raman.

$$SNR_{RAMAN}(\lambda_i) = \frac{S_1(\lambda_i)}{\sqrt{S_1(\lambda_i) + F_1(\lambda_i)}} \quad (4)$$

$$SNR_{SERDS}(\lambda_i) = \left| \frac{S_1(\lambda_i) - S_2(\lambda_i)}{\sqrt{S_1(\lambda_i) + F_1(\lambda_i) + S_2(\lambda_i) + F_2(\lambda_i)}} \right| \quad (5)$$

for $S \ll F$ and $F_1(\lambda_i) \approx F_2(\lambda_i)$

$$SNR_{SERDS}(\lambda_i) = \frac{1}{\sqrt{2}} \left| \frac{S_1(\lambda_i) - S_2(\lambda_i)}{\sqrt{S_1(\lambda_i) + F_1(\lambda_i)}} \right| \quad (6)$$

for identical acquisition parameters for Raman and SERDS $t_{SERDS} = 2 \cdot t_{RAMAN}$

$$SNR_{RAMAN}(\lambda_i) = \frac{2 \cdot S_1(\lambda_i)}{\sqrt{2} \cdot \sqrt{S_1(\lambda_i) + F_1(\lambda_i)}} \quad (7)$$

$$\frac{SNR_{SERDS}(\lambda_i)}{SNR_{RAMAN}(\lambda_i)} = \frac{1}{2} \cdot \left| \frac{S_1(\lambda_i) - S_2(\lambda_i)}{S_1(\lambda_i)} \right| \quad (8)$$

$$SNR_{SERDS}(\lambda_i) = \frac{SNR_{RAMAN}(\lambda_i)}{2} \cdot \left(\left| 1 - \frac{S_2(\lambda_i)}{S_1(\lambda_i)} \right| \right) \quad (9)$$

$$SNR_{SERDS} = \frac{1}{2} \cdot \sum_{i=1}^n SNR_{RAMAN}(\lambda_i) \cdot \left(\left| 1 - \frac{S_2(\lambda_i)}{S_1(\lambda_i)} \right| \right) \text{ for } S_1 \geq 1 \quad (10)$$

with S —Raman signal; F —fluorescence signal; λ_i —wavelength; t —acquisition time.

3.2. Experimental Approach

Since the simulations showed the influence of the shift in excitation wavelength on the SERDS spectra, SERDS measurements of tissue samples were performed with different wavelength shifts. Because the largest shift that could be realized in our experimental setup was 2 nm (ca. 32 cm^{-1}), four different shifts in excitation wavelength were measured in a 0.5 nm interval. In Figure 4 these different mean SERDS spectra of raw data for the lipid cluster of a tissue sample are shown. They show the same tendencies that could be seen in the simulations: the largest shift (blue) has the highest intensity, while the lowest can be observed for the smallest shift (black). This 0.5 nm shift is so small that the retained background is significant to the retained signal and cannot correct the spectra efficiently. It is also evident that the subtraction of raw spectra does not remove the background completely.

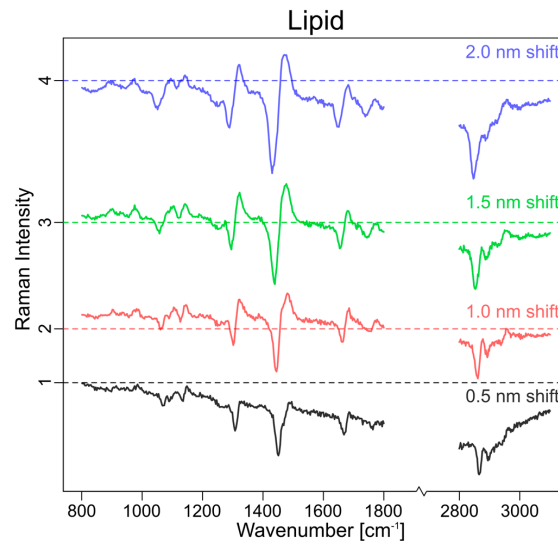


Figure 4. Measured difference mean raw spectra of a lipid cluster at different excitation wavelength shifts (shift: 0.5 nm (black), 1.0 nm (red), 1.5 nm (green), 2.0 nm (blue)).

For the comparison of SERDS and EMSC, the largest possible shift was applied for the experimental measurements. Raw spectra ($\lambda_1 = 786 \text{ nm}$, $\lambda_2 = 784 \text{ nm}$, $\lambda_{SERDS} = \lambda_1 - \lambda_2$) were used to generate the SERDS spectra. The EMSC correction was performed on the spectra measured at 785.0 nm.

The correction of real data with the computational background correction method EMSC can be demanding, if there are no pure component spectra available for the measuring system. For a

system where all contributing spectral components are known this method works very well even for spectra with a high fluorescence background. The fluorescence background can be approximated by a higher polynomial and used as a background component. For a Raman image of a complex tissue with multiple spectra of different components, background estimation for fluorescence can be challenging since the contribution might vary locally. Even if multiple fluorescence background estimates are used for the EMSC algorithm, unknown varying backgrounds can cause performance problems for the EMSC background correction. On the other hand, SERDS difference spectra are hard to interpret since the band position cannot be reconstructed easily. Since difference spectra can be compared to the 1st derivative of a Raman spectrum, the 1st derivative of the EMSC corrected Raman spectra were calculated (Figure 5g–i). The black vertical lines show the band position in the EMSC corrected spectra (Figure 5d–f). For the lipid spectrum the band positions of the EMSC corrected spectrum overlaps quite nicely with the inflection points of the 1st derivative and the SERDS spectrum as seen in Figure 5a,d,g. For protein spectra, the band position of the EMSC corrected spectra also overlap with the inflection points of the 1st derivative of the EMSC and the SERDS spectra (Figure 5b,e,h and Figure 5c,f,i). However, the difference spectra are noisy and the bands are not easily located. It is even worse for the 1st derivative EMSC corrected spectra of proteins, which has a very high noise level. In the weaker protein spectrum in Figure 5c,f,i, bands are very hard to discern because of the high noise in the 1st derivative spectrum.

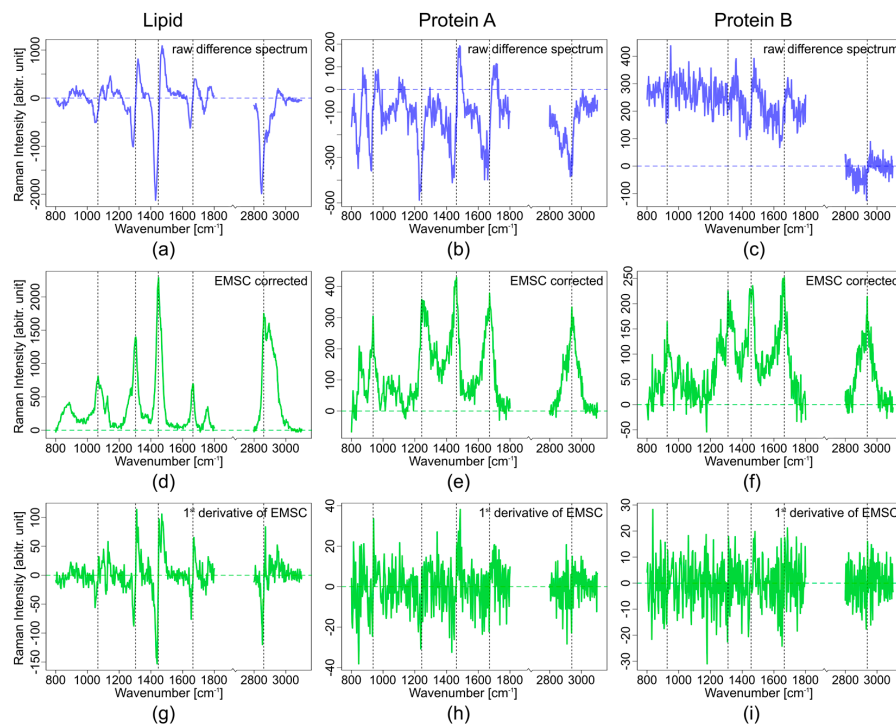


Figure 5. Comparison of measured lipid spectrum (a,d,g) and two protein spectra (b,e,h) and (c,f,i). Raw SERDS difference spectra (2 nm shift, (a–c), blue); EMSC corrected spectra at 785 nm ((d–f), green); 1st derivative of the EMSC corrected spectra at 785 nm ((g–i), green); the vertical black lines mark band positions.

The intensity loss due to the subtraction of two raw spectra to generate the SERDS spectrum is clearly evident. The SERDS intensity is approximately half of the intensity of the EMSC spectra as seen in Figure 5. The SNR for the SERDS spectra is also lower than for the EMSC corrected spectra.

Unlike in the simulated data the measured Raman spectra cannot be corrected by subtraction of one Raman spectrum from another. As shown in Figure 5 (blue spectra) and Figure 6a,b (black spectra), a simple subtraction of the raw spectra does not result in background-free difference spectra. For example, the mean spectrum of lipids is below zero intensity and has a bent in the spectral profile (Figure 6, black spectra). Photobleaching and variation in the laser power at the different excitation wavelengths cause changes in the background and total intensity, making the simple correction approach not suitable for most biological samples. A better overlap of the SERDS pair has to be accomplished, which requires further data processing before calculating the difference spectra.

Spectral normalization is one possible approach to obtain same relative intensities for all excitation wavelengths. Two different normalization procedures, as well as a subtraction optimization, were applied to the raw spectra as explained in the methods section. In Figure 4 the effect of the different spectral processing methods on lipid and protein spectra with fluorescence contributions are shown.

Lipids have a high Raman scattering cross-section and frequently occur at high local concentrations and therefore have a high Raman intensity as in comparison to protein for identical acquisition conditions, leading to strong difference bands. Due to the high intensity in comparison to the noise contribution, the noise-related standard deviation of the lipid difference spectra is low in comparison to protein spectra. Proteins have a smaller Raman scattering cross-section in comparison to lipids and have a lower local concentration, and a higher noise-related standard deviation in the protein difference spectra.

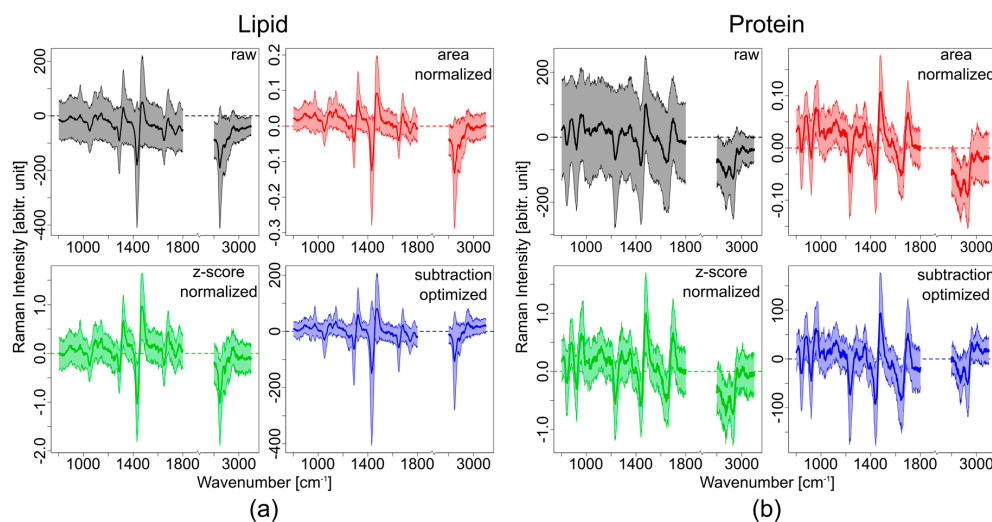


Figure 6. Comparison of different SERDS data processing methods with a 2 nm shift for (a) measured lipid spectra and (b) measured protein spectra. For every method the mean spectrum (darker shade) along with its standard deviation is shown. Black: difference spectra obtained by subtraction of raw data; red: difference spectra after area normalization; green: difference spectra after z-score normalization; blue: difference spectra after subtraction optimization.

By applying area normalization to the SERDS spectra before subtraction, an improvement of the background correction can be observed. This improvement is a result of the better overlap between the spectra (Figure 6a,b, red spectra). There are still background contributions left in the difference spectra, which are clearly visible in the bending and the offset of the protein spectra (Figure 6b, red spectrum).

The z-score normalization results in an even better overlap between the spectra (Figure 6a,b, green spectra). The background in the difference spectra is minimized and the mean spectra are close to zero intensity for areas with no signal. Especially for the lipid spectra the z-score normalized difference

spectrum has almost no background and no bending. For the high wavenumber region, however, this normalization also does not work well.

A further approach, which was tested, is based on subtraction optimization. Due to minimization of the area under the difference spectra, artifacts based on different laser intensities at the different excitation wavelength, and filter throughput of the different wavelength can be corrected. Still, after the subtraction optimization small background contributions are left (Figure 6a,b, blue spectra). Although the difference spectra are closer to zero where there is no signal, there is still a deviation visible especially in the protein difference spectrum. The intensity differences of the Raman bands in the difference spectrum are more pronounced than in the other methods and the standard deviation is minimized. The high wavenumber region is better corrected than for the other methods.

The results show that a simple subtraction of the raw spectra is not suitable to remove background contributions in a Raman spectrum with high auto-fluorescence contributions. With preprocessing of the spectra based on normalization or subtraction optimization a better overlap of the SERDS pair can be achieved. Nevertheless, some background artifacts still remain. Especially the difference spectra of the broad envelope of CH_n bands between 2800 and 3100 cm^{-1} result in not very pronounced difference bands. This shows that the small wavelength shift of 2 nm is not sufficient to have a clear separation of the broad CH_n bands. Hence, the CH_n bands are canceled out by subtracting the two spectra. Z-score normalization and the subtraction optimization both result in a better spectral overlap of the background and provide a better correction than the area normalization. The remaining background of the difference spectra can be corrected, using a polynomial fitting approach.

4. Discussion

The goal of this research was to compare an instrumental with a computational background correction method for Raman spectroscopy of biological samples. One of the most common instrumentation-based methods for background correction of Raman spectra is SERDS, which was compared to the computational method EMSC. The evaluation between the methods was first performed on simulated fluorescence and noise levels, and then on measured spectra.

The simulation of the effect of fluorescence and shot noise showed that Raman bands can be barely distinguished even if the fluorescence intensity is just five times higher than the maximal Raman band of the lipid signal, because of the shot noise resulting from fluorescence background. The SNR at each wavenumber of the simulated spectra was calculated and an estimated value was used to evaluate the overall SNR for different fluorescence signal intensities and difference spectra. This demonstrated that the SNR of the difference spectrum is lower than for a normal Raman spectrum, because the signal is subtractive while the noise is additive. It was also shown that the SNR is reduced inversely proportional to the square root of the fluorescence background for a Raman spectrum with fixed signal intensity. In contrary to previous suggestions to use very small shifts, which correspond to the full width at half maximum of a Raman band, a new criterion was proposed: i.e., the optimal shift is defined as the wavelength shift that retains the most information in the spectrum. By using the autocorrelation function, an optimal shift for lipids and proteins, using the proposed criterion was estimated. It was found that there is a region between 5 and 7.5 nm (for lipid) that retains the highest information and results in the highest SNR. This corresponds to a wavenumber shift of 80 to 120 cm^{-1} . If the spectra are shifted by more than 7.5 nm, the correlation between the spectra will result in reduced signal after the subtraction. The reduction is due to an increase in an overlap between bands, which do not correspond to the same vibrations, being shifted into each other, resulting in misleading Raman difference information.

For EMSC it was shown that broad polynomial backgrounds could be removed without distorting the Raman bands and compromising the signal intensity nor adding additional noise to the spectra. Furthermore, EMSC can be superior to SERDS, since the spectral acquisition of SERDS requires the acquisition of two spectra, and hence, twice the acquisition time.

For the experimental implementation of SERDS a shift of 5 to 7.5 nm, as required for lipid spectra, can currently not be implemented in our setup, due to limits imposed by the used filters and the intensity stability of the excitation source. A wavelength shift of 2.0 nm was the largest implementable shift without a loss in excitation power. Still, the experimental data supported the simulated results, i.e., the larger the shift, the higher the retained intensities in SERDS spectra, which was shown experimentally for shifts of 0.5 nm, 1.0 nm, 1.5 nm and 2.0 nm for lipids, and the better the SNR. The experiments have shown that for protein and lipid spectra a simple subtraction of the shifted raw spectra, as is usually done for SERDS, does not suffice to obtain background-free SERDS spectra, and more complex computational methods, such as normalization or optimization, have to be used. From the three tested methods, z-score normalization and the subtraction optimization gave the best results. After performing EMSC on single Raman spectra, it was shown theoretically and experimentally that the EMSC corrected spectra can recover the main Raman bands for lipids and proteins. The simulation of the EMSC corrected spectra provided the same information as the original spectra, even when shot noise was added. In contrast to the SERDS difference spectra, the spectral interpretation of the Raman bands is not affected. To have a better comparison between difference spectra and EMSC corrected spectra, the 1st derivatives of the EMSC corrected spectra were calculated based on the experimental data set. It is clearly visible that SERDS experiences a high loss of intensity information due to the subtraction. Since for SERDS two Raman spectra have to be acquired, the measurement time is doubled compared to conventional Raman spectroscopy, leading to long acquisition times for Raman imaging of tissue samples. However, a drawback of the EMSC method is the estimation of very complex unknown backgrounds or multiple different fluorescence backgrounds, which can occur in a single Raman images, due to photobleaching or presence of different fluorophores in the sample.

5. Conclusions

For SERDS a reasonably good SNR is necessary to achieve a good background correction. The spectra have to be normalized or optimized before calculation of the SERDS spectra to compensate for fluctuations in signal intensity of the fluorescence background. Even then a further background correction is needed to obtain background-free difference spectra. The larger the shift of the excitation wavelength, the more signal intensity in a spectrum can be retained after the subtraction. For lipids the optimal shift is at 110 cm^{-1} (7 nm for 785 nm excitation) and for protein at 160 cm^{-1} (10 nm for 785 nm excitation). The proposed wavelength shifts are rather large, and can lead to changes in fluorescence intensity or, in the worst case, can excite different fluorophores and result in completely different fluorescence profiles. The interpretation of the difference spectra can be challenging, since it is hard to determine the exact band positions. On the other hand, SERDS is advantageous because no previous knowledge of the background is necessary for a correction.

Background correction with EMSC gives promising results for the simulated and the experimental data. It can, however, be challenging when dealing with complex samples and complex backgrounds. Pure spectra have to be generated and fluorescence background components have to be approximated. For Raman images with different fluorescence backgrounds, this can be tedious since more than one fluorescence component will be necessary.

In summary, SERDS and EMSC are both powerful tools for fluorescence background correction, with distinct advantages and disadvantages. When background spectra can be estimated, EMSC outperforms SERDS, because it keeps the fidelity of the Raman spectrum, does not require additional equipment, and guarantees a higher SNR. When, however, backgrounds are too complex to be estimated, SERDS could be a good choice as a background correction method.

Acknowledgments: We thank Claudia Beleites for the helpful discussion about the optimization of the experimental dataset. This work is supported by the EU-funded project MIB (No 667933) and by the Leibniz Association through the project HYPERAM (SAW-2016-IPHT-2). The publication of this article was funded by the Open Access Fund of the Leibniz Association.

Author Contributions: I.W.S. and C.S. designed the experiments; E.C. and I.W.S performed the simulations and the theoretical evaluation of the methods; I.W.S. developed the program for device controlling of SERDS imaging; F.K. and C.S. performed the experiments and analyzed the experimental data; E.C., F.K., I.W.S., C.S., C.K., and J.P. wrote the paper.

Conflicts of Interest: The authors declare no conflict of interest.

References and Notes

1. Krafft, C.; Schie, I.; Meyer, T.; Schmitt, M.; Popp, J. Development in spontaneous and coherent Raman scattering microscopic imaging for biomedical applications. *Chem. Soc. Rev.* **2016**, *45*, 1819–1849. [[CrossRef](#)] [[PubMed](#)]
2. Krafft, C.; Schmitt, M.; Schie, I.; Cialla-May, D.; Matthäus, C.; Bocklitz, T.; Popp, J. Label-free molecular imaging of biological cells and tissues by linear and non-linear Raman spectroscopic approaches. *Angew. Chem.* **2017**, *56*, 4392–4430. [[CrossRef](#)] [[PubMed](#)]
3. Stone, N. The use of Raman spectroscopy to provide an estimation of the gross biochemistry associated with urological pathologies. *Anal. Bioanal. Chem.* **2007**, *387*, 1657–1668. [[CrossRef](#)] [[PubMed](#)]
4. Crow, P.; Uff, J.A.; Farmer, J.A.; Wright, M.P.; Stone, N. The use of Raman spectroscopy to identify and characterize transitional cell carcinoma in vitro. *BJU Int.* **2004**, *93*, 1232–1236. [[CrossRef](#)] [[PubMed](#)]
5. Kerr, L.T.; Domikan, K.; Cullen, I.; Hennelly, B.M. Applications of Raman spectroscopy to the urinary bladder for cancer diagnostics. *Photonics Lasers Med.* **2014**, *3*, 193–224. [[CrossRef](#)]
6. Crow, P.; Molckovsky, A.; Stone, N.; Uff, J.; Wilson, B.; Wongkeesong, L.-M. Assessment of fiberoptic Near-infrared Raman spectroscopy for diagnostics of bladder and prostate cancer. *J. Urol.* **2005**, *65*, 1126–1130. [[CrossRef](#)] [[PubMed](#)]
7. Bergholt, M.S.; Zheng, W.; Ho, K.Y.; Teh, M.; Yeoh, K.G.; So, J.B.Y.; Shabbir, A.; Huang, Z. Fiberoptic confocal Raman spectroscopy for real-time in vivo diagnosis of dysplasia in Barrett's esophagus. *Gastroenterology* **2014**, *146*, 27–32. [[CrossRef](#)] [[PubMed](#)]
8. Eberhardt, K.; Stiebing, C.; Matthäus, C.; Schmitt, M.; Popp, J. Advantages and limitations of Raman spectroscopy for molecular diagnostics: An update. *Expert Rev. Mol. Diagn.* **2015**, *15*, 773–787. [[CrossRef](#)] [[PubMed](#)]
9. Motz, J.T.; Gandhi, S.J.; Scepanovic, O.R.; Feld, M.S. Real-time Raman system for in vivo disease diagnosis. *J. Biomed. Opt.* **2005**, *10*, 031113. [[CrossRef](#)] [[PubMed](#)]
10. Draga, R.O.P.; Grimbergen, M.C.M.; Vijverberg, P.L.M.; Bosch, J.L.H.R. In Vivo Bladder Cancer Diagnosis by High-Volume Raman Spectroscopy. *Anal. Chem.* **2010**, *82*, 5993–5999. [[CrossRef](#)] [[PubMed](#)]
11. De Jong, B.W.D.; Schut, T.C.B.; Wolffenbuttel, K.P.; Nijman, J.M.; Kok, D.J.; Puppels, G.J. Identification of bladder wall layers by Raman spectroscopy. *J. Urol.* **2002**, *168*, 1771–1778. [[CrossRef](#)]
12. Monici, M. Cell and tissue autofluorescence research and diagnostic applications. *Biotechnol. Annu. Rev.* **2005**, *11*, 227–256. [[PubMed](#)]
13. McCain, S.T.; Willett, R.M.; Brady, D.J. Multi-excitation Raman Spectroscopy Technique for Fluorescence Rejection. *Opt. Express* **2008**, *16*, 10975–10991. [[CrossRef](#)] [[PubMed](#)]
14. Macdonald, A.M.; Wyeth, P. On the use of photobleaching to reduce fluorescence background in Raman spectroscopy to improve the reliability of pigment identification on painted textiles. *J. Raman Spectrosc.* **2006**, *37*, 830–835. [[CrossRef](#)]
15. Zięba-Palus, J.; Michalska, A. Photobleaching as a useful technique in reducing of fluorescence in Raman spectra of blue automobile paint samples. *Vib. Spectrosc.* **2014**, *74*, 6–12. [[CrossRef](#)]
16. Da Silva, M.A.; Riveiro, D.G.; Pereira, E.A.; Martin, A.A.; Fontes, A.; da Silva Martinho, H. Shifted-excitation difference spectroscopy for in vitro and in vivo biological samples analysis. *Biomed. Opt. Express* **2017**, *1*, 617–626.
17. Zhang, Z.-M.; Chen, S.; Liang, Y.-Z.; Liu, Z.-X.; Zhang, Q.-M.; Ding, L.-X.; Yec, F.; Zhou, H. An intelligent background-correction algorithm for highly fluorescent samples in Raman spectroscopy. *J. Raman Spectrosc.* **2009**, *41*, 659–669. [[CrossRef](#)]
18. Venables, B.; Hornik, K.; Maechler, M. Polynom: A Collection of Functions to Implement a Class for Univariate Polynomial Manipulations. R Package v 1.3-8. 2014. Available online: <https://rdrr.io/github/eestileib/ComplexPoly/> (accessed on 26 July 2017).

19. Kourkoumelis, N.; Polymeros, A.; Tzaphlidou, M. Background estimation of biomedical Raman spectra using a geometric approach. *Spectrosc. Int. J.* **2012**, *27*, 441–447. [[CrossRef](#)]
20. Gautam, R.; Vanga, S.; Ariese, F.; Umopathy, S. Review of multidimensional data processing approaches for Raman and infrared spectroscopy. *EPJ Tech. Instrum.* **2015**, *2*, 8. [[CrossRef](#)]
21. Lieber, C.A.; Mahadevan-Jansen, A. Automated Method for Subtraction of Fluorescence from Biological Raman Spectra. *Appl. Spectrosc.* **2003**, *57*, 1363–1367. [[CrossRef](#)] [[PubMed](#)]
22. Cadusch, P.J.; Hlaing, M.M.; Wade, S.A.; MxArthur, S.L.; Stoddart, P.R. Improved methods for fluorescence background subtraction from Raman spectra. *Mater. Sci.* **2013**, *44*, 1587–1595.
23. Martens, H.; Nielsen, J.P.; Engelsen, S.B. Light scattering and light absorbance separated by extended multiplicative signal correction. Application to near-infrared transmission analysis of powder mixtures. *Anal. Chem.* **2003**, *75*, 593–604. [[CrossRef](#)]
24. Mecozzi, M. A Polynomial Curve Fitting Method for Baseline Drift Correction in the Chromatographic Analysis of Hydrocarbons in Environmental Samples. *APCBEE Procedia* **2014**, *10*, 2–6. [[CrossRef](#)]
25. Massart, D.L.; Vandeginste, B.G.M.; Buydens, L.C.M.; Jong, S.D.; Lewi, P.J.; Smeyers-Verbeke, J. *Data Handling in Science and Technology, Handbook of Chemometrics and Qualimetrics, Vols. 20A and 20B*; Elsevier: Amsterdam, The Netherlands, 1997.
26. Vinzi, V.E.; Chin, W.W.; Henseler, J.; Wang, H. *Handbook of Partial Least Squares: Concepts, Methods and Applications*; Springer Science & Business Media: Berlin, Germany, 2010.
27. Baek, S.J.; Park, A.; Ahn, Y.J.; Choo, J. Baseline correction using asymmetrically reweighted penalized least squares smoothing. *Analyst* **2014**, *140*, 17–38. [[CrossRef](#)] [[PubMed](#)]
28. Liland, K.H.; Kohler, A.; Afseth, N.K. Model-based pre-processing in Raman spectroscopy of biological samples. *J. Raman Spectrosc.* **2015**, *47*, 643–650. [[CrossRef](#)]
29. Hasegawaa, T.; Nishijoa, J.; Umemurab, J. Separation of Raman spectra from fluorescence emission background by principal component analysis. *Chem. Phys. Lett.* **2000**, *317*, 642–646. [[CrossRef](#)]
30. Asfour, H.; Swift, L.M.; Sarvazyan, N.; Doroslovacki, M.; Kay, M.W. Signal Decomposition of Transmembrane Voltage-Sensitive Dye Fluorescence Using a Multiresolution Wavelet Analysis. *IEEE Trans. Biomed. Eng.* **2011**, *58*, 2083–2093. [[CrossRef](#)] [[PubMed](#)]
31. Qu, H.-B.; Ou, D.-L.; Cheng, Y.-Y. Background correction in near-infrared spectra of plant extracts by orthogonal signal correction. *J. Zhejiang Univ. Sci. B* **2015**, *6*, 838–843. [[CrossRef](#)] [[PubMed](#)]
32. Dennis, A. *Photo-Bleaching and Automatic Baseline Correction for Raman Spectroscopy*; R Package v 1.2-1; PerkinElmer: Waltham, MA, USA, 2007.
33. Knorr, F.; Smith, Z.J.; Wachsmann-Hogiu, S. Development of a time-gated system for Raman spectroscopy of biological samples. *J. Opt. Soc. Am.* **2010**, *18*, 20049–20058. [[CrossRef](#)] [[PubMed](#)]
34. Shreve, A.P.; Cherepy, N.J.; Mathies, R.A. Effective Rejection of Fluorescence Interference in Raman Spectroscopy Using a Shifted Excitation Difference Technique. *Spectrosc. Tech.* **1992**, *46*, 707. [[CrossRef](#)]
35. De Luca, A.C.; Mazilu, M.; Riches, A.; Herrington, C.S.; Dholakia, K. Online Fluorescence Suppression in Modulated Raman Spectroscopy. *Anal. Chem.* **2010**, *82*, 738–745. [[CrossRef](#)] [[PubMed](#)]
36. Dongy, S.; Melnik, E.D.; Ban, V.S.; Volodin, B.L. A novel Method for practical implementation of shifted-excitation Raman difference spectroscopy (SERDS). *Spectroscopy* **2012**, *47*, 198–209.
37. Gebrekidan, M.T.; Knipfer, C.; Stelzle, F.; Popp, J.; Will, S.; Braeuer, A. A shifted-excitation Raman difference spectroscopy (SERDS) evaluation strategy for the efficient isolation of Raman spectra from extreme fluorescence interference. *J. Raman Spectrosc.* **2015**, *47*, 198–209. [[CrossRef](#)]
38. Osticioli, I.; Zoppi, A.; Castellucci, E.M. Shift-Excitation Raman difference spectroscopy-difference deconvolution methods for the luminescence background rejection from Raman spectra of solid samples. *Appl. Spectrosc.* **2007**, *61*, 839–844. [[CrossRef](#)] [[PubMed](#)]
39. Oshima, Y.; Komachi, Y.; Furihata, C.; Tashiro, H.; Sato, H. Fluorescence-suppressed Raman technique for quantitative analysis of protein solution using a micro-Raman probe, the shifted excitation method, and partial least squares regression analysis. *Appl Spectrosc.* **2006**, *60*, 964–970. [[CrossRef](#)] [[PubMed](#)]
40. Dochow, S.; Ma, D.; Latka, I.; Bocklitz, T.; Hartl, B.; Bec, J.; Fatakdawala, H.; Marple, E.; Urmey, K.; Wachsmann-Hogiu, S.; et al. Combined fiber probe for fluorescence lifetime and Raman spectroscopy. *Anal. Bioanal. Chem.* **2015**, *407*, 8291–8301. [[CrossRef](#)] [[PubMed](#)]
41. Zhao, J.; Short, M.; Braun, T.; Lui, H.; McLean, D.; Zeng, H. Clinical Raman measurements under special ambient lighting illumination. *J. Biomed. Opt.* **2014**, *19*, 111609. [[CrossRef](#)] [[PubMed](#)]

42. Maiwald, M.; Müller, A.; Sumpf, B.; Erbert, G.; Tränkle, G. Capability of shifted excitation Raman difference spectroscopy under ambient daylight. *Appl. Opt.* **2015**, *54*, 5520–5524. [[CrossRef](#)] [[PubMed](#)]
43. Zhao, J.; Carrabba, M.M.; Allen, F.S. Automated Fluorescence Rejection Using Shifted Excitation Raman Difference Spectroscopy. *Appl. Spectrosc.* **2002**, *56*, 834–845. [[CrossRef](#)]
44. Dochow, S.; Bergner, N.; Krafft, C.; Clement, J.; Mazilu, M.; Praveen, B.B.; Ashok, P.C.; Marchington, R.; Dholakia, K.; Popp, J. Classification of Raman spectra of single cells with autofluorescence suppression by wavelength modulated excitation. *Anal. Methods* **2013**, *5*, 4608–4614. [[CrossRef](#)]
45. Mazilu, M.; Luca, A.C.D.; Riches, A.; Herrington, C.S.; Dholakia, K. Optimal algorithm for fluorescence suppression of modulated Raman spectroscopy. *Opt. Express* **2010**, *18*, 11382–11395. [[CrossRef](#)] [[PubMed](#)]
46. Krafft, C.; Dochow, S.; Bergner, N.; Clement, J.H.; Praveen, B.B.; Mazilu, M.; Marchington, R.; Dholakia, K.; Popp, J. Raman spectra of single cells with autofluorescence suppression by modulated wavelength excitation. In Proceedings of the Biomedical Vibrational Spectroscopy V: Advances in Research and Industry, San Francisco, CA, USA, 9 February 2012.
47. Schmidt, H.; Sowoidnich, K.; Kronfeldt, H.-D. A Prototype Hand-Held Raman Sensor for the in situ Characterization of Meat Quality. *Appl. Spectrosc.* **2010**, *64*, 888–894. [[CrossRef](#)] [[PubMed](#)]
48. Bell, S.E.J.; Bourguignon, E.S.O.; Dennis, A. Analysis of luminescent samples using subtracted shifted Raman spectroscopy. *Analyst* **1998**, *123*, 1729–1734. [[CrossRef](#)]
49. Matousek, P.; Towrie, M.; Parker, A.W. Simple reconstruction algorithm for shifted excitation Raman difference spectroscopy. *Appl. Spectrosc.* **2005**, *59*, 848–851. [[CrossRef](#)] [[PubMed](#)]
50. Willett, R. Multiscale reconstruction for photon-limited shifted excitation Raman spectroscopy. In Proceedings of the IEEE International Conference on Acoustics, Speech and Signal Processing—ICASSP, Honolulu, HI, USA, 16–20 April 2007.
51. Schmidt, H.; Kaiser, D.P.; Maiwald, M. Method for Generating and for Detecting a Raman Spectrum. U.S. Patent 8,310, 672, 28 June 2012.
52. Team, R.C. *R: A Language and Environment for Statistical Computing*; R Foundation for Statistical Computing: Vienna, Austria, 2016.
53. Beleites, C.; Sergo, V. HyperSpec: A Package to Handle Hyperspectral Data Sets in R. R package v 0.98-20150805. 2015.
54. Liland, K.H.; Mevik, B.-H. Baseline: Baseline Correction of Spectra. R Package v 1.2-1. 2015. Available online: <https://cran.r-project.org/web/packages/baseline/index.html> (accessed on 26 July 2017).
55. Borchers, H.W. Pracma: Practical Numerical Math Functions. R Package v 1.9.9. 2017. Available online: <https://www.rdocumentation.org/packages/pracma/versions/1.9.9> (accessed on 26 July 2017).
56. Beleites, C. Ramancal: Calibration Routines for Raman Spectrometers. R Package v 0.1. 2013.
57. Hyndman, R. (Partial) Autocorrelation and Cross Correlation Function Estimation. From Forecast v7.3. 2016. Available online: <https://www.rdocumentation.org/packages/forecast/versions/7.3> (accessed on 26 July 2017).
58. Hyndman, R.J. Forecast: Forecasting Functions for Time Series and Linear Models. 2017. Available online: <https://rdrr.io/cran/forecast/> (accessed on 26 July 2017).
59. Beleites, C. Cbmodels: Collection of “Combined” Models: PCA-LDA, PLS-LDA, PLS-LR as Well as EMSC. R Package v 0.5-20160412. 2016.
60. McCreery, R.L. *Raman Spectroscopy for Chemical Analysis*; Wiley-interscience: Hoboken, NJ, USA, 2000.
61. Kiselev, R.; Schie, I.W.; Askrabic, S.; Krafft, C.; Popp, J. Design and first applications of a flexible Raman micro-spectroscopic system for biological imaging. *Biomed. Spectrosc. Imaging* **2016**, *5*, 115–127. [[CrossRef](#)]
62. Ryabchikov, O. Spikes: Spike Correction of Raman Spectral Data. R Package v 1.0. 2016.
63. Ryabchikov, O.; Bocklitz, T.; Ramoji, A.; Neugebauer, U.; Foerster, M.; Kroegel, C.; Bauer, M.; Kiehnopf, M.; Popp, J. Automatization of spike correction in Raman spectra of biological samples. *Chemom. Intell. Lab. Syst.* **2016**, *155*, 1–6. [[CrossRef](#)]
64. Dhanoa, M.S.; Barnes, R.J.; Lister, S.J. Standard normal variate transformation and de-trending of near-infrared diffuse reflectance spectra. *Appl. Spectrosc.* **1989**, *43*, 772–777.
65. Slobodan, S. *Pharmaceutical Applications of Raman Spectroscopy*; John Wiley & Sons, Inc.: Sandwich, UK, 2008.
66. Long, D.A. *The Raman Effect: A Unified Treatment of the Theory of Raman Scattering by Molecules*; John Wiley & Sons Ltd.: Bradford, UK, 2002.

67. Maiwald, M.; Müller, A.; Sumpf, B.; Tränkle, G. A portable shifted excitation Raman difference spectroscopy system: Device and field demonstration. *J. Raman Spectrosc.* **2016**, *47*, 1180–1184. [[CrossRef](#)]
68. De Luca, A.C.; Dholakia, K.; Mazilu, M. Modulated Raman Spectroscopy for Enhanced Cancer Diagnosis at the Cellular Level. *Sensors* **2015**, *15*, 13680–13704. [[CrossRef](#)] [[PubMed](#)]



© 2017 by the authors. Licensee MDPI, Basel, Switzerland. This article is an open access article distributed under the terms and conditions of the Creative Commons Attribution (CC BY) license (<http://creativecommons.org/licenses/by/4.0/>).

7.2 Bladder Tissue Characterization Using Probe-Based Raman Spectroscopy: Evaluation of Tissue Heterogeneity and Influence on The Model Prediction

Eliana Cordero, Jan Ruger, Dominik Marti, Abdullah S. Mondol, Thomas Hasselager, Karin Mogensen, Gregers G. Hermann, Jurgen Popp, and Iwan W. Schie, Journal of Biophotonics, 2019

Der Nachdruck der folgende Publikation erscheint mit freundlicher Genehmigung von Journal of Biophotonics. Reprinted with kind permission from Journal of Biophotonics.

Erklarung zu den Eigenantenteilen der Promovendin sowie der weiteren Doktoranden/Doktorandinnen als Co-Autoren an der Publikation

Doktoranden	Eliana Cordero
Konzeption des Forschungsansatzes	x
Planung der Untersuchungen	x
Datenerhebung	x
Datenanalyse und -interpretation	x
Schreiben des Manuskripts	x
Vorschlag Anrechnung Publikationsaquivalente	1,0

FULL ARTICLE

Bladder tissue characterization using probe-based Raman spectroscopy: Evaluation of tissue heterogeneity and influence on the model prediction

Eliana Cordero¹ | Jan R uger¹ | Dominik Marti² | Abdullah S. Mondol¹ |
 Thomas Hasselager³ | Karin Mogensen³ | Gregers G. Hermann³ |
 J rgen Popp^{1,4} | Iwan W. Schie^{1,5*} 

¹Department of Spectroscopy and Imaging, Leibniz Institute of Photonic Technology (Leibniz-IPHT), Jena, Germany

²Department of Health Technology, Technical University of Denmark (DTU), Roskilde, Denmark

³Department of Urology, Herlev Hospital, Herlev, Denmark

⁴Institute of Physical Chemistry, Friedrich Schiller University Jena, Jena, Germany

⁵Department of Medical Engineering and Biotechnology, University of Applied Sciences, Jena, Jena, Germany

***Correspondence**

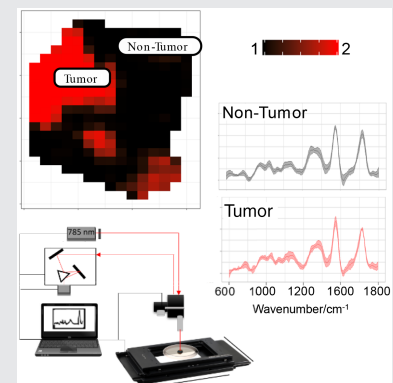
Iwan W. Schie, Leibniz Institute of Photonic Technology (Leibniz-IPHT), Albert-Einstein-Stra e 9, Jena, Germany.
 Email: iwan.schie@leibniz-ipht.de

Funding information

Horizon 2020 Framework Programme, Grant/Award Number: 667933

Abstract

Existing approaches for early-stage bladder tumor diagnosis largely depend on invasive and time-consuming procedures, resulting in hospitalization, bleeding, bladder perforation, infection and other health risks for the patient. The reduction of current risk factors, while maintaining or even improving the diagnostic precision, is an underlying factor in clinical instrumentation research. For example, for clinic surveillance of patients with a history of noninvasive bladder tumors real-time tumor diagnosis can enable immediate laser-based removal of tumors using flexible cystoscopes in the outpatient clinic. Therefore, novel diagnostic modalities are required that can provide real-time in vivo tumor diagnosis. Raman spectroscopy provides biochemical information of tissue samples ex vivo and in vivo and without the need for complicated sample preparation and staining procedures. For the past decade there has been a rise in applications to diagnose and characterize early cancer in different organs, such as in head and neck, colon and stomach, but also different pathologies, for example, inflammation and atherosclerotic plaques. Bladder pathology has also been studied but only with little attention to aspects that can influence the diagnosis, such as tissue heterogeneity, data preprocessing and model development. The present study presents a clinical investigative study on bladder biopsies to characterize the tumor grading ex vivo, using a compact fiber probe-based imaging Raman system, as a crucial step towards in vivo Raman endoscopy. Furthermore, this study presents an evaluation of the tissue heterogeneity of highly fluorescent bladder tissues, and



the multivariate statistical analysis for discrimination between nontumor tissue, and low- and high-grade tumor.

KEYWORDS

bladder cancer, imaging-based Raman, PLS-LDA, Raman probe, Raman spectroscopy

1 | INTRODUCTION

Bladder cancer is ranking as the ninth most frequently diagnosed epithelial cancer worldwide. In 2012, around 549 393 new bladder cancers cases were reported globally, out of which 200 000 cases were fatal, and approximately 75% of the deceased were males [1, 2]. About 75% of the patients suffer from nonmuscle invasive bladder cancer displaying favorable prognosis, although 30%-80% of cases will recur [3]. Bladder cancer histopathological diagnosis is based on stage and grade of the tumor, where the stage refers to tumor invasion into the bladder wall and grade to aggressiveness of the cells. Stage and grade are judged by pathologist's examination of an excisional tissue biopsy obtained via an endoscope inserted through the urethra to the bladder, having the patient most often in general anesthesia in the operating theater. The tissue from suspected abnormal areas of the bladder is sliced and stained for further morphological evaluation by a pathologist. To monitor progression and recurrence a frequent screening is required, making the current bladder cancer diagnosis and treatment one of the priciest medical practices with average lifetime costs estimated at over \$230 000 per patient [4–6]. The histopathological procedure provides morphological tissue features at the intra- and intercellular level, nevertheless, the underlying biochemical information is not assessed [7]. Moreover, the diagnosis is not available instantly due to histological/cytological preparations preceding final microscopy by the pathologist. In order to improve treatment, real-time differentiation between healthy and tumor tissue, high- and low-grade lesions at early stage is urgently needed [8–10]. In the past two decades new optical methods for clinical diagnostics, such as fluorescence endoscopy [11], optical coherence tomography [12], narrow band imaging [8], and others, have emerged. Most of these techniques effectively provide contrast to detect tumor lesions and allow for differential diagnostics, that is, tumor vs healthy tissue, but largely lack the means to assess the biomolecular, which may assist the urologist to decide treatment without delay. Knowing the molecular fingerprint of cells not only allows for precise diagnostic characterization of

the tumor, but also enables new pathological insight into the disease progression. Raman spectroscopy has emerged as an incipient tool for *in vivo* diagnostics, which provides a comprehensive and label-free biochemical characterization of tissue samples [13]. The method has been widely used in clinical *ex vivo* and *in vivo* investigations for the diagnosis of inflammatory diseases and cancers in different organs [13–28], demonstrating the great potential for label-free histopathology [29], cytology [30], biopsy surgical targeting and monitoring studies. This spectroscopic technique has readily been used to characterize bladder tissue by De Jong et al and Stone et al in 2002 [13, 31], demonstrating its capability to distinguish tumor malignances in epithelial tissues [19]. A review on the applications of Raman spectroscopy for the interrogation of bladder tissue for cancer diagnosis is summarized in [32].

Raman spectroscopy has been applied *in vivo* to characterize tumor tissue, assisting surgeons during transurethral resection of tissue to differentiate on site malignant tumor [33]. As a first instance of *in vivo* bladder characterization, Draga et al reported the *ex vivo* and *in vivo* characterization of bladder tissue, employing a fiber-optic Raman probe to detect tumor bladder from normal bladder with a sensitivity of 85% [34]. Notwithstanding, tumor resection of biopsies is still invasive; the target is to adapt Raman spectroscopy to an endoscope in order to minimize the invasion during the tissue inspection in surgery. The present study explicitly aims at providing an in-depth characterization of bladder cancer and outlines strategies for data processing and establishes parameters for future *in vivo* label-free diagnosis [35]. Therefore, greater extend of *ex vivo* investigations are crucial to further move this technology into this direction, in this connection the presented study plays an essential role.

The translation of Raman spectroscopy as a clinical standard tool to assist current diagnosis of bladder tumor grading still must tackle technological and methodical challenges. For instance, proper correction of tissue autofluorescence issue, routines to validate the robustness of the system for clinical use of the equipment, and the consensus on optimal data preprocessing methods will have to be further investigated [36].

The aim of the present study is to demonstrate the feasibility of Raman spectroscopy to further complement clinical trials by differentiating the tumor grading of bladder biopsies and correlating the main changes in molecular constituents to characterize the tissue heterogeneity. We provide a comprehensive overview of sample and data handling, followed by detailed description of the implemented system. We elucidated problems of tissue heterogeneity, which can significantly reduce the performance of a model. In addition, we present a comparison between model-based prediction for tumor and non-tumor and changes in the molecular signatures associated with the pathological differences. Our presented evaluation will help to improve the comprehension of the molecular differences between underlying molecular changes in bladder pathology.

2 | MATERIALS AND METHODS

2.1 | Study population and procedures

Biopsies were obtained from patients, admitted to the urology department in Herlev hospital, suffering from bladder tumor or suspicion of bladder tumor disproved during surgery. The clinical study protocol was approved by the local Danish ethical committee No: H-17015549. Flow of sensitive data was secured and approved by the Danish Data Protection Agency via data management agreements between research centers. After patients were informed and written consent was conferred, biopsies were obtained at the operating theater during transurethral resection of bladder tumors. The biopsies were obtained from healthy bladder wall and from bladder tumors. Each biopsy was divided into two parts, of which one biopsy was sent for a histopathological diagnosis and the other was placed on acetate paper and saline buffer added for spectroscopic examination. In contrast to previously reported studies [13, 37], an entire extracted biopsy without thin-sectioning was used in this study with the purpose of maintaining the integrity of the tissue, since sectioning and staining can severely alter the structure of the biopsy. The summary of the present pathologies is outlined in Table S1.

A total of 67 biopsies were obtained from 28 patients with bladder tumor (8 females; 20 males; median age: 73 years) from which 19 biopsies from seven patients were excluded from the data analysis due to either being of other tissue, that is, benign prostate (n = 4), prostate cancer (n = 2), unknown histopathology (n = 6) or measured under different experimental conditions (n = 7) (Figure 1). Of the remaining biopsies a total of 42 biopsies were examined immediately after surgery and six

were frozen at -80°C , and analyzed at a later time point.

2.2 | Setup description

Raman spectra were collected on a custom-made Raman system equipped with a fiber-optic Raman probe (InPhotonics, RPB), which was connected to a 785-nm single-mode excitation laser (XTRA, Toptica) with a nominal output power of 300 mW, and a spectrometer (IsoPlane 160, Princeton Instruments) equipped with a 400 groves/mm grating and a back-illuminated deep depletion CCD camera (PIXIS400, Princeton Instruments) with a 1340×400 imaging array and $20 \mu\text{m} \times 20 \mu\text{m}$ sized pixels. The excitation light was filtered inside the probe to remove unwanted background contributions from the delivery fiber and focused by a lens into a spot of $100 \mu\text{m}$. The generated Raman signal was collected by the same lens. The signal was separated from the excitation with a dichroic mirror, and then focused into the entrance aperture of a multimode collection fiber with a core diameter of $200 \mu\text{m}$ and an numerical apperture (NA) of 0.22, which is connected to the spectrometer. The samples were placed on a calcium fluoride (CaF_2) slide (Crystal, Germany) that was mounted on the motorized translational stage (MLS203, Thorlabs). The setup is illustrated in Figure 2.

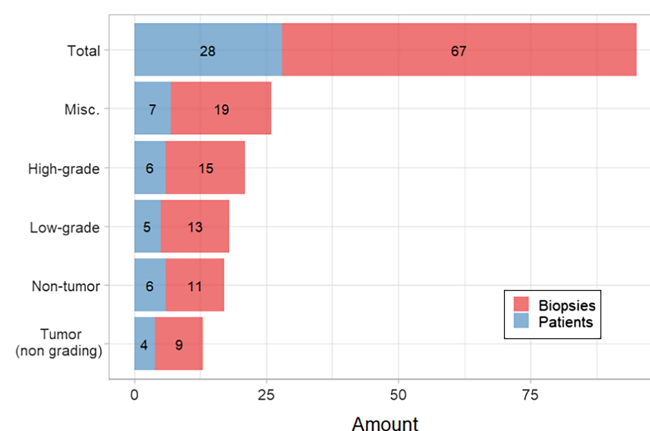


FIGURE 1 Summary and breakdown of patients and biopsies. Misc. refers to miscellaneous nonbladder tumor histopathology (four benign prostatic tissues, two cancer prostate tissue, six biopsies with unknown histopathology), and biopsies measured under different experimental conditions. Biopsies belonging to this group were not selected to train the model. Tumor (nongrading) refers to histopathological assignment indicating tumor without grading. This data was used just to create the models that differentiate tumor and nontumor regions

Raman images of the biopsies were acquired by raster-scanning the sample, while keeping the probe stationary. A conventional CMOS camera (DCC1545M, Thorlabs), which was located next to the Raman probe, allowed the acquisition of a brightfield image of the sample and the selection of a region of interest (ROI) for the Raman measurements. The acquisition of Raman spectra from the biopsy was performed automatically, using in-house software for instrument controlling written in LabView. Each of the samples was placed on the CaF₂ slide with the urothelial surface pointing to the Raman probe. Similar to previously reported studies, a 785-nm excitation wavelength was selected to avoid high fluorescence [38, 39], with an excitation power of 100 mW, which allows obtaining a sufficient signal to noise ratio, without any obvious damage to the tissue. Each spectrum was acquired at an acquisition time of 3 seconds, but the total spectral collection time was dependent on the ROI size. For the averaged sample size of approximately 4 mm² the measurement of 400 spectra took around 20 minutes.

2.3 | Data analysis

All data pretreatment and analysis steps were performed using the RStudio software for statistical computing and graphics [40, 41]. The data import, export, the preprocessing algorithms and the development of the classification model were performed using hyperSpec and cbmodels packages [42].

2.3.1 | Preprocessing

Raman spectra of bladder tissue exhibit very high tissue autofluorescence (Figure 3A). To extract the Raman signal from the raw spectra the data was preprocessed, that is, calibrated and corrected for cosmic spikes and background contributions, respectively. The wavenumber calibration was performed using the relative peak positions of *N*-acetyl-*p*-aminophenol powder (Acetaminophen, Sigma-Aldrich) and intensity calibration was performed by using the reference spectrum of a white light source standardized by the National Institute of Standards and Technology (Kaiser HCA calibration accessory). The correction for the constant offset bias and the dark current was implemented by subtracting a recorded dark spectrum. Following this, cosmic spikes were removed using a correction algorithm developed by Ryabchykov et al [43]. The calibrated spectra were noise-filtered using the `prcomp` function of the `stats` package in R, followed by a Savitsky-Golay filtering [44].

As introduced in this section, one of the main challenges for the data preprocessing is the high fluorescence background, as it can be observed in Figure 3A. This background mainly originates from the presence of endogenous fluorophores, such as pyridinic (NADPH) and flavin coenzymes as well as collagen and elastin from the extracellular matrix [45]. Besides the high autofluorescence from the tissue that obscures the Raman signal, there is some additional background from the fiber probe. Among the background correction methods asymmetric least squares (ALS) [46], the

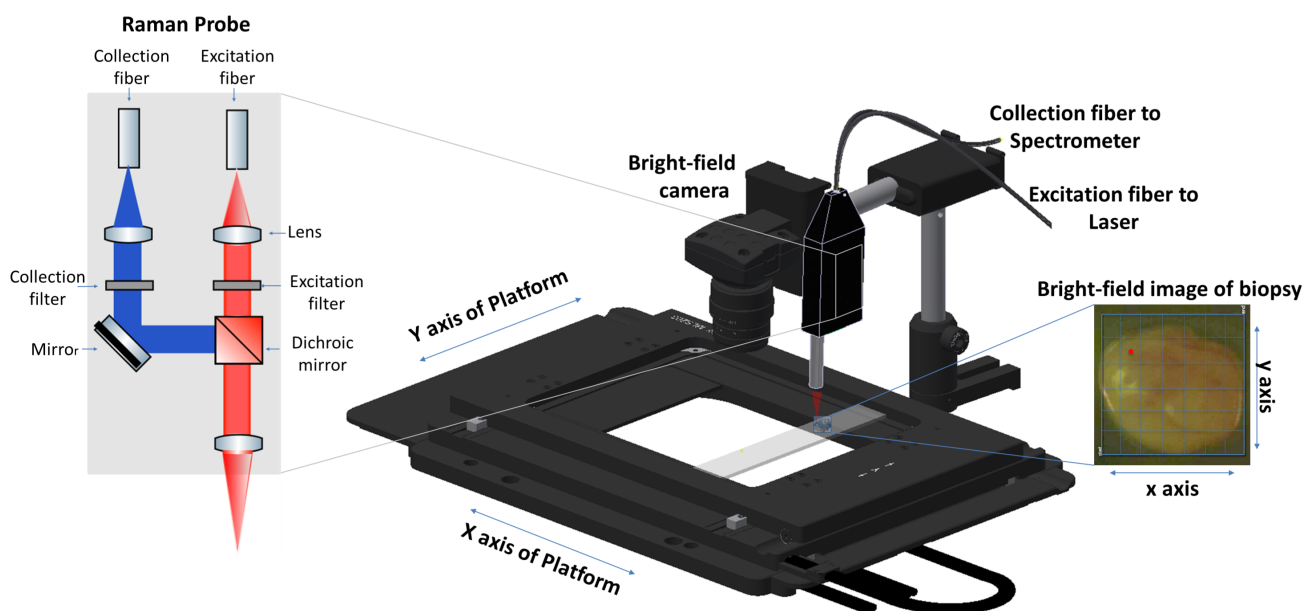


FIGURE 2 Schematic representation of the Raman imaging system combined with a Raman fiber-optic probe. The optical design of the fiber-optic Raman probe is indicated in more detail on the left-hand side

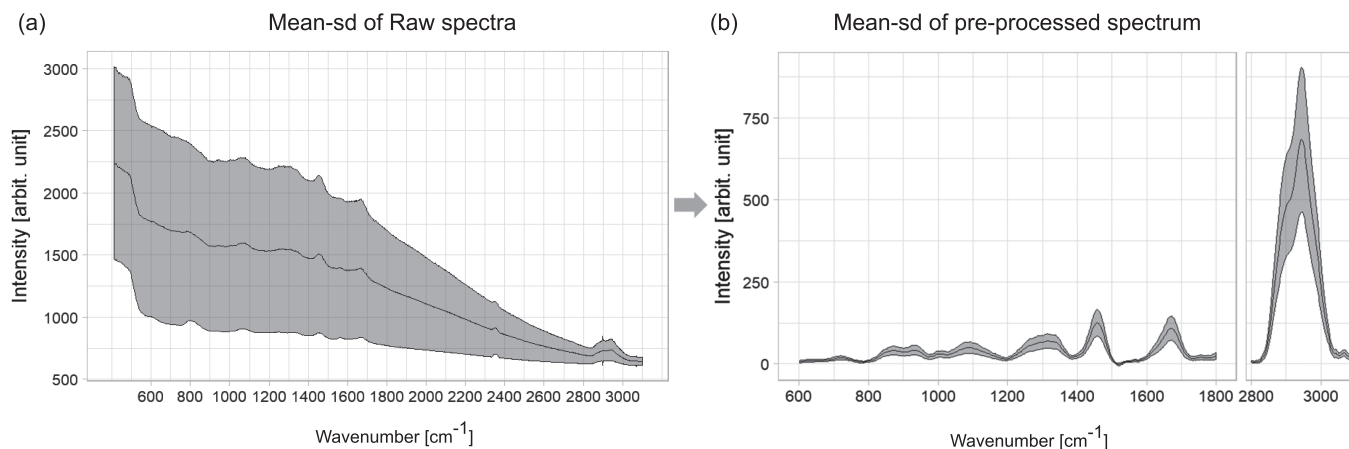


FIGURE 3 Mean and SD spectra of (A) raw Raman spectra for the entire dataset and (B) a mean Raman spectrum after the preprocessing

modified polynomial fitting of Lieber and Mahadevan-Jansen [47], statistics-sensitive nonlinear iterative peak-clipping algorithm (SNIP) correction [48] and extended multiplicative signal correction (EMSC) were tested. Figure S1 displays the individual results for a visual comparison. The best performance for background correction was achieved by EMSC, Figure S1A, and is based on a least squares fitting of predefined background spectra, n -order polynomials, and pure components spectra [49]. To provide a comparison, the other methods are also shown: ALS corrected spectra, Figure S1B, presented overfitting in the low- and high-wavenumber region and background contributions from fiber and substrate were not removed, the same is observed applying the polynomial fitting approach (Figure S1C). The SNIP correction, Figure S1D, can remove background coming from fiber and substrate as EMSC does, however, it is slower than EMSC and the SD due to the background is higher in comparison to EMSC. Following the background correction, the data was normalized to unity. The resulting mean spectrum with the spectral information from 600 to 3100 cm^{-1} is shown in Figure 3B, where the main spectral contributions are related to proteins, collagen, nucleic acids and lipids.

2.3.2 | Classification model

The classification was performed combining partial least squares regression (PLS) as dimension reduction technique with linear discriminant analysis (LDA) to differentiate three main classes from the biopsies: nontumor (NT) tissue, low-grade (LG) and high-grade (HG) tumor. The combination of the PLS and LDA classifier allows to have an insight in the underlying interclass differences in the molecular signature via loadings and weights. In addition, the combination of

the methods has demonstrated that it can cope with large variable to sample ratios [50].

In the PLS-LDA model, the linear discriminant (LD) classifier uses the number of components determined by the partial least squares, also known as the latent variables, as input space. The dimension reduction technique helps to select relevant variables correlating the best with the class attributes [50, 51]. The partial least squares regression was performed using the function `pls` of the `pls` package [52]. The predictor matrix was based on several mean spectra per biopsy and the response vector contained the histopathological assignment. The number of components was determined based on leave-one-out-cross-validation, while assessing the highest correlation vs the least error [53].

2.3.3 | Cross-validation

To prevent overfitting of the classifier, cross-validation (CV) was performed by applying a hierarchical scheme for classification models, as presented in more detail by Guo et al [54]. Hereby, a two-layer CV was applied where the first layer or internal CV, known as training dataset, was employed to construct the model and the external CV or testing dataset was used for validation. The performance of the classification model was validated by applying hierarchical splitting of the data, where a two-level model was created, and is referred in the rest of the text as model level 1 (ML1) for tumor and NT differentiation, while model level 2 (ML2) refers to the differentiation of LG and HG tumor, respectively. To test the influence of the sampling area for ML1, between 1 and 80 spectra were taken from random pixel locations of each biopsy, and a mean spectrum was calculated. The dataset was partitioned into fivefold with 10 iterations, resulting in

50 different models for each set, as illustrated in Figure 4. The prediction for the tumor area is displayed in Figure S3, where the prediction for the tumor and NT location is indicated for a typical biopsy, and an indicated number of spectra. To better summarize the results, the prediction of the models for the indicated number of spectra is plotted as the ratio of tumor region and total region to the number of spectra used to build the model (Figure S4). In most situations the ML1 model performs independently of the number of spectra used. To ensure that only spectra from tumor areas enter the subsequent modeling ML2 phase, the predictions for each single spectrum per biopsy were aggregated and the respective spectrum was considered as “tumor” at a mean prediction value above 1.5 and as “NT” at a value below 1.5, respectively. Spectra with the predictive value 1.5 were not assigned to any group. This range was selected by calculating the kernel density of the mean prediction of each biopsy, where it was found that for this range the likelihood for belonging to any of the group NT (1) or tumor (2) is 0. Shortly, the calculated mean prediction was performed on each spectrum of each biopsy and just the set of spectra predicted as tumor was subsequently used for next modeling phase, this is represented in Figure 4. Based on selected spectra from malignant tissue

the ML2 were created by using fivefold CV with 10 iterations. The whole workflow is described in more detail in Figure 4.

3 | RESULTS AND DISCUSSION

In total 67 biopsies were measured out of which 48 were used to create and validate the ML1 model and of those 28 biopsies were used to generate and validate ML2. Spectra from biopsies were assigned to three groups according to the histopathological grading of the tissue, that is, NT, LG and HG tumor, Figure 5. The mean spectra and SD of each group of spectra have been calculated and plotted in Figure 6. The main bands associated to lipid, collagen, protein and nucleic acids have been labeled to allow an assignment of the main differences between each group and its molecular constituents. The goal of the investigation was, firstly, to characterize and to discriminate bladder cancerous tissue and to perform tumor grading, using an in-house developed fiber probe-based Raman-imaging platform, which effectively mimics the in vivo conditions. Secondly, to provide and compare a comprehensive data preprocessing and analysis

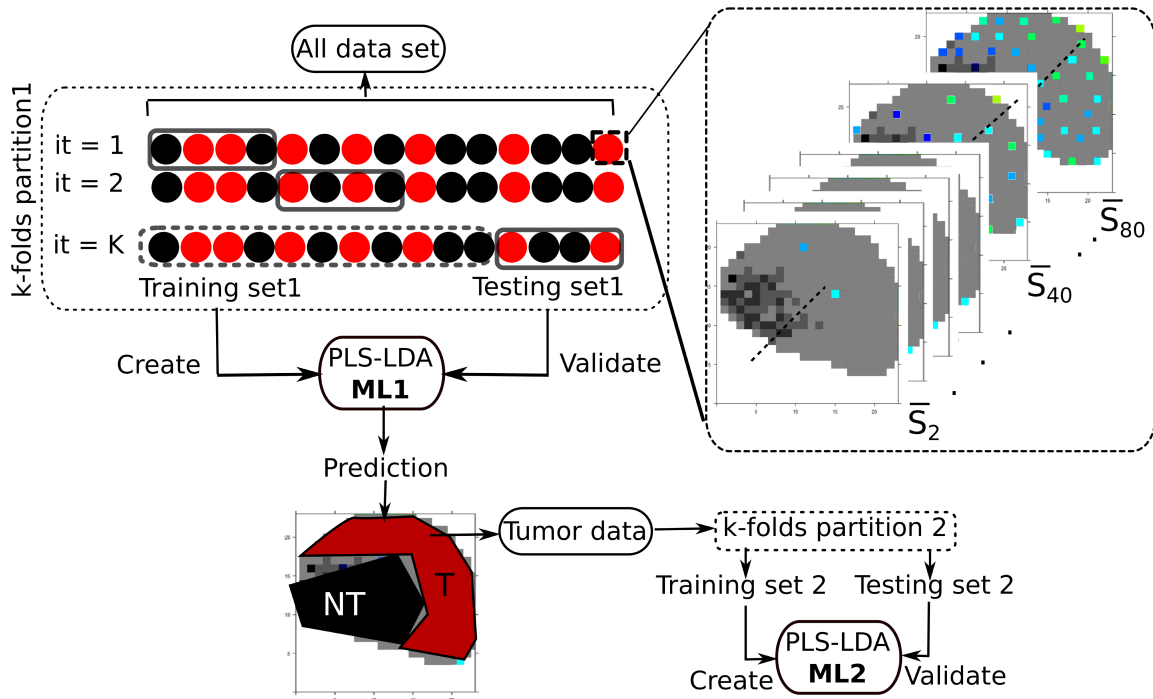


FIGURE 4 Workflow of the data splitting method used for the k -fold cross-validation of the models. Hierarchical splitting of data, the data was split in fivefold groups to create (training set 1) and validate (testing set 1) the first level models (ML1): nontumor and tumor; the models of the first level are used to select the tumor areas of the tumor data, just the tumor data resulted from the predictions of ML1 is further partitioned in fivefold to obtain 5 groups of training set 2 and testing set 2, creating and validating the second level models (ML2), respectively. The zoomed area represent how the mean set for each biopsy is obtained, random points from 1 to 80 are selected and for each of the random groups a mean spectra is determined and each biopsy has a group of 80 mean spectra

workflow that can deal with commonly occurring background contributions, for example, fiber and autofluorescence background, and to introduce a

robust analysis strategy, which extracts compressive information from the biopsies and classifies tumor and cancerous grade in bladder. Thirdly, to evaluate the

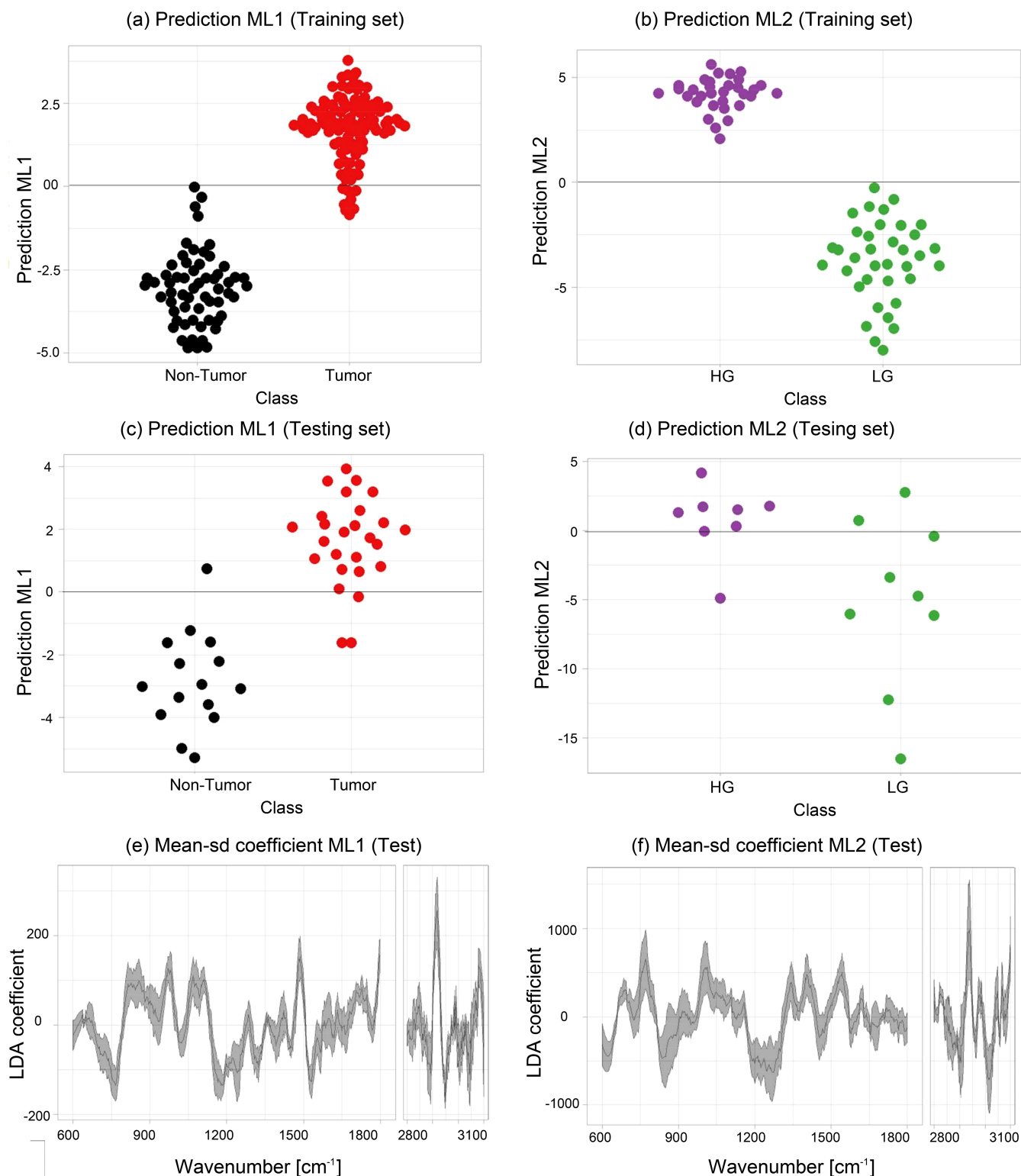


FIGURE 5 Beeswarm plots of the LDA scores of classification models mean \pm SD of the coefficients for a single iteration. Figure 5A,B beeswarm plot after predicting the models level 1 with the training sets 1 and models level 2 with the training sets 2, respectively. Figure 5C, D beeswarm plot after validating the models level 1 with the testing sets 1 and the models level 2 with the testing sets 2, respectively. Figure 5E,F mean \pm SD of the coefficients for the predictions after validating ML1 and ML2

effects of intrinsic tissue heterogeneity on the performance of the models and to explore the spatial variation of Raman bands representative for dominant constituents of cancerous/healthy bladder tissue.

3.1 | Chemometric modeling of biopsy grading

As outlined in Section 2.3.3, a two-level PLS-LDA classification model was built to differentiate between tumor from NT ML1 and LG from HG tumor tissue ML2. Figure 5A,C shows the beeswarm plots of the LD scores

for the training and testing dataset of a fivefold iteration for ML1, respectively. The figures indicate that the model performs very well to separate tumor (red) from NT (black) biopsies with a sensitivity of 92% and a specificity of 93%, Table 1. The achieved values to discriminate tumor and NT tissue are well within the range reported in previous studies [31, 32]. Despite that grade differentiation is not as high, similar results were also reported [32, 55]. While most of the reported studies used microscopy setups, here measurements were performed using a small hand-held probe, which allowed to significantly reduce the footprint of the entire device. The achieved classification values were also potentially influenced by

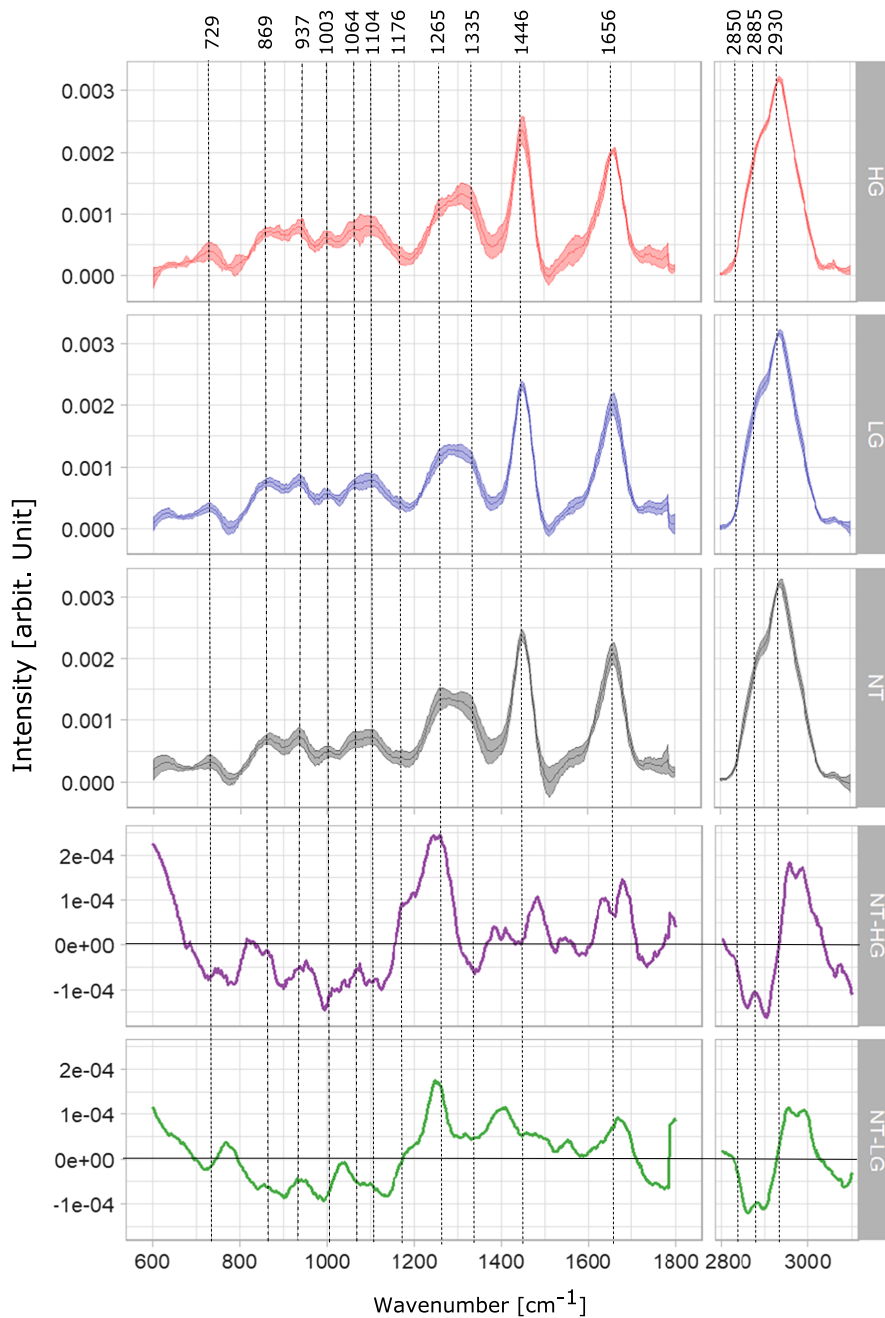


FIGURE 6 Mean Raman spectra with corresponding standard deviation of biopsies diagnosed as nontumor (NT, black), low-grade (LG, blue) and high-grade (HG, red) tumor tissue, respectively. The two bottom panels are difference spectra derived from mean spectra from NT and HG tumor and the difference spectrum between the mean of NT and LG tumor. The vertical lines indicate major bands

the heterogeneity of the measured biopsies, and the fact that, even though the biopsies were taken in close vicinity slight differences which could have influence the validation of the model, might have been present.

The mean and the SD of respective LD coefficients of ML1 are shown in Figure 5E. It is important to point out that for ML1 the negative LD coefficients correlate with the bands that indicate features related to NT tissue, while the positive coefficients values indicate bands related to tumor tissue. Positive features around 1299 and 1313 cm^{-1} indicate dominant presence of lipid bands in tumor tissue, and negative features in the same region indicate the dominant presence of collagen in NT tissue. The performance of the ML2 is represented in Figure 5B, D where the LDA scores are shown in a beeswarm plot and a clear separation between the LG (green) and HG (lila) classes is observed. The negative coefficients in Figure 5F are indicators of spectral features to distinguish LG from HG tumor. ML2 achieve an adequate tumor grading in terms of predictive performance with a sensitivity of 85% and an overall model accuracy of 84% (Table 1).

Different classifiers were tested to establish the best classifier for this dataset. Figure S2A displays the performance of the employed classifiers after applying PLS-based dimension reduction for LDA, QDA (quadratic discriminant analysis) and LR (logistic regression). LDA demonstrated to be the classifier with the best performance, achieving highest accuracy and sensitivity for ML1 and ML2. LR was also tested, nevertheless, in comparison to LDA, the differences in the performance were minimal. LDA is less prone to overfitting in comparison to QDA and does not require as big sample size to guaranty robustness. While SVM (support vector machine) achieved the highest specificity, it had also the lowest sensitivity. The new proposed hierarchical second level classification model, which employs ML1 and ML2, achieved better classification scores when discriminating tumor and NT bladder tissue as the classical one level classification model approaches, reported recently in fiber-based Raman bladder diagnosis investigations [34, 55]. Figure S2B illustrates the performance comparison for classifying LG and HG by using three different

approaches, the level 1 model classification approach using a mean spectra per biopsy did not meet efficient scores to differentiate LG from HG, discriminating with very low accuracy (51%). Due to the heterogeneous nature of some biopsies, applying the classical one-layer approach with a set of random pixels per biopsy, for example, 80 random pixels, and computing the mean spectra termed mean random pixel (MRP), the outcome improves, but is still too low to be of clinical value. When applying the two-layer approach, using different sets of MRPs, as employed in this study, the achieved performance provides an improved discrimination between LG and HG tumor with an accuracy of 84%. In order to test the classification performance for tumor and NT tissue differentiation based on the biochemical information of particular bands only, two prominent bands, that is, collagen band (1305 cm^{-1}) intensities and lipid band (2850 cm^{-1}), were used for the training of a model. The band information alone allowed to achieve a reasonable classification accuracy of 87% (Figure S2C).

3.2 | Band assignments in Raman spectra of nontumor, low- and high-grade tumor tissue

The mean spectra of the LG and HG samples were calculated with the predicted tumor areas of the biopsies using ML1 and are plotted together with the mean spectra of healthy tissue, in Figure 6. Spectral contributions of collagen and protein bands are resolved at 729, 937, 1003, 1104 and 1265 cm^{-1} , where C—C stretching of protein is observed at 729 cm^{-1} and the C—C vibration of collagen backbone is evident at 937 cm^{-1} [56, 57]. The presence of phenylalanyl protein at 1003 and 1104 cm^{-1} differs between the mean spectra of LG and HG tumor. Strong presence of amide III of collagen is observed at 1265 cm^{-1} , where the band intensity of the NT mean spectrum is higher than the band intensity of both LG and HG tumor mean spectra; those differences in collagen bands were also reported by De Jong et al and Stone et al [37, 58].

Main spectral contributions of lipids are resolved at 1064, 1446, 1656 cm^{-1} and the high wavenumber region at 2850 and 2930 cm^{-1} , where an increase in band intensities of the tumor spectra (LG and HG) in comparison with the NT spectrum indicates and increment in lipid content for tumor tissue. In addition, the difference spectra between NT and HG (purple), NT and LG (green), Figure 6, show a higher lipid content in both, LG and HG biopsies, which can be observed in the negative peaks of the bands at 1064, 2850 and 2885 cm^{-1} . Significant lipid bands are resolved at the CH_2 bending mode of lipids

TABLE 1 Statistics of the model by class

Class	ML1 (%)	ML2 (%)
Sensitivity	92	85
Specificity	93	83
Accuracy	92	84
Confidence interval	(89-95)	(78-89)

Note: The confidence interval is calculated for the accuracy.

and CH₂ symmetric stretching of protein and lipids evident at 1446, 2850, 2885 and 2930 cm⁻¹, respectively [59]. The band assignments are summarized in Table 2. Main variations between LG and HG tumor spectra are resolved at protein bands 1176 and 1446 cm⁻¹, as well as in the high wavenumber region at 2930 cm⁻¹. The spectral features for LG and HG spectra have also been previously reported by Stone et al [58].

3.3 | Evaluation of biopsy heterogeneity

Tumor heterogeneity can be understood in multiple ways: it can be described in terms of observable features, such as morphology, nanoscale structure [60], cellular arrangement, histology [61], genotypes and protein expression [62]. Likewise, it can be studied at different levels, such as molecular, intracellular or bulk levels. A previous study demonstrated that Raman spectroscopic imaging can provide high spatial resolution measurements of the distribution profiles from tissue constituents, such as collagen and glycosaminoglycans in tissue [63] and nucleic acid, protein and lipid in eukaryotic cells [64, 65]. Heterogeneity is particularly challenging for classification problems, where heterogeneous data can significantly affect the reliability and performance of the models. Furthermore, for clinical in vivo applications it is important to understand if there is a need to perform Raman imaging to do an accurate characterization of the tumor grading, or if point measurements using, for example, a fiber optic Raman probe suffices. Two approaches were investigated at the bulk level. The first approach uses the classification model's predictions (ML1) to estimate the tumor and NT fraction of the biopsy. The second approach consists in the visual inspection of the distribution of main constituents, collagen, protein and lipids in corresponding Raman images of the biopsy at relevant bands. There is currently no Raman-based study, which characterizes the heterogeneity of bladder tissue. The presented work considers the intrinsic biomolecular heterogeneity of tumor tissue and attempts to elucidate the molecular fingerprint, which allows to discriminate between the different pathologies.

3.3.1 | Heterogeneity of the biopsy based on the prediction of ML1

For classification problems, heterogeneous data can affect the reliability and performance of the models, resulting in reduced sensitivity and specificity. For biopsies, heterogeneity is frequently also related to the fact that the extracted tissue samples not only have the tissue of

TABLE 2 Raman band assignments for spectra in Figure 6 [67]

Wavenumber (cm ⁻¹)	Bond assignment	Macromolecules
729	C—C stretching, proline	Collagen [56]
869	C—C stretching, choline group	Collagen and lipid [68]
937	(C—C) vibration of the collagen backbone	Collagen [56, 57]
1003	Phenylalanine, C—C skeletal, phosphate group	Collagen and lipid [57, 68]
1064	Skeletal C—C stretch	Lipid [57]
1103	Phosphate group and symmetric ring breathing of phenylalanine	Proteins (collagen) and lipid [57, 69]
1176	C—H bending tyrosine	Proteins [57]
1265	Amide III of collagen, ν(CN), δ(NH) amide III	Collagen [56, 57, 70]
1335	CH ₃ CH ₂ wagging	Collagen [18, 57]
1446	CH ₂ bending mode of proteins and lipids, CH ₂ deformation	Lipids and proteins [19, 57]
1656	C=C lipids, amide I (proteins)	Lipids and proteins [69]
2850	ν _s CH ₂ , lipids, fatty acids CH ₂ symmetric	Lipids [57, 59]
2885	ν _{as} (=CH ₂), ν _s CH ₃ , lipids, fatty acids	Lipids [57, 59]
2930	CH ₂ sym. stretching, chain-end CH ₃ sym. stretching	Protein and lipids [59, 71]

interest, that is, tumor tissue, but also contain normal tissue located in the proximity of the tumor tissue, or due to the proper orientation of the tissue for measurement. From brightfield images it is impossible to differentiate tumor and NT regions. In consequence, taking spectral information from the entire biopsy can affect the performance of the models, or result in not well reproducible data. It is, therefore, important to find a method to split the heterogeneous data into a set of homogeneous groups of data.

There are two key questions, firstly, how the tissue heterogeneity can be bypassed to do a proper classification of tumor grading and secondly how the proposed

model generation method can effectively group the data into homogeneous units. To answer these questions, the generated ML1 was employed to predict all the spectra of each tumor biopsy, as it was described in Section 2.3. Each individual spectrum of a biopsy was tested and cross-validated by the model and a mean of the resulting predictive values was calculated. This mean prediction value was plotted at each location of the hyperspectral image of each biopsy. Four cases are shown in Figure 7, where 1 encodes a purely NT (black) and 2 a purely tumor spectrum (red), respectively. For further analysis we set the boundary condition such that values below 1.5 to NT tissue and values above 1.5 to be tumor tissue. As can be seen in Figure 7 biopsies significantly differ from each other.

For example, the biopsy in Figure 7A,B are very homogeneous, that is, independently of the location of the acquired spectrum ML1 would mostly predict for (A) healthy tissue and (B) tumor tissue. The pathological diagnosis was healthy and HG tumor, respectively. The biopsies mapped in Figure 7C,D, on the other hand, are highly heterogeneous and present multiple NT regions,

which if included into the model building would negatively affect the results. From the examples shown here it is clear that many of tumor biopsies actually contain areas that are NT, and if included into the modeling, would substantially influence the performance of the model.

3.3.2 | Heterogeneity at the bulk level based on the molecular content in the biopsy

Raman imaging can be used to learn about the heterogeneity of healthy and tumor bladder tissue at the bulk level by mapping the Raman intensity of specific bands on a biopsy. In Figure 8 the distributions of relevant constituents of the biopsies, that is, collagen (1265 cm^{-1}) and lipid (2885 cm^{-1}) Raman bands for two selected biopsies diagnosed as high-grade tumor (left panels) and inflammation (right panels), respectively, are visualized. For comparison, Figure 8A illustrates the mean prediction of ML1 on homogeneous tumor and NT biopsies and Figure 8B,C illustrates the relative Raman intensity of

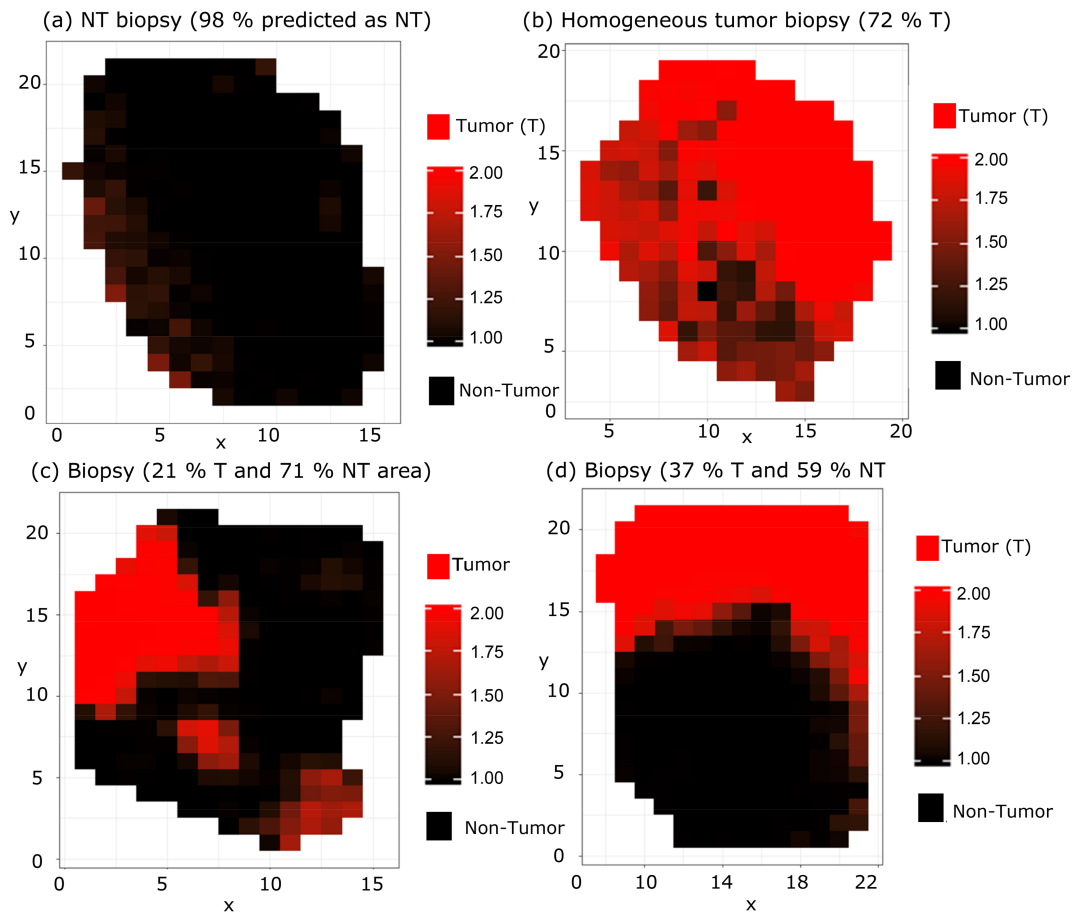


FIGURE 7 Mean prediction map for tumor and nontumor (NT) regions of test biopsies: (A) NT biopsy 98% of the spectra predicted as NT, (B) homogeneous tumor biopsy with 72% of tumor (T) area, (C) biopsy with 21% of tumor (T) area and 71% of NT area, and (D) test biopsy with 37% of T area and 59% of NT area

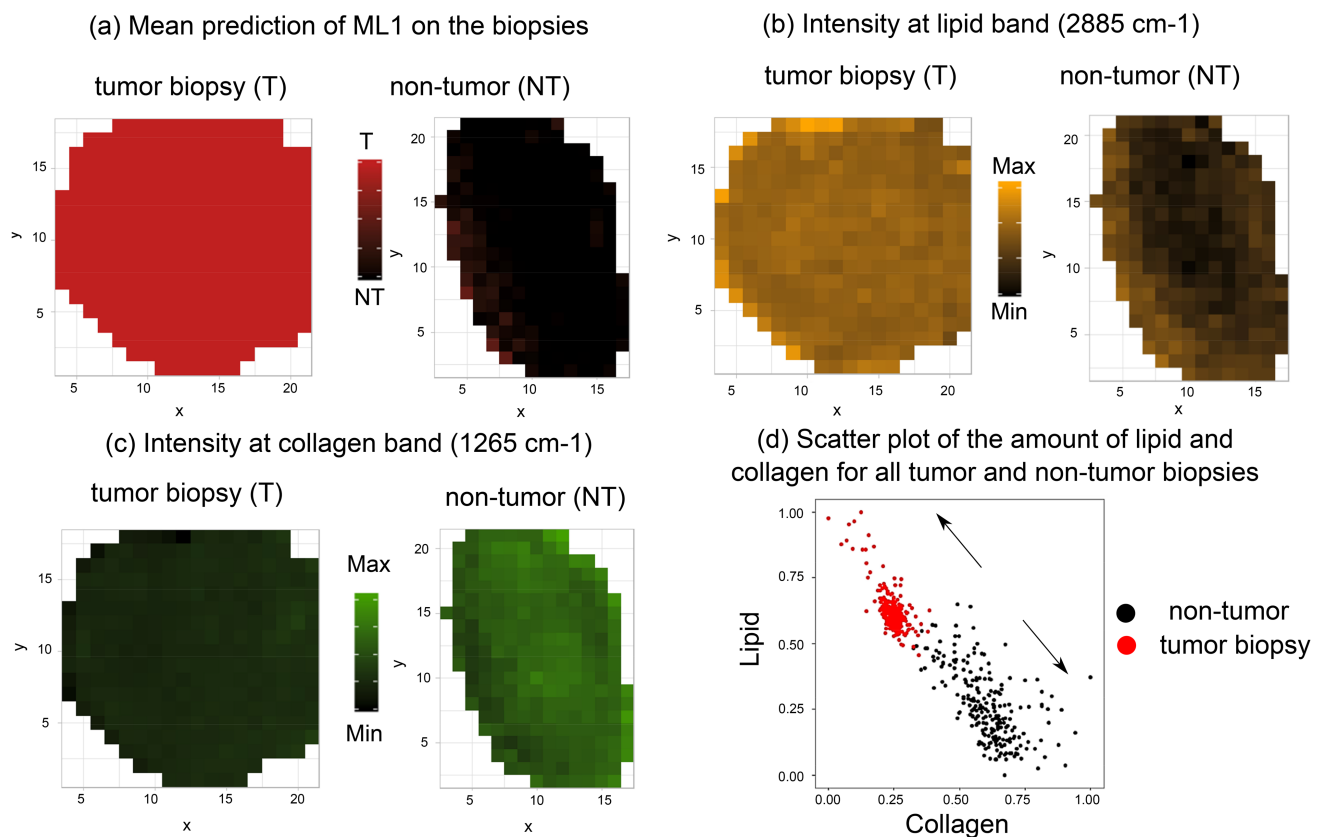


FIGURE 8 Images of tumor and nontumor based on: (A) mean prediction of the ML1 for homogeneous tumor and nontumor biopsies, where red is predicted as tumor and black as nontumor; Raman intensity image of the same tumor and nontumor tissue at: (B) lipid band (2885 cm^{-1}) and (C) collagen band (1265 cm^{-1}). The color information represents different chemical constituents, that is, green for collagen and yellow for lipid. The scatter plot (E) of the relative intensity of lipid and collagen for all biopsies shows the relation between the main constituents and the tissue characterization (nontumor and tumor). The intensity of the bands at the mentioned wavenumbers was normalized to min-max

the bands at selected wavenumbers. Based on Figure 8B it can be seen how lipid contributions are more dominant in the tumor biopsy in comparison to the NT biopsy. The presence of collagen is observed in Figure 8C where amide III of collagen exhibits higher intensity in the NT biopsy in contrast to the tumor biopsy. To get a better comprehension of the imaging data a scatter plot of the relative intensity of lipid and collagen from all biopsies was used to depict the relative concentrations of lipid and collagen, Figure 8D. The point clouds were visualized in a 2D scatter plot, which encodes the relative number of points from tumor (red) and NT spectra (black). Consistently, most Raman spectra belonging to NT tissue according to ML1 show higher amounts of collagen in comparison to those from biopsies predicted as tumor. On the other hand, spectra from tumor tissue prove to have higher relative amounts of lipid. Both, Raman images shown in Figure 8A-C and the scatter plot in Figure 8D provide evidence for significant spectral changes in bladder tissue undergoing tumor development and are consistent with results from biochemical investigations of previous studies [32, 58, 66].

4 | CONCLUSION

In this study, we demonstrated that Raman spectroscopic imaging employing a hand-held probe can be used as a valuable tool to characterize bladder tissue at the molecular level. We provide an extensive biochemical characterization of bladder cancer pathology to facilitate real-time assessment of tumor tissue in future studies. The optical fiber Raman probe imitates the optical performance expected in an in vivo setting, presenting initial operation benchmarks and influential factors to consider for future in vivo investigations. A hierarchical classification was performed, where the first level models (ML1) predict the main differences between tumor and NT tissue and the second level models (ML2) differentiate between HG and LG tumor. The model-based evaluation has shown that the changes in collagen bands and the increase of the lipid intensity can be associated in differences between tumor and NT tissue, and changes in the protein bands can be used as an indicator to differentiate between LG and HG. The PLS-LDA models can differentiate tumor from NT with a sensitivity of 92% and a specificity of 93%, while

the achieved sensitivity to differentiate LG from HG tumor is 85%. In our selected test group, NT tissue is assigned with an overall accuracy of 92% with confidence levels between 89% and 95%. The LG and HG can be predicted with 84% accuracy in a confidence interval between 78% and 89%. The findings of this study also serve as indication of biopsy heterogeneity, where the prediction of the models, which classify tumor and NT, are used to map the tumor areas on the biopsy. This results in a better performance of the second level models, which use only the tumor areas to train and validate the models to differentiate LG and HG tumors. In addition, the mapping of the intensity at representative lipid, collagen and protein bands of different biopsies served to follow changes of these main constituents. It was demonstrated that a fiber-based Raman system may complement the well-established methods, such as cystoscopy, to achieve an immediate bladder tumor diagnosis and thus give the possibility to treat tumor immediately instead of waiting for histopathological diagnosis of a biopsy from the bladder lesion. Ultimately, Raman probe assisted bladder endoscopy can be performed in the outpatient department using small and less traumatizing instruments, resulting in additional health cost savings and significant improvement in patients' prognosis and quality of life. Simultaneously, immediate tumor diagnosis will allow for the instant decision whether the patient can be treated immediately in the outpatient department or needs admittance to the urology ward, as LG noninvasive bladder tumors less than 1.5 cm can be treated in the outpatient department.

ACKNOWLEDGMENTS

This work is financially supported by the Institute of Photonics Technology and Herlev & Gentofte Hospital, Copenhagen University, Denmark, and has received funding from the European Union's Horizon 2020 research and innovation program under grant agreement no. 667933 (MIB). We thank Shuxia Guo for the helpful discussion about the cross-validation approaches.

AUTHOR BIOGRAPHIES

Please see Supporting Information online.

ORCID

Iwan W. Schie  <https://orcid.org/0000-0003-0336-3168>

REFERENCES

- [1] S. Antoni, J. Ferlay, I. Soerjomataram, A. Znaor, A. Jemal, F. Bray, *Eur. Urol.* **2017**, *71*, 96.
- [2] P.-U. Malmström, S. Agrawal, M. Bläckberg, P. J. Boström, B. Malavaud, D. Zaak, G. G. Hermann, *Scand. J. Urol.* **2017**, *51*, 87.
- [3] V. K. Sangar, N. Ragavan, S. S. Matanhelia, M. W. Watson, R. A. Blades, *BJU Int.* **2005**, *95*, 59.
- [4] R. Madeb, D. Golijanin, J. Knopf, E. M. Messing, *Expert Rev. Anticancer Ther.* **2007**, *7*, 981.
- [5] J. Leal, R. Luengo-Fernandez, R. Sullivan, J. A. Witjes, *Eur. Urol.* **2016**, *69*, 438.
- [6] A. C. James, J. L. Gore, *Urol. Clin. North Am.* **2013**, *40*, 261.
- [7] J. S. Engelskjerd, C. M. Deibert, Cystoscopy. in *StatPearls*, StatPearls Publishing, Treasure Island, FL **2018**.
- [8] C. C. Cauberg Evelyne, J. J. M. C. H. de la Rosette, T. M. de Reijke, *Indian J. Urol.* **2011**, *27*, 245.
- [9] J. A. Witjes, D. O. T. M. Melissen, L. A. L. M. Kiemeny, *Eur. Urol.* **2006**, *49*, 478.
- [10] M. Babjuk, A. Böhle, M. Burger, O. Capoun, D. Cohen, E. M. Compérat, V. Hernández, E. Kaasinen, J. Palou, M. Roupřet, B. W. G. van Rhijn, S. F. Shariat, V. Soukup, R. J. Sylvester, R. Zigeuner, *Eur. Urol.* **2017**, *71*, 447.
- [11] C. R. Riedl, D. Danilchenko, F. Koenig, R. Simak, S. A. Loening, H. Pflueger, *J. Urol.* **2001**, *165*, 1121.
- [12] R. Wessels, D. M. De Bruin, D. J. Faber, T. G. Van Leeuwen, M. Van Beurden, T. J. M. Ruers, *Lasers Med. Sci.* **2014**, *29*, 1297.
- [13] B. W. D. De Jong, T. B. Schut, K. P. Wolffenbuttel, J. M. Nijman, D. J. Kok, G. J. Puppels, *J. Urol.* **2002**, *168*, 1771.
- [14] P. J. Caspers, G. W. Lucassen, R. Wolthuis, H. A. Bruining, G. J. Puppels, *Biospectroscopy*, **1998**, *4*, S31.
- [15] T. C. Bakker Schut, R. Wolthuis, P. J. Caspers, G. J. Puppels, *J. Raman Spectrosc.* **2002**, *33*, 580.
- [16] E. B. Hanlon, R. Manoharan, T.-W. Koo, K. E. Shafer, J. T. Motz, M. Fitzmaurice, J. R. Kramer, I. Itzkan, R. R. Dasari, M. S. Feld, *Phys. Med. Biol.* **2000**, *45*, R1.
- [17] B. W. D. de Jong, T. C. B. Schut, J. Coppens, K. P. Wolffenbuttel, D. J. Kok, G. J. Puppels, *Vib. Spectrosc.* **2003**, *32*, 57.
- [18] Z. Huang, A. McWilliams, H. Lui, D. I. McLean, S. Lam, H. Zeng, *Int. J. Cancer* **2003**, *107*, 1047.
- [19] N. Stone, C. Kendall, J. Smith, P. Crow, H. Barr, *Faraday Discuss.* **2004**, *126*, 141.
- [20] S. Koljenović, T. C. Bakker Schut, R. Wolthuis, B. de Jong, L. Santos, P. J. Caspers, J. M. Kros, G. J. Puppels, *J. Biomed. Opt.* **2005**, *10*, 031116.
- [21] B. Brożek-Pluska, I. Placek, K. Kurczewski, Z. Morawiec, M. Tazbir, H. Abramczyk, *J. Mol. Liq.* **2008**, *141*, 145.
- [22] C. A. Lieber, S. K. Majumder, D. L. Ellis, D. D. Billheimer, A. Mahadevan-Jansen, *Lasers Surg. Med.* **2008**, *40*, 461.
- [23] S. K. Teh, W. Zheng, K. Y. Ho, M. Teh, K. G. Yeoh, Z. Huang, *J. Biomed. Opt.* **2008**, *13*, 034013.
- [24] A. Beljebbar, O. Bouché, M. D. Diébold, P. J. Guillou, J. P. Palot, D. Eudes, M. Manfait, *Crit. Rev. Oncol. Hematol.* **2009**, *72*, 255.
- [25] M. D. Keller, S. K. Majumder, A. Mahadevan-Jansen, *Opt. Lett.* **2009**, *34*, 926.
- [26] J. Mo, W. Zheng, J. J. H. Low, J. Ng, A. Ilancheran, Z. Huang, *Anal. Chem.* **2009**, *81*, 8908.
- [27] O. R. Šćepanović, Z. Volynskaya, C.-R. Kong, L. H. Galindo, R. R. Dasari, M. S. Feld, *Rev. Sci. Instrum.* **2009**, *80*, 043103.
- [28] Z. Huang, M. S. Bergholt, W. Zheng, K. Lin, K. Y. Ho, M. Teh, K. G. Yeoh, *J. Biomed. Opt.* **2010**, *15*, 037017.
- [29] S. D. Krauß, R. Roy, H. K. Yosef, T. Lehtonen, S. F. El-Mashtoly, K. Gerwert, A. Mosig, *J. Biophotonics* **2018**, *11*, e201800022.
- [30] H. K. Yosef, S. D. Krauß, T. Lehtonen, H. Jütte, A. Tannapfel, H. U. Käfferlein, T. Brüning, F. Roghmann, J. Noldus, A. Mosig, S. F. el-Mashtoly, K. Gerwert, *Anal. Chem.* **2017**, *89*, 6893.

- [31] N. Stone, C. Kendall, N. Shepherd, P. Crow, H. Barr, *J. Raman Spectrosc.* **2002**, *33*, 564.
- [32] L. T. Kerr, K. Domijan, I. Cullen, B. M. Hennelly, *Photonics Lasers Med.* **2014**, *3*, 193.
- [33] G. W. Auner, S. K. Koya, C. Huang, B. Broadbent, M. Trexler, Z. Auner, A. Elias, K. C. Mehne, M. A. Brusatori, *Cancer Metastasis Rev.* **2018**, *37*, 691.
- [34] R. O. P. Draga, M. C. M. Grimbergen, P. L. M. Vijverberg, C. F. P. van Swol, T. G. N. Jonges, J. A. Kummer, J. L. H. Ruud Bosch, *Anal. Chem.* **2010**, *82*, 5993.
- [35] I. P. Santos, E. M. Barroso, T. C. Bakker Schut, P. J. Caspers, C. G. F. van Lanschot, D.-H. Choi, M. F. van der Kamp, R. W. H. Smits, R. van Doorn, R. M. Verdijk, V. Noordhoek Hegt, J. H. von der Thüsen, C. H. M. van Deurzen, L. B. Koppert, G. J. L. H. van Leenders, P. C. Ewing-Graham, H. C. van Doorn, C. M. F. Dirven, M. B. Busstra, J. Hardillo, A. Sewnaik, I. ten Hove, H. Mast, D. A. Monserez, C. Meeuwis, T. Nijsten, E. B. Wolvius, R. J. Baatenburg de Jong, G. J. Puppels, S. Koljenović, *Analyst* **2017**, *142*, 3025.
- [36] M. J. Baker, H. J. Byrne, J. Chalmers, P. Gardner, R. Goodacre, A. Henderson, S. G. Kazarian, F. L. Martin, J. Moger, N. Stone, J. Sulé-Suso, *Analyst* **2018**, *143*, 1735.
- [37] B. W. D. de Jong, T. C. Bakker Schut, K. Maquelin, T. van der Kwast, C. H. Bangma, D.-J. Kok, G. J. Puppels, *Anal. Chem.* **2006**, *78*, 7761.
- [38] J. T. Motz, S. J. Gandhi, O. R. Scepanovic, A. S. Haka, J. R. Kramer, R. R. Dasari, M. S. Feld, *J. Biomed. Opt.* **2005**, *10*, 031113.
- [39] J. Zhao, H. Lui, D. I. McLean, H. Zeng, *Skin Res. Technol.* **2008**, *14*, 484.
- [40] R Core Team, *R: A Language and Environment for Statistical Computing*, R Foundation for Statistical Computing, Vienna, Austria **2013**.
- [41] RStudio Team, *RStudio: Integrated Development Environment for R*, RStudio, Inc., Boston, MA **2015**.
- [42] C. Beleites, V. Sergo, *hyperSpec: a package to handle hyperspectral data sets in R*, [Software] **2018**.
- [43] O. Ryabchykov, T. Bocklitz, A. Ramoji, U. Neugebauer, M. Foerster, C. Kroegel, M. Bauer, M. Kiehntopf, J. Popp, *Chemom. Intel. Lab. Syst.* **2016**, *155*, 1.
- [44] U. Ligges, *Signal Process.* [Software]. **2015**.
- [45] M. Monici, *Biotechnol. Annu. Rev.* **2005**, *11*, 227.
- [46] P. H. C. Eilers, *Anal. Chem.* **2003**, *75*, 3631.
- [47] C. A. Lieber, A. Mahadevan-Jansen, *Appl. Spectrosc.* **2003**, *57*, 1363.
- [48] M. Morhác, V. Matousek, *Appl. Spectrosc.* **2008**, *62*, 91.
- [49] E. Cordero, F. Korinth, C. Stiebing, C. Krafft, I. W. Schie, J. Popp, *Sensors* **2017**, *17*, 1.
- [50] R. G. Brereton, G. R. Lloyd, *J. Chemometr.* **2014**, *28*, 213.
- [51] A.-L. Boulesteix, *Stat. Appl. Genet. Mol. Biol.* **2004**, *3*, 1.
- [52] B.-H. Mevik, R. Wehrens, K. Liland, *The pls Package*, **2016**.
- [53] B.-H. Mevik, R. Wehrens, T. N. San Michele all'Adige, *Introduction to the pls Package. Help Sect. "pls" Package RStudio Software*, **2015**, 1-23.
- [54] S. Guo, T. Bocklitz, U. Neugebauer, J. Popp, *Anal. Methods* **2017**, *9*, 4410.
- [55] H. Chen, X. Li, N. Broderick, Y. Liu, Y. Zhou, J. Han, W. Xu, *J. Biophotonics* **2018**, *11*, e201800016.
- [56] C. J. Frank, R. L. McCreery, D. C. Redd, *Anal. Chem.* **1995**, *67*, 777.
- [57] Z. Movasaghi, S. Rehman, I. U. Rehman, *Appl. Spectrosc. Rev.* **2007**, *42*, 493.
- [58] N. Stone, M. C. Hart Prieto, P. Crow, J. Uff, A. W. Ritchie, *Anal. Bioanal. Chem.* **2007**, *387*, 1657.
- [59] K. Czamara, K. Majzner, M. Z. Pacia, K. Kochan, A. Kaczor, M. Baranska, *J. Raman Spectrosc.* **2015**, *46*, 4.
- [60] J. Chen, T. Ahn, I. D. Colón-Bernal, J. Kim, M. M. Banaszak Holl, *ACS Nano* **2017**, *11*, 10665.
- [61] S. J. Potts, J. S. Krueger, N. D. Landis, D. A. Eberhard, G. D. Young, S. C. Schmechel, H. Lange, *Lab. Invest.* **2012**, *92*, 1342.
- [62] M. J. Gerdes, A. Sood, C. Sevinsky, A. D. Pris, M. I. Zavadzsky, F. Ginty, *Front. Oncol.* **2014**, *4*, 1.
- [63] M. B. Albro, M. S. Bergholt, J. P. St-Pierre, A. Vinals Guitart, H. M. Zlotnick, E. G. Evita, M. M. Stevens, *NPJ Regen. Med.* **2018**, *3*, 3.
- [64] I. W. Schie, L. Alber, A. L. Gryshuk, J. W. Chan, *Analyst* **2014**, *139*, 2726.
- [65] I. W. Schie, J. W. Chan, *J. Raman Spectrosc.* **2016**, *47*, 384.
- [66] R. O. P. Draga, *Optimizing the diagnosis and treatment of bladder cancer using fluorescence cytometry and Raman spectroscopy*, **2013**.
- [67] J. De Gelder, K. De Gussem, P. Vandenabeele, L. Moens, *J. Raman Spectrosc.* **2007**, *38*, 1133.
- [68] C. Krafft, *Raman spectroscopy and microscopy of cells and tissues*. in *Encyclopedia of Biophysics* (Ed: G. C. K. Roberts), Springer, Berlin, Heidelberg **2013**, p. 2178.
- [69] R. Jyothi Lakshmi, V. B. Kartha, C. Murali Krishna, J. G. R. Solomon, G. Ullas, P. Uma Devi, *Radiat. Res.* **2002**, *157*, 175.
- [70] Z. Huang, A. McWilliams, S. Lam, J. English, D. I. McLean, H. Lui, H. Zeng, *Int. J. Oncol.* **2003**, *23*, 649.
- [71] H. Abramczyk, J. Surmacki, M. Kopeć, A. K. Olejnik, K. Lubecka-Pietruszewska, K. Fabianowska-Majewska, *Analyst* **2015**, *140*, 2224.

SUPPORTING INFORMATION

Additional supporting information may be found online in the Supporting Information section at the end of this article.

How to cite this article: Cordero E, Rüger J, Marti D, et al. Bladder tissue characterization using probe-based Raman spectroscopy: Evaluation of tissue heterogeneity and influence on the model prediction. *J. Biophotonics*. 2020;13:e201960025. <https://doi.org/10.1002/jbio.201960025>

7.3 Morpho-molecular ex vivo characterization and grading of non-muscle-invasive bladder cancer biopsies using forward imaging probe based multimodal optical coherence tomography and Raman spectroscopy

Fabian Placzek*, Eliana Cordero B.*, Simon Kretschmer, Lara M. Wurster, Florian Knorr, Gerardo González-Cerdas, Mikael T. Erkkilä, Çağlar Ataman, Gregers G. Hermann, Karin Mogensen, Thomas Hasselager, Peter E. Andersen, Hans Zappe, Jürgen Popp, f, Wolfgang Drexler, Rainer A. Leitgeb, and Iwan W. Schie, submitted to the Analyst, 2019

Der Nachdruck der folgende Publikation erscheint mit freundlicher Genehmigung von The Analyst. Reprinted with kind permission from The Analyst.




Erklärung zu den Eigenanteilen der Promovendin sowie der weiteren Doktoranden/Doktorandinnen als Co-Autoren an der Publikation

Doktoranden	Eliana Cordero	Fabian Placzek
Konzeption des Forschungsansatzes	x	x
Planung der Untersuchungen	x	x
Datenerhebung	x	x
Datenanalyse und -interpretation Raman	x	
Datenanalyse und -interpretation OCT		x
Korrelation Raman und OCT	x	x
Schreiben des Manuskripts	x	x
Vorschlag Anrechnung Publikationsäquivalente	1,0	



Cite this: DOI: 10.1039/c9an01911a

Morpho-molecular *ex vivo* detection and grading of non-muscle-invasive bladder cancer using forward imaging probe based multimodal optical coherence tomography and Raman spectroscopy†

Fabian Placzek,[‡] ^a Eliana Cordero Bautista,[‡] ^b Simon Kretschmer,^c Lara M. Wurster,^a Florian Knorr,^b Gerardo González-Cerdas,^c Mikael T. Erkkilä,^a Patrick Stein,^c Çağlar Ataman,^c Gregers G. Hermann,^d Karin Mogensen,^d Thomas Hasselager,^e Peter E. Andersen,^f Hans Zappe,^c Jürgen Popp,^{b,g} Wolfgang Drexler,^a Rainer A. Leitgeb^a and Iwan W. Schie ^{*b,h}

Non-muscle-invasive bladder cancer affects millions of people worldwide, resulting in significant discomfort to the patient and potential death. Today, cystoscopy is the gold standard for bladder cancer assessment, using white light endoscopy to detect tumor suspected lesion areas, followed by resection of these areas and subsequent histopathological evaluation. Not only does the pathological examination take days, but due to the invasive nature, the performed biopsy can result in significant harm to the patient. Nowadays, optical modalities, such as optical coherence tomography (OCT) and Raman spectroscopy (RS), have proven to detect cancer in real time and can provide more detailed clinical information of a lesion, e.g. its penetration depth (stage) and the differentiation of the cells (grade). In this paper, we present an *ex vivo* study performed with a combined piezoelectric tube-based OCT-probe and fiber optic RS-probe imaging system that allows large field-of-view imaging of bladder biopsies, using both modalities and co-registered visualization, detection and grading of cancerous bladder lesions. In the present study, 119 examined biopsies were characterized, showing that fiber-optic based OCT provides a sensitivity of 78% and a specificity of 69% for the detection of non-muscle-invasive bladder cancer, while RS, on the other hand, provides a sensitivity of 81% and a specificity of 61% for the grading of low- and high-grade tissues. Moreover, the study shows that a piezoelectric tube-based OCT probe can have significant endurance, suitable for future long-lasting *in vivo* applications. These results also indicate that combined OCT and RS fiber probe-based characterization offers an exciting possibility for label-free and morpho-chemical optical biopsies for bladder cancer diagnostics.

Received 25th September 2019,
Accepted 2nd December 2019

DOI: 10.1039/c9an01911a

rsc.li/analyst

^aCenter for Medical Physics and Biomedical Engineering, Medical University of Vienna, Waehringer Guertel 18-20, 4L, 1090 Vienna, Austria

^bLeibniz Institute of Photonic Technology (Leibniz-IPHT), Albert-Einstein-Straße 9, Jena, Germany. E-mail: iwan.schie@leibniz-ipht.de

^cGisela and Erwin Sick Chair of Micro-optics, Department of Microsystems Engineering, University of Freiburg, Freiburg, Germany

^dDepartment of Urology, Copenhagen University, Herlev/Gentofte hospital, Borgmester Ib Juuls Vej 23A, DK-2730 Herlev, Copenhagen, Denmark

^eDepartment of Pathology, Copenhagen University, Herlev/Gentofte hospital, Borgmester Ib Juuls Vej 23A, DK-2730 Herlev, Copenhagen, Denmark

^fTechnical University of Denmark, Department of Health Technology (DTU Health Tech), Ørstedes Plads, Building 345C, DK-2800Kgs. Lyngby, Denmark

^gInstitute of Physical Chemistry, Friedrich Schiller University Jena, Helmholtzweg 4, 07743 Jena, Germany

^hUniversity of Applied Sciences-Jena, Department of Medical Engineering and Biotechnology, Carl-Zeiss-Promenade 2, 07745 Jena, Germany

†Electronic supplementary information (ESI) available. See DOI: 10.1039/c9an01911a

‡These authors contributed equally to this work.

Introduction

There are currently 3.4 million people affected by bladder cancer worldwide,¹ with 75% of the newly diagnosed cases being non-muscle-invasive bladder cancer (NMIBC) and thereby non-muscle-invasive disease.² Among the different types of NMIBC, the five year recurrence rate is 20–80%.³ The risk of recurrence and repeated surveillance cystoscopy in the outpatient department (OPD), which is the standard procedure when suspicious lesions are detected, subsequently jeopardizes the health of the patient.⁴ The current gold standard in bladder cancer assessment is cystoscopy, which provides a visualization of the bladder mucosa by white light endoscopy (WL). Although the detection rate for muscle-invasive bladder cancer using WL is very high, 97–100%, the detection of



NMIBC is still challenging.⁵ Significant efforts go into developments to remedy this situation.

Along with the examination by WL, a biopsy is performed and the resected suspicious tissue is inspected by pathologists.⁶ This allows access to clinically relevant information on the stage and grade of a lesion. The tumor stage classifies the invasion depth into the bladder wall. The tumor grade, on the other hand, describes the level of differentiation from healthy cells.⁷ Histological diagnosis is defined in accordance with UICC's 2017 TNM classification⁸ and the 2016 WHO classification.⁹ There is a significant need to allow instant diagnosis during surveillance cystoscopy in the OPD, thus avoiding admittance to the operating theatre for diagnostic surgery.

In situ diagnostic procedures of stage and grade during surgery are currently not available, resulting in unnecessary tissue resection, which can cause significant negative effects on the patient's well-being. Photodynamic diagnosis (PDD), using hexylaminolevulinic acid as a photosensitizing compound for fluorescence guidance, is a promising approach, which may assist the presented optical diagnostic method.^{6,10} Moreover, PDD does not provide clinically relevant information on stage and grade for immediate treatment decision. Due to these current shortcomings for the onsite diagnosis of NMIBC, there is a significant need for real-time assessment of the tumor stage and grade during cystoscopy.

Autofluorescence and diffuse reflectance have also been applied in bladder biopsies, demonstrating the capability to differentiate tumor and healthy bladder tissue with high sensitivities and specificities, where significant changes of tryptophan and collagen at 340 nm and 390 nm emission peaks were reported.^{11,12} Nevertheless, in order to differentiate tumor grade in the bladder tissue, more biochemical information about the sample that can be associated with the main molecular changes related to tumor grading is needed.

In recent years, there have been extensive developments in optical technologies and their translation to clinical diagnostic applications, *e.g.* interference-based approaches, such as optical coherence tomography (OCT), and label-free molecular specific spectroscopy-based approaches, such as Raman spectroscopy (RS). OCT is widely used in ophthalmology to indicate anatomical changes in the retina by providing cross-sectional images in depth at micrometer resolution, allowing access to structural tissue information.^{13,14} Since the eye is optically easily accessible, the retina can be examined non-invasively using a laser beam. However, to acquire information from the internal organs, OCT has to be extended with an optical endoscope. Such endoscopic OCT-based imaging has been reported for the cardiovascular system, the gastrointestinal tract and the urinary tract.^{15–18} These implementations, however, only achieved B-scans and endoscopic volume images of the bladder tissue, which are paramount to characterize the tumor tissue, were not previously presented. A comprehensive overview on OCT methodology and applications is given elsewhere.¹⁹ While OCT can rapidly provide morphological information from different depths, it lacks chemical information on the underlying molecular composition.

Raman spectroscopy, on the other hand, is based on inelastic light scattering between a photon and a molecule, providing label-free information on the molecular composition of a sample. RS provides information on molecular changes at a single cell level,^{20–23} and has been extensively used for clinical tissue characterization.^{24–26} It has been broadly applied in numerous studies for the diagnosis of cardiovascular diseases,²⁷ biochemical characterization of human cells²⁸ and organs,²⁹ including the discrimination of brain tumors^{30,31} and malignant breast tissues,^{32–34} and extensive research in cervical cancer,^{35–37} lung cancer,³⁸ and colon,³⁹ prostate⁴⁰ and bladder cancers.^{41,42} RS has been readily implemented in fiber optic probes for a variety of pathologies of different organs.⁴³

While each modality has intriguing capabilities, individually they can cover only a certain but complementary diagnostic aspect. As such, only a combination of both modalities can harvest the full diagnostic potential, and provide information on the invasiveness of the tumor, *i.e.* stage, by taking cross-sectional images of the bladder wall at a micrometer scale, using OCT, and obtain information about the grade by assessing the biochemical composition of the superficial tissue, using RS.⁴⁴

Ko *et al.* reported on the first multimodal approach of combining OCT and RS to detect and characterize dental diseases.⁴⁵ Ever since, multimodal optical coherence tomography and Raman spectroscopy (OCT-RS) has been reported for imaging *ex vivo* human breast tissue samples and *in vivo* wound healing,⁴⁶ *ex vivo* human retina,⁴⁷ *in vivo* and *ex vivo* skin,^{48–51} *ex vivo* atherosclerotic plaque deposition⁵² and *ex vivo* rectal mucosa.⁵³ Furthermore, Ashok *et al.* combined OCT and RS to increase the sensitivity and specificity of colon cancer detection.⁵⁴ In this study, microscopy-based OCT achieved a sensitivity, specificity and accuracy of 78%, 74% and 75%, respectively. RS achieved 89% sensitivity, 77% specificity and 82% accuracy. Recently, Bovenkamp *et al.* showed the ability of microscopic OCT and RS to provide diagnostic information regarding stage and grade of bladder cancer. For differentiating the pT2 stage from the pTa stage, they reported a sensitivity, specificity and accuracy of 80%, 60% and 71%, respectively. Furthermore, the sensitivity of detecting high grade lesions with RS was 99%, whereas the specificity was 87%, indicating correct detection of low grade lesions.⁵⁵

To use these techniques *in vivo* in the clinics, they need to be integrated into rigid or flexible cystoscopes to allow *in situ* assessment of the bladder wall. As a first step in this direction, we report on the development of a combined OCT-Raman system for stage and grade examination of bladder biopsies, based on fiber-optical probes. The combined system mimics the optical performance of an endoscopic probe combining OCT and RS. It gives insight into *in vivo* conditions and the expectable outcome with the first performance benchmarks. Moreover, it allows one to co-register morphological and molecular information of NMIBC, using fiber optical probes, and enables new opportunities to interpret the data, by the assessment of co-localized molecular and morphological signals. The developed system was used to characterize a total of 119 biopsies in an imaging fashion that mimics *in vivo* conditions,



for the diagnostic evaluation for the detection of NMIBC, and for the grading of low- and high-grade tissues.

Materials and methods

Biopsy handling

The study was approved by the Ethical Committee at the Capital Region of Denmark, H-17015549, and a data processor agreement between the universities in Jena and Vienna and the Capital Region of Denmark was made (HGH-2018-038. I-suite nr. 6639). Prior to the operations, the patients gave their written informed consent to have biopsies for the study taken. All operations were performed according to the guidelines of the Urological Department at Herlev Hospital, Capital Region of Denmark and the experiments were performed in accordance with the above approvals obtained. For the experiments, 119 biopsies from 44 patients were obtained during resection of the bladder tumor in the operation theatre. Immediately after the procedure, the biopsies were moistened with a sodium chloride solution and delivered to the imaging laboratory within 15 minutes. In case a sample could not be examined within 20 minutes after removal, it was snap-frozen to $-20\text{ }^{\circ}\text{C}$ and imaged on the following 1–2 days. For examination on the OCT-RS setup, the biopsies were carefully placed on CaF_2 glass slides and positioned on the translational stage (Fig. 1 and 2). After the combined analysis using OCT-RS, the biopsies were fixed and stained. The pathologist then staged

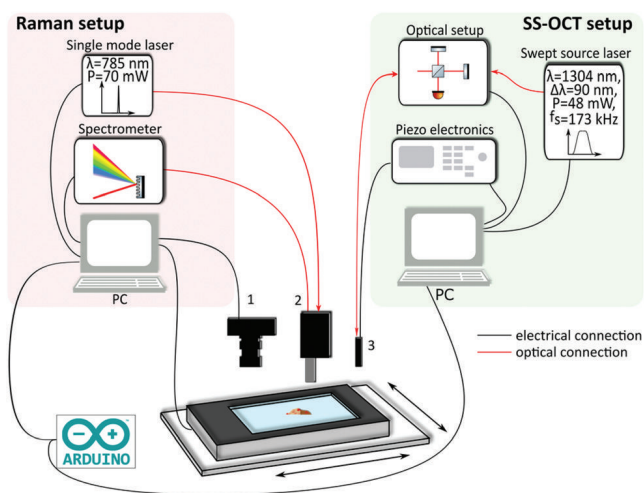


Fig. 1 Combined multimodal imaging system. The Raman setup consists of a single mode laser, a spectrometer and a PC. Besides a bright field camera (1), the Arduino board is also connected to the Raman PC. The Raman probe (2) receives the excitation light from the laser and guides back the Raman signal to the spectrometer. The swept source OCT (SS-OCT) setup includes an akinetic laser source, the interferometric optical setup including the photodiodes, driving electronics for the endoscope and a PC. The OCT probe (3) is optically connected to the optical setup. Moreover, the OCT probe is electrically connected to the piezo amplifier. The communication is realized via an Arduino board, triggering the acquisition and the translation of the two-axis stage, which is connected to the Raman PC.

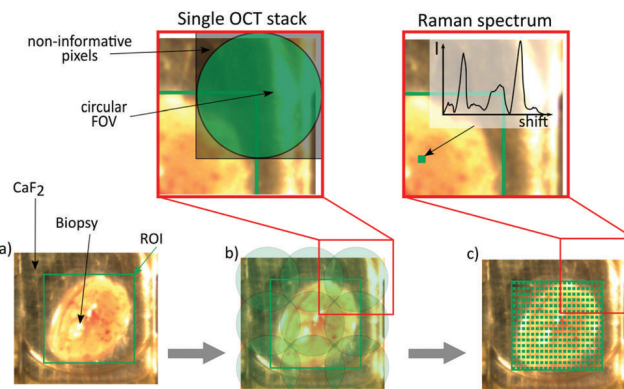


Fig. 2 Image acquisition workflow. (a) A certain region of interest (ROI) is chosen out of the bright field image. Starting the acquisition leads to the translation underneath the OCT endoscope. (b) Bottom: The calculated number of scans is performed consecutively. (c) Bottom: The biopsy is translated to the Raman probe and the ROI is scanned, pixel by pixel, to achieve a Raman map. After choosing the ROI, the data acquisition is fully automated. (b) Top: Single OCT stack, which has a size of 500×500 pixels. It includes non-informative pixels due to the remapping described in OCT data acquisition. (c) Top: Single Raman point measurement, showing the acquired spectrum at this position.

Table 1 Description of the collected biopsies. PUNLMP: papillary urothelial neoplasm of low malignant potential. PUNLMP is not yet a cancerous lesion and possesses a very limited probability of progression.⁵⁶ The number of patients is indicated in brackets. The patient with PUNLMP is added to the non-tumor group

Non-tumor	PUNLMP	Cancerous	Total
66 (22)	3	50 (22)	116 (44)

Table 2 Detailed description of the tumor samples. The number of patients is indicated in brackets. Since one patient can exhibit different stages or grades of cancerous lesions, the number of samples is higher than the number of patients with cancerous lesions

Stage	Grade			
	pTa	pT1a	High	Low
CIS				
1 (1)	48 (22)	1 (1)	12 (6)	38 (19)

and graded the biopsies based on the underlying histology. The histopathological results are summarized in Tables 1 and 2. The quantity of the extracted malignant biopsies reflects NMIBC samples. Since pTa and CIS are confined to the urothelium⁵⁷ and pT1a has only invaded the superficial lamina propria, they are considered non-muscle-invasive bladder cancer⁵⁸ and by that early stage.

Instrumentation

Swept source OCT (SS-OCT) system. The experiments were performed using a miniaturized imaging device that mimics an *in vivo* situation where the measurement would be per-



formed using a fiber-optic probe. The OCT system (see Fig. 1) used an akinetic swept source laser (Insight Photonic Solutions, Inc., Lafayette, Colorado)⁵⁹ with a central wavelength of 1304 nm, a bandwidth of ~ 90 nm (at 0 dB level) and a sweep frequency of ~ 173 kHz. The OCT system⁶⁰ was based on a Mach-Zehnder interferometer configuration, with an output power of 11 mW at the tip of the endoscope. A system sensitivity of 104 dB was achieved, which is reduced to 99 dB in combination with the fiber-optic probe. The detailed description of the system incorporating the endoscopic probe can be found elsewhere.⁶¹ For OCT imaging, a piezoelectric tube-based forward viewing endoscope with a diameter of 3 mm and a rigid length of 15.6 mm was used. The optical components were arranged in a Fourier-plane configuration to allow telecentric scanning across the tissue plane.⁶² The field of view (FOV) was adjusted at stable scanning behavior to a diameter of 1–1.4 mm. The piezoelectric tube was driven at a quasi-resonance frequency of 510 Hz and scanned the attached optical fiber in a spiral pattern. The measured axial and lateral resolution was 12 μm and 28 μm in air, respectively. The confocal parameter was ~ 950 μm . The working distance was ~ 500 μm .

OCT data acquisition. For the three-dimensional remapping of the OCT data acquired with the piezoelectric tube-based scanning probe, a positional calibration was performed prior to the measurements. During this step, the scan pattern was imaged onto a position-sensitive device (PSD – SpotOn Analog SPOTANA-9L, Duma Optronics Ltd), the parameters were optimized for an optimal scan pattern, and a look-up table (LUT) was created. To reconstruct the volumetric OCT stacks with a size of 500×500 pixels, an algorithm in combination with the LUT was used to remap the spiral-shaped scan pattern onto a square-Cartesian grid. Due to the circular scan pattern, the final 3D-volume had a cylindrical shape. The time for an entire spiral – rising and collapsing – was 2 seconds, which can be reduced to less than a second by changing the resonance frequency of the scanned fiber. However, the data during the rising spiral was recorded for an OCT stack, and the acquisition rate was 0.5 Hz. The OCT volume scan consisted of 510 consecutive circles (B-scans) with 340 A-scans per B-scan. Because the FOV of one single spiral was not large enough to image an entire biopsy with a size between 1 mm^2 and 15 mm^2 , subsequent scans were performed in a raster scan pattern. These stacks were stitched together in a post-processing step to obtain an image of the entire biopsy (Fig. 2b). The OCT data were acquired in such a way that the round FOVs were overlapping with the neighboring FOVs. To stitch the individual OCT FOVs, the volume scans were aligned by rotating the 3D stacks and cropping, in order to create rectangular stacks. These were combined in the same order the data were acquired.

Raman system. The acquisition of the Raman spectra was performed by collecting the Raman signal with an in-house developed Raman fiber-optic probe, which was connected to a spectrometer (Acton Series LS785, Princeton Instruments) with a spectral resolution of 5 cm^{-1} . The spectrometer was equipped with a back-illuminated deep-depletion charge-

coupled device (BI-DD-CCD) (PIXIS 100BR_eXcelon, Princeton Instruments) with a 1340×100 imaging array and $20 \times 20 \mu\text{m}$ sized pixels. The excitation fiber of the Raman probe was coupled to a 785 nm single-mode excitation laser (Fergy-Laser, Princeton Instruments) with an output power of 70 mW at the end of the fiber probe. This power could be safely used in *in vivo* applications. The excitation light from the optical fiber was coupled out from the fiber probe using a lens, and after passing through a narrow-band clean-up filter and a dichroic-longpass filter focused onto a spot size of 100 μm . The generated Raman signal was collected using the same lens, and after passing through the dichroic-longpass filter and an additional longpass filter focused onto a multimodal collection fiber, with a diameter of 200 μm , which was coupled to the spectrometer. The biological sample was scanned pixel-by-pixel resulting in a two-dimensional hyperspectral Raman map (Fig. 2c).

Combined OCT and Raman setup. The measurements of morpho-molecular tissue information of a biopsy were performed sequentially. To achieve the data sampling from the same sample locations, the fiber-optical probes were mounted on an in-house designed holder with a known positional offset between the OCT and the Raman probe, and were mounted above a translational stage (MLS203, Thorlabs). Since the device controlling software for OCT acquisition and Raman acquisition was running on two separate computers, and the translational stage was controlled by the Raman unit, a trigger-based communication was established between the systems, using an Arduino UNO board (Board model UNO/R3). This allowed the sending of triggering events between the two systems to initiate an acquisition for both modalities from the same region of interest (ROI). Both systems incorporated self-built LABVIEW software for acquisition and driving of the imaging systems. Fig. 1 shows the combination of the Raman and SS-OCT setups. The automated imaging procedure can be described as given below.

First, a region of interest on the biopsy was selected by using a bright field image acquired with a standard camera (DCC1645C, Thorlabs) (Fig. 2a). Based on the specific FOV covered by the OCT probe, the software calculated the required number of tiles in x and y for the OCT measurement. The number of points for the Raman acquisition was kept constant to 30×30 points. After the start of the data acquisition procedure, the biopsy was moved below the OCT probe, and an OCT stack was acquired. After the acquisition of the first tile was performed, the OCT software sent a trigger through the Arduino board, indicating that the OCT stack was acquired, and the Raman computer executed a command to translate the biopsy to the next location. This was repeated until the entire ROI on the biopsy was sampled. After all OCT frames were acquired, the biopsy was automatically moved below the Raman probe, followed by a scan of the identical ROI as in OCT. The acquisition time for each imaging modality depended on the biopsy size: for example, imaging a biopsy with a size of $\sim 4 \text{ mm}^2$ took 1 minute for the acquisition of nine (3×3) OCT stacks and 13 minutes for 900 (30×30) Raman-point measurements. The goal of the study was to



sample the entire biopsy to allow for a comprehensive characterization of the underlying morpho-molecular changes occurring in malignant tissues. For the measurements in an *in vivo* setting, the acquisition time for OCT imaging and single point Raman spectroscopy is less than 5 s each.

Data analysis

OCT texture analysis. Texture analysis has been shown to be a suitable approach to perform an automated image classification for OCT images⁶³ and has been successfully used to differentiate benign and malignant biological tissues.⁶⁴ Consequently, this method was chosen to analyze the OCT images.^{54,55} The texture analysis approach described by Bovenkamp *et al.* was used in the present study.⁵⁵ In contrast to the reported procedure, the single OCT stacks were divided into 25×25 equally sized fragments and only the middle 5×5 subframes were used for the texture analysis. This excluded the border area of the single scanned FOVs only containing zero pixels due to the circular shape of the scanning pattern (Fig. 2b). Furthermore, the outermost circles might be under-sampled at a large FOV or distorted due to slight changes in the resonance frequency of the scanner during operation. Because OCT measurements were performed on biopsies placed on the CaF₂ glass slide, some of the OCT stacks contained high glass reflections. Therefore, only a subset of OCT stacks per biopsy was chosen. The stacks, containing glass reflections, exhibit texture feature artifacts not found in stacks that contain information about the biopsy only. These features were used to exclude the glass stacks, which are not relevant for classifying malignant and benign tissues. As a result, the classification was built on 80 features per observation and 29 006 observations in total. The classification was carried out using a fine Gaussian support vector machine (SVM) with a 20% holdout validation.

Spectral analysis of Raman data: pre-processing. Before any analysis of the Raman data was performed, all spectra were identically pre-processed. The spectra were first corrected for cosmic spikes, using an algorithm developed by Ryabchykov *et al.*⁶⁵ The wavenumber calibration was performed based on a reference spectrum of 4-acetamidophenol. Subsequently, the measured spectra were de-noised by using the first 8 PCA components. The spectra were corrected for dark current followed by an intensity calibration, using the spectra of a National Institute of Standards and Technology (NIST)-standardized white light source (Kaiser HCA accessory). The measured intensity lamp spectra were fitted to the reference spectra of the lamp and a transfer function was estimated to calibrate the intensity of the measured spectra. The baseline correction was performed using asymmetric least squares (AsLS) and extended multiplicative signal correction (EMSC).⁶⁶ As the last two steps of the pre-treatment workflow, all Raman spectra were further treated using the Savitzky–Golay filter and area normalized within the regions from 600 to 1750 cm⁻¹ and 2800 to 3000 cm⁻¹. These regions were afterwards used to construct the classification models, using partial least squares linear discriminant analysis (PLS-LDA) to classify between

tumor and non-tumor. All computations were performed using the statistical programming language R and Python.

Classification model and cross-validation of Raman data

The classification was performed using a PLS-LDA algorithm, which combines partial least squares and linear discriminant analysis using a 5-fold cross-validation. A hierarchical approach to create and validate each model was adopted, where the first layer model system ML1 focusses on classifying between tumor and non-tumor, and the second layer model system ML2 uses the tumor predictions to differentiate low- and high-grade tumors (Fig. 3).

The created models were validated by applying *k*-fold partitioning of the data, where each layer has a specific partition according to the existent data for each variable of classification. For the first classification layer (ML1), 10 iterations for each partitioning were performed. The generated ML1-models were validated by the test data. In order to test all spectra of each biopsy, 10% of the created models were selected randomly. For each spectral point, a mean of the predictions was calculated, and this prediction map per pixel is displayed in the flowchart (Fig. 3). The mean prediction maps were used to select the spectra predicted as tumor and non-tumor. The second layer classification model system (ML2) used the tumor-defined areas of the biopsies. A mean spectrum per biopsy was calculated for those areas. The resulting data was

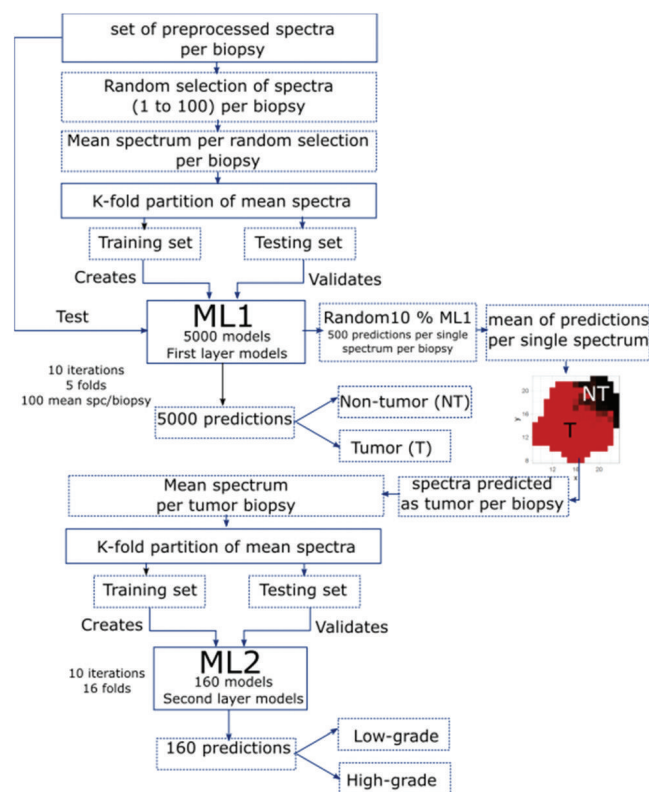


Fig. 3 Flowchart of all main steps employed to create and validate the first- and second-layer model systems ML1 and ML2, respectively.



k -fold partitioned and a set of training and testing biopsies was selected. The ML2 was created with the training data set that results from 16-fold partitions and was validated with the testing biopsies; 10 iterations of 16 different partitions were employed to create and validate ML2 (Fig. 3). The described method has previously been reported in Cordero *et al.*⁶⁷

Multivariate curve resolution alternating least squares (MCR-ALS) for collagen distribution of Raman data

Initially, the pure components for each biopsy were determined by using an orthogonal projection approach (OPA) algorithm. This function extracts the initial 'pure' components of the set of spectra based on spectral dissimilarity of the data set. It is important to note that the pure component spectra can contain contributions from other substances and can deviate to some degree to pure component spectra of the native substance. The OPA estimates the dispersion matrix of the mean spectrum of the data set: the higher the dissimilarity, the purer the component. The estimated pure components of tumor and non-tumor spectra were correlated to the literature.⁴¹ It was found that for non-tumor biopsies, there are most of the relevant bands of collagen 1 spectrum, which can be linked to the dominant presence of collagen in non-tumor spectra. All the non-tumor biopsies were used to find the collagen pure component, which was calculated by employing the OPA function, which provides the first estimation of pure components of the dataset. Afterwards, the mean standard deviation of the OPA pure collagen obtained from each biopsy was used to further calculate the MCR concentrations, where ALS complement the MCR function fitting the concentrations to improve the estimations of the pure components. The MCR-ALS algorithm used the extracted mean collagen pure component and consequently calculates the relative concentration at each measured location of each biopsy. The concentration matrix indicates how intense the presence of collagen in the biopsy is and was calculated for each biopsy.

Results and discussion

Correlation of OCT to histopathological images

To visually compare the morphological information obtained from OCT with the histopathological information, OCT and the corresponding histopathology for two different biopsies are shown in Fig. 4. In the non-tumor case (Fig. 4a), the layered appearance of the bladder wall is visible by OCT. The thin dark top layer in the OCT image is correlated to the mucosa, delimiting the bladder from the inner lumen. The second bright layer corresponds to the connective tissue, also referred to as lamina propria. Besides nerves and blood vessels, the bright appearance in the OCT images indicates a strong scattering tissue constituent, such as collagen fibers. The deepest visible layer in the OCT image is the muscularis propria, the muscle layer. It has a clear demarcation from the lamina propria and appears rather dark. In Fig. 4b, the corresponding OCT and histopathological image of a pTa lesion is shown. Here, the thickened urothelium is

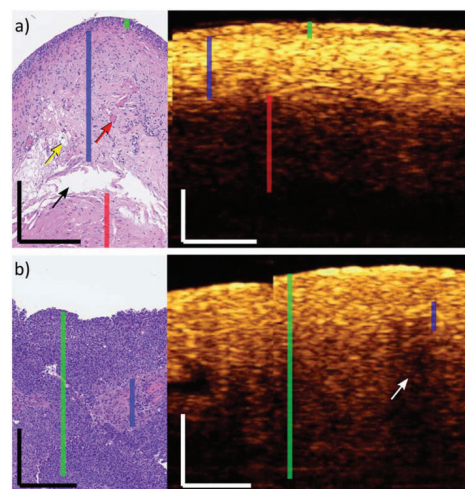


Fig. 4 OCT image correlation to histopathological images. (a) Representative example of a non-tumor bladder wall. The green line indicates the mucosa/urothelium layer, the blue line shows the lamina propria and the red line is the muscularis layer. The red arrow points to a vessel, the yellow arrow indicates fat accumulation and the black arrow indicates mechanical rupture. (b) Representative example of a pTa low grade tumor bladder wall. Here, the mucosa/urothelium is thickened (green line). The white arrow indicates a region of less intensity, because the lamina propria (blue line) is highly scattering. The visible edge in (b) is a stitching artefact. The corresponding histopathological images are not co-localized to the OCT B-scans. The OCT insets are maximum projections of 10 B-scans. Scale bars: 250 μm .

clearly visible. Whereas the pTa staged tumor has not infiltrated the lamina propria, the demarcation between the urothelium and lamina propria is still intact.

These correlations show the ability of the presented endoscopic OCT probe to identify early stage lesions due to morphological changes in the mucosa of the bladder wall. The used OCT probe design is thereby suitable to detect NMIBC. Even though some biopsies can be distinctly correlated, in general, the correlation between OCT and histopathological images is difficult and was not feasible for all biopsies. For example, the biopsy-collection procedure relies on forceps, which mechanically stresses the biopsy. Additionally, the biopsy can get twisted during transportation from the operation theatre to the OCT-RS setup. Furthermore, the fixation process for histopathological slicing includes formalin, which can cause the biopsy to shrink, inducing discrepancies in dimensions. For example, in renal and intestinal biopsies, shrinkage between 11% and 33% was reported, respectively.^{68,69} For quantitative classification of the OCT data, texture analysis was carried out.

Texture analysis of the OCT data

The classification was performed on 116 non-tumor and tumor biopsies. The stacks were labeled with histopathological results obtained for the biopsies and the results of the texture analysis are summarized in Table 3. Sensitivity indicates the correct detection of tumor in accordance with the histopatho-



Table 3 Performance of OCT and Raman spectroscopy (RS): texture analysis differentiating non-tumor from NMIBC (OCT), the model level 1 (ML1) separating tumor (T) from non-tumor (NT) and the model level 2 (ML2) discriminating high grade (HG) from low grade (LG)

	OCT (%)	RS – T/NT (%)	RS – HG/LG (%)
Accuracy	73.4	92	77
Sensitivity	78	95	81
Specificity	69	88	68
Confidence interval	(72.9–73.9)	(92.2–92.6)	(73–81)

logical result. An accuracy of 73.4% was achieved. Bovenkamp *et al.* focused on the differentiation of advanced tumor stages.⁵⁵ In contrast, in this study, we concentrated on the detection of NMIBC lesions, as the number of available samples for pTa(1) was small, *i.e.* one single sample. We have, therefore, not separately included the two samples, staged as pT1a and CIS, in the texture analysis, since the statistical basis for a significant classification outcome is not given. Since the advanced stages of muscle-invasive bladder cancer are visually detectable, it is of higher clinical relevance to detect NMIBC by OCT. From the four texture features, the contrast texture property at 45, 90 and 135 degrees contributed the most (92%) to the differentiation between healthy and diseased tissues. While malignant tissues always showed lower contrast values, benign tissues showed a higher contrast. This is understandable, as malignant tissues are characterized by structural loss of the bladder wall anatomy as soon as cancer progresses. This observation confirms the preliminary results of Bovenkamp *et al.* on a larger study cohort. The results for accuracy are comparable to other publications using microscopes for OCT image acquisition and texture analysis for cancer classification.^{54,55} The deviation is primarily due to the use of a fiber-probe-based scanning approach, where compromises

with respect to the optical performance are made. But on the other hand, there is clear evidence that the optical performance of the probe is sufficient for NMIBC. Furthermore, the remaining glass reflection artifacts from the substrate can additionally reduce the performance. This, however, should be of no concern for *in vivo* measurements. Nevertheless, the performance of the texture analysis was further compromised, because the classification of the histopathological results provides only a single label for the entire biopsy corresponding to the highest pathologic severity observed. The OCT images, on the other hand, are spatially resolved, and contain a variety of regions. For instance, a pTa staged biopsy may contain areas of healthy bladder wall, which does not influence the histopathological outcome. In contrast, the classification is sensitive to these transitions and the heterogeneity of the lesion within one particular biopsy. The sensitivity for pTa, for instance, increases to 90%, if two blinded experts, familiar with OCT images of the bladder wall, are classifying the OCT images. If the decision was inconclusive between the two experts, the pathologically more severe statement was taken to label the biopsy. The heterogeneity of the biopsy can be a significant factor that reduces the accuracy of the OCT texture analysis (see Fig. 7).

Raman analysis

For Raman spectroscopy, a two-layer model system was created and validated to distinguish tumor from non-tumor tissues, followed by grading of tumor regions. The first model level differentiates tumor and non-tumor with an accuracy of 92%. As described in the first section, the two-layer model was created with a different set of spectra, summarized in the flow-chart shown in Fig. 3. For the second modeling step ML2, which differentiates low-grade from high-grade, an accuracy of 77% was achieved. Fig. 5a shows the mean spectrum of all

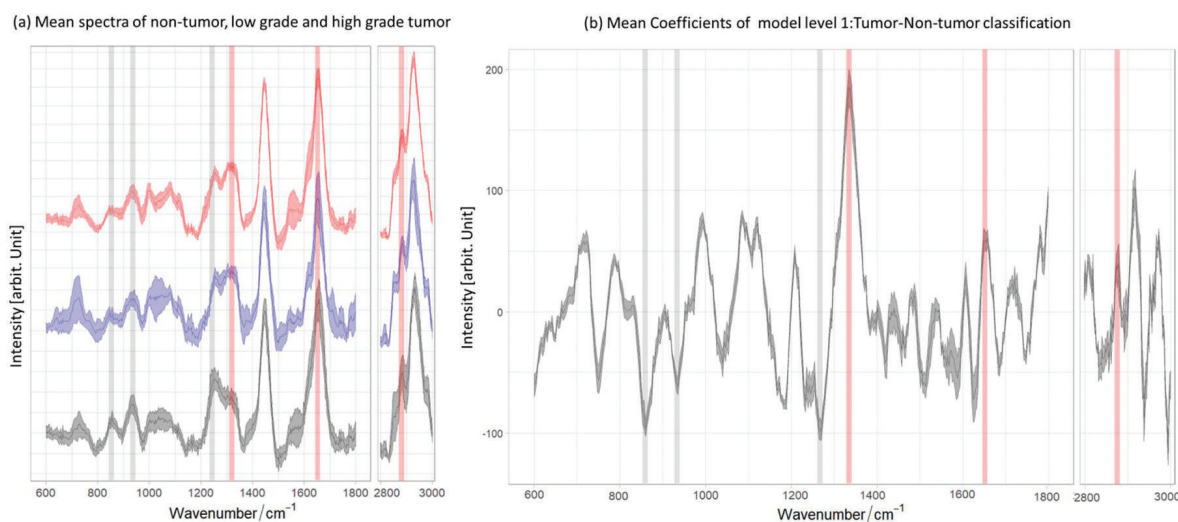


Fig. 5 Relation between the mean and the mean coefficients of ML1. (a) Mean spectra of non-tumor (black) and low grade (blue) and high grade (red) tumor. (b) Mean coefficients of ML1 resulted from the tumor/non-tumor classification. The red bands are characteristic lipid bands and the grey bands are typical collagen bands. One can observe that the lipid bands are related to the positive coefficients for tumor and the collagen bands to the negative coefficients for non-tumor biopsies.



non-tumor (black) and low- (blue) and high-grade (red) tumor biopsies, in which the lipid and collagen bands are highlighted. The mean coefficient of the model system layer 1 (ML1) is shown in Fig. 5b. The same bands are also highlighted, illustrating the relation between negative coefficients and the spectral bands for collagen at 856 cm^{-1} , 937 cm^{-1} and 1265 cm^{-1} , which indicate the C–C vibrations and amide II of collagen,⁷⁰ respectively. The collagen bands and the negative LDA coefficients show a clear relationship between the constituent and the non-tumor class. The marked lipid bands at 1300 cm^{-1} , 1656 cm^{-1} and 2854 cm^{-1} correspond to the CH_2 deformation, twist vibration, C=C and the symmetric stretching of lipids, respectively.^{70,71} As can be seen from the comparison, there is a relation between the main lipid bands, positive LDA coefficients, and the tumor class. These observations are consistent with previous findings,^{41,72} where non-tumor tissues are mainly characterized for having a dominant presence of collagen. The two-layer model (ML1 and ML2) performance is summarized in Table 3: ML2 can identify the true positive LG easily than the true negative HG, with an achieved sensitivity of 81% to differentiate low-grade tumour from high-grade tumor. The achieved specificity of 68% to differentiate the grading indicates that the models need more spectral information of the true negative HG in order to better distinguish the main differences between tumor grading. As Fig. 5a shows, low and high grade mean spectra have very little variations and more HG-biopsies are required to allow the models to classify properly between the two classes.

MCR analysis and collagen distribution. The classification models show a distinct relation between the collagen presence in non-tumor and tumor samples; therefore the collagen distribution can be related to the mean predictions of model ML1. As previously described, each biopsy has a set of spectra that has a mean prediction obtained from model ML1, which allows providing information on the heterogeneity or homogeneity of a biopsy. An MCR algorithm is applied to use the extracted pure components of collagen for the non-tumor biopsies to find the constituent distribution in the biopsy by estimating the concentration of the component for each spectrum of the biopsy.

Fig. 6a shows the mean and standard deviation spectra of the homogeneous non-tumor (black) and tumor (red) biopsy and the extracted MCR collagen component (green) from all non-tumor biopsies, as described in the previous sections. Fig. 6b displays the mapping of the mean prediction (left) and the collagen distribution (right), showing how the presence of collagen dominates in the biopsy that is predicted as a homogeneous non-tumor tissue. This is consistent with Fig. 6c, where the mapping of a heterogeneous non-tumor biopsy shows that the areas predicted as tumor (red areas) have less presence of collagen (darker green) in comparison with the areas predicted as non-tumor (black areas). In the same way, Fig. 6d and e show the mapping of mean prediction and collagen concentrations in homogeneous and heterogeneous tumor biopsies, respectively.

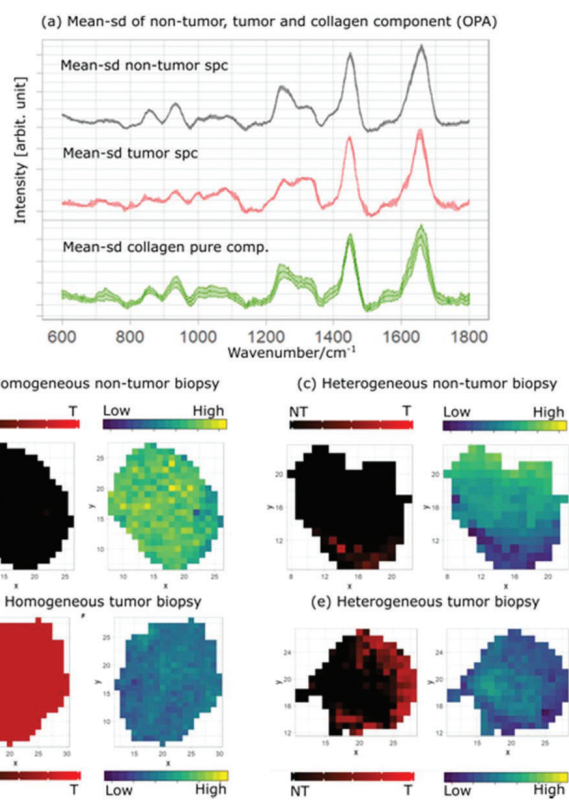


Fig. 6 Mean-sd (standard deviation) spectra and the corresponding collagen pure component: (a) mean and standard deviation of non-tumor spectra of the homogeneous non-tumor biopsy (black), homogeneous tumor biopsy (red) and extracted pure collagen from non-tumor biopsies (green). Mean prediction and MCR collagen concentration for (b) homogeneous non-tumor, (c) heterogeneous non-tumor, (d) heterogeneous tumor and (e) heterogeneous tumor biopsies. The minimum collagen concentration value is 0.043 and the maximum value is 0.052.

The homogeneous tumor biopsy shows a distinct difference when compared to the homogeneous non-tumor biopsy, where the dark colored area indicates a low presence of collagen. Similarly, the areas predicted as non-tumor in Fig. 6d are brighter than the areas predicted as tumor for the heterogeneous tumor tissue. This contrast is depicted easily by comparing the prediction and collagen distribution maps in Fig. 6. The black area of the prediction map (left) is non-tumor and is lighter colored in the collagen distribution map (right). The correlation between the prediction maps and the collagen distribution maps provides an insight into the relation between one of the main bladder tissue constituents and the tumor regions of the analyzed tissue.

OCT-Raman combination

The combination of RS and OCT opens a new means to better comprehend the essential basis of the data. Even though both modalities are based on different physical origins, *i.e.* OCT depends on the light scattering due to changes of the index of refraction in the tissue, and RS relies on the molecular vibrational bonds in the sample, both origins are inherently



coupled. The collected imaging data of the two complementary modalities were acquired in a co-registered manner, offering the possibility to correlate molecular and morphological features from the same locations.

The correlation was performed, first by stitching the OCT stacks and applying an in-house developed algorithm to compute the surface curvature of the biopsy, which allowed for the flattening of the surface. After the curvature correction, the mean of the biopsy in the z-dimension was calculated, and the obtained image was employed to compute a mask for locations belonging to the biopsy and locations outside the biopsy. The RS data were pre-treated as described in the Materials and methods section, and the mean prediction Raman map was employed to correlate the OCT and RS data. The RS mean prediction map was interpolated to account for the size difference between the Raman map and the OCT image. Furthermore, because the OCT scan covered more area than the RS map, the RS map was used as a mask for the OCT image. Transparency was applied to the RS map in order to provide visual information of both the OCT image and the Raman map.

Fig. 7 shows the transition of tumor to non-tumor area using the combined information of both modalities. To better visualize the data, images were displayed for both modalities indicating a healthy bladder wall structure within a cancerous lesion. An OCT cross-sectional and en-face image of a biopsy, which was histopathologically diagnosed as pTa low-grade tumor is shown in Fig. 7a. The overlaid Raman information of the tumor margin, where the red shade is the predicted tumor fraction and the black shade is the predicted non-tumor fraction as established by the ML1 model, is shown in Fig. 7b. The bright features of the lamina propria appear in the OCT

image, which indicates a pronounced transition between the urothelium and the lamina propria in the healthy bladder wall and are well correlated to the regions that were predicted as non-tumor tissues by RS. To better visualize the information, cross-sectional images of the indicated regions marked by the colored lines are framed in green and yellow. The cross-sectional images are maximum projections of 10 scans around the indicated position. This combination of both modalities enables a better comprehension of the underlying signal origin and enables further localized pathological analysis of the biopsies with localized diagnosis to provide more detailed histopathological labels. This can lead to increased accuracy given by computer-assisted classification of tumor and non-tumor areas, providing a strong indication that the combination of optical label-free modalities can provide a comprehensive, localized diagnostic value.

Although biopsy handling and the pathological examination, such as biopsy torsion or discrete biopsy labels, influence the performance, the achieved accuracies of 73% and 77% for OCT and RS, respectively, are promising for future *in vivo* tests, allowing the determination of the stage and grade simultaneously *in vivo*. Here, artefacts from sample handling will become completely negligible, additionally improving the accuracy.

Conclusions

In summary, we have demonstrated that fiber-probe based OCT and RS are suitable to provide clinically relevant information for detection and grading of NMIBC biopsies. Here, a

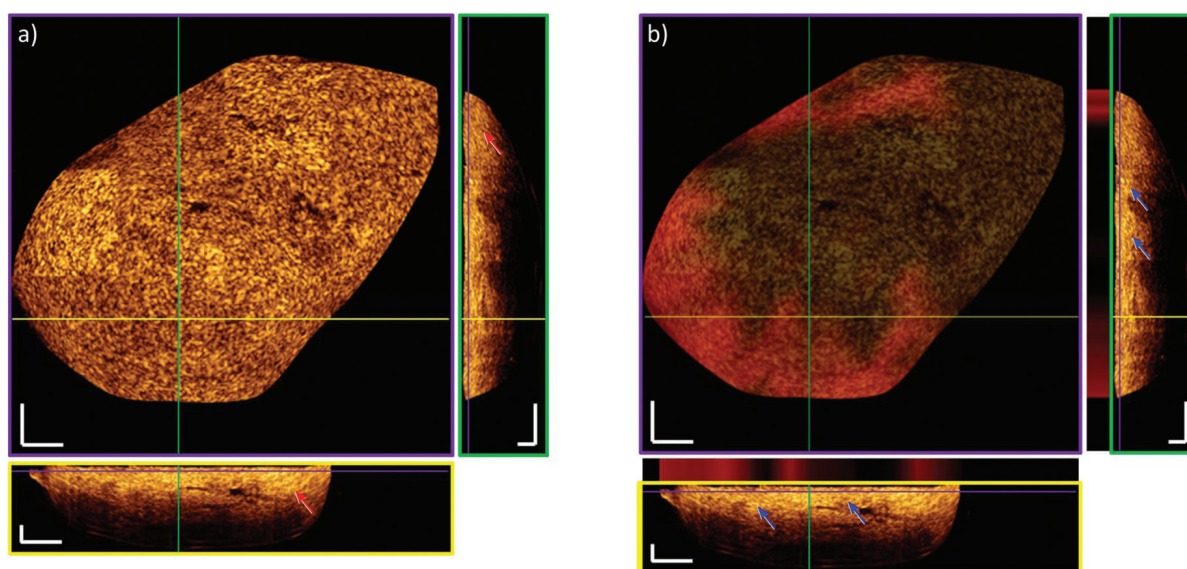


Fig. 7 Heterogeneity of a pTa low grade labelled biopsy. (a) OCT scan: Red arrows indicate loss of transition between the urothelium and the lamina propria showing a pTa stage cancer. (b) OCT-RS combination: Model system ML1 highlights tumor (red) and non-tumor (black) areas and it is overlapped to the OCT image (en-face and B-scans). The blue arrows point to regions of present lamina propria. The lamina propria appears bright in the OCT image and RS predicts the non-tumor tissue (black color within the stripes above the B-scans). The purple framed image indicates the en-face image. Cross-sectional images are framed in green and yellow. Locations within the 3D stack are marked with colored lines. Cross-sectional images are maximum projections of 10 scans around the shown position. Scale bars: 250 μm .



forward looking, piezoelectric tube-based OCT probe is used for a comprehensive characterization of bladder cancer lesions for the first time, providing volumetric morphological information of entire biopsies. The presented OCT probe provides sufficiently high optical performance to determine small morphological structures in depth. Raman spectroscopy, on the other hand, demonstrates clear spectral differentiation of tumor and non-tumor, and low- and high-grade lesions in the bladder tissue based on the biomolecular composition. By developing an imaging platform that combines both modalities using forward-viewing fiber-optical probes, it was possible to acquire morphological volumetric images of biopsies and to create co-localized and co-registered hyperspectral molecular maps for the sample, providing comprehensive diagnostic information for the penetration and grade of bladder cancer at an early stage. By performing the study using fiber-optic probes and a large number of samples, it was possible to evaluate the relevant parameters of the probes for the *in vivo* application of OCT and RS. For example, it was possible to show that the piezoelectric tube-based OCT probe is mechanically stable to conduct a reproducible measurement of more than 100 biopsies with more than 1000 individual stack acquisitions over an extended period of time. Probe parameters, such as the outer dimension, meet the restrictions given by surgical instruments for *in vivo* applications, including additional sheathing for biocompatibility and safety. The parameter evaluation reveals adequate power levels and performance for visualization of the clinically relevant data for both modalities. The presented axial and lateral resolution for OCT and a sensitivity of 99 dB are sufficient. The FOV should be as big as possible, but a diameter of 1 mm is enough to identify and characterize relevant lesions. The excitation power of 70 mW and 11 mW used by RS and OCT, respectively, are well within the limit for maximum permissible exposure on skin and suitable for *in vivo* applications. The required acquisition times of 0.5 s and 2 s for RS and OCT, respectively, are suitable for interoperative handling by urologists during bladder examination. Comparing OCT and RS, one can see that OCT can acquire information from a larger FOV faster, allowing for the detection of cancerous lesions. RS, on the other hand, provides higher sensitivity, specificity and accuracy for differentiating tumor from non-tumor tissues, and additionally allows the grading of tumors. As such, OCT can be used as a red-flag technology and RS can be used to provide diagnostic information. Moreover, the results serve substantially as the next step towards *in vivo* testing of the OCT-RS combination. The presented findings pave the way for the development of multimodal, endoscopic probes enabling OCT and RS to supply the clinicians with clinically important, localized information in real time, which is until now only accessible after histopathological examination.

Conflicts of interest

There are no conflicts to declare.

Acknowledgements

This project has received funding from the European Union project MIB (Horizon 2020, grant agreement No 667933) and the European Union's Horizon 2020 research and innovation program under the Marie Skłodowska-Curie grant agreement No 721766, FBI.

References

- 1 T. Vos, C. Allen, M. Arora, R. M. Barber, Z. A. Bhutta, A. Brown, *et al.*, *Lancet*, 2016, **388**, 1545–1602.
- 2 M. Burger, J. W. F. Catto, G. Dalbagni, H. B. Grossman, H. Herr, P. Karakiewicz, W. Kassouf, L. A. Kiemeny, C. La Vecchia, S. Shariat and Y. Lotan, *Eur. Urol.*, 2013, **63**, 234–241.
- 3 B. W. G. van Rhijn, M. Burger, Y. Lotan, E. Solsona, C. G. Stief, R. J. Sylvester, J. A. Witjes and A. R. Zlotta, *Eur. Urol.*, 2009, **56**, 430–442.
- 4 R. Madeb, D. Golijanin, J. Knopf and E. M. Messing, *Expert Rev. Anticancer Ther.*, 2007, **7**, 981–987.
- 5 J. Schmidbauer, F. Witjes, N. Schmeller, R. Donat, M. Susani and M. Marberger and, Members Of The Hexvix PCB301/01 Study Group, *J. Urol.*, 2004, **171**, 135–138.
- 6 M. Babjuk, A. Böhle, M. Burger, O. Capoun, D. Cohen, E. M. Compérat, V. Hernández, E. Kaasinen, J. Palou, M. Rouprêt, B. W. G. van Rhijn, S. F. Shariat, V. Soukup, R. J. Sylvester and R. Zigeuner, *Eur. Urol.*, 2017, **71**, 447–461.
- 7 C. J. Down, R. Nair and R. Thurairaja, *Surgery*, 2016, **34**, 532–539.
- 8 J. D. Brierley, M. K. Gospodarowicz and C. Wittekind, *TNM Classification of Malignant Tumours*, John Wiley & Sons, 8th edn, 2016, pp. 204–208.
- 9 P. A. Humphrey, H. Moch, A. L. Cubilla, T. M. Ulbright and V. E. Reuter, *Eur. Urol.*, 2016, **70**, 106–119.
- 10 I. Kausch, M. Sommerauer, F. Montorsi, A. Stenzl, D. Jacqmin, P. Jichlinski, D. Jocham, A. Ziegler and R. Vonthein, *Eur. Urol.*, 2010, **57**, 595–606.
- 11 W. Zheng, W. Lau, C. Cheng, K. C. Soo and M. Olivo, *Int. J. Cancer*, 2003, **104**, 477–481.
- 12 E. Pery, W. C. P. M. Blondel, S. Tindel, M. Ghribi, A. Leroux and F. Guillemin, *IEEE Trans. Biomed. Eng.*, 2014, **61**, 207–216.
- 13 D. Huang, E. Swanson, C. Lin, J. Schuman, W. Stinson, W. Chang, M. Hee, T. Flotte, K. Gregory, C. Puliafito, *et al.*, *Science*, 1991, **254**, 1178.
- 14 W. Drexler and J. Fujimoto, *Prog. Retinal Eye Res.*, 2008, **27**, 45–88.
- 15 G. J. Tearney, S. A. Boppart, B. E. Bouma, M. E. Brezinski, N. J. Weissman, J. F. Southern and J. G. Fujimoto, *Opt. Lett.*, 1996, **21**, 543–545.
- 16 T. Xie, H. Xie, G. K. Fedder and Y. Pan, *Appl. Opt.*, 2003, **42**, 6422–6426.



- 17 M. J. Gora, J. S. Sauk, R. W. Carruth, K. A. Gallagher, M. J. Suter, N. S. Nishioka, L. E. Kava, M. Rosenberg, B. E. Bouma and G. J. Tearney, *Nat. Med.*, 2013, **19**, 238–240.
- 18 E. Zagaynova, N. Gladkova, N. Shakhova, G. Gelikonov and V. Gelikonov, *J. Biophotonics*, 2008, **1**, 114–128.
- 19 *Optical coherence tomography: technology and applications*, ed. W. Drexler and J. G. Fujimoto, Springer, Cham, 2nd edn, 2015.
- 20 I. W. Schie and T. Huser, *Appl. Spectrosc.*, 2013, **67**, 813–828.
- 21 C. Krafft, in *Encyclopedia of Biophysics*, ed. G. C. K. Roberts, Springer Berlin Heidelberg, Berlin, Heidelberg, 2013, pp. 2178–2185.
- 22 A. De Luca, K. Dholakia and M. Mazilu, *Sensors*, 2015, **15**, 13680–13704.
- 23 I. W. Schie and J. W. Chan, *J. Raman Spectrosc.*, 2016, **47**, 384–390.
- 24 T. C. Bakker Schut, R. Wolthuis, P. J. Caspers and G. J. Puppels, *J. Raman Spectrosc.*, 2002, **33**, 580–585.
- 25 A. Beljebbar, O. Bouché, M. D. Diébold, P. J. Guillou, J. P. Palot, D. Eudes and M. Manfait, *Crit. Rev. Oncol. Hematol.*, 2009, **72**, 255–264.
- 26 L. F. C. S. Carvalho, M. S. Nogueira, L. P. M. Neto, T. T. Bhattacharjee and A. A. Martin, *Biomed. Opt. Express*, 2017, **8**, 5218.
- 27 A. Chaichi, A. Prasad and M. R. Gartia, *Biosensors*, 2018, **8**, 107.
- 28 R. Smith, K. L. Wright and L. Ashton, *Analyst*, 2016, **141**, 3590–3600.
- 29 P. Chen, A. Shen, X. Zhou and J. Hu, *Anal. Methods*, 2011, **3**, 1257–1269.
- 30 N. Bergner, T. Bocklitz, B. F. M. Romeike, R. Reichart, R. Kalff, C. Krafft and J. Popp, *Chemom. Intell. Lab. Syst.*, 2012, **117**, 224–232.
- 31 M. Ji, D. A. Orringer, C. W. Freudiger, S. Ramkissoon, X. Liu, D. Lau, A. J. Golby, I. Norton, M. Hayashi, N. Y. R. Agar, G. S. Young, C. Spino, S. Santagata, S. Camelo-Piragua, K. L. Ligon, O. Sagher and X. S. Xie, *Sci. Transl. Med.*, 2013, **5**, 201ra119–201ra119.
- 32 B. Brożek-Pluska, I. Placek, K. Kurczewski, Z. Morawiec, M. Tazbir and H. Abramczyk, *J. Mol. Liq.*, 2008, **141**, 145–148.
- 33 H. Abramczyk, B. Brożek-Pluska, J. Surmacki, J. Jablonska-Gajewicz and R. Kordek, *Prog. Biophys. Mol. Biol.*, 2012, **108**, 74–81.
- 34 K. Deng, C. Zhu, X. Ma, H. Jia, Z. Wei, Y. Xiao and J. Xu, *PLoS One*, 2016, **11**, e0159860.
- 35 S. Duraipandian, W. Zheng, J. Ng, J. J. H. Low, A. Ilancheran and Z. Huang, *Anal. Chem.*, 2012, **84**, 5913–5919.
- 36 S. Duraipandian, W. Zheng, J. Ng, J. J. H. Low, A. Ilancheran and Z. Huang, in *Integrated fingerprint and high wavenumber confocal Raman spectroscopy for in vivo diagnosis of cervical precancer*, ed. A. Mahadevan-Jansen, T. Vo-Dinh and W. S. Grundfest, San Francisco, California, USA, 2013, p. 85720Z.
- 37 C. M. O'Brien, E. Vargis, C. Slaughter, A. P. Rudin, J. L. Herington, K. A. Bennett, J. Reese and A. Mahadevan-Jansen, in *Characterization of human cervical remodeling throughout pregnancy using in vivo Raman spectroscopy*, ed. B. Choi, N. Kollias, H. Zeng, H. W. Kang, B. J. F. Wong, J. F. Ilgner, A. Nuttal, C.-P. Richter, M. C. Skala, M. W. Dewhirst, G. J. Tearney, K. W. Gregory, L. Marcu, A. Mandelis and M. D. Morris, San Francisco, California, United States, 2015, p. 93032F.
- 38 Z. Huang, A. McWilliams, H. Lui, D. I. McLean, S. Lam and H. Zeng, *Int. J. Cancer*, 2003, **107**, 1047–1052.
- 39 M. S. Bergholt, W. Zheng, K. Lin, J. Wang, H. Xu, J. Ren, K. Y. Ho, M. Teh, K. G. Yeoh and Z. Huang, *Anal. Chem.*, 2015, **87**, 960–966.
- 40 S. Devpura, J. S. Thakur, F. H. Sarkar, W. A. Sakr, V. M. Naik and R. Naik, *Vib. Spectrosc.*, 2010, **53**, 227–232.
- 41 N. Stone, M. C. Hart Prieto, P. Crow, J. Uff and A. W. Ritchie, *Anal. Bioanal. Chem.*, 2007, **387**, 1657–1668.
- 42 H. Chen, X. Li, N. Broderick, Y. Liu, Y. Zhou, J. Han and W. Xu, *J. Biophotonics*, 2018, **11**, e201800016.
- 43 E. Cordero, *J. Biomed. Opt.*, 2018, **23**, 1.
- 44 L. T. Kerr, K. Domijan, I. Cullen and B. M. Hennelly, *Photonics Lasers Med.*, 2014, **3**, 193–224.
- 45 A. C.-T. Ko, L.-P. Choo-Smith, M. Hewko, L. Leonardi, M. G. Sowa, C. C. S. Dong, P. Williams and B. Cleghorn, *J. Biomed. Opt.*, 2005, **10**, 031118.
- 46 C. A. Patil, N. Bosschaart, M. D. Keller, T. G. van Leeuwen and A. Mahadevan-Jansen, *Opt. Lett.*, 2008, **33**, 1135.
- 47 J. W. Evans, R. J. Zawadzki, R. Liu, J. W. Chan, S. M. Lane and J. S. Werner, *J. Biophotonics*, 2009, **2**, 398–406.
- 48 K. Egodage, S. Dochow, T. Bocklitz, O. Chernavskaia, C. Matthäus, M. Schmitt and J. Popp, *J. Biomed. Photonics Eng.*, 2015, 169–177.
- 49 M. Mazurenka, L. Behrendt, M. Meinhardt-Wollweber, U. Morgner and B. Roth, *Rev. Sci. Instrum.*, 2017, **88**, 105103.
- 50 A. Varkentin, M. Mazurenka, E. Blumenröther, L. Behrendt, S. Emmert, U. Morgner, M. Meinhardt-Wollweber, M. Rahlves and B. Roth, *J. Biophotonics*, 2018, **11**, e201700288.
- 51 L. P. Rangaraju, G. Kunapuli, D. Every, O. D. Ayala, P. Ganapathy and A. Mahadevan-Jansen, *Burns*, 2019, **45**, 659–670.
- 52 K. Egodage, K. Egodage, C. Matthäus, C. Matthäus, S. Dochow, S. Dochow, I. W. Schie, I. W. Schie, C. Härdtnner, I. Hilgendorf, J. Popp and J. Popp, *Chin. Opt. Lett.*, 2017, **15**, 090008.
- 53 A. L. Presnell, O. Chuchuen, M. G. Simons, J. R. Maher and D. F. Katz, *Drug Delivery Transl. Res.*, 2018, **8**, 843–852.
- 54 P. C. Ashok, B. B. Praveen, N. Bellini, A. Riches, K. Dholakia and C. S. Herrington, *Biomed. Opt. Express*, 2013, **4**, 2179.
- 55 D. Bovenkamp, R. Sentosa, E. Rank, M. Erkkilä, F. Placzek, J. Püls, W. Drexler, R. Leitgeb, N. Garstka, S. Shariat,



- C. Stiebing, I. Schie, J. Popp, M. Andreana and A. Unterhuber, *Appl. Sci.*, 2018, **8**, 2371.
- 56 T. D. Jones and L. Cheng, *J. Urol.*, 2006, **175**, 1995–2003.
- 57 S. P. Lerner, A. C. Goh, N. J. Tresser and S. S. Shen, *Urology*, 2008, **72**, 133–137.
- 58 S. P. Lerner, M. P. Schoenberg and C. N. Sternberg, *Bladder Cancer: Diagnosis and Clinical Management*, Wiley-Blackwell, 2015.
- 59 M. Bonesi, M. P. Minneman, J. Ensher, B. Zabihian, H. Sattmann, P. Boschert, E. Hoover, R. A. Leitgeb, M. Crawford and W. Drexler, *Opt. Express*, 2014, **22**, 2632.
- 60 Z. Chen, M. Liu, M. Minneman, L. Ginner, E. Hoover, H. Sattmann, M. Bonesi, W. Drexler and R. A. Leitgeb, *Biomed. Opt. Express*, 2016, **7**, 3032–3048.
- 61 L. M. Wurster, R. N. Shah, F. Placzek, S. Kretschmer, M. Niederleithner, L. Ginner, J. Ensher, M. P. Minneman, E. E. Hoover, H. Zappe, W. Drexler, R. A. Leitgeb and Ç. Ataman, *J. Biophotonics*, 2019, **12**, e201800382.
- 62 S. Vilches, S. Kretschmer, Ç. Ataman and H. Zappe, *J. Micromech. Microeng.*, 2017, **27**, 105015.
- 63 K. W. Gossage, T. S. Tkaczyk, J. J. Rodriguez and J. K. Barton, *J. Biomed. Opt.*, 2003, **8**, 570.
- 64 M. Bhattacharjee, P. C. Ashok, K. D. Rao, S. K. Majumder, Y. Verma and P. K. Gupta, *J. Innovative Opt. Health Sci.*, 2011, **04**, 59–66.
- 65 O. Ryabchykov, T. Bocklitz, A. Ramoji, U. Neugebauer, M. Foerster, C. Kroegel, M. Bauer, M. Kiehntopf and J. Popp, *Chemom. Intell. Lab. Syst.*, 2016, **155**, 1–6.
- 66 E. Cordero, F. Korinth, C. Stiebing, C. Krafft, I. Schie and J. Popp, *Sensors*, 2017, **17**, 1724.
- 67 E. Cordero, J. Rüger, D. Marti, A. S. Mondol, T. Hasselager, K. Mogensen, G. G. Hermann, J. Popp and I. W. Schie, *J. Biophotonics.*, 2019, e201960025.
- 68 T. Tran, C. P. Sundaram, C. D. Bahler, J. N. Eble, D. J. Grignon, M. F. Monn, N. B. Simper and L. Cheng, *J. Cancer*, 2015, **6**, 759–766.
- 69 B. S. Clarke, T. A. Banks and L. Findji, *Can. J. Vet. Res.*, 2014, **78**, 46–49.
- 70 Z. Movasaghi, S. Rehman and I. U. Rehman, *Appl. Spectrosc. Rev.*, 2007, **42**, 493–541.
- 71 K. Czamara, K. Majzner, M. Z. Pacia, K. Kochan, A. Kaczor and M. Baranska, *J. Raman Spectrosc.*, 2015, **46**, 4–20.
- 72 B. W. D. de Jong, T. C. Bakker Schut, K. Maquelin, T. van der Kwast, C. H. Bangma, D.-J. Kok and G. J. Puppels, *Anal. Chem.*, 2006, **78**, 7761–7769.



7.4 In-vivo Raman spectroscopy: from basics to applications

Eliana Cordero*, Ines Latka*, Christian Matthäu, Iwan W. Schie, and Jürgen Popp,
Journal of Biomedical Optics, 2018, 23(7):1-23, doi: 10.1117/1.JBO.23.7.071210.

Der Nachdruck der folgende Publikation erscheint mit freundlicher Genehmigung von Journal of Biomedical Optics. Reprinted with kind permission from Journal of Biomedical Optics.

Erklärung zu den Eigenantenteilen der Promovendin sowie der weiteren Doktoranden/Doktorandinnen als Co-Autoren an der Publikation

Doktoranden	Eliana Cordero
Schreiben des Manuskripts	x
Vorschlag Anrechnung Publikationsäquivalente	0,5

Journal of Biomedical Optics

BiomedicalOptics.SPIEDigitalLibrary.org

***In-vivo* Raman spectroscopy: from basics to applications**

Eliana Cordero
Ines Latka
Christian Matthäus
Iwan W. Schie
Jürgen Popp

SPIE.

Eliana Cordero, Ines Latka, Christian Matthäus, Iwan W. Schie, Jürgen Popp, “*In-vivo* Raman spectroscopy: from basics to applications,” *J. Biomed. Opt.* **23**(7), 071210 (2018),
doi: 10.1117/1.JBO.23.7.071210.

In-vivo Raman spectroscopy: from basics to applications

Eliana Cordero,^{a,†} Ines Latka,^{a,†} Christian Matthäus,^{a,b} Iwan W. Schie,^{a,*} and Jürgen Popp^{a,b}

^aLeibniz Institute of Photonic Technology, Albert-Einstein-Straße 9, Jena, Germany

^bFriedrich Schiller University Jena, Institute of Physical Chemistry and Abbe Center of Photonics, Jena, Germany

Abstract. For more than two decades, Raman spectroscopy has found widespread use in biological and medical applications. The instrumentation and the statistical evaluation procedures have matured, enabling the lengthy transition from *ex-vivo* demonstration to *in-vivo* examinations. This transition goes hand-in-hand with many technological developments and tightly bound requirements for a successful implementation in a clinical environment, which are often difficult to assess for novice scientists in the field. This review outlines the required instrumentation and instrumentation parameters, designs, and developments of fiber optic probes for the *in-vivo* applications in a clinical setting. It aims at providing an overview of contemporary technology and clinical trials and attempts to identify future developments necessary to bring the emerging technology to the clinical end users. A comprehensive overview of *in-vivo* applications of fiber optic Raman probes to characterize different tissue and disease types is also given. © The Authors. Published by SPIE under a Creative Commons Attribution 3.0 Unported License. Distribution or reproduction of this work in whole or in part requires full attribution of the original publication, including its DOI. [DOI: [10.1117/1.JBO.23.7.071210](https://doi.org/10.1117/1.JBO.23.7.071210)]

Keywords: *in vivo*; Raman spectroscopy; label-free; intraoperative.

Paper 180127SSTR received Mar. 2, 2018; accepted for publication May 23, 2018; published online Jun. 28, 2018.

1 Introduction

Raman spectroscopy is a label-free, nondestructive, and non-invasive method that provides information about the molecular composition and structure of a sample. It has found widespread use in the fields of material sciences, pharmaceutical analysis, inline and offline process controlling, airport security, and many others. In the last few decades, Raman spectroscopy has also begun to emerge as a promising tool for biomedical analytics and clinical diagnostics, such as the detection and staging of cancer, and has been validated in countless *ex-vivo* studies.^{1–11} Due to the highly promising results, there has been an incredible effort to move Raman spectroscopy to clinical *in-vivo* applications, where the method can unfold its full diagnostic potential. Although these *in-vivo* studies demonstrate a superb diagnostic potential of Raman spectroscopy in clinical surroundings, they also reveal technological challenges and shortcomings of the method. Due to the highly complex implementation of the technique for *in-vivo* applications it is often difficult, especially for novice scientists in the field of *in-vivo* Raman spectroscopy, to assess the relevant instrumental design parameters and their influence on the detected signal, the different available fiber optical Raman probe designs, and the readily evaluated *in-vivo* applications.

The implementation of Raman spectroscopy for clinical applications significantly differs from Raman-based analysis of prokaryotic and eukaryotic cells. For example, to provide easy access to most anatomical locations *in-vivo*, fiber optic Raman probes, which are designed for specific applications

and are available in a large number of configurations, are required. Due to the generation of a strong Raman background in the fiber, the development of those probes is highly complex and complicates the development of single-use probes. Moreover, probes have to be designed in a way that allows sustainable sterilization procedures to be routinely used in a medical environment. Because fiber optic Raman probes are usually single-point sensors, efforts have to be made to register the measurement spot at the body site to determine the precise location of the optical biopsy. This is often achieved through image guidance, and the combination with other modalities, such as white-light or fluorescence imaging, optical coherence tomography (OCT), optoacoustic or magnetic resonance (MR) tomography, and many others. The additional imaging modalities can also deliver complementary information of the target region and can significantly boost sensitivity and specificity. It is well-known that in biomedical applications intrinsic autofluorescence can easily obscure the weak Raman signal.¹² This can, for the most part, be circumvented using 785 or 830 nm as the excitation wavelength and often in combination with other software¹³ or hardware-based methods,¹⁴ such as time gating,¹⁵ frequency modulation,¹⁶ and shifted excitation.^{17,18}

In addition to the Raman probes, the entire Raman system, including the narrowband laser source, the optical and electronic components, the software for the device controlling, and data processing are underlying stringent requirements to achieve desirable results. Moreover, the Raman device has to be developed in agreement with local and global medical regulatory standards for the application in clinical studies. This includes risk analysis, which has to prove that the benefits provided by the method outweigh possible risks. An ongoing problem in the field is also the frequently observed inconsistencies of spectral biomarkers for the same diseases. When proper spectral

*Address all correspondence to: Iwan W. Schie, E-mail: iwan.schie@leibniz-ipht.de

[†]Equally contributing authors

disease markers are available, real-time analysis of the measured Raman spectra is a key requirement for clinical applications. This normally requires a sophisticated statistical analysis,¹⁹⁻²¹ relying on pre-established databases with a multitude of stored sample data.

This review aims to provide an overview of the different aspects and challenges for moving Raman spectroscopy from research laboratories to clinics to novice scientists in the field of *in-vivo* Raman spectroscopy. The overview starts with the basic requirements for the instrumentation and outlines the relevant instrumental parameters, which are needed to reliably detect the weak Raman signal, following an outline of common fiber optic Raman probe developments and common geometries for *in-vivo* applications. Finally, the review provides a comprehensive summary focusing specifically on *in-vivo* applications, using Raman spectroscopy of different disease types and different organs.

2 Raman Instrumentation

The successful implementation of any application using Raman spectroscopy is tightly bound by the instrumental parameters, which have to be chosen very carefully to measure the weak Raman signals often in the presence of a high background. As such, this section outlines the most important factors for the required components, such as excitation sources, detectors, and spectrometers, and relates the information to the relevant parameters, such as linewidth, noise sources, and resolution. A comprehensive overview of all discussed parameters is summarized in Table 1.

In comparison with most eukaryotic and prokaryotic cells, the Raman signals of histopathological tissue biopsies and *in-vivo* measurements are highly prone to exhibit a strong autofluorescence. While other methods such as fluorescence

lifetime microscopy (FLIM) rely on the presence of tissue autofluorescence, in Raman spectroscopy the presence of fluorescence creates significant complications. To overcome these drawbacks, near-infrared lasers, most commonly 785 and 830 nm, are used for the excitation of a Raman signal from tissue samples. Due to the narrow spectral width of vibrational bands, which are on the order of a few cm^{-1} , the linewidth for the excitation lasers is constrained, which means that the excitation linewidth should be <0.1 nm to achieve high-resolution spectra. Most of the excitation sources used for biomedical Raman spectroscopy exhibit linewidths of a few picometers with a high excitation power, resulting in higher cost. For low-cost implementations it is, therefore, worthwhile to consider the appropriate laser parameters.

For imaging applications on *ex-vivo* biopsies, the sample is usually placed on an $x - y$ translational stage with submicrometer step-size resolution and illuminated using an objective lens with a high numerical aperture (NA), typically $>NA$ 0.5 and most commonly close to NA 1.0. This is further combined with appropriate illumination and collection optics, which ensure a signal generation and collection from a diffraction-limited spot. When the proper aperture is added in the conjugate focal plane, the Raman acquisition can be operated confocally and enables a three-dimensional (3-D) sectioning of the biopsy sample. Using a confocal Raman implementation, a biopsy probe can be easily mapped, and the biochemical information can be directly correlated to the histopathological hematoxylin and eosin (H&E) staining. A typical Raman imaging setup is shown in Fig. 1(a) and two exemplary Raman spectra of lipid-rich and protein-rich tissue are shown in Fig. 1(b). A comprehensive overview of different Raman-instrumentation schemes, which can be combined with the various probe designs, is given in Refs. 2 and 22.

Table 1 These device parameters are most commonly found in clinical *in-vivo* Raman spectroscopy. The table provides only a general overview of the available parameter space. In some implementations, the parameters can vary from the parameters in the table. Moreover, keep in mind that many of the parameters are coupled.

Device	Relevant parameters	Typical parameter values	Influences
Detector	QE	30 to 90% @ 900 nm	SNR, acquisition time
	Read-out-speed	16 kHz to 8 MHz	SNR; number of frames/s
	Read noise	3 to 20 e ⁻ /pixel	SNR; acquisition time
	Dark current	0.0001 to 0.03 e ⁻ /s/pixel @ at -80°C	SNR; acquisition time
	Number of pixels	Horizontally: 532 to 2048	Spectral range
	Pixel size	Vertically: 100 to 2048	Etendue
		$13 \times 13 \mu\text{m}^2$ to $26 \times 26 \mu\text{m}^2$	Resolution
Excitation sources	Wavelengths	785 nm; 830 nm; 1064 nm	Autofluorescence; SNR
	Spectral linewidth	typ. <100 pm	Resolution
	Excitation power	10 to 150 mW	SNR; sample damage
Spectrometer	$f/\#$	1.8 to 9.7	Light gathering ability
	Slit width	50 to 200 μm	Resolution
	Focal length	150 to 750 μm	Resolution

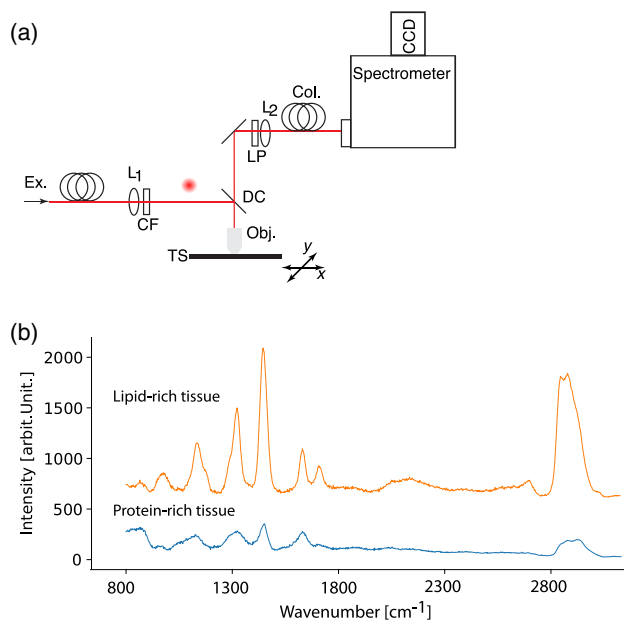


Fig. 1 (a) Typical Raman setup for the acquisition of Raman images of biopsies. Required components are L1-2-fiber coupling lens, CL, cleanup filter; DC, dichroic filter; LP, longpass filter; Obj., objective lens; collection and illumination fiber; and TS, translational stage; (b) typical Raman spectra from lipid- and protein-rich areas of a tissue sample.

Due to long acquisition times, typically on the order of seconds for a single spectrum, Raman imaging is usually not an option for *in-vivo* applications. *In-vivo* measurements are, therefore, most commonly performed by acquiring single-point Raman spectra using fiber optic probes. The design of such Raman probes will be discussed in detail in Sec. 3 of this review.

The key component of a Raman system is the detector, which in most cases is a charged coupled device (CCD). Several important factors have to be considered when choosing the appropriate CCD array for any Raman spectroscopy application. Specifically, the noise level and the quantum efficiency are of great importance. Because of the very low intensity of a Raman signal, typically on the order of 10^4 to 10^5 collected photons for an entire Raman spectrum from a protein-rich tissue sample, using a 785-nm excitation with an excitation of about 50-mW power in the sample plane, a collection NA of 0.35, and 100- μm spot size, it is crucial that the quantum efficiency is high. Keeping in mind that while 10^5 photons are quite a large number in comparison with many other applications, the total number of photons is typically distributed over 600 CCD-pixels, which results on average in <170 photons per pixel. For high-performance scientific CCD cameras that are currently commercially available, the QE is above 90% for the low-wavenumber region, which is between 800 and 910 nm, corresponding to 238 and 1750 cm^{-1} , respectively, for a 785-nm excitation laser. This allows the photons generated in the low-wavenumber region to be efficiently detected. For the high-wavenumber region, which is located between 1006 and 1030 nm for a 785-nm excitation laser, corresponding to 2800 and 3000 cm^{-1} , respectively, the QE is significantly reduced due to the band gap of silica. The OH stretching region of water, which extends all the way to 3800 cm^{-1} , corresponding to 1120 nm, exhibits an even lower QE, i.e., <10%. Generally, photons are not detectable

above 1100 nm using silicon-based CCD detectors. This is of interest because it has been previously demonstrated that the water region can provide valuable information in differentiating tumor from nontumor tissue.²³

There are several different architecture-types of CCDs available, e.g., front-illuminated (FI), back-illuminated (BI), and back-illuminated deep-depletion (BI-DD) cameras. FI cameras have QEs well below 50% for the wavelength regions mentioned above and are only suitable for applications where this lack of QE can be compensated for by the excitation power or acquisition time. However, FI cameras are also available at a lower price, compared with the two other designs, and have nearly no dark current. The BI-CCD cameras have significantly higher QE than FI-CCD cameras but can suffer from etaloning, which is specifically disruptive when dealing with high fluorescence backgrounds. Etaloning is created by NIR photons that were not absorbed in the photosensitive region but reflected at the detector interface, creating a ringing pattern on the spectrum and significantly altering the Raman spectrum. BI-DD-CCD cameras have a thicker photosensitive region, which helps to reduce the etaloning effect and provides the highest QE in the NIR region, but it also comes at a higher cost.

There have been new developments toward the implementation of InGaAs detectors for the short-wave infrared (SWIR) region. Although some promising first results have been demonstrated by the group around Puppels,²⁴ one of the main problems is the significantly higher dark noise and read noise, which can be quite challenging for some applications. Moreover, due to the $1/\lambda^4$ dependency of the Raman intensity on the excitation wavelength λ , the Raman signal generation for a 1064-nm excitation is reduced 3.4-fold in comparison with a 785-nm excitation.

There are two main noise sources for the signal acquisition using CCD cameras: read noise and dark noise. As the name suggests, read noise is generated during the read-out process of the charges from the chip and the preamplification step on the CCD camera. In addition to the device-associated noise sources, for most applications the fundamental limit for the recovery of a Raman signal is the photon shot noise. Read noise depends on the acquisition speed and varies for commonly used scientific CCD detectors between 3 and 20 electrons per pixel for comparable models from different manufacturers. Hence, specifically for low-signal applications, it is important to ensure that the right acquisition speed is chosen to ensure the highest achievable signal-to-noise ratio (SNR). Electron multiplying CCDs (EMCCDs) are frequently mentioned and have readily been used in Raman spectroscopy of biological samples. These, however, only help to circumvent the read noise using electron amplification before the electron-to-voltage conversion in the AD unit. An often-unmentioned fact about EMCCDs is that they have a higher charge transfer noise, which is given by a factor of $\sqrt{2}$. This means that only for acquisition at a very low-signal level, i.e., 10 to 20 photons per pixel, does the EMCCD outperform a CCD. However, due to the higher noise factor for longer acquisition times and higher photon levels, which is the most common case for Raman spectroscopy, the noise level of an EMCCD will be higher than for a CCD. Also, the cost for an EMCCD detector is significantly higher than any of the standard CCD detectors. A good comparison for the noise performance of different detectors is given in Ref. 25. To measure the read noise of a CCD detector, one can simply acquire a dark spectrum at a short

acquisition time, e.g., 50 ms, and very small number of vertical pixels, ensuring that the dark current becomes negligible. When no specific imaging information is required, it is possible to perform a vertical hardware binning of the entire CCD-chip or a defined region. This can help to increase the signal and ensures that read noise is only affecting individual pixels. However, for some implementations, such as line-excitation or spatial-offset Raman spectroscopy (SORS), it is important to retain the vertical information on the detector because it is correlated to spatial information in the sample. Here, the SNR level is reduced in comparison with comparable measurements with full vertical binning.

In addition to the read noise, dark noise is an important factor to consider when choosing the right CCD detector for biomedical Raman applications. Dark noise occurs from thermally generated electrons in the silicon structure of the CCD and is highly temperature dependent. Hence, all common detectors in Raman spectroscopy are cooled. Nowadays, thermoelectric cooling is the method of choice, whereas liquid-nitrogen-cooled detectors are found less frequently in laboratories. The large and cumbersome liquid-nitrogen-cooled detectors would also further complicate the transition of Raman devices to clinics, where space in the operating theater is very limited. Typical values for the dark current at -80°C vary between 0.0001 and 0.03 electrons per second per pixel, with significantly lower values for FI-CCDs than for BI-DD-CCDs. The generation of dark noise has also to be considered for any Raman spectroscopy application. For short acquisition times, i.e., <1 s, and a vertical binning of a few dozen of pixels, the dark noise contribution is negligible and way below the read noise level. If, however, the signal acquisition is on the order of a few seconds, or a large number of pixels are vertically binned, which is common when using Raman fiber probes with multiple collection fibers, it can become the limiting factor. Considering typical fiber probes with 10 collection fibers, with a core diameter of $200\ \mu\text{m}$, an imaging ratio, which is the magnification of the entrance slit into the detection plane, of the spectrometer of one, and a pixel size of $20\ \mu\text{m}$, a total of 100 pixels will be illuminated. Performing a vertical binning over 100 pixels and an acquisition time of 10 s, the dark current for typical BB-DD CCDs is readily 30 electrons per second per pixel, resulting in a dark noise of 5.4 electrons per pixel, which is higher than the read noise for some available detectors. Nevertheless, for most *in-vivo* and *ex-vivo* Raman applications, the main noise factor stems from shot noise of the fluorescence signal, as fluorescence can seldom be completely avoided. Shot noise is the random statistical fluctuation of the arrival time of photons at the detector, and it follows a Poisson distribution. The fluctuation in the number of arrived photons is described by \sqrt{N} , where N is the number of photons. For Raman spectroscopy, this specifically means that if the fluorescence signal is large, the random fluctuation in the photon arrival can be just as high or higher as the measured Raman signal, which places a fundamental limit on the Raman signal detection. For example, when 20 Raman photons arrive on a single detector pixel and the number of fluorescence photons at the same pixel is 400, the SNR just due to shot noise is already 1, in combination with the other noise sources, the SNR will be <1 . For any meaningful classification, an SNR > 5 is usually required.

The generated Raman signal is dispersed onto the CCD detector through a spectrometer. There are several types of spectrometers that are employed for Raman spectroscopy, such as

lens-based and Czerny–Turner arrangements, each having specific advantages and disadvantages. There are a few factors that have to be considered when choosing the right spectrometer, such as spectral resolution, light-collection ability, the diffraction efficiency, imaging artifacts, and scattering suppression. Many of those parameters are closely interconnected. The most obvious parameter for a spectrometer is the achievable spectral resolution. The resolution depends primarily on the focal length, which is the focal length of the mirror or lens, slit-width, groove density of the diffraction grating, and the detector pixel dimension. In most Raman fiber probe schemes, the linearly arranged collection fibers act as the entrance slit and define the aperture size. In general, it is desirable to detect the entire spectral region between ~ 300 and $3800\ \text{cm}^{-1}$ at once, which puts a constraint on the usable grating and the achievable spectral resolution, considering a fixed sensor size. There are implementations that allow imaging the low-wavenumber and high-wavenumber regions, vertically offset on the same detector, enabling measurement of the full spectral range at increased resolution. The desired spectral resolution also constrains the focal length and the light-collection ability of a spectrometer, i.e., the higher the resolution, the longer the spectrometer and the lower the light-collection ability. The typical f -numbers ($f/\#$), which is the system's focal length to the entrance aperture ratio, range between $f/1.8$ and $f/6.5$ for typical Raman spectrometers, where the lower number means a higher light-collection ability. Please keep in mind that if a fiber is used to couple the light to the spectrometer, the fiber has to match the $f/\#$ to ensure optimal coupling and best imaging performance of the spectrometer. Another factor to consider when using a spectrometer is the imaging performance, which is explicitly important when working with Raman fiber probes with multiple collection fibers that are imaged on the CCD detector. For example, most Czerny–Turner spectrometer designs can exhibit strong astigmatism, which leads to the so-called bowtie effect when using fibers. Here, only the center wavelength is properly imaged onto the detector while wavelengths further away from the central wavelength experience a vertical spreading. This becomes a significant problem when using fibers arranged vertically in a line because the signals from the individual fibers start bleeding into the neighboring ones. Lens-based spectrometers exhibit excellent imaging properties with nearly no bowtie effect, but they have, on the other hand, a significant problem with out-of-plane diffraction, which is caused by the diffraction grating and rays vertically offset to the optical axis. This results in a curvature of the input from an input fiber-line array.²⁶ There are, however, computational options to correct for those artifacts.²⁷ Recently, new commercially available spectrometers that offer superb imaging properties with little aberration have been launched.

3 Fiber and Probe Development

The key component for moving Raman spectroscopy to clinical *in-vivo* applications is fiber optical Raman probes. Over the years, a large literature body has emerged on the different types of Raman probe configurations, often too large to be assessed by a novice scientist. Each specific probe configuration can lead to different types of information, resulting in a differentiated interpretation of the data. Moreover, the number of available probe designs is constantly increasing because new probes not only are designed to perform Raman spectroscopy but also include other optical modalities, such as

autofluorescence, OCT, reflectance, just to name a few. As such, it is paramount to understand the different probe designs, how they differ, and what type of information they can provide. In this article, we give a detailed overview of different probe configurations and provide information on the possible applications.

Optical fiber sensors are increasingly used in health monitoring devices. The characteristic features of silica optical fibers, i.e., small diameter, user-defined length, and high mechanical flexibility, allow facilitating the positioning of the sensor head at remote or otherwise difficult-to-access (body) sites. This permits the development of Raman probes that can fit in the instrument channel of standard medical endoscopes, and the insensitivity of optical fibers to electromagnetic fields enables applications in combination with magnetic resonance imaging (MRI). Additionally, fiber-based sensors do not interfere with conventional electronics, are nontoxic and chemically inert, and enable Raman spectroscopy to access hard-to-reach locations *in vivo*. The implementation of such optical Raman fiber probes can be quite complex. For example, the intensity of the Raman signal generated along the length of silica-based optical fibers can overshadow the generated Raman signal from the sample. Therefore, excitation and detection paths are usually separated into individual fibers to apply appropriate filtering at the distal fiber ends. The excitation fiber is supplemented with a narrowband or a shortpass filter to suppress the silica-based Raman background. In the collection path, on the other hand, a longpass filter is needed to prevent reflected or backscattered laser light from re-entering the fiber. Oftentimes, a multitude of collection fibers is used to improve collection efficiency. At the proximal end, the collection fibers are aligned to efficiently couple the detected Raman signal into the spectrometer. Huang et al.²⁸ designed a special round-to-parabolic fiber bundle comprising 64 fibers (100- μm -core diameter, NA, 0.22) packed in a round geometry at the collection end but spread out into a parabolic linear array in an orientation opposite to the image aberration of the lens-based spectrograph at the spectrograph's entrance site.

In addition to standard optical fibers, there are a variety of optical fiber types that have also been employed, e.g., hollow,²⁹ microstructured,³⁰ bandgap,³¹ or multicore³² fibers. However, the development in recent years shows that, due to easy availability and low cost, mostly standard silica fibers are used. An overview of basic Raman fiber probe designs is given in Ref. 33. Here, the focus will be on fiber optic Raman probes used or intended for *in-vivo* applications.

The Raman fiber probe design is strongly dependent on the application. It is obvious that different constraints exist when using the Raman probe, e.g., within a cardiovascular catheter as compared with measurements in the oral cavity or on the skin. Therefore, not only are spectroscopic parameters, such as the design of the filters, the collection efficiency, and the beam steering properties, important, but first and foremost, the probe diameter and flexibility of the probe have to be considered. Of course, size restrictions are less limiting for skin applications in comparison with cardiovascular applications. Additionally, for applications in hospitals, the designs of fiber optic probes have to conform to hospital guidelines, i.e., the entire fiber-spectroscopic system has to be enclosed to avoid stray light and fit on a small transportable cart for the operating theater. The clearance for the European market requires CE certification. With this marking, the manufacturer or importer declares

compliance with the relevant EU legislation applicable to a product, regardless of where it was manufactured. Concerning the laser powers at the sample position, the guidelines are defined by ANSI Standard Z136.3–2011 “Safe Use of Lasers in Health Care” for the U.S. and EN 60825-1/A2 for Europe. Because of performing *in-vivo* experiments in patients, biocompatible materials should be used to avoid toxic effects.³⁴ Furthermore, the optical fiber probe has to withstand hospital sterilization procedures.¹

3.1 Basic Raman Probe Setups

One major difference between endoscopic Raman probes is whether they are confocal or volume probes. For illustration purposes, Fig. 2(a) shows an endoscopic volume probe, also known as a nonsuperficial or nonconfocal probe. These are endoscopic probes without any focusing optics and are the simplest endoscopic fiber optical Raman probes. Figure 2(b) shows a confocal endoscopic fiber optical Raman probe, which is more complex than the nonconfocal probe due to the addition of extra optical components, such as ball lens, gradient index lens (GRIN lens),³⁵ or aspheric lenses.³⁶ To allow for side-viewing application, mirrors [Fig. 2(c)], or prisms can be added. One possible confocal handheld Raman probe design described in Ref. 37 is shown in Fig. 2(d). The handheld Raman probe comprises two optical arms: one for the delivery of the excitation light, the other for the collection of the Raman scattered signal, integrated with optical filtering modules. The excitation light is focused on

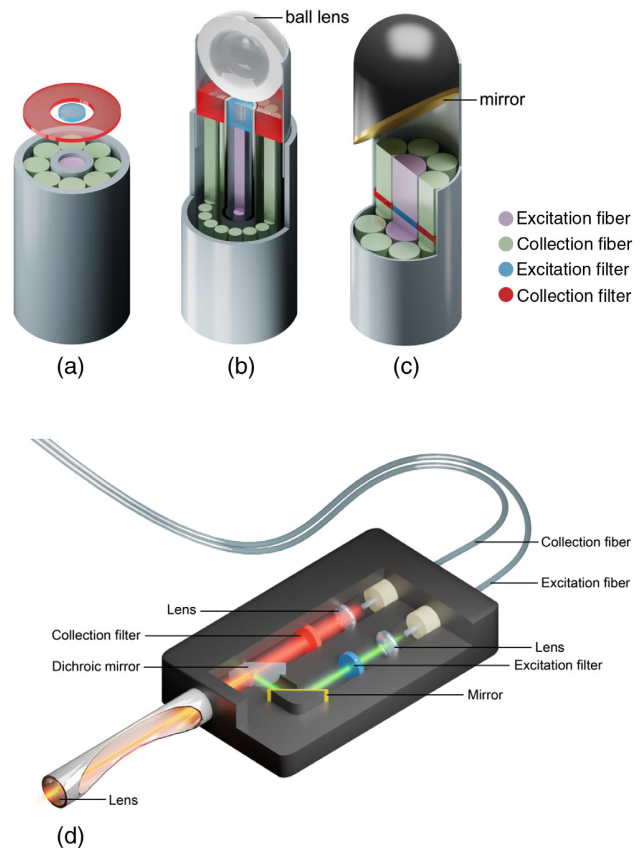


Fig. 2 Different fiber optical Raman probes. (a) Basic endoscopic probe, (b) with ball lens for focusing, (c) with side-view option, and (d) handheld Raman probe.

the tissue by an NIR-coated sapphire ball lens to a focal spot diameter of ~ 0.2 mm. The lens is mounted on the tip of the Raman probe and has a diameter of 5 mm. This probe and the more compact version,³⁸ with a total outer diameter of 8 mm were used for *in-vivo* cervical tissue measurements,^{37,39} as well as measurement of the oral cavity.⁴⁰ Using Monte Carlo simulations, the depth selectivity of ball lens-coupled probes and its dependence on refractive index and diameter of the ball lens have also been demonstrated.⁴¹

To reduce interference from deeper tissue layers during endoscopy, a beveled confocal fiber optic Raman probe coupled with a ball lens was introduced in Ref. 42. It was shown that the ratios of the Raman photons collected from epithelium versus stromal depend on the bevel-angle of the fibers.⁴² *In-vivo* measurements during endoscopy also revealed that the Raman spectra acquired using the confocal Raman probe are not easily comparable with a volume-type Raman probe⁴³ because of the different probed tissue volumes. It was found that about 85% of the collected signal arose from the top 200- μm epithelium layer of the gastric tissue, whereas 15% arose from a range between 200 and 800 μm . In addition, the beveled Raman probe provides approximately twofold improvements in tissue Raman-to-autofluorescence intensity ratios as compared with the use of a volume Raman probe.⁴⁴ Beveled probes were used in a large trial to acquire spectra from 373 patients with different histological subtypes in the upper gastrointestinal (GI) tract and to construct a comprehensive Raman library with >12,000 Raman spectra.⁴⁵ For the online analysis of the *in-vivo* spectra, dedicated MATLAB-based software was used with automated data acquisition and spectra preprocessing, allowing also discarding of noncontact spectra.⁴⁶ In further trials,^{40,47,48} the advantage of using both the high and the low-wavenumber range was shown. A comparative study demonstrates that the Raman spectroscopic technique coupled with beveled fiber optic Raman probe has great potential to enhance *in-vivo* diagnostics of gastric precancer and early cancer at endoscopy,⁴⁴ as compared with a volume probe.

Another clinical setup was introduced by Motz et al.,⁴⁹ which uses a sapphire ball lens with a 2-mm diameter and a coupled fiber probe with 15 collection fibers.⁵⁰ Here, filters deposited on a special glass substrate were used, instead of directly coating the fiber ends.⁴³ The probe was applied for margin assessment during breast surgery⁵¹ and in combination with a fluorescence/diffuse reflectance probe for skin cancer diagnostics.⁵² A commercial handheld fiber probe (InPhotonics, Norwood, Massachusetts) consisting of a 105- μm excitation fiber and a 200- μm collection fiber was used to study cervical⁵³ as well as oral cancers.⁵⁴

Short et al.⁵⁵ introduced a probe intended for lung cancer diagnostics. The probe comprises two filter stages: one set coated at the distal end of the probe, and the other is placed in the parallel light path; see Fig. 3. In contrast to contact probes of other groups, this noncontact probe had a probe tip to tissue distance of between 5 and 10 mm and was used to generate an excitation illumination spot diameter on the tissue surface between 2 and 4 mm. An *in-vivo* application with the aforementioned probe showed that high-grade dysplasia and malignant lung lesions can be detected with a high sensitivity of 90% and a specificity of 65%,⁵⁶ using only the high wavenumber range, i.e., above 2800 cm^{-1} . To accurately indicate the area being measured, a 532-nm guide laser was added and connected to three of the 31 collection fibers.⁵⁷

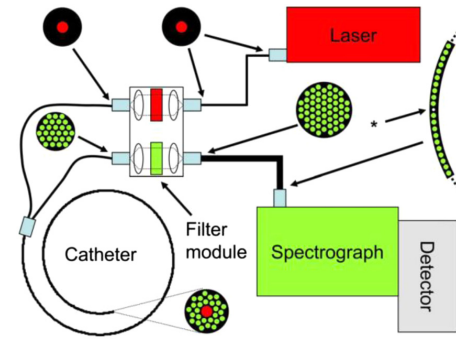


Fig. 3 Schematic diagram of the endoscopic laser Raman spectroscopy system. The inserts show the arrangement of the excitation (red) and collection fibers (green). The collection fibers were connected to the spectrograph through a special round-to-parabolic fiber bundle to correct the spectral imaging distortion. With permission from Ref. 56.

Custom-made commercial probes are also in widespread use. Agenant et al.⁵⁸ compared a nonsuperficial (or volume probe)⁵⁹ with a superficial Raman probe, both from EMVision LLC⁶⁰ (Loxahatchee, Florida) with respect to their sampling range. Both use seven collection fibers surrounding a single excitation fiber. The superficial probe had additionally a two-component converging lens, which is a 1-mm-thick flat window of fused silica, and a proximal element of a plano-convex sapphire lens; see Fig. 4. This configuration allows overlapping the excitation and collection light at the sample without interference from the sapphire Raman signal and an ~ 0.5 -mm surface diameter of the sampled region. Using a layered phantom model, they found that the optimal sampling range of the superficial probe is between 0 and 200 μm and for the nonsuperficial probe between 0 and 300 μm .⁵⁸ With this range, the superficial probe measures close to the origin of urothelial carcinomas 100 to 200 μm below the surface. It is designed to comply with the regulations of the Medical Device Directive, made of biocompatible materials, and can withstand repeated plasma (STERRAD[®]) sterilization. With its outer diameter of 2.1 mm, it fits through the endoscopic channel of a cystoscope⁵⁸ or a colonoscope.⁶¹ The same type of superficial probe has been used for intraoperative brain cancer detection.⁶²⁻⁶⁴ Using the fiber probe on 17 patients with WHO grade 2 to 4 gliomas, it was possible to accurately differentiate normal brain from dense cancer and normal brain invaded by cancer cells, with a sensitivity of 93% and

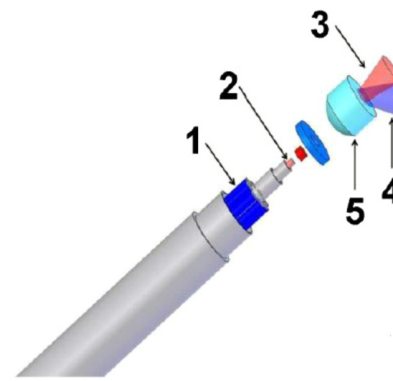


Fig. 4 Superficial probe (1 = 7 times collection fibers, 2 = excitation fiber, 3 = Raman laser cone, 4 = Raman collection cone, and 5 = two-component front lens). With permission from Ref. 58.

a specificity of 91%.⁶⁴ The group around Mahadevan–Jansen used this probe to characterize human cervical remodeling throughout pregnancy⁶⁵ and inflammatory bowel disease (IBD).⁶⁶ For the examination of soft-tissue sarcoma immediately after excision, the slim body of the probe was made pen-like and housed, resulting to an outer diameter of 6 mm.⁶⁷ The tissue of 42 patients was measured by bringing the tip of the fiber optic probe in direct contact with the regions of interest, i.e., tumor bed, control of normal muscle tissue, and fat tissue.

Optical filters are usually employed to prevent the reentry of reflected laser light into collection fibers. Another approach is to use a noncollinear arrangement of excitation and collection fibers, which additionally offers advantages concerning the Raman fiber background.²⁸ The probe was designed as a Raman probe for skin analysis^{26,68} and applied with the collection arm perpendicular to the skin surface. To collect the signal 58, optical fibers with a core diameter of 100 μm were used. The fibers are arranged along a curvature and coupled into the spectrometer. As described in Refs. 68 and 69, this probe was used for the detection of benign and malignant skin cancer lesions, respectively. The results published in 2012 showed sensitivities between 95% and 99% and specificities between 15% and 54%.⁶⁸ Related patents are licensed to Verisante Technology Inc., Germany, which gained market access in 2011 for the evaluation of suspicious skin lesions in terms of diagnosing melanoma, squamous cell carcinoma, and/or basal cell carcinoma.⁷⁰ Another handheld probe for skin measurements⁷¹ was introduced in Ref. 72, additionally containing positioning elements to enable automated positioning of the objective making it somewhat bulky, with an outer dimension of 12.7 \times 20.3 cm. As this handheld system contains no visual imaging capabilities, a targeting system, consisting of a guiding collar with a removable reticle, was developed to allow accurate identification of the measurement location. As for skin applications, a special probe design is not required as the one-around-seven probe from EMVision can also be employed, as was demonstrated in Ref. 73. For skin analysis not related to cancer, but to characterize depth profiles of stratum corneum, e.g., penetration studies of drugs or cosmetic products, in numerous cases a model 3510 Skin Composition Analyzer (River Diagnostics, Rotterdam, The Netherlands) was frequently employed.^{74–78}

An alternative miniaturized, confocal fiber optic probe intended to fit within the instrument channel of a standard medical endoscope, with a diameter of 2.8 mm, was developed by Day et al.³⁶ It was optimized for the study of the carcinogenesis process of esophageal malignancy. The optical layout is related to the probe shown in Fig. 2(d). The group used a monolithic filter/mirror component and developed wet-etched silicon motherboards and the jigs to ensure sufficient positioning accuracy of the optical parts. Although the probe is designed for *in-vivo* application, up to now it has been used to study resected tissues only.^{35,79,80} Almond et al.³⁵ turned it into a contact probe by replacing the aspheric lens with a grin lens.³⁶

3.2 Unfiltered Probes

The necessary spectral filtering to suppress the background makes the design and implementation of fiber optic Raman probes for the fingerprint region rather complex. At wavenumbers larger than $\sim 2000\text{ cm}^{-1}$, the silica core and the cladding of the fiber generate considerably lower Raman background signal. This implies that the costly filters at the distal end of the probes could be omitted if the monitoring would be restricted to the

high-wavenumber range, which was defined in Sec. 2. Hence, the diagnostic properties of the high-wavenumber range in comparison with the full or only the low-wavenumber range have been of significant interest and were widely investigated.^{57,81,82} A comparison between the predictive strength of high- and low-wavenumber range was performed using a filtered and an unfiltered probe, respectively.⁸¹ Applying this approach on colon lesions and employing multivariate analyses, the researchers found that detecting the high wavenumber Raman profiles might provide sufficient information for predicting the pathology. This has also been confirmed by others,⁸³ where a single fiber was used for both excitation as well as collection.

3.3 Spatially Offset Raman Spectroscopy

SORS is a method for the effective retrieval of Raman spectra of subsurface layers in diffusely scattering media and was introduced by Matousek et al.⁸⁴ The concept behind SORS is that there is a spatial separation between the point of laser illumination and the point of Raman signal collection on the sample surface.^{84,85} There are two main categories: SORS with a central illumination point and a collection ring and inverse-SORS with an illumination ring and a central collection area; see Fig. 5. A method to quantitatively determine the optimal offset for a given chemical sample is introduced in Ref. 86. Commercial devices are available and routinely used for airport security or in pharmaceuticals,⁸⁷ i.e., for measurements through packages. Starting in 2006,⁸⁸ it has been used for *in-vivo* transcutaneous measurement of bone tissue,^{89–92} mainly by inverse-SORS. Using a custom-built instrument (Cobalt Light Systems Ltd., Oxfordshire, UK) with offsets of up to 9.5-mm, photon migration properties and Raman signal recovery from the depth within three selected bone types have been assessed.⁸⁹ SORS can also be employed for soft-tissue characterization, e.g., for breast tumors beneath a layer of normal tissue.^{93–95} An SORS probe for the diagnostics of breast tumors was developed, arranging the collection fibers in four circle segments⁹⁴ and not in full circles as shown in Fig. 5. Raman signal collection from three coaxial annuli of optical fibers was demonstrated.⁹⁶ In very recent publications,

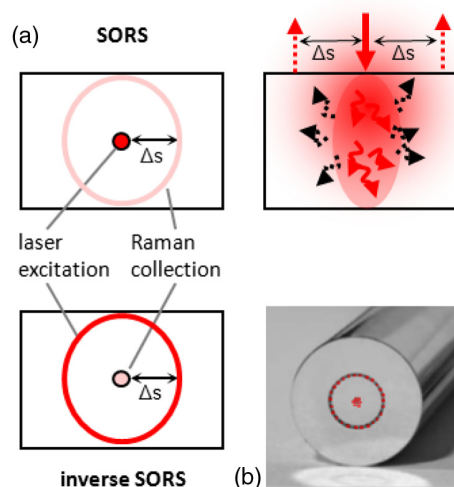


Fig. 5 Spatially offset Raman spectroscopy (a) sketch of SORS and inverse SORS principle and (b) SORS annular fiber probe with an inner and outer ring of collecting fibers. With permission from Ref. 33.

alternative approaches for depth-resolved Raman measurements, namely frequency offset Raman spectroscopy (FORS)⁹⁷ and time-domain Raman diffuse spectroscopy,⁹⁸ were introduced. With FORS, depth probing can be achieved by exploiting the different values of the optical properties of the medium at different frequencies, whereas time-domain approach exploits differing arrival times of photons.

3.4 Multimodal Probes

Already in 2008, Patil et al.⁹⁹ introduced a dual-modal device capable of performing sequential acquisition of Raman spectra and OCT images along a common optical axis. An integrated system with a common sample arm as well as common detection path was also demonstrated.¹⁰⁰ Here, both coregistered datasets are recorded sequentially with the same spectrometer. As a continuation of Ref. 99, the clinical OCT/Raman setup of Patil et al.¹⁰¹ allowed screening areas of up to 15-mm transverse and 2.4 mm in depth with OCT to identify measurement locations of interest for Raman measurements. However, the overall probe size of $10.2 \times 12.7 \times 20.3$ cm makes it mainly suitable for skin applications. A side-view hybrid probe for *in-vivo* real-time measurements was developed,^{102,103} making use of the complementary information provided by OCT and Raman spectroscopy. The handheld OCT/RS probe has a length of ~ 120 mm with a probe head size of ~ 13 mm \times 8 mm, making it suitable for *in-vivo* tissue measurements on human organs, such as the oral cavity, cervix, and skin, or for intraoperative monitoring, e.g., brain surgeries. With this, both the tissue morphology and biochemical information can be acquired simultaneously *in vivo*. However, making full use of the potential of combined Raman-OCT will require the development of analytical techniques that appropriately correlate the information from both types of data, i.e., imaging and spectroscopy.¹⁰¹ In Ref. 103, it was demonstrated that the diagnostic strength of the combination is improved in comparison with Raman spectroscopy or OCT alone. To address the issue of obtaining both morphological and molecular information at depth, a hybrid approach integrating OCT with wavelength modulated spatially offset Raman spectroscopy (WM-SORS) was introduced.¹⁰⁴ Using polystyrene in lard phantom, coregistered Raman spectroscopy and OCT measurements at depths of up to 1.2 mm were demonstrated. The wavelength modulation additionally suppresses fluorescence background.^{16,105} A Raman-OCT probe for the prospective *in-vivo* clinical melanoma skin cancer screening was integrated into a commercial spectral domain OCT-setup (Telesto II, Thorlabs).¹⁰⁶ To allow a future upgrade with an opto-acoustic detector, a pulsed excitation source for Raman spectroscopy was used. For first *in-vivo* measurements, an elliptically illuminated skin area with axes of 9 and 7 mm and integration times of 100 s were used.

Scepanovic et al.¹⁰⁷ developed a multimodal system that combined Raman spectroscopy, autofluorescence, and diffuse reflectance and comprising three light sources that are sequentially coupled to the probe by an optical fiber switch. It was employed for *in-vivo* detection of vulnerable or thrombotic plaques during femoral bypass and carotid endarterectomy surgeries.¹⁰⁸ The ball lens-coupled probe contained a single excitation fiber and a concentric ring of 15 collection fibers, 10 of which were used to collect Raman spectra, and the remaining five to collect reflectance and fluorescence data.

A multispectroscopy surgical probe from EMVision, similar to the probes described in US patents 8,175,423 and 8,702,321,

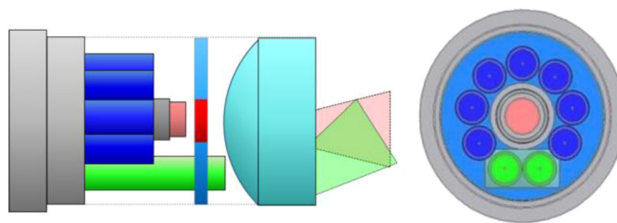


Fig. 6 Schematic view of the probe with filters, lenses, and beam propagation cones. Front view of the probe distal end. The fibers shown in blue are used for collecting the Raman scattering. The fiber shown in red transmits the light for the Raman excitation. The fibers shown in green are for generating the fluorescence/white-light signal. With permission from Ref. 110.

allows sequential acquisition of Raman spectra and fluorescence signals for two excitation wavelengths and the reflection of a white-light source, controlled by an optical switch.¹⁰⁹ Depending on the read-out technique, fluorescence intensity or fluorescence lifetime¹¹⁰ can be recorded. Figure 6 shows the principal setup, consisting of seven collection fibers around an excitation fiber for Raman spectra and, in green, two fibers for the collection of the other modalities. A multimodal setup, designed for skin cancer diagnostics, was introduced in Ref. 111. It is nearly identical to the probe shown in Fig. 7, except that three fibers with a 200- μ m-core diameter are arranged in a triangle and used for fluorescence and diffuse reflectance spectroscopy (DFS). In addition, eight fibers, i.e., seven 300- μ m-core collection fibers and one 200- μ m-core excitation fiber, are used for Raman spectroscopy. Another difference is that three “non-Raman” fibers bypass not only the donut-shaped longpass filter but also the front lens to correct for spectral aberrations.

3.5 Image Guidance

Recent developments in biomedical Raman spectroscopy indicate that image guidance for Raman measurements is highly advantageous, especially with regard to future computer-assisted and robotic surgery. In Ref. 113, integration and visualization of an image-registered Raman probe were demonstrated. It was shown that the position of the probe can be tracked and registered to any imaging modality, e.g., computed tomography (CT) scans. During brain surgery, a navigation attachment (Medtronic SureTrak) was used for spatial registration with the Medtronic StealthStation system, enabling MR guidance of measurement and tissue sample collection locations.^{62,64} A commercial Raman probe from EMVision LLC was adapted to the ARAKNES¹¹⁴ robotic platform and tested using tissue samples. The final intent is to identify ambiguous tissue margins during robot-assisted endoluminal surgeries.¹¹⁵ As Raman probes can only perform single-point measurements, the knowledge of the exact measurement point is of great importance¹¹⁶ because the samples are often very heterogeneous. Schleusener et al.¹¹⁷ have, therefore, designed a macroscopic Raman probe with a video-recorded measurement spot. Image guidance is also very advantageous for endoscopy as it helps to correlate the Raman measurements with histopathological findings. In 2009, Huang et al.⁴³ introduced image-guided endoscopy in combination with Raman spectroscopy (Fig. 8). The group used a trimodal widefield setup, i.e., white-light reflectance (WLR), autofluorescence, and narrow-band imaging in combination with point-wise

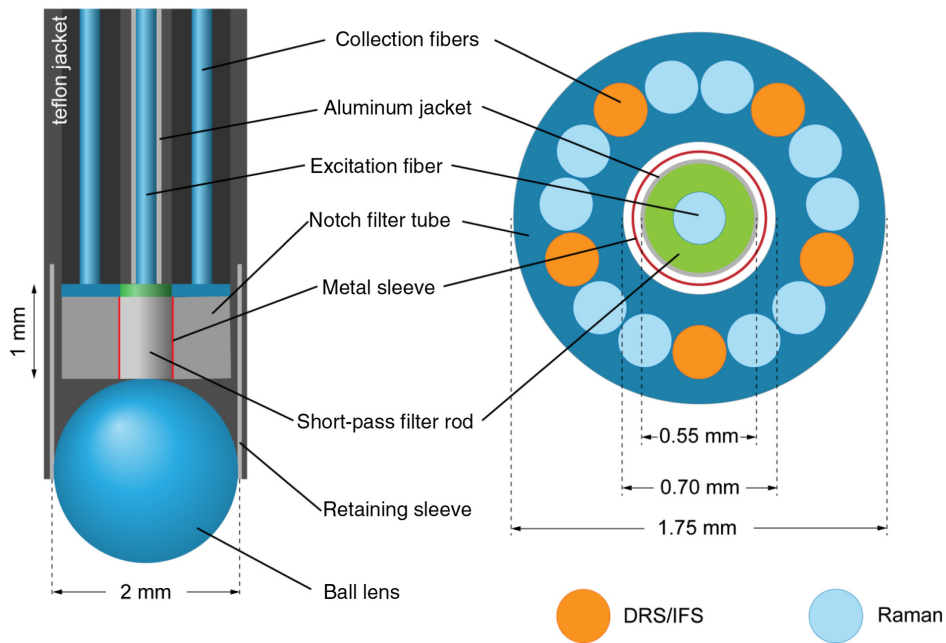


Fig. 7 Schematic of the multimodal spectroscopy probe with a side view on the left and a cross sectional view on the right. A central excitation fiber 200- μm core diameter, 0.22 NA is surrounded by 15 collection fibers, 10 of which collect Raman spectra and five of which collect DRS/IFS return light. The probe tip contains a module to filter the excitation and collection light and a sapphire ball lens to optimize collection. Adapted from Ref. 107.

Raman measurements. A Raman endoscopic probe with an outer diameter of 1.8 mm was constructed to fit through the instrument channel of a medical endoscope. This is a more direct approach as compared with MR or CT guidance. Confocal, as well as volume probes, can be employed, as long as the size restrictions given by the instrument channel are observed. The Raman probe developed by Huang et al.⁴³ consisted of 33 optical fibers: one for excitation and 32 for Raman signal collection. The distal end of the fiber probe was coated with two different types of filters; the central excitation fiber is

coated with a narrow bandpass filter, centered at 785 nm, with an FWHM of ± 2.5 nm. The surrounding collection fibers were coated with edge longpass filters and a cutoff at 800 nm. The Huang-group has published several papers, using the described Raman probe for a variety of *in-vivo* applications.^{46,82,118–121} For example, to construct a spectral database to build a model for gastric cancer diagnostics, they acquired 2748 spectra of gastric tissue from 305 patients *in vivo* using the described real-time system.⁴⁶ To get a universal tool, organ-specific diagnostic models were implemented,

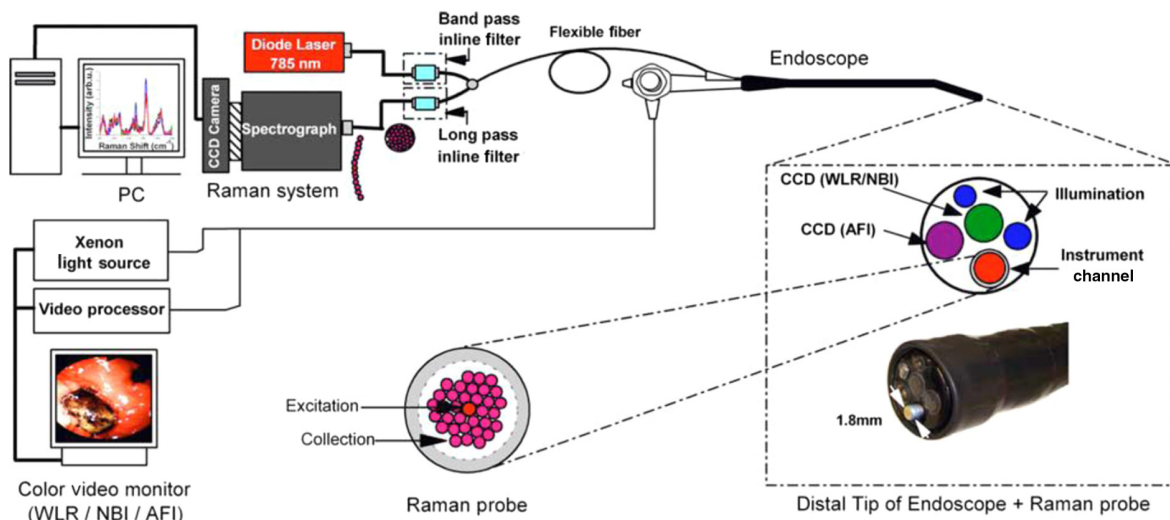


Fig. 8 Schematic of the integrated Raman spectroscopy and trimodal endoscopic imaging system developed for *in-vivo* tissue Raman measurements at endoscopy. With permission from Ref. 43.

enabling instant switching among the spectral databases of different organs, e.g., esophagus, gastric, colon, cervix, bladder, lung, nasopharynx, larynx, and the oral cavity, including the hard palate, soft palate, buccal, inner lip, ventral, and the tongue.⁴⁶ This instrumental setup was also used with a confocal probe and improved depth resolution for the characterization of nasopharyngeal cancer.⁴⁸ In this study, spectra from 95 patients were recorded. As biopsies were taken only from suspicious sites, relying on otolaryngologists' observations, the researchers state that the "healthy baseline" may not be fully corrected, which could result in errors in tissue Raman classification.⁴⁸ More clinical information regarding the mentioned publications can be found in Sec. 4.

3.6 Clinical Use

Several technical challenges remain for clinical use, such as a robust control over the laser radiation dose and measurement repeatability during endoscopy. A decrease in the SNR, due to the aging of the Raman probe after repeated cycles of harsh reprocessing procedures, is also of concern. To address such issues, disposable, biocompatible, and sterile sheaths for manufacturing endoscopic fiber optic Raman probes is being designed and tested.^{115,122} Sterilization is realized mostly by either cold gas ethylene oxide or Sterrad R (Advanced Sterilization Products, Irvine, California).^{58,108}

To save costs, unfiltered probes have also been investigated and would make single-use probes more feasible as reprocessing can damage the probe or alter its spectral behavior.⁸¹ For some applications, a large excitation spot is preferred as a larger laser intensity can be used while still complying with the maximum permissible exposure (MPE) guidelines.¹²² However, a lack of precision in controlling the sampling distance was anticipated under most operating circumstances. Using an EMVision Raman probe¹¹⁷ with an added light suppression shield, Schleusener et al.¹² investigated the perturbation factors in the clinical surrounding, such as ambient light, contact force, and immersion fluids. Also, user induced, e.g., caused by varying contact force and angle, and system-induced variabilities were investigated.¹²³ Using an unfocused seven-plus-one probe (EMVision), only small user influence was observed.

During surgery, there can be interference from light sources, as for example, surgical spotlights, white-light sources, and LCD-monitor light. The same holds true when combining Raman systems with image guidance. Spectral interference from the imaging light, which gives rise to spectral artifacts, can easily obscure the weak Raman signal and reduce the predictive accuracy of the analysis. Switching the imaging light off during a Raman measurement increases the risk of puncturing the tissue, and the point of spectral acquisition cannot be visually confirmed.⁵⁷ Desroches et al.⁶³ more thoroughly researched the impact of surrounding light and found arrangements, which avoid measurements in complete darkness, i.e., standard operating room lights can be left turned on as long as they are pointed away from the sample. In a follow-up publication,¹²⁴ a filter adapter for the surgical microscope composed of two shortpass filters was designed. This adapter in combination with background removal efficiently suppressed the interference of the operating microscope light source.

Depending on the clinical surrounding, special approaches are necessary. For Raman measurements during interventional MRI, a special fiber probe is needed, with no metal parts in the probe head. Ashok et al. developed an MRI compatible

fiber optical Raman probe with a disposable probe head, which also maintains sterility. To make the probe head a single-use component, the filtering was decoupled from the head and the commonly used steel capillaries were replaced by a heat-shrinkable sleeve.

Furthermore, efficient calibration procedures have to be applied to ensure reproducible system performance. Wavenumber calibration is typically accomplished using calibration standards,¹⁰⁹ such as acetaminophen, naphthalene, and a calibration light source. The spectral system response can be calibrated using a tungsten-halogen lamp.^{67,111} For quantitative analysis of *in-vivo* tissue, Raman measurements in real-time univariate¹²⁵ or multivariate¹²⁶ reference signals can be used.

4 Medical In-Vivo Applications

Raman spectroscopy has been used extensively for the characterization of *ex-vivo* biopsy samples; however, the real benefit of the method can only be explored through *in-vivo* applications. As such, there has been a significant movement from *ex-vivo* to *in-vivo* studies in recent years. This section presents the latest *in-vivo* studies and applications of Raman spectroscopy as a potential tool for intraoperative assistance and for the medical diagnostics on a variety of diseases and tissue types, such as cardiovascular and inflammatory disease and lung, breast, digestive and urinary tract, brain, and skin cancer.

4.1 Cardiovascular Diseases

Cardiovascular diseases are the leading causes of death worldwide.¹²⁷ Due to the aging of blood vessels lining, the inner walls of arteries become susceptible to deposition and permeation of various lipids circulating through the bloodstream, resulting in a clogging of the vessel walls, a disease which is called atherosclerosis (AT). The associated swelling can severely reduce the blood flow and thus the nutritional supply of the affected organs, which is one of the leading causes of cardiovascular events.

Apart from diagnosing the presence of atherosclerotic plaques, it is well-known that the severity of a plaque and its stability are strongly correlated with its biochemical composition.¹²⁸ For instance, the identification of vulnerable plaques remains one of the most important and challenging aspects of cardiology. There are several types of vulnerable plaques, which have distinct biochemical compositions that are characterized by lipid cores, thin fibrous caps infiltrated by macrophages, proteoglycan matrices in a smooth muscle cell-rich environment, intraplaque hemorrhage, or calcified nodules protruding into the vessel lumen.¹²⁹ Thus, specific information about the composition of a plaque would greatly improve the risk assessment and management.

Several spectroscopic techniques based on near-infrared absorption, Raman spectroscopy, or fluorescence are currently under investigation or being developed.¹³⁰ Due to a high-molecular specificity and sensitivity for lipids and crystalline calcium, which are the main constituting biochemical components of atherosclerotic plaque, Raman spectroscopy is a predestined tool to perform this characterization. Furthermore, it is readily possible to distinguish between subclasses of lipids, such as triglycerides, cholesterol, and different cholesterol esters. The coupling of Raman spectroscopy to miniaturized probes allows a catheter-based implementation that can be

performed during a routine catheter administered cardiovascular intervention, such as stenting or balloon-induced angioplasty. The development of miniaturized Raman probes would allow a combination with cardiac catheterization and could potentially facilitate the diagnosis. It can also be combined with other intravascular imaging techniques.

First, *in-vivo* experiments were reported as early as 2000 on lipid plaque observed in sheep.¹³¹ In 2006, Raman spectroscopy was tested during carotid endarterectomy and femoral artery bypass surgeries.¹³² Experiments in combination with other spectroscopic techniques, in particular with DRS and autofluorescence, often referred to as intrinsic fluorescence spectroscopy (IFS),^{108,133} demonstrated that Raman spectroscopy is very sensitive to lipid pools. Concurrently, obtained DRS data have been related to the presence of β -carotenoids and superficial foam cells. Autofluorescence, on the other hand, has been used to detect the thickness of fibrous caps. Depending on the Raman probe design, the currently available Raman probes for cardiovascular applications are about 1 mm in diameter, which is generally subject to improvement. At this point, it is noteworthy to mention that Raman excitation within the NIR is not hindered by the presence of blood, and the intensity of the occurring autofluorescence is not too high and does not obscure relevant Raman signals.¹³⁴

In contrast to other modalities, Raman spectroscopy offers enormous benefits because of its potential to provide quantitative data. Early on in cardiovascular applications with Raman spectroscopy, it has been demonstrated that individual plaque components can be quantified. Because of unique compositional parameters, different plaque types can be analyzed in a nonsubjective manner that can assist in the recognition of vulnerable plaques and improve the aforementioned risk management. It is also possible to combine Raman spectroscopy with OCT for fast image contrast on the plaque morphology. *In-vivo* Raman spectroscopy in combination with OCT has been applied consecutively on rabbits (Fig. 9),¹¹² The allocation of the collected OCT and Raman data can be assured by X-ray angiography during the operation; however, a probe that allows both modalities would be of significant impact. The OCT images and the Raman spectral information of distinct abnormal positions of early plaque formations were recorded. The morphology of early plaque formations was characterized by the OCT images and the Raman data obtained clearly showed the lipid nature of the depositions. All reported studies, mostly *ex vivo*, focused on proof of principle experiments. In particular, the application of Raman probes within arteries under *in-vivo* conditions is still very basic. The current challenges are predominantly of a technical nature, i.e., to design Raman probes that fulfill the technical requirements for applications in human.

Intravascular FLIM has also been compared with Raman spectroscopy. Both modalities were simultaneously acquired from two human coronary specimens using a bimodal probe.¹³⁵ Raman spectroscopy could distinguish lipid from necrotic cores, whereas FLIM extracted information could identify fibrous caps.

4.2 Inflammatory Diseases

Inflammatory diseases are linked to a vast array of disorders characterized by inflammation and include allergic asthma, autoimmune disease, hepatitis, and IBD, among others. The diagnosis of inflammatory changes is crucial for the early diagnosis and treatment of autoimmune infections and metastatic

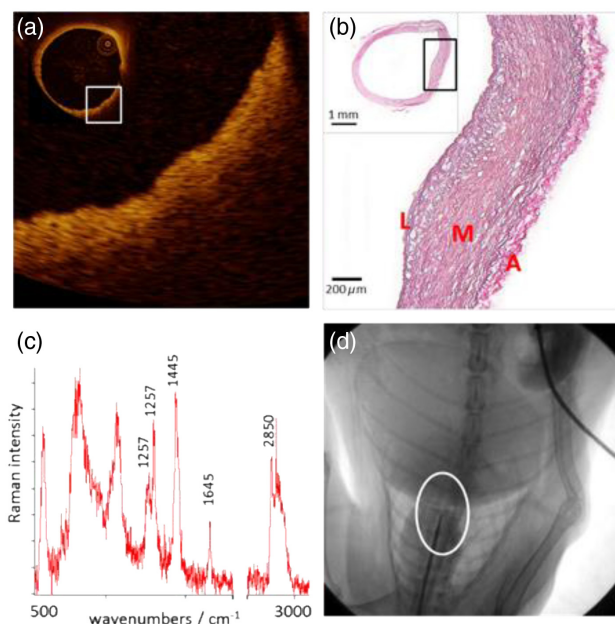


Fig. 9 Enlarged OCT image (a) from the section shown in comparison with an EvG stain (b) of a section from the same region; L, lumen or artery; M, muscularis media; A, adventitia. Graph (c) shows a Raman spectrum with characteristic lipid bands collected within the region, where the OCT image was obtained. The position of the Raman probe is shown in (d). Reprinted with permission Matthäus et al., "Detection and characterization of early plaque formations by Raman probe spectroscopy and OCT: an *in-vivo* study on a rabbit model" with permission of the *Journal of Biomedical Optics*.¹¹²

diseases.¹³⁶ *Ex-vivo* Raman-based diagnostics of asthma and hepatitis was investigated by analyzing serum and blood plasma samples.^{137,138}

Ulcerative colitis (UC) and Crohn's disease are two distinct types of IBD. The ability to endoscopically, pathologically, and radiologically diagnose and analyze the disease severity still needs improvement.¹³⁹ The potential of Raman spectroscopy to detect molecular alterations in UC and Crohn's (CC) has already been demonstrated.¹⁴⁰ Pence et al.¹⁴¹ tested a colonoscopy-coupled Raman fiber probe on 53 patients. Raman spectra were collected from the cecum, transverse, and sigmoid sites of the colon with integration times of 0.5 s and an excitation power of 80 mW. To improve the signal collection, a shallow focus design through a focusing microlens at the probe tip was implemented.¹⁴² The authors employed a sparse multinomial logistic regression algorithm to discriminate between UC and CC. The model was based on a Bayesian machine learning framework of statistical pattern recognition and allowed an overall classification accuracy of 95%. Recently, Pence et al.⁶⁶ reported a pilot *in-vivo* Raman study to characterize IBD in 23 patients including healthy subjects that underwent a routine surveillance and evaluation colonoscopy, with biopsies collected. The classifiers did not achieve optimal sensitivity and specificity, with 62% and 22%, respectively, when discriminating colitis from the quiescent disease. Nevertheless, the analyzed Raman spectra provided enough information to discriminate between IBD and normal colon, demonstrating the potential of Raman spectroscopy for providing unknown biochemical information that can be used as a diagnostic tool for IBD.

4.3 Cancer

4.3.1 Lung

Lung and bronchus cancers are the most common causes of cancer deaths worldwide,¹⁴³ and smoking is the leading cause for this kind of cancer.¹⁴⁴ Techniques, such as CT, chest X-ray, and sputum cytology, are commonly employed for lung cancer screening, but by the time of diagnosis in more than half of the patients the cancer has already metastasized. Early detection is urgently required to allow appropriate treatment and a reduction of mortality rates.¹⁴⁵ For example, using low-dose CT scanning, it was demonstrated that screening a high-risk population for lung cancer has led to a mortality reduction.^{146,147} White-light bronchoscopy has also been tested for early detection of cancer. However, it was reported that this technique cannot diagnose early cancers and precancerous lesions, such as angiogenic squamous dysplasia and squamous cell carcinoma *in situ*, and only 29% carcinoma *in situ* (CIS) and 69% of microinvasive tumors were detectable.¹⁴⁸ Fluorescence bronchoscopy has been tested and remains a promising tool for early detection of lung cancer.¹⁴⁹ Nevertheless, a main limitation is the specificity and the ability to only detect the proximal bronchial tree.¹⁵⁰ Early *ex-vivo* and *in-vivo* Raman studies demonstrated the potential of Raman spectroscopy to differentiate accurately tumor from healthy tissue.^{151,152} Recently, McGregor demonstrated that Raman spectroscopy together with multivariable analysis allowed differentiation of high-grade dysplasia and malignant lung lesions from tumor tissue and benign lung lesions with a high sensitivity and good specificity for 280 tissue sites of 80 patients.⁵⁶ The authors acquired Raman spectra mainly from the high wavenumber region (2775 to 3040 cm^{-1}), with an acquisition time of 1 s. It was observed that spectra with malignant lesions presented a distinctive loss in lipid at 2850 cm^{-1} . The analysis of this vibrational band allowed the discrimination of tumor from normal tissue with a sensitivity of 90% and specificity of 65%, respectively. It was further shown that the low specificity could be improved when Raman spectroscopy was combined with autofluorescence and white-light bronchoscopy.¹⁵³ Thereby, the efficiency of Raman spectroscopy has been demonstrated for lung and bronchus cancers detection. Nevertheless, so far it remains investigational and larger clinical trials are required to validate its effectiveness in the early cancer diagnostics.

4.3.2 Breast

The second most common cancer and one of the most frequent malignancies in women worldwide is breast cancer, with 1.7 million new cases per year.¹⁵⁴ Many diagnostic methods have been investigated to diagnose early-stage breast cancer, including MRI, ultrasonography (US), positron emission tomography (PET), and CT, and are routinely used in the clinics.¹⁵⁵ Nevertheless, the sensitivity for the detection of early-stage breast cancer is rather low, and an intrasurgical assessment of the tumor margins is often quite challenging. In addition, there are cost and time constraints that still need to be addressed, and these create a demand for highly-sensitive and rapid methods to assess tumor margins during the surgery of early-stage breast cancer.^{155,156} An early study employing 321 Raman spectra from 44 patients demonstrated the potential of Raman spectroscopy to effectively diagnose early-stage breast cancer with a sensitivity of 72% for malignant tissue and 62% for benign

tissue and a specificity for normal tissue of 83%.¹⁵⁷ The authors found that the normal tissue exhibits characteristic bands of carotenoids at 1150 and 1520 cm^{-1} , which can be assigned to C—C and C=C stretching vibrations, respectively. Other characteristic changes were observed in the symmetric and asymmetric C—H vibrations at 2850 and 2940 cm^{-1} , respectively, which are representative of lipids. These characteristic bands were not observed or did exhibit altered appearance in malignant breast tumor tissue. In addition, the group found that the fatty acid composition in cancerous breast tissue had an increased content of 20-carbon essential fatty acid, which is significantly different from the fatty acid profiles present in normal breast tissue. This was also observed by Abramczyk et al.^{158,159} after testing the Raman same system on 150 patients. One possible interpretation is that the noncancerous tissue is dominated by monounsaturated oleic acid.¹⁵⁹ Saha et al.¹⁶⁰ reported on the potential of Raman spectroscopy for the real-time identification of microcalcifications as an early sign of breast cancer during stereotactic breast core needle biopsies. The study included *ex-vivo* Raman measurements from 159 tissue sites of 33 patients to detect microcalcifications in breast tissue biopsies. Using a probe described by Motz et al.,⁵⁰ the authors employed ordinary least squares fitting to approximate the acquired spectra with a breast model that was developed in a previous study.¹⁶¹ The authors showed that it was possible to distinguish the types of microcalcifications based on the presence or absence of vibrational bands characteristic of calcium oxalate at 912 and 1477 cm^{-1} ; see Fig. 10(a). The specific location in the biopsy from where the spectrum was acquired is shown in Fig. 10(b). In contrast, Fig. 10(c) highlights the prominent band 960 cm^{-1} , which is characteristic for calcium hydroxyapatite/(microcalcification type II). The specific location in the biopsy is shown in Fig. 10(d).

Additionally, Horsnell¹⁶² and Haka et al.¹⁶³ evaluated the potential of Raman spectroscopy for *in-vivo* diagnostics for breast cancer. Both report on the feasibility to use the method in an operational theatre environment during surgery. The study by Haka et al. included nine patients and 31 Raman spectra were acquired. With their classification model, they reached an overall accuracy of 93% (28 of 30).⁵¹ The work by Horsnell et al.¹⁶² included 38 lymph node samples from 17 patients, achieving sensitivities and specificities of 90% in unsupervised test. The classification algorithm, as the one applied here described by Li et al.,¹⁶⁴ was able to classify the normal from tumor biopsies with a sensitivity of 94.9% and a specificity of 93.8%.

During the last 5 years, there have been no further records of *in-vivo* studies using Raman spectroscopy for the detection of early breast cancer.

4.3.3 Digestive and urinary systems

According to the international agency for research on cancer, one of the most commonly diagnosed cancers worldwide is colorectal cancer with 1.4 million cases per year. The third most frequent cause of cancer death is stomach cancer with 0.7 million cases (8.8%),¹⁶⁵ while esophageal cancer is the eighth most frequent cancer (3.2%) and the sixth most common cause of death (4.9%).^{166,167} The research group around Huang has widely performed *in-vivo* studies with Raman spectroscopy to differentiate normal and tumor tissue in colon, stomach, and the esophagus.^{46,47,119,121,168–172} Early work by this group demonstrated the potential of Raman spectroscopy in the stomach by differentiating dysplasia from normal tissue. The authors use

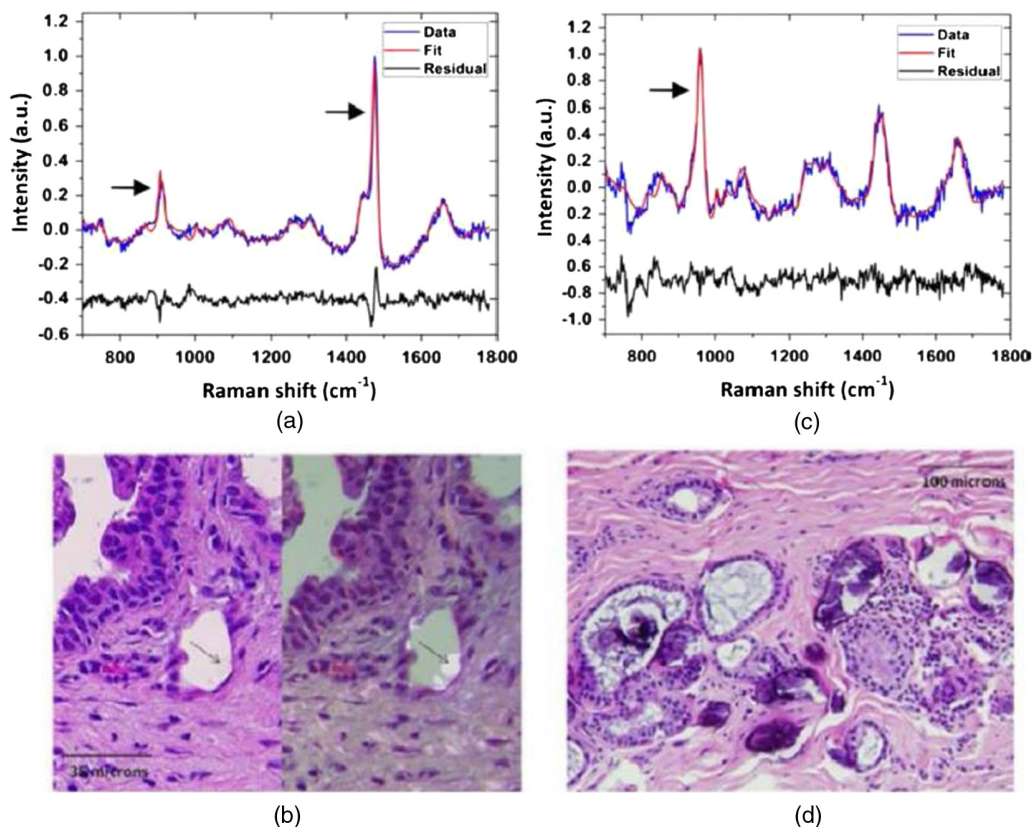


Fig. 10 Raman spectra and histopathology of breast lesions with types I and II microcalcifications. (a) Microcalcifications type I shows bands at 912 and 1477 cm^{-1} , (b) shows the calcium oxalate crystals (type I), left panel do not bind H&E and right panel viewed under polarized light, (c) Raman spectrum of type II microcalcifications with bands at 960 cm^{-1} , and (d) calcium hydroxyapatite appear as basophilic concretions on the H&E stain. Reprinted from A. Saha et al., "Raman spectroscopy: a real-time tool for identifying microcalcifications during stereotactic breast core needle biopsies" with permission of *Biomedical Optics Express* (OSA).¹⁶⁰

a 785-nm excitation laser and measured 76 gastric tissue samples from 44 patients, with 55 normal tissue samples and 21 tissue sample exhibiting dysplasia.¹⁷³ Data were analyzed by the variation in the band intensity ratio at the band 875 cm^{-1} , i.e., C–C stretching of hydroxyproline, and the band at 1450 cm^{-1} , i.e., CH₂ bending of proteins/lipids, resulting in a sensitivity of 85.7% and a specificity of 80%.

Huang and Bergholt^{174,175} have also performed *in-vivo* Raman measurements in the stomach for a label-free diagnostics of epithelial neoplasia, benign, and malign stomach ulcers. The results of these studies demonstrated that the diagnostic capability is optimized through the combination of near-infrared autofluorescence with Raman spectroscopy. A total of 1098 normal tissue and 140 cancer gastric tissue samples from 81 patients were measured with a spectral acquisition time of 0.5 s. The differentiation between gastric cancer and normal tissue was achieved with a sensitivity of 97.9% and specificity of 91.5%. The main advantage of combining Raman spectroscopy with autofluorescence is that the latter provides additional information, such as changes in morphological structures, tissue scattering, absorption, and endogenous fluorophore content of sample.¹²¹ Bergholt et al.¹¹⁹ also performed *in-vivo* diagnostics of esophageal cancer with image-guided Raman endoscopy by combining widefield endoscopic imaging, narrow band imaging, and autofluorescence imaging in 75 esophageal tissue

sites from 27 patients, where 42 Raman spectra were acquired from normal tissues. It was found that the esophageal cancer tissue exhibits Raman bands associated with cell proliferation, lipid reduction, and neovascularization. The LDA-based diagnostic model allowed differentiating tumor from normal tissue with a sensitivity of 97% and specificity of 95%. Examples of *in-vivo* Raman spectra and Raman difference spectra of normal and cancerous esophageal tissue from this publication are plotted in Fig. 11. The difference spectra between the distal and proximal esophageal sites of normal tissue show insignificant detectable biomolecular variability; see Fig. 11(b). Figure 11(c) shows the difference spectrum between tumor and normal esophageal tissue, which resolves meaningful biomolecular changes that are related to neoplastic tissue transformation.^{176,177} Other relevant studies on the esophagus, although *ex vivo* but worth mentioning, were carried out by the Stone's group.^{79,80} Kendall et al. performed the diagnostics of esophageal cancer using a Raman probe on 123 esophageal biopsies collected from 49 patients. The authors demonstrated that high levels of sensitivity (81%) and specificity (98%) can be achieved using the miniature confocal fiber optic Raman probe at 50 mW, laser excitation of 830 nm, and acquisition times between 2 and 10 s from random locations on the surface of each sample.^{36,79}

Recently, Wang et al.¹⁷¹ demonstrated that the acquisition of both the low and the high wavenumber regions of a Raman

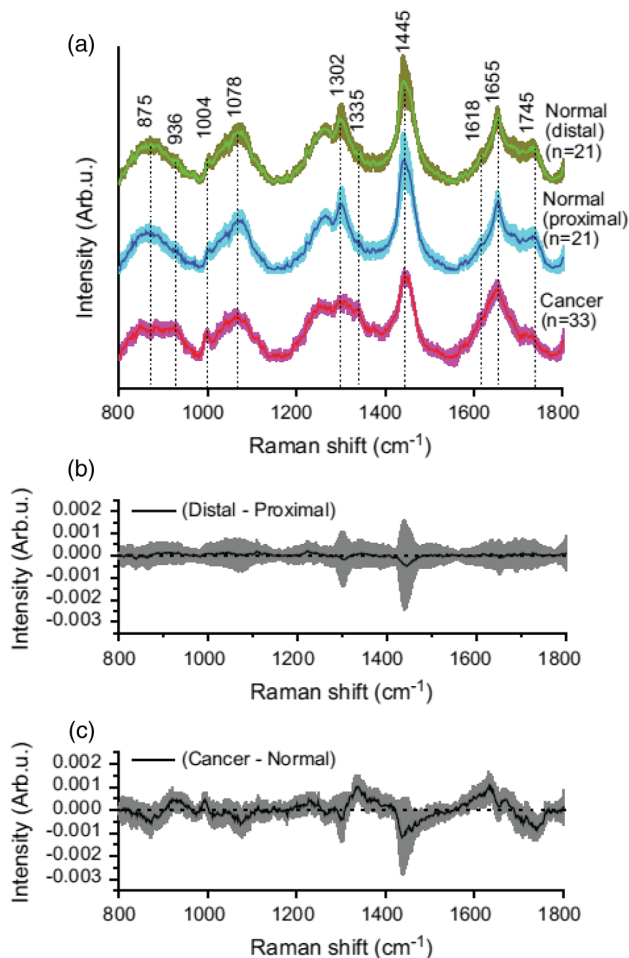


Fig. 11 (a) Mean Raman spectra obtained *in vivo* and standard deviations of normal and cancerous esophageal tissue, the spectra are shifted vertically to observe easily the change, (b) The difference spectrum of the mean normal Raman spectra between the distal and proximal esophageal tissue, and (c) difference spectrum of the mean Raman spectra between cancer and normal esophageal tissue. Adapted with permission from Bergholt et al., “*In-vivo* diagnosis of esophageal cancer using image-guided Raman endoscopy and biomolecular modeling” with permission of the *Journal of Technology in Cancer Research and Treatment*.¹¹⁹

spectrum meaningfully enhances the detection of esophageal neoplasia *in vivo* in comparison with each region alone. The authors measured Raman spectra from 48 esophageal patients under endoscopic examination, with 80% of the data used to train a model and the remaining data used for testing the data acquired with a confocal beveled fiber optic Raman probe.⁴² The classification was performed using partial least squares discriminant analysis with cross validation, resulting in a diagnostic sensitivity of 97% and specificity of 97.4% of the esophageal squamous cell carcinoma. The changes were attributed to a reduction of the Raman band intensities at 1078 cm⁻¹, which is associated with a reduction in lipid content that occurs mainly due to the thickening of the cancerous esophageal mucosa.¹⁷⁸ In a follow-up study, Wang et al.⁴⁷ also reported an *in-vivo* investigation into diagnostics gastric dysplasia, mostly known as a precursor of gastric cancer. The authors tested the fiber Raman probe system employed in the previous study^{45,171} to differentiate normal, dysplastic, and

cancerous gastric tissue, achieving much higher specificity in comparison with WLR endoscopy, 95.9% and 51%, respectively. The study obtained a total of 5792 Raman spectra of gastric tissue, i.e., 89% normal, 2% high-grade dysplasia, and 8% adenocarcinoma from 191 gastric patients and 441 tissue sites. Bergholt et al.¹⁷⁹ also reported for the first time depth-resolved Raman endoscopy as a tool for the *in-vivo* detection of dysplasia in Barrett’s epithelium, with a total of 43 patients that were tested with Raman endoscopy. The fiber optic Raman probe was used in direct contact with the GI epithelia. The Raman signal was acquired from a layer of a depth of ~200 μm, with a 785-nm excitation trimodal Raman spectroscopic platform, which allowed the resolution of histopathological features of endogenous biomolecules in the epithelium.

Lin et al.¹⁷² reported diagnosing gastric intestinal metaplasia (IM) *in vivo* using the beveled fiber optic Raman probe previously developed.^{42,44} The authors acquired 4520 gastric Raman spectra from 157 gastric patients, i.e., normal 92% and IM 8%. Relevant differences between normal and IM tissue were reductions in the band intensities at 875 and 1078 cm⁻¹, which are associated with collagen and lipid contents, respectively.

Bergholt et al.¹⁸⁰ demonstrated in 2015 in an *in-vivo* study that specific biomolecular variations picked-up by Raman spectroscopy in different anatomical locations within the colorectum of normal colorectal tissue is negligible compared with cancer tissue.

The authors acquired Raman spectra from 1129 sites of five different locations, i.e., ascending colon 16%, transverse colon 22%, descending colon 11%, sigmoid 19%, and rectum 32%, in 50 patients. To complement this work, Ding et al.¹⁸¹ investigated different physiological factors on biochemical properties of colon tissue. After measuring 455 Raman spectra from 56 subjects, between 28 and 85 years of age, it was found that ethnicity, gender, and age in relation with body mass index (BMI) are key factors of variability in the spectra within the normal tissue, mainly from contrasting abundance between lipids and proteins. The authors report that the intensity of Raman bands at 1303, 1445, and 1656 cm⁻¹ increased substantially in obese and overweighted patients compared with the normal subjects. In contrast, protein decreased in both groups. It is, therefore, reasonable to consider the BMI a relevant factor when applying Raman spectroscopy for label-free *in-vivo* diagnostics.

Worldwide bladder cancer has become the ninth most common cancer, with a mortality rate of >60%.¹⁸² Early studies on biopsies demonstrated the potential of Raman spectroscopy to detect different bladder tumors (CIS, G1 to G3) from normal bladder tissue.^{183–186} For instance, it was found that the DNA content increases for pathologies within the bladder and the prostate, while in contrast the collagen content decreases. In addition, a higher level of cholesterol with an increased severity of the tumor was observed.¹⁸⁷ These investigations were complemented by another *ex-vivo* study that employed confocal Raman probes acquiring 140 Raman spectra from 28 fresh biopsies of 14 patients optimizing the classification algorithm and achieving a sensitivity of 85.7% and specificity of 100% for the diagnostic performance.¹⁸⁵ Further steps were taken by Stone and coworkers¹⁸⁸ in collaboration with Motz et al.⁴⁹ The authors reported on a clinical fiber optic Raman system for the discrimination between benign and malignant snap-frozen bladder samples with an overall accuracy of 84%.^{50,188} This initial work allowed the translation of the Raman-based diagnostic approach from *ex vivo* to *in-vivo* bladder cancer

diagnostics. A highly cited study on *in-vivo* bladder cancer diagnostics was reported by Draga and coworkers,⁵⁹ who performed measurements on 38 patients, using a Raman spectroscopic probe, reported previously by Magee et al.¹⁵¹ For each sample, a leave-one-out cross validation was used to distinguish cancer from normal tissue, achieving a sensitivity of 85% and specificity of 79%.

4.3.4 Head and neck

Head and neck squamous cell carcinoma (HNSCC) includes a variety of tumors in the lip, oral cavity, hypopharynx, oropharynx, nasopharynx, and larynx. HNSCC is the sixth most common malignancy worldwide,¹⁸⁹ with about 85,000 incident cases and over 50,000 reported deaths from nasopharyngeal carcinoma (NPC) in 2012.¹⁹⁰ As an alternative to the standard tissue biopsy methods, optical spectroscopy techniques, such as light scattering, Raman and fluorescence spectroscopies have been tested for the detection of early-stage NPC.^{191–193}

The application of Raman spectroscopy for cancer diagnostics of head and neck has been reported for several cases.^{191,194–196} For example, Lin et al.⁸² implemented transnasal image-guided Raman spectroscopy in the higher wavenumber region to detect laryngeal tumor tissue with a miniaturized fiber optical Raman probe in the larynx, acquiring 94 Raman spectra with 23% normal and 77% tumor sites from 39 patients that underwent laryngoscopic screening. The measured spectra presented prominent differences between normal and tumor tissue in the Raman band intensities at 2845, 2880, and 2920 cm^{-1} associated with CH_2 stretching of lipids, and the 2940 cm^{-1} band, which is assigned to the CH_3 stretching vibration of proteins. The authors were able to differentiate laryngeal tumor from normal with a diagnostic sensitivity of 90.3% and specificity of 90.9%.

Further studies in the nasopharynx and larynx allowed the first implementation of *in-vivo* real-time transnasal image-guided Raman endoscopy,¹¹⁶ where the authors employed an earlier described Raman probe⁴³ to acquire 874 Raman spectra of 60% posterior nasopharynx, 18% of the fossa of Rosenmüller, and 22% true laryngeal vocal cords (LVCs) from 23 patients without any previous carcinosis. The spectra provided characteristic information about the composition and morphology variations in the normal nasopharynx and larynx tissue. The mean spectra of each intersubject nasal track are shown in Fig. 12, where each spectrum was acquired within 0.1 s. The WLR images of the upper (PN), mid (FOR), and lower (LVCs) nasal track are also shown. In another study, the *in-vivo* anatomical variability of the oral cavity was investigated, and Raman spectra from 26 healthy volunteers and 113 patients registered for medical examination without a history of malignancy or dysplasia were acquired. The authors performed unsupervised classification to identify anatomical differences of the measured sites, whereby the anatomical clustering yielded an overall accuracy of 95%.¹⁹⁷ Wang et al.¹⁰³ characterized biochemical and morphological changes of clinically relevant locations of oral tissue, i.e., alveolar process, the floor of the mouth, and lateral tongue *in vivo* by combining Raman spectroscopy with optical coherence tomography (RS-OCT). The study was carried out on 26 healthy volunteers with 1049 Raman spectra acquired from alveolar process (31%), lateral tongue (33%), and floor of mouth (36%). OCT images were acquired to reveal the inter-anatomical morphological dissimilarities. Partial least squares discriminant analysis was used to train the dataset

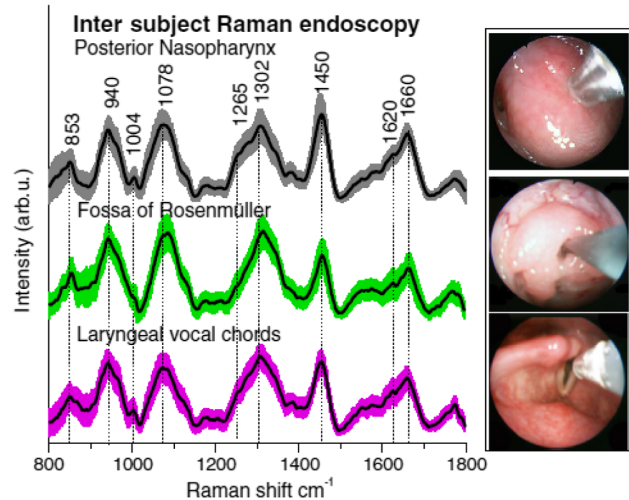


Fig. 12 Mean Raman spectra obtained *in vivo* of posterior nasopharynx (PN), fossa of Rosenmüller (FOR), and LVCs. The mean spectra are oriented vertically. In addition, *in-vivo* fiber optic Raman endoscopic acquisitions from upper-, mid-, and lower-nasal track under WLR and narrow band imaging guidance are presented (Reprinted with permission of JBO).¹¹⁶

obtained with the RS-OCT, yielding a higher diagnostic sensitivity of 100%, 76.5%, and 51.3% and specificity of 95.1%, 77.6%, and 89.6%, respectively, than obtained by just using Raman spectroscopy, i.e., sensitivities of 90.2%, 77.5%, and 48.8%, and specificities of 95.8%, 72.1%, and 88.8% for the differentiation of tumor and normal tissue of alveolar process, lateral tongue, and floor mouth, respectively.

Huang and coworkers⁴² investigated a micro-optical Raman probe for the *in-vivo* diagnostics of laryngeal cancer, acquiring 2124 Raman spectra, i.e., 62% normal and 38% tumor tissue from 60 patients under routine endoscopic examination. They reported that laryngeal tumor differs from normal tissue and that the changes are associated with the water content in the larynx, as well as the composition of proteins, lipids, and nucleic acids. The measured spectra were analyzed with partial least squares discriminant analysis, achieving a sensitivity of 93.3% and specificity of 90.1% and diagnostic accuracy of 91.1%.¹⁹⁸ In a follow-up publication, the authors also confirmed that observed Raman bands at 940 cm^{-1} for proline and valine and 1078 cm^{-1} for lipids decrease as a consequence of the thickening of the epithelium associated with cancerous progression, which obscures the collagen Raman emission from deeper tissue layers.¹⁹⁹ Furthermore, the group also tested the probe for *in-vivo* diagnostics of nasopharyngeal in 95 patients, acquiring 3731 spectra, 47% of them from normal tissue, and applying PCA-LDA together with leave-one-subject-out cross-validation (LOO-CV), obtaining a diagnostic accuracy of 93.1%.⁴⁸

4.3.5 Brain

Surgical removal of the entire tumor tissue in brain, even meningiomas (benign tumor), is crucial for optimal treatment of the affected patient.²⁰⁰ US, PET, CT, and MRI allow defining the border for tumor excision.^{201,202} However, despite the extended use, even intraoperative MRI, US, and PET have several drawbacks, such as the application of radioactive tracers, spatial resolution, scanning, and patient transport time.²⁰³ A further complication occurs in the correlation between any imaging



Fig. 13 Raman handheld probe being used in the operating room at the Montreal neurological Institute and Hospital by neurosurgeon Dr. Kevin Petrecca. The sources of ambient light can be observed including the microscope white-light, operating room overhead lights, and LCD screens (Reprinted with permission of JBO).²³⁰

modality performed before a craniotomy and the true location of the brain after the craniotomy. A method that can provide biochemical information to differentiate tumor from nontumor tissue can provide supplemental information to current techniques.²⁰⁴ The potential of Raman spectroscopy for intraoperative differentiation of brain tumor from normal brain tissue has been evaluated.^{205–207} One recent study demonstrates the potential of Raman spectroscopy for intraoperative brain cancer detection. The handheld contact Raman probe (EMVision) (see Fig. 13) was tested on 17 patients by collecting 161 measurements per sample with an integration time of 0.2 s with a laser power between 37 and 64 mW. The researchers were able to distinguish normal brain from dense cancer with a sensitivity of 93% and specificity of 91%, enabling also the detection of brain cancer cells in patients with grade 2 to 4 gliomas.^{64,208} The work was partially consistent with previously published results. The samples with cancer cells in comparison with normal brain showed differences in the lipid bands at 700 and 1142 cm^{-1} ; the additional changes in the 1540 to 1645 cm^{-1} bands indicate the higher content of nucleic acid in cancer cells.²⁰⁹ It has to be emphasized that it is crucial to properly correct the signal when strong background from autofluorescence or from ambient light is present. In addition to the significant shot noise level, a convolution of the broad polynomial background with the filter function can easily result in additional peaks and can even emulate to some degree Raman spectra, making the analysis very challenging and the results often misleading. Jermyn and coauthors also demonstrated the potential of boosted trees¹⁰⁹ and artificial neuronal networks (ANN)²¹⁰ to distinguish tissue with and without the presence of light artifacts, concluding that ANN achieves an accuracy of 90%, sensitivity of 91%, and specificity of 89% when measuring with light artifacts. In contrast, boosted trees have a lower accuracy.¹⁰⁹ A recent study characterized the SNR of a Raman probe system for intraoperative brain tissue on 10 patients. The authors proved that by increasing the integration time from 0.05 to 0.1 s and reducing the CCD camera temperature to -80°C , the SNR increases by 41% and 35%, respectively, in addition they showed that the system response is linear by relating laser power and integration time with relevant bands ratios. This study also demonstrated that necrosis can be distinguish from tumor and healthy brain tissue with an accuracy, sensitivity, and specificity above 84%;⁶³ the authors performed the test with an excitation laser operated between

40 and 60 mW at 0.05-s integration time. The probe was sterilized with a STERRAD system in a standard low temperature procedure that uses plasma gas.

4.3.6 Prostate and cervix

Prostate cancer is one of the leading causes of cancer mortality among men with 1.4 million reported cases and 293,000 deaths worldwide in 2013.²¹¹ There is a comparable number for cervical cancer with an estimated 266,000 deaths worldwide in 2012.²¹² Diagnostic techniques for early detection of cervical cancer, such as screening methods, e.g., pap smear, visual inspection with acetic acid (VIA), and excisional biopsy, have been investigated, but poor sensitivity and specificity have been reported.^{213,214} The potential of optical spectroscopic techniques has been extensively studied; for instance, *in-vivo* fluorescence and reflectance spectroscopy have demonstrated sufficient sensitivity at low cost.^{215,216} Nevertheless, studies using Raman spectroscopy demonstrated that *in-vivo* diagnostics of cervical cancer with higher accuracy is possible.^{39,217} An early *in-vivo* high-wavenumber Raman spectroscopy study on 46 women, using a handheld fiber optic Raman probe coupled with a ball lens, demonstrated that dysplasia tissue could be identified with a sensitivity of 93.5% and specificity of 97%.³⁷ Comparing Raman spectra of normal and dysplasia cervical tissue, distinct intensity differences were observed at CH_2 stretching bands of lipids (2850 and 2885 cm^{-1}) and at CH_3 stretching bands of proteins (2940 cm^{-1}), respectively.³⁷ The authors evaluated the intensity ratio of protein to lipid bands, resulting in ratios of 5.05 for dysplasia tissue and a lower ratio of 4.16 for normal tissue. The differences were linked to a decrease in content of membrane lipids, combined with an increase in short-chain fatty acids. Changes induced by dysplasia led to an increase in the nucleic hyperchromatism and density.²¹⁹ In one of the first studies, Duraipandian et al.³⁹ reported an *in-vivo* investigation on cervical precancer detection, using Raman spectroscopy, based on the measurement of 105 near-infrared Raman spectra from 57 sites *in vivo* of 29 patients, with 65 spectra from normal and 40 from cervical precancerous sites. The authors employed a genetic algorithm partial least squares discriminant analysis (GA-PLS-DA-dCV) to identify seven significant bands associated to lipids, proteins, and nucleic acids in tissue and were able to differentiate low and high-grade precancerous lesions with a diagnostic accuracy of 82.9%. To further increase the diagnostic accuracy, the authors also incorporated spectral variations linked to confounding factors, such as age, race, smoking habits, and menopausal status in cervical Raman spectra from previous studies to the GA-PLS-DA-dCV model.²²⁰ The authors also investigated variations in the high wavenumber region aimed to improve the classification accuracy of cervical precancer. The acquired Raman spectra were stratified based on the menopausal status of the cervix of 15 patients, increasing the accuracy from 71% to 91%.²²¹ A follow-up study by Duraipandian et al.²¹⁷ explored the advantages of using both the low- and the high-wavenumber regions for *in-vivo* detection of cervical precancer, acquiring 473 Raman spectra (349 normal) from 35 patients. The researchers observed intensity increases in the bands at 1001, 1095, and 1313 cm^{-1} of dysplastic cervical tissue in comparison with normal tissue. In a second follow-up study, the authors investigated composite NIR AF/Raman spectroscopy for cervical precancer diagnostics. Here, 1240 NIR AF/Raman spectra were acquired *in vivo* from 115 normal sites

of 84 nonpregnant female patients, between 18 and 70 years of age, undergoing a colposcopy revision linked to abnormal pap smears. The combination of near-infrared Raman spectroscopy with autofluorescence yielded a diagnostic accuracy of 84.1% for *in-vivo* discrimination of dysplastic cervix. Nevertheless, the autofluorescence intensity change associated with dysplastic progression was not significant, which indicated that confocal-based NIR AF spectroscopy alone is inefficient for precancer identification.²²² In a further investigation using NIR Raman spectroscopy, the author reported that Raman spectral biomarkers can be used for monitoring the multistage cervical precarcinogenesis at the molecular level.²²³ A semiquantitative modeling based on the major biochemical macromolecules in cervical tissue, i.e., DNA, histone, collagen, triolein, and glycogen, contains the stepwise accumulation of biomolecular changes associated with progressive cervical precarcinogenesis.

The potential of Raman spectroscopy for prostate cancer was investigated by Crow et al.,²²⁴ who developed a diagnostic algorithm to differentiate between pathological groups, i.e., benign prostatic hyperplasia and adenocarcinoma-Gleason, with an accuracy of 89%. The authors found reduced glycogen content and increased nucleic acid content in malignant samples compared with benign pathologies. In a follow-up study, the authors also tested an NIR fiber optic Raman system to acquire 220 Raman spectra from 29 bladder samples in cystoscopic procedures and 197 Raman spectra from 38 prostate samples.¹⁸⁸ The developed algorithm differentiated benign prostatic hyperplasia and prostatitis from prostate cancer with 86% overall accuracy. Further studies using Raman spectroscopy reported accurate differentiation of benign and malignant prostate tissue.²²⁵ For instance, the differences in the band intensities at 782 cm^{-1} in the cancer samples compared with benign samples can be interpreted as an increase in the DNA content in cancer prostate tissue.²²⁵ *In-vivo* investigations in prostate have not been reported, but the potential of Raman for *in-vivo* prostate cancer diagnostics has been demonstrated and should be expanded to the *in-vivo* diagnostics of prostate cancer.

4.3.7 Skin

As one of the most exposed organs of the human body, the skin has been studied and is routinely investigated by various optical modalities. Clinical routine investigations range from large screening dermoscopy and whole-body photography to the assessment of a few atypical and preselected regions that are investigated by pathologists.⁷⁰ The gold standard for risk evaluation of skin abnormalities and the diagnosis of skin cancer is based on biopsy extraction and subsequent histopathology, which is usually time consuming. The need for real-time and noninvasive examination of skin abnormalities arises from the growing number of skin cancer cases. Apart from supporting on-site evaluation, fast diagnosis can be beneficial as most skin cancers can be cured if recognized early enough.²²⁶ Several spectroscopy methods, such as Raman, reflectance, and fluorescence spectroscopy, have been widely investigated.²²⁷ Lui et al.⁶⁸ have demonstrated the feasibility of Raman spectroscopy in combination with multivariate data analysis to distinguish cancerous from benign lesions, showing promising results for skin cancer. The group used a Raman probe that consists of a $200\text{-}\mu\text{m}$ -core diameter single fiber to collect the generated Raman signal and one fiber to illuminate a 3.5-mm diameter skin area. The collected single-point spectra were recorded in 1 s and subjected to principal component with generalized

discriminant analysis (PC-GDA) and PLS for statistical data evaluation. All together 453 patients were examined, with abnormalities including melanomas, basal cell carcinomas, squamous cell carcinomas, actinic keratoses, atypical nevi, melanocytic nevi, blue nevi, and seborrheic keratoses. The sensitivities to differentiate skin cancers and precancers from benign skin lesions, melanomas from nonmelanoma pigmented lesions, and melanomas from seborrheic keratoses ranged between 95% and 99%. The achieved specificities of about 15% were still higher than that of studies based on inspections by clinicians.²²⁸ Another probe-based approach was suggested by the University of Texas (Austin) in collaboration with EmVision.¹¹¹ They employed a seven-around-one fiber optic Raman probe in combination with fluorescence and reflectance measurements. In a clinical study, the group investigated 137 lesions from 76 patients with cases of MM, nonmelanoma pigmented lesion (PL), BCC, actinic keratosis (AK), and SCC.⁵² The sensitivity was 100% and specificity values ranged between 95% and 71%, depending on the differentiation between individual abnormalities. The best classification performance for nonmelanoma skin cancer was obtained using multiple modalities. The best melanoma classification was evaluated based on the Raman data alone. To support the data analysis, the group also analyzed the spectral contributions of individual skin components such as collagen, elastin, triolein, nuclei, keratin, ceramide, melanin, and water, by fitting spectra obtained *in vitro* using Raman microscopy.²²⁹ A probe design using 785-nm excitation was used in a larger clinical study involving 104 patients being suspected of having MM ($n = 36$), BCC ($n = 39$), and SCC ($n = 29$).⁷³ The probe design focuses the excitation beam to a spot size of $104\text{ }\mu\text{m}$ and 17 mW on a sapphire finishing lens surface, which results in an asymmetrical detection spot with dimensions in the range of 500 to $600\text{ }\mu\text{m}$. The probe was designed for contact mode, and the backscattered light is guided by three $100\text{-}\mu\text{m}$ collecting fibers into the spectrometer. The incorporated lens potentially allows penetration depths of $100\text{ }\mu\text{m}$ or more, which can be crucial to reach the epidermal site of the basal membrane as a potential site of early cancer development. NMSC, MM, and pigmented nevi (PN) were discriminated with high accuracies of 73% for BCC, 85% for SCC, and 91% for the pigmented cases. There have also been approaches to combine Raman spectroscopy with OCT as it is probably the imaging modality that has the best potential to be used as a routine clinical screening technique. The first *in-vivo* experiments were reported in 2011 by the group of Mahadevan-Jansen.¹⁰¹ The described multimodal setup employs focusing optics for the Raman excitation with an estimated spot size of $44\text{ }\mu\text{m}$ at the sample with a depth penetration of $\sim 530\text{ }\mu\text{m}$ at an excitation power of 40 mW. The Raman spectra of normal skin and BCC were compared and showed significant differences mainly around 1090 , 1340 , and 1440 cm^{-1} .

5 Summary and Outlook

In-vivo Raman spectroscopy has a great potential to enable non-invasive clinical diagnostics for a variety of diseases because it provides label-free information about the biomolecular fingerprint of the sample and can be used to characterize and to differentiate different disease stages. In the recent years, there have been significant technological achievements and a considerable number of clinical applications readily performed. This review provides a comprehensive overview of the different technical aspects and clinical *in-vivo* applications. It describes

instrumentational aspects, starting with the choice of the appropriate components, such as excitation source, detector, and spectrometer, but it also describes in detail the different fiber optical Raman probes, which have been shown in different experimental settings. Any successful *in-vivo* Raman measurement is tightly bound by the instrumentation parameters and has to be carefully assessed by the developer before measurements can be performed. Instrumentation parameters, such as the line-width of the laser, the read noise level and dark current of the detector, and the spectral resolution of the spectrometer unit, are just a few that have to be carefully evaluated. Although the performance can usually be ensured by high-end scientific devices, it is also important to emphasize that cost can play a significant role in moving Raman spectroscopy to the clinical environment. It is, therefore, highly important to evaluate how parameters, such as spectral resolution, spatial sampling size, and spectral SNR, can be sacrificed while maintaining adequate label-free clinical diagnostics. The simplification of device structure will ultimately lead to reduction in cost and a wider availability of the method. In addition to the instruments, it is highly important to consider the designs, development, and performance of the specific fiber optic Raman probes. Here, new designs based on fiber technologies have to be addressed and tested to reduce the complexity of constructing Raman fiber probes. This will result in low-cost, single-use probes, which can further help to make Raman spectroscopy an invaluable diagnostics tool. The implementation of Raman-probes tailored to the working channels of commercially available endoscopes has already been shown by several groups. The combination with other spectroscopy and imaging modalities will further expand on the applicability of the method, and additional multimodal probe designs will appear in the near future. The clinical applications outlined in this review clearly demonstrate the great potential for *in-vivo* use of biomedical Raman spectroscopy. Ultimately, as efficiently summarized in Ref. 4, the advantage of Raman spectroscopy over existing medical devices has to be demonstrated in large cohort studies based on patient outcomes and compared with accepted gold standard methodologies. Overall, in the last several years, there has been significant progress in moving Raman spectroscopy from a pure scientific research method to a mature tool, which bears significant promise to provide label-free *in-vivo* diagnostics.

Disclosures

The authors have no potential conflicts of interest to disclose.

Acknowledgments

This work was supported by the EU-funded project MIB (No. 667933).

References

1. E. B. Hanlon et al., "Prospects for in vivo Raman spectroscopy," *Phys. Med. Biol.* **45**, R1–59 (2000).
2. I. W. Schie and T. Huser, "Methods and applications of Raman microspectroscopy to single-cell analysis," *Appl. Spectrosc.* **67**(8), 813–828 (2013).
3. O. Stevens et al., "Developing fibre optic Raman probes for applications in clinical spectroscopy," *Chem. Soc. Rev.* **45**, 1919–1934 (2016).
4. I. J. Pence and A. Mahadevan-jansen, "Clinical instrumentation and applications of Raman spectroscopy," *Chem. Soc. Rev.* **45**(7), 1958–1979 (2016).
5. D. W. S. Shipp, F. S. Sinjab, and I. Notinger, "Raman spectroscopy: techniques and applications in the life sciences," *Adv. Opt. Photonics* **9**(2), 1–70 (2017).
6. A. Mahadevan-jansen and R. R. Richards-Kortum, "Raman spectroscopy for the detection of cancers and precancers," *J. Biomed. Opt.* **1**(1), 31–70 (1996).
7. M. Diem et al., "Applications of infrared and Raman microspectroscopy of cells and tissue in medical diagnostics: present status and future promises," *Spectrosc. An Int. J.* **27**(5–6), 463–496 (2012).
8. S. Wachsmann-Hogiu, T. Weeks, and T. Huser, "Chemical analysis in vivo and in vitro by Raman spectroscopy—from single cells to humans," *Curr. Opin. Biotechnol.* **20**(1), 63–73 (2009).
9. Q. Tu and C. Chang, "Diagnostic applications of Raman spectroscopy," *Biol. Med.* **8**, 545–558 (2012).
10. L. A. Austin, S. Osseiran, and C. L. Evans, "Raman technologies in cancer diagnostics," *Analyst* **141**(2), 476–503 (2016).
11. M. Jermyn et al., "A review of Raman spectroscopy advances with an emphasis on clinical translation challenges in oncology," *Phys. Med. Biol.* **61**, R370–R400 (2016).
12. J. Schleusener et al., "Perturbation factors in the clinical handling of a fiber-coupled Raman probe for cutaneous in vivo diagnostic Raman spectroscopy," *Appl. Spectrosc.* **69**(2), 243–256 (2015).
13. E. Cordero et al., "Evaluation of shifted excitation Raman difference spectroscopy and comparison to computational background correction methods applied to biochemical Raman spectra," *Sensors* **17**(8), 1724 (2017).
14. D. Wei, S. Chen, and Q. Liu, "Review of fluorescence suppression techniques in Raman spectroscopy," *Appl. Spectrosc. Rev.* **50**, 387–406 (2015).
15. T. Rojalin et al., "Fluorescence-suppressed time-resolved Raman spectroscopy of pharmaceuticals using complementary metal-oxide semiconductor (CMOS) single-photon avalanche diode (SPAD) detector," *Anal. Bioanal. Chem.* **408**(3), 761–774 (2016).
16. E. Canetta et al., "Modulated Raman spectroscopy for enhanced identification of bladder tumor cells in urine samples," *J. Biomed. Opt.* **16**(3), 037002 (2011).
17. M. T. Gebrekidan et al., "A shifted-excitation Raman difference spectroscopy (SERDS) evaluation strategy for the efficient isolation of Raman spectra from extreme fluorescence interference," *J. Raman Spectrosc.* **47**(2), 198–209 (2016).
18. K. Christian et al., "Raman difference spectroscopy: a non-invasive method for identification of oral squamous cell carcinoma," *Biomed. Opt. Express* **5**(9), 3252–3265 (2014).
19. R. Gautam et al., "Review of multidimensional data processing approaches for Raman and infrared spectroscopy," *EPJ Tech. Instrum.* **2**(1), 8 (2015).
20. T. W. Bocklitz et al., "A comprehensive study of classification methods for medical diagnosis," *J. Raman Spectrosc.* **40**(12), 1759–1765 (2009).
21. T. W. Bocklitz et al., "How to pre-process Raman spectra for reliable and stable models?," *Anal. Chim. Acta* **704**(1–2), 47–56 (2011).
22. C. Krafft et al., "Developments in spontaneous and coherent Raman scattering microscopic imaging for biomedical applications," *Chem. Soc. Rev.* **45**(7), 1819–1849 (2016).
23. E. M. Barroso et al., "Water concentration analysis by Raman spectroscopy to determine the location of the tumor border in oral cancer surgery," *Cancer Res.* **76**(20), 5945–5953 (2016).
24. I. P. Santos et al., "Implementation of a novel low-noise InGaAs detector enabling rapid near-infrared multichannel Raman spectroscopy of pigmented biological samples," *J. Raman Spectrosc.* **46**(7), 652–660 (2015).
25. D. Dussault and P. Hoess, "Noise performance comparison of ICCD with CCD and EMCCD cameras," *Proc. SPIE* **5563**, 195 (2004).
26. J. Zhao et al., "Integrated real-time Raman system for clinical in vivo skin analysis," *Ski. Res. Technol. Off. J. Int. Soc. Bioeng. Ski. [and] Int. Soc. Digit. Imaging Ski. [and] Int. Soc. Ski. Imaging* **14**(4), 484–492 (2008).
27. J. Qi, K. L. Bechtel, and W.-C. Shih, "Automated image curvature assessment and correction for high-throughput Raman spectroscopy and microscopy," *Biomed. Spectrosc. Imaging* **3**(4), 359–368 (2014).
28. Z. Huang et al., "Rapid near-infrared Raman spectroscopy system for real-time in vivo skin measurements," *Opt. Lett.* **26**(22), 1782–1784 (2001).
29. Y. Komachi et al., "Raman probe using a single hollow waveguide," *Opt. Lett.* **30**(21), 2942–2944 (2005).

30. S. O. Konorov et al., "Hollow-core photonic crystal fiber-optic probes for Raman spectroscopy," *Opt. Lett.* **31**(12), 1911–1913 (2006).
31. K. M. Tan et al., "Near-infrared Raman spectroscopy using hollow-core photonic bandgap fibers," *Opt. Commun.* **283**(16), 3204–3206 (2010).
32. S. Dochow et al., "Multicore fiber with integrated fiber Bragg gratings for background-free Raman sensing," *Opt. Express* **20**(18), 20156–20169 (2012).
33. I. Latka et al., "Fiber optic probes for linear and nonlinear Raman applications—current trends and future development," *Laser Photonics Rev.* **7**(5), 698–731 (2013).
34. U. Utzinger and R. R. Richards-Kortum, "Fiber optic probes for biomedical optical spectroscopy," *J. Biomed. Opt.* **8**(1), 121–147 (2003).
35. L. M. Almond et al., "Assessment of a custom-built Raman spectroscopic probe for diagnosis of early oesophageal neoplasia," *J. Biomed. Opt.* **17**(8), 081421 (2012).
36. J. C. C. Day et al., "A miniature confocal Raman probe for endoscopic use," *Phys. Med. Biol.* **54**(23), 7077–7087 (2009).
37. J. Mo et al., "High wavenumber Raman spectroscopy for in vivo detection of cervical dysplasia," *Anal. Chem.* **81**(21), 8908–8915 (2009).
38. S. Duraipandian et al., "Simultaneous fingerprint and high-wavenumber confocal Raman spectroscopy enhances early detection of cervical precancer in vivo," *Anal. Chem.* **84**, 5913–5919 (2012).
39. S. Duraipandian et al., "In vivo diagnosis of cervical precancer using Raman spectroscopy and genetic algorithm techniques," *Analyst* **136**(20), 4328 (2011).
40. M. S. Bergholt, W. Zheng, and Z. Huang, "Characterizing variability in in vivo Raman spectroscopic properties of different anatomical sites of normal tissue in the oral cavity," *J. Raman Spectrosc.* **43**(2), 255–262 (2012).
41. J. Mo, W. Zheng, and Z. Huang, "Fiber-optic Raman probe couples ball lens for depth-selected Raman measurements of epithelial tissue," *Biomed. Opt. Express* **1**(1), 17–30 (2010).
42. J. Wang et al., "Development of a beveled fiber-optic confocal Raman probe for enhancing in vivo epithelial tissue Raman measurements at endoscopy," *Opt. Lett.* **38**(13), 2321–2323 (2013).
43. Z. Huang et al., "Integrated Raman spectroscopy and trimodal wide-field imaging techniques for real-time in vivo tissue Raman measurements at endoscopy," *Opt. Lett.* **34**(6), 758–760 (2009).
44. J. Wang et al., "Comparative study of the endoscope-based bevelled and volume fiber-optic Raman probes for optical diagnosis of gastric dysplasia in vivo at endoscopy," *Anal. Bioanal. Chem.* **407**(27), 8303–8310 (2015).
45. M. S. Bergholt et al., "Fiberoptic confocal Raman spectroscopy for real-time in vivo diagnosis of dysplasia in Barrett's esophagus," *Gastroenterology* **146**(1), 27–32 (2014).
46. S. Duraipandian et al., "Real-time Raman spectroscopy for in vivo, online gastric cancer diagnosis during clinical endoscopic examination," *J. Biomed. Opt.* **17**(8), 081418 (2012).
47. J. Wang et al., "Fiber-optic Raman spectroscopy for in vivo diagnosis of gastric dysplasia," *Faraday Discuss.* **187**, 377–392 (2016).
48. K. Lin et al., "Real-time in vivo diagnosis of nasopharyngeal carcinoma using rapid fiber-optic Raman spectroscopy," *Theranostics* **7**(14), 3517–3526 (2017).
49. J. T. Motz et al., "Real-time Raman system for in vivo disease diagnosis," *J. Biomed. Opt.* **10**(3), 031113 (2007).
50. J. T. Motz et al., "Optical fiber probe for biomedical Raman spectroscopy," *Appl. Opt.* **43**(3), 542–554 (2004).
51. A. S. Haka et al., "In vivo margin assessment during partial mastectomy breast surgery using Raman spectroscopy," *Cancer Res.* **66**(6), 3317–3322 (2006).
52. L. Lim et al., "Clinical study of noninvasive in vivo melanoma and nonmelanoma skin cancers using multimodal spectral diagnosis," *J. Biomed. Opt.* **19**(11), 117003 (2014).
53. R. Shaikh et al., "In vivo Raman spectroscopy of human uterine cervix: exploring the utility of vagina as an internal control," *J. Biomed. Opt.* **19**(8), 087001 (2014).
54. A. Malik et al., "In vivo Raman spectroscopy-assisted early identification of potential second primary/recurrences in oral cancers: an exploratory study," *Head Neck* **39**(11), 2216–2223 (2017).
55. M. A. Short et al., "Development and preliminary results of an endoscopic Raman probe for potential in vivo diagnosis of lung cancers," *Opt. Lett.* **33**(7), 711–713 (2008).
56. H. C. McGregor et al., "Real-time endoscopic Raman spectroscopy for in vivo early lung cancer detection," *J. Biophotonics* **13**(1), 98–110 (2016).
57. M. A. Short et al., "Development and in vivo testing of a high frequency endoscopic Raman spectroscopy system for potential applications in the detection of early colonic neoplasia," *J. Biophotonics* **9**(1–2), 44–48 (2016).
58. M. Agenant et al., "Clinical superficial Raman probe aimed for epithelial tumor detection: phantom model results," *Biomed. Opt. Express* **5**(4), 1203 (2014).
59. R. O. P. Draga et al., "In vivo bladder cancer diagnosis by high-volume Raman spectroscopy," *Anal. Chem.* **82**(14), 5993–5999 (2010).
60. EmVision Advanced Optical Designs.
61. H. Ding et al., "In vivo analysis of mucosal lipids reveals histological disease activity in ulcerative colitis using endoscope-coupled Raman spectroscopy," *Biomed. Opt. Express* **8**(7), 3426–3439 (2017).
62. M. Jermyn et al., "Raman spectroscopy detects distant invasive brain cancer cells centimeters beyond MRI capability in humans," *Biomed. Opt. Express* **7**(12), 5129–5137 (2016).
63. J. Desroches et al., "Characterization of a Raman spectroscopy probe system for intraoperative brain tissue classification," *Biomed. Opt. Express* **6**(7), 2380 (2015).
64. M. Jermyn et al., "Intraoperative brain cancer detection with Raman spectroscopy in humans," *Sci. Transl. Med.* **7**(274), 274ra19 (2015).
65. C. M. O'Brien et al., "Characterization of human cervical remodeling throughout pregnancy using in vivo Raman spectroscopy," *J. Biomed. Opt.* **1**(1), 93032F (2015).
66. I. J. Pence et al., "Clinical characterization of in vivo inflammatory bowel disease with Raman spectroscopy," *Biomed. Opt. Express* **8**(2), 524–535 (2017).
67. J. Q. Nguyen et al., "Intraoperative Raman spectroscopy of soft tissue sarcomas," *Lasers Surg. Med.* **48**(8), 774–781 (2016).
68. H. Lui et al., "Real-time Raman spectroscopy for in vivo skin cancer diagnosis," *Cancer Res.* **72**(10), 2491–2500 (2012).
69. W. Wang et al., "Real-time in vivo cancer diagnosis using Raman spectroscopy: real-time in vivo cancer diagnosis using Raman spectroscopy," *J. Biophotonics* **8**(7), 527–545 (2015).
70. C. Fink and H. Haenssle, "Non-invasive tools for the diagnosis of cutaneous melanoma," *Ski. Res. Technol.* **23**(3), 261–271 (2017).
71. C. A. Lieber et al., "In vivo nonmelanoma skin cancer diagnosis using Raman microspectroscopy," *Lasers Surg. Med.* **40**(7), 461–467 (2008).
72. C. A. Lieber and A. Mahadevan-Jansen, "Development of a handheld Raman microspectrometer for clinical dermatologic applications," *Opt. Express* **15**(19), 11874–11882 (2007).
73. J. Schleusener et al., "In vivo study for the discrimination of cancerous and normal skin using fibre probe-based Raman spectroscopy," *Exp. Dermatol.* **24**(10), 767–772 (2015).
74. E. Y. M. Bonnist et al., "Understanding the dandruff scalp before and after treatment: an in vivo Raman spectroscopic study," *Int. J. Cosmet. Sci.* **36**(4), 347–354 (2014).
75. J. Lademann et al., "In vivo Raman spectroscopy detects increased epidermal antioxidative potential with topically applied carotenoids," *Laser Phys. Lett.* **6**(1), 76–79 (2009).
76. J. W. Fluhr et al., "Infant epidermal skin physiology: adaptation after birth," *Br. J. Dermatol.* **166**(3), 483–490 (2012).
77. C. Choe et al., "In vivo confocal Raman microscopic determination of depth profiles of the stratum corneum lipid organization influenced by application of various oils," *J. Dermatol. Sci.* **87**(2), 183–191 (2017).
78. M. B. Lopes et al., "In vivo confocal Raman spectroscopic analysis of the effects of infrared radiation in the human skin dermis," *Photochem. Photobiol.* **93**(2), 613–618 (2017).
79. C. Kendall et al., "Evaluation of Raman probe for oesophageal cancer diagnostics," *Analyst* **135**(12), 3038 (2010).
80. L. M. Almond et al., "Endoscopic Raman spectroscopy enables objective diagnosis of dysplasia in Barrett's esophagus," *Gastrointest. Endosc.* **79**(1), 37–45 (2014).
81. M. A. Short et al., "Using high frequency Raman spectra for colonic neoplasia detection," *Opt. Express* **21**(4), 5025–5034 (2013).
82. K. Lin, D. L. P. Cheng, and Z. Huang, "Optical diagnosis of laryngeal cancer using high wavenumber Raman spectroscopy," *Biosens. Bioelectron.* **35**(1), 213–217 (2012).

83. S. Koljenović et al., "Tissue characterization using high wave number Raman spectroscopy," *J. Biomed. Opt.* **10**(3), 031116 (2005).
84. P. Matousek et al., "Subsurface probing in diffusely scattering media using spatially offset Raman spectroscopy," *Appl. Spectrosc.* **59**(4), 393–400 (2005).
85. P. Matousek et al., "Numerical simulations of subsurface probing in diffusely scattering media using spatially offset Raman spectroscopy," *Appl. Spectrosc.* **59**(12), 1485–1492 (2005).
86. J. R. Maher and A. J. Berger, "Determination of ideal offset for spatially offset Raman spectroscopy," *Appl. Spectrosc.* **64**(1), 61–65 (2010).
87. "Spatially offset Raman spectroscopy (SORS)," Agilent.
88. P. Matousek et al., "Noninvasive Raman spectroscopy of human tissue in vivo," *Appl. Spectrosc.* **60**(7), 758–763 (2006).
89. K. Sowoidnich et al., "Spatially offset Raman spectroscopy for photon migration studies in bones with different mineralization levels," *Analyst* **142**(17), 3219–3226 (2017).
90. K. Buckley et al., "Towards the in vivo prediction of fragility fractures with Raman spectroscopy," *J. Raman Spectrosc.* **46**(7), 610–618 (2015).
91. K. Buckley et al., "Decomposition of in vivo spatially offset Raman spectroscopy data using multivariate analysis techniques," *J. Raman Spectrosc.* **45**(2), 188–192 (2014).
92. K. Buckley et al., "Measurement of abnormal bone composition in vivo using noninvasive Raman spectroscopy," *IBMS Bonekey* **11**, 602 (2014).
93. M. D. Keller, S. K. Majumder, and A. Mahadevan-Jansen, "Spatially offset Raman spectroscopy of layered soft tissues," *Opt. Lett.* **34**(7), 926–928 (2009).
94. M. D. Keller et al., "Development of a spatially offset Raman spectroscopy probe for breast tumor surgical margin evaluation," *J. Biomed. Opt.* **16**(7), 077006 (2011).
95. M. D. Keller et al., "Monte Carlo model of spatially offset Raman spectroscopy for breast tumor margin analysis," *Appl. Spectrosc.* **64**(6), 607–614 (2010).
96. G. Feng et al., "Sensitivity of spatially offset Raman spectroscopy (SORS) to subcortical bone tissue," *J. Biophotonics* **10**(8), 990–996 (2017).
97. S. V. K. Sekar et al., "Frequency offset Raman spectroscopy (FORS) for subsurface probing of diffusive medium," *Opt. Express* **25**, 889–896 (2017).
98. S. Konugolu Venkata Sekar et al., "Time domain diffuse Raman spectrometer based on novel TCSPC camera for depth analysis of diffusive media," *Opt. Lett.* **43**, 2134–2137 (2018).
99. C. A. Patil et al., "Combined Raman spectroscopy and optical coherence tomography device for tissue characterization," *Opt. Lett.* **33**(10), 1135–1137 (2008).
100. C. A. Patil et al., "Integrated system for combined Raman spectroscopy-spectral domain optical coherence tomography," *J. Biomed. Opt.* **16**(1), 011007 (2011).
101. C. A. Patil et al., "A clinical instrument for combined Raman spectroscopy-optical coherence tomography of skin cancers," *Lasers Surg. Med.* **2**, 143–151 (2011).
102. J. Wang et al., "Development of a hybrid Raman spectroscopy and optical coherence tomography technique for real-time in vivo tissue measurements," *Opt. Lett.* **41**(13), 3045–3048 (2016).
103. J. Wang et al., "Characterizing biochemical and morphological variations of clinically relevant anatomical locations of oral tissue in vivo with hybrid Raman spectroscopy and optical coherence tomography technique," *J. Biophotonics* **11**, e201700113 (2017).
104. M. Chen et al., "Depth-resolved multimodal imaging: wavelength modulated spatially offset Raman spectroscopy with optical coherence tomography," *J. Biophotonics* (2017).
105. A. C. De Luca et al., "Online fluorescence suppression in modulated Raman spectroscopy," *Anal. Chem.* **82**(2), 738–745 (2010).
106. M. Mazurenka et al., "Development of a combined OCT-Raman probe for the prospective in vivo clinical melanoma skin cancer screening," *Rev. Sci. Instrum.* **88**(10), 105103 (2017).
107. O. R. Šćepanović et al., "A multimodal spectroscopy system for real-time disease diagnosis," *Rev. Sci. Instrum.* **80**(4), 43103 (2009).
108. O. R. Šćepanović et al., "Multimodal spectroscopy detects features of vulnerable atherosclerotic plaque," *J. Biomed. Opt.* **16**(1), 011009 (2011).
109. M. Jermyn et al., "Highly accurate detection of cancer in situ with intraoperative, label-free, multimodal optical spectroscopy," *Cancer Res.* **77**(14), 1–10 (2017).
110. S. Dochow et al., "Combined fiber probe for fluorescence lifetime and Raman spectroscopy," *Anal. Bioanal. Chem.* **407**(27), 8291–8301 (2015).
111. M. Sharma et al., "Design and characterization of a novel multimodal fiber-optic probe and spectroscopy system for skin cancer applications," *Rev. Sci. Instrum.* **85**(8), 83101 (2014).
112. C. Matthäus et al., "Detection and characterization of early plaque formations by Raman probe spectroscopy and optical coherence tomography: an in vivo study on a rabbit model," *J. Biomed. Opt.* **23**(1), 015004 (2018).
113. L. A. Reisner et al., "A prototype biosensor-integrated image-guided surgery system," *Int. J. Med. Robot. Comput. Assist. Surg.* **3**(1), 82–88 (2007).
114. Araknes The BioRobotics Institute.
115. P. C. Ashok et al., "A Raman spectroscopy bio-sensor for tissue discrimination in surgical robotics," *J. Biophotonics* **7**(1–2), 103–109 (2014).
116. M. S. Bergholt et al., "In vivo, real-time, transnasal, image-guided Raman endoscopy: defining spectral properties in the nasopharynx and larynx," *J. Biomed. Opt.* **17**(7), 077002 (2012).
117. J. Schleusener et al., "Design and technical evaluation of fibre-coupled Raman probes for the image-guided discrimination of cancerous skin," *Meas. Sci. Technol.* **25**(3), 35701 (2014).
118. M. S. Bergholt et al., "Characterizing variability in in vivo Raman spectra of different anatomical locations in the upper gastrointestinal tract toward cancer detection," *J. Biomed. Opt.* **16**(3), 037003 (2011).
119. M. S. Bergholt et al., "In vivo diagnosis of gastric cancer using Raman endoscopy and ant colony optimization techniques," *Int. J. Cancer* **128**(11), 2673–2680 (2011).
120. M. S. Bergholt et al., "Fiber-optic Raman spectroscopy probes gastric carcinogenesis in vivo at endoscopy," *J. Biophotonics* **6**(1), 49–59 (2013).
121. M. S. Bergholt et al., "Combining near-infrared-excited autofluorescence and Raman spectroscopy improves in vivo diagnosis of gastric cancer," *Biosens. Bioelectron.* **26**(10), 4104–4110 (2011).
122. W. Wang et al., "Disposable sheath that facilitates endoscopic Raman spectroscopy," *J. Biomed. Opt.* **21**(2), 025001 (2016).
123. I. J. Pence, E. Vargis, and A. Mahadevan-Jansen, "Assessing variability of in vivo tissue Raman spectra," *Appl. Spectrosc.* **67**(7), 789–800 (2013).
124. J. Desroches et al., "Raman spectroscopy in microsurgery: impact of operating microscope illumination sources on data quality and tissue classification," *Analyst* **142**, 1185–1191 (2017).
125. P. I. Okagbare and M. D. Morris, "Polymer-capped fiber-optic Raman probe for non-invasive Raman spectroscopy," *Analyst* **137**(1), 77–81 (2012).
126. M. S. Bergholt et al., "Multivariate reference technique for quantitative analysis of fiber-optic tissue Raman spectroscopy," *Anal. Chem.* **85**(23), 11297–11303 (2013).
127. "WHO Global atlas on cardiovascular disease prevention and control," WHO.
128. P. R. Moreno, B. Marshik, and J. E. Muller, "Near-infrared spectroscopy," Chapter 16 in *The Vulnerable Atherosclerotic Plaque*, R. V. MD et al., Eds., pp. 257–262, Blackwell Publishing, Oxford, United Kingdom (2006).
129. M. Naghavi et al., "From vulnerable plaque to vulnerable patient: a call for new definitions and risk assessment strategies: part II," *Circulation* **108**(15), 1772–1778 (2003).
130. C. V. Bourantas et al., "Hybrid intravascular imaging: recent advances, technical considerations, and current applications in the study of plaque pathophysiology," *Eur. Heart J.* **38**(6), 400–412 (2017).
131. H. P. J. Buschman et al., "In vivo determination of the molecular composition of artery wall by intravascular Raman spectroscopy," *Anal. Chem.* **72**(16), 3771–3775 (2000).
132. J. T. Motz et al., "In vivo Raman spectral pathology of human atherosclerosis and vulnerable plaque," *J. Biomed. Opt.* **11**(2), 021003 (2006).
133. O. R. Šćepanović et al., "Detection of morphological markers of vulnerable atherosclerotic plaque using multimodal spectroscopy," *J. Biomed. Opt.* **11**(2), 021007 (2006).

134. C. Matthäus et al., "In vivo characterization of atherosclerotic plaque depositions by Raman-probe spectroscopy and in vitro coherent anti-stokes Raman scattering microscopic imaging on a rabbit model," *Anal. Chem.* **84**(18), 7845–7851 (2012).
135. S. Dochow et al., "Comparing Raman and fluorescence lifetime spectroscopy from human atherosclerotic lesions using a bimodal probe," *J. Biophotonics* **9**(9), 958–966 (2016).
136. R. McQueenie et al., "Detection of inflammation in vivo by surface-enhanced Raman scattering provides higher sensitivity than conventional fluorescence imaging," *Anal. Chem.* **84**(14), 5968–5975 (2012).
137. A. Sahu et al., "Serum based diagnosis of asthma using Raman spectroscopy: an early phase pilot study," *PLoS One* **8**(11), e78921 (2013).
138. H. Nawaz et al., "Prediction of viral loads for diagnosis of hepatitis C infection in human plasma samples using Raman spectroscopy coupled with partial least squares regression analysis," *J. Raman Spectrosc.* **48**(5), 697–704 (2017).
139. G. E. Tontini et al., "Differential diagnosis in inflammatory bowel disease colitis: state of the art and future perspectives," *World J. Gastroenterol.* **21**(1), 21–46 (2015).
140. X. Bi et al., "Development of spectral markers for the discrimination of ulcerative colitis and Crohn's disease using Raman spectroscopy," *Dis. Colon Rectum* **54**(1), 48–53 (2011).
141. I. J. Pence et al., "Endoscopy-coupled Raman spectroscopy for in vivo discrimination of inflammatory bowel disease," *Proc. SPIE* **8939**, 89390R (2014).
142. B. Krishnapuram et al., "Sparse multinomial logistic regression: fast algorithms and generalization bounds," *IEEE Trans. Pattern Anal. Mach. Intell.* **27**(6), 957–968 (2005).
143. R. L. Siegel, K. D. Miller, and A. Jemal, "Cancer statistics, 2017," *CA. Cancer J. Clin.* **67**(1), 7–30 (2017).
144. F. Islami, L. A. Torre, and A. Jemal, "Global trends of lung cancer mortality and smoking prevalence," *Transl. Lung Cancer Res.* **4**(4), 327–338 (2015).
145. "Screening by chest radiograph and lung cancer mortality: the prostate, lung, colorectal, and ovarian (PLCO) randomized trial," *JAMA* **306**(17), 1865–1873 (2011).
146. D. Sharma, T. G. Newman, and W. S. Aronow, "Lung cancer screening: history, current perspectives, and future directions," *Arch. Med. Sci. AMS* **11**(5), 1033–1043 (2015).
147. P. Zarogoulidis, K. Zarogoulidis, and K. Tsakiridis, "Lung cancer: an update on current and future diagnostic and treatment techniques," *J. Thorac. Dis.* **5**(4), S341 (2013).
148. N. Ikeda et al., "Comprehensive diagnostic bronchoscopy of central type early stage lung cancer," *Lung Cancer* **56**(3), 295–302 (2007).
149. M. Andolfi et al., "The role of bronchoscopy in the diagnosis of early lung cancer: a review," *J. Thoracic Dis.* **8**(11), 3329–3337 (2016).
150. J. Sun et al., "The value of autofluorescence bronchoscopy combined with white light bronchoscopy compared with white light alone in the diagnosis of intraepithelial neoplasia and invasive lung cancer: a meta-analysis," *J. Thorac. Oncol.* **6**(8), 1336–1344 (2011).
151. N. D. Magee et al., "Ex vivo diagnosis of lung cancer using a Raman miniprobe," *J. Phys. Chem. B* **113**(23), 8137–8141 (2009).
152. H. Zeng et al., "In vivo Raman spectroscopy for early lung cancer detection," *Cancer Res.* **2**, 7112 (2011).
153. H. C. McGregor et al., "In vivo real-time endoscopic Raman spectroscopy for improving early lung cancer detection," in *Asia Communications and Photonics Conf. (2015)* (2015).
154. M. Ghoncheh, Z. Pournamdar, and H. Salehiniya, "Incidence and mortality and epidemiology of breast cancer in the World," *Asian Pacific J. Cancer Prev.* **17**(Suppl. 3), 43–46 (2016).
155. D. Roganovic et al., "Breast MRI, digital mammography and breast tomosynthesis: comparison of three methods for early detection of breast cancer," *Bosn. J. Basic Med. Sci.* **15**(4), 64–68 (2015).
156. A. L. Siu, "Screening for Breast Cancer: U.S. preventive services task force recommendation statement," *Ann. Intern. Med.* **164**(4), 279 (2016).
157. B. Brożek-Pluska et al., "Breast cancer diagnostics by Raman spectroscopy," *J. Mol. Liq.* **141**(3), 145–148 (2008).
158. H. Abramczyk et al., "The label-free Raman imaging of human breast cancer," *J. Mol. Liq.* **164**(1–2), 123–131 (2011).
159. H. Abramczyk et al., "Raman 'optical biopsy' of human breast cancer," *Prog. Biophys. Mol. Biol.* **108**(1–2), 74–81 (2012).
160. A. Saha et al., "Raman spectroscopy: a real-time tool for identifying microcalcifications during stereotactic breast core needle biopsies," *Biomed. Opt. Express* **2**(10), 2792 (2011).
161. K. E. Shafer-Peltier et al., "Raman microspectroscopic model of human breast tissue: implications for breast cancer diagnosis in vivo," *J. Raman Spectrosc.* **33**(7), 552–563 (2002).
162. J. Horsnell, "The use of Raman spectroscopy for the intra-operative assessment of axillary lymph nodes in breast cancer," PhD Thesis, Cranfield University (2012).
163. A. S. Haka et al., "Diagnosing breast cancer using Raman spectroscopy: prospective analysis," *J. Biomed. Opt.* **14**(5), 054023 (2009).
164. Q. Li, Q. Gao, and G. Zhang, "Classification for breast cancer diagnosis with Raman spectroscopy," *Biomed. Opt. Express* **5**(7), 2435 (2014).
165. F. Bray et al., "Global estimates of cancer prevalence for 27 sites in the adult population in 2008," *Int. J. Cancer* **132**(5), 1133–1145 (2013).
166. D. Forman et al., *Cancer Incidence in Five Continents*, Vol. X, IARC Scientific Publication No. 164 (2014).
167. G. K. Malhotra et al., "Global trends in esophageal cancer," *J. Surg. Oncol.* **115**(5), 564–579 (2017).
168. S. K. Teh et al., "Diagnosis of gastric cancer using near-infrared Raman spectroscopy and classification and regression tree techniques," *J. Biomed. Opt.* **13**(3), 034013 (2008).
169. Z. Huang et al., "In vivo early diagnosis of gastric dysplasia using narrow-band image-guided Raman endoscopy," *J. Biomed. Opt.* **15**(3), 037017 (2010).
170. S. K. Teh et al., "Near-infrared Raman spectroscopy for early diagnosis and typing of adenocarcinoma in the stomach," *Br. J. Surg.* **97**(4), 550–557 (2010).
171. J. Wang et al., "Simultaneous fingerprint and high-wavenumber fiber-optic Raman spectroscopy improves in vivo diagnosis of esophageal squamous cell carcinoma at endoscopy," *Sci. Rep.* **5**(1), 12957 (2015).
172. K. Lin et al., "Rapid fiber-optic Raman spectroscopy for real-time in vivo detection of gastric intestinal metaplasia during clinical gastroscopy," *Cancer Prev. Res.* **9**(6), 476–483 (2016).
173. S. K. Teh et al., "Diagnostic potential of near-infrared Raman spectroscopy in the stomach: differentiating dysplasia from normal tissue," *Br. J. Cancer* **98**(2), 457–465 (2008).
174. Z. Huang et al., "In vivo detection of epithelial neoplasia in the stomach using image-guided Raman endoscopy," *Biosens. Bioelectron.* **26**(2), 383–389 (2010).
175. M. S. Bergholt et al., "Raman endoscopy for in vivo differentiation between benign and malignant ulcers in the stomach," *Analyst* **135**(12), 3162 (2010).
176. S. K. Teh et al., "Spectroscopic diagnosis of laryngeal carcinoma using near-infrared Raman spectroscopy and random recursive partitioning ensemble techniques," *Analyst* **134**(6), 1232–1239 (2009).
177. G. Shetty et al., "Raman spectroscopy: elucidation of biochemical changes in carcinogenesis of oesophagus," *Br. J. Cancer* **94**(10), 1460–1464 (2006).
178. A. May et al., "Accuracy of staging in early oesophageal cancer using high resolution endoscopy and high resolution endosonography: a comparative, prospective, and blinded trial," *Gut* **53**(5), 634–640 (2004).
179. M. S. Bergholt et al., "Real-time depth-resolved fiber optic Raman endoscopy for in vivo diagnosis of gastric precancer," *Proc. SPIE* **8939**, 89390M (2014).
180. M. S. Bergholt et al., "Characterizing variability of in vivo Raman spectroscopic properties of different anatomical sites of normal colorectal tissue towards cancer diagnosis at colonoscopy," *Anal. Chem.* **87**(2), 960–966 (2015).
181. H. Ding et al., "Effect of physiological factors on the biochemical properties of colon tissue—an in vivo Raman spectroscopy study: physiological factors on the biochemical properties of colon tissue," *J. Raman Spectrosc.* **48**(7), 902–909 (2017).
182. S. Antoni et al., "Bladder cancer incidence and mortality: a global overview and recent trends," in *Eur. Urol.* **71**(1), 96–108 (2017).
183. B. W. D. De Jong et al., "Raman spectroscopic detection of changes in molecular composition of bladder muscle tissue caused by outlet obstruction," *Vib. Spectrosc.* **32**(1), 57–65 (2003).
184. B. W. D. De Jong et al., "Discrimination between nontumor bladder tissue and tumor by Raman spectroscopy," *Anal. Chem.* **78**(22), 7761–7769 (2006).

185. I. Barman et al., "Selective sampling using confocal Raman spectroscopy provides enhanced specificity for urinary bladder cancer diagnosis," *Anal. Bioanal. Chem.* **404**(10), 3091–3099 (2012).
186. M. C. M. Grimbergen et al., "Bladder cancer diagnosis during cystoscopy using Raman spectroscopy," *Proc. SPIE* **7161**, 716114 (2009).
187. N. Stone et al., "The use of Raman spectroscopy to provide an estimation of the gross biochemistry associated with urological pathologies," *Anal. Bioanal. Chem.* **387**(5), 1657–1668 (2007).
188. P. Crow et al., "Assessment of fiberoptic near-infrared Raman spectroscopy for diagnosis of bladder and prostate cancer," *Urology* **65**(6), 1126–1130 (2005).
189. C. R. Leemans, B. J. M. Braakhuis, and R. H. Brakenhoff, "The molecular biology of head and neck cancer," *Nat. Rev. Cancer* **11**(1), 9 (2011).
190. G. Carioli et al., "Global trends in nasopharyngeal cancer mortality since 1970 and predictions for 2020: focus on low-risk areas," *Int. J. Cancer* **140**(10), 2256–2264 (2017).
191. D. P. Lau et al., "Raman spectroscopy for optical diagnosis in the larynx: preliminary findings," *Lasers Surg. Med.* **37**(3), 192–200 (2005).
192. H. Chang et al., "Light-induced autofluorescence spectroscopy for detection of nasopharyngeal carcinoma in vivo," *Appl. Spectrosc.* **56**(10), 1361–1367 (2002).
193. L. T. Perelman, "Optical diagnostic technology based on light scattering spectroscopy for early cancer detection," *Expert Rev. Med. Dev.* **3**(6), 787–803 (2006).
194. D. P. Lau et al., "Raman spectroscopy for optical diagnosis in normal and cancerous tissue of the nasopharynx—preliminary findings," *Lasers Surg. Med.* **32**(3), 210–214 (2003).
195. S. Devpura et al., "Diagnosis of head and neck squamous cell carcinoma using Raman spectroscopy: tongue tissues," *J. Raman Spectrosc.* **43**(4), 490–496 (2012).
196. E. M. Barroso et al., "Discrimination between oral cancer and healthy tissue based on water content determined by Raman spectroscopy," *Anal. Chem.* **87**(4), 2419–2426 (2015).
197. H. Krishna et al., "Anatomical variability of in vivo Raman spectra of normal oral cavity and its effect on oral tissue classification," *Biomed. Spectrosc. Imaging* **2**(3), 199–217 (2013).
198. K. Lin et al., "Real-time in vivo diagnosis of laryngeal carcinoma with rapid fiber-optic Raman spectroscopy," *Biomed. Opt. Express* **7**(9), 3705–3715 (2016).
199. Z. Huang et al., "Raman spectroscopy in combination with background near-infrared autofluorescence enhances the in vivo assessment of malignant tissues," *Photochem. Photobiol.* **81**(5), 1219–1226 (2005).
200. G. A. Alexiou et al., "Management of meningiomas," *Clin. Neurol. Neurosurg.* **112**(3), 177–182 (2010).
201. O. Schillaci et al., "Single-photon emission computed tomography/computed tomography in brain tumors," *Semin. Nucl. Med.* **37**(1), 34–47 (2007).
202. S. M. K. Belhawi et al., "Early postoperative MRI overestimates residual tumour after resection of gliomas with no or minimal enhancement," *Eur. Radiol.* **21**(7), 1526–1534 (2011).
203. T. W. Vitaz, "Techniques to improve the extent of brain tumor resection—awake speech and motor mapping, and intraoperative MRI," in *Molecular Considerations and Evolving Surgical Management Issues in the Treatment of Patients with a Brain Tumor*, T. Lichtor, Ed., IntechOpen Limited, London, United Kingdom (2015).
204. T. B. Belsuzarri, R. A. Sangenis, and J. M. Araujo, "Brain tumor surgery: supplemental intra-operative imaging techniques and future challenges," *J. Cancer Metastasis Treat.* **2**, 70–79 (2016).
205. M. Kirsch et al., "Raman spectroscopic imaging for in vivo detection of cerebral brain metastases," *Anal. Bioanal. Chem.* **398**(4), 1707–1713 (2010).
206. J. Zhang et al., "Accuracy of Raman spectroscopy in differentiating brain tumor from normal brain tissue," *Oncotarget* **8**(22), 36824–36831 (2017).
207. D. G. Leslie et al., "Identification of pediatric brain neoplasms using Raman spectroscopy," *Pediatr. Neurosurg.* **48**(2), 109–117 (2012).
208. F. Leblond et al., "Intraoperative detection of cancerous brain tissue using Raman spectroscopy," *SPIE Newsroom* 4–6 (2015).
209. A. Beljebbar et al., "Ex vivo and in vivo diagnosis of C6 glioblastoma development by Raman spectroscopy coupled to a microprobe," *Anal. Bioanal. Chem.* **398**(1), 477–487 (2010).
210. T. Liu et al., "Evaluation of Raman spectra of human brain tumor tissue using the learning vector quantization neural network," *Laser Phys.* **26**(5), 55606 (2016).
211. S.-L. Chen et al., "Prostate cancer mortality-to-incidence ratios are associated with cancer care disparities in 35 countries," *Sci. Rep.* **7**, 40003 (2017).
212. GLOBOCAN cancer fact sheets: cervical cancer.
213. L. Rotter et al., "Dysplasia and cervical cancer: current diagnostic possibilities," *Ces. Gynkol.* **79**(4), 314–320 (2014).
214. A. J. Blatt et al., "Comparison of cervical cancer screening results among 256, 648 women in multiple clinical practices," *Cancer Cytopathol.* **123**(5), 282–288 (2015).
215. R. S. DaCosta, B. C. Wilson, and N. E. Marcon, "Fluorescence and spectral imaging," *Sci. World J.* **7**, 2046–2071 (2007).
216. Y. N. Mirabal et al., "Reflectance spectroscopy for in vivo detection of cervical precancer," *J. Biomed. Opt.* **7**(4), 587–594 (2002).
217. S. Duraipandian et al., "Integrated fingerprint and high wavenumber confocal Raman spectroscopy for in vivo diagnosis of cervical precancer," *Proc. SPIE* **8572**, 85720Z (2013).
218. A. Robichaux-Viehoever et al., "Characterization of Raman spectra measured in vivo for the detection of cervical dysplasia," *Appl. Spectrosc.* **61**(9), 986–993 (2007).
219. J. T. Marquês et al., "Biomembrane organization and function: the decisive role of ordered lipid domains," in *Advances in Planar Lipid Bilayers and Liposomes* Vol. **22**, A. Iglič, C. V. Kulkarni, and M. Rappolt, Eds., pp. 65–96, Academic Press, London, United Kingdom (2015).
220. E. Vargis et al., "Sensitivity of Raman spectroscopy to normal patient variability," *J. Biomed. Opt.* **16**(11), 117004 (2011).
221. S. Duraipandian et al., "Effect of hormonal variation on in vivo high wavenumber Raman spectra improves cervical precancer detection," *Proc. SPIE* **8214**, 82140A (2012).
222. S. Duraipandian et al., "Near-infrared-excited confocal Raman spectroscopy advances in vivo diagnosis of cervical precancer," *J. Biomed. Opt.* **18**(6), 067007 (2013).
223. S. Duraipandian et al., "Near-infrared Raman spectroscopy for assessing biochemical changes of cervical tissue associated with precarcinogenic transformation," *Analyst* **139**(21), 5379–5386 (2014).
224. P. Crow et al., "The use of Raman spectroscopy to identify and grade prostatic adenocarcinoma in vitro," *Br. J. Cancer* **89**(1), 106 (2003).
225. S. Devpura et al., "Detection of benign epithelia, prostatic intraepithelial neoplasia, and cancer regions in radical prostatectomy tissues using Raman spectroscopy," *Vib. Spectrosc.* **53**(2), 227–232 (2010).
226. N. Kourkoumelis et al., "Advances in the in vivo Raman spectroscopy of malignant skin tumors using portable instrumentation," *Int. J. Mol. Sci.* **16**(7), 14554–14570 (2015).
227. J. Zhao et al., "Using Raman spectroscopy to detect and diagnose skin cancer in vivo," *Dermatol. Clin.* **35**, 495–504 (2017).
228. G. Monheit et al., "The performance of MelaFind: a prospective multicenter study," *Arch. Dermatol.* **147**(2), 188–194 (2010).
229. X. Feng et al., "Raman active components of skin cancer," *Biomed. Opt. Express* **8**(6), 2835–2850 (2017).
230. M. Jermyn et al., "Neural networks improve brain cancer detection with Raman spectroscopy in the presence of light artifacts," *Proc. SPIE* **9690**, 96900B (2016).

Eliana Cordero obtained her BSc degree in mechatronic engineering from the University of Pamplona in 2011 and her MSc degree in scientific instrumentation from Ernst Abbe University of Applied Science of Jena. She enrolled PhD studies at the faculty for chemistry and earth sciences, Friedrich Schiller University of Jena in 2016. Since there, she is employed at the Leibniz institute of Photonic Technology, where she works in the development of Raman probes for endoscopic applications.

Ines Latka studied physics at the Technical University Ilmenau and the Friedrich-Schiller University Jena. After her diploma thesis she worked several years on the field of fiber optic sensors, particularly with fiber Bragg gratings. In 2009, she joined the molecular imaging group at IPHT in Jena/Germany, focusing on CARS. Her current

interests are focused on the development of fiber optic endoscopes for medical applications, e.g., employing Raman spectroscopy, in conjunction with multimodal instrumentation.

Christian Matthäus is working as a research assistant at Leibniz Institute for Photonic Technology (IPHT), Jena, Germany. His current interests are Raman spectroscopy, nonlinear imaging techniques, and MALDI-TOF. He received his PhD from City University of New York in 2006 in the field of spectroscopic imaging. After a postdoc position at Northeastern University, Boston, he joined the group of Prof. Jürgen Popp at the IPHT in 2009.

Iwan W. Schie studied medical engineering at Beuth University of Applied Science, Berlin, and received his PhD in biomedical engineering from the University of California, Davis. During his PhD his research focus was on instrument development and medical applications for multiphoton microscopy and spontaneous Raman

spectroscopy. Since 2014, he has been working as a postdoctoral researcher at the Leibniz-IPHT and established the group for “Multimodal Instrumentation” at the Leibniz-IPHT in 2017, with the research focus on high-throughput Raman spectroscopy systems for single cell classification, fiber-probe development, and instrumentation for medical in-vivo applications.

Jürgen Popp studied chemistry at the universities of Erlangen and Würzburg. After his PhD in chemistry he joined Yale University for postdoctoral work. He subsequently returned to Würzburg University where he finished his habilitation in 2002. Since 2002, he has held a chair for Physical Chemistry at the Friedrich–Schiller University Jena. Since 2006, he is also the scientific director of the Leibniz Institute of Photonic Technology, Jena. His research interests are mainly concerned with biophotonics. In particular his expertise in the development and application of innovative Raman techniques for biomedical diagnosis should be emphasized.

8

Erklärungen

Erklärung

Ich erkläre,

dass mir die geltende Promotionsordnung der Fakultät bekannt ist;

dass ich die Dissertation selbst angefertigt, keine Textabschnitte eines Dritten oder eigener Prüfungsarbeiten ohne Kennzeichnung übernommen und alle von mir benutzten Hilfsmittel, persönlichen Mitteilungen und Quellen in meiner Arbeit angegeben habe;

dass mich ausschließlich die folgenden Personen bei der Auswahl und Auswertung des Materials sowie bei der Herstellung des Manuskripts unterstützt haben: siehe Danksagung in der Dissertation;

dass die Hilfe einer kommerziellen Promotionsvermittlung nicht in Anspruch genommen wurde und dass Dritte weder unmittelbar noch mittelbar geldwerte Leistungen von mir für Arbeiten erhalten haben, die im Zusammenhang mit dem Inhalt der vorgelegten Dissertation stehen;

dass ich die Dissertation noch nicht als Prüfungsarbeit für eine staatliche oder andere wissenschaftliche Prüfung eingereicht habe;

dass ich nicht die gleiche, eine in wesentlichen Teilen ähnliche oder eine andere Abhandlung bei einer anderen Hochschule als Dissertation eingereicht habe.

Ort, Datum

Unterschrift

Selbständigkeitserklärung

Ich erkläre, dass ich die vorliegende Arbeit selbständig und unter Verwendung der angegebenen Hilfsmittel, persönlichen Mitteilungen und Quellen angefertigt habe.

Ort, Datum

Unterschrift

Erklärung zu den Eigenanteilen der Promovendin sowie der weiteren Doktoranden/Doktorandinnen als Koautoren an den Publikationen und Zweitpublikationsrechten bei einer kumulativen Dissertation

Für alle in dieser kumulativen Dissertation verwendeten Manuskripte liegen die notwendigen Genehmigungen der Verlage ("Reprint permissions") für die Zweitpublikation vor.

Die Co-Autoren der in dieser kumulativen Dissertation verwendeten Manuskripte sind sowohl über die Nutzung, als auch über die oben angegebenen Eigenanteile der weiteren Doktoranden als Co-Autoren an den Publikationen und Zweitpublikationsrechten bei einer kumulativen Dissertation informiert und stimmen dem zu.

Jena, den

Bestätigt:



Eliana F. Cordero B

Doktorand Leibniz IPHT

Bestätigung des Einverständnisses des Betreuers

Ich bin mit der Abfassung der Dissertation als publikationsbasiert, d.h. kumulativ, einverstanden und bestätige die vorstehenden Angaben. Eine entsprechend begründete Befürwortung mit Angabe des wissenschaftlichen Anteils der Doktorandin an den verwendeten Publikationen werde ich parallel an den Rat der Fakultät der Chemisch-Geowissenschaftlichen Fakultät richten

Jena, den

Bestätigt:

20/11/2019



Prof. Dr. Jürgen Popp

Direktor Leibniz IPHT

Conference contribution

- **Fiber-Based Raman imaging System for Bladder Tissue Analysis**
FT-IR Workshop in Spectroscopy in Microbiological and Medical Diagnostics- Berlin, Germany 2017 (Poster presented) Eliana Cordero, Iwan Schie, and Jürgen Popp
- **Bladder Tissue Characterization by a Compact Raman-Imaging System**
SPEC - Glasgow, Schottland 2018 (Poster presented) Eliana Cordero, Iwan Schie, and Jürgen Popp
- **Fiber-Based Raman Imaging System for Bladder Tissue Analysis ICORS -**
Jeju, South Korea 2018 (Talk) Eliana Cordero, Iwan Schie, and Jürgen Popp
- **Fiber-Based Raman imaging System for Bladder Tissue Analysis DokDok -**
Soul, Germany 2017 (Poster presented) Eliana Cordero, Iwan Schie, and Jürgen Popp
- **Fiber-Based Characterization of Urinary Bladder Cancer Bunsentagung -** Jena, Germany 2019 (Poster presented) Eliana Cordero, Iwan Schie, and Jürgen Popp
- **Ex-vivo Fiber Based Combination of Raman Spectroscopy and Optical Coherence Tomography to Characterize Tumor Bladder Cancer DokDok -** Eisenach, Germany 2019 (Poster presented) Eliana Cordero, Iwan Schie, and Jürgen Popp

Workshops

- **Fiber-Based Raman imaging System for Bladder Tissue Analysis** Biophotonics Summerschool - Ven, Sweden 2017 (Poster presented and 5 ECTS obtained) Eliana Cordero, Iwan Schie, and Jürgen Popp
- **Fiber-Based Raman imaging System for Bladder Tissue Analysis** Raman4Clinics - Belgrad, Serbia 2017 (Poster) Eliana Cordero, Iwan Schie, and Jürgen Popp
- **Women in Physics Workshop – Triest, Italy 2017 (Poster)**
- **Fiber-Based Raman imaging System for Bladder Tissue Analysis** JEDIS Summerschool - Jena, Germany 2018 (Poster) Eliana Cordero, Iwan Schie, and Jürgen Popp
- **Leibniz Kolleg Career development workshop - Postdam, Germany 2018**

9

Acknowledgments

I would like to express gratitude to Prof. Dr. Jürgen Popp for giving me the opportunity to do my doctoral research in this interdisciplinary working group, for all his remarks and support. I would like to express my deep gratitude to my supervisor Prof. Dr. Iwan W. Schie. I learnt many things under his supervision. I am very grateful for all his advice, all the useful remarks, comments and engagement through the learning process of this doctoral thesis.

Additionally, I would like to thank to Gregers Hermann and Karin Mogense for the clinical cooperation, the work on the ethical approval, the support during the clinical experiments in Denmark, the medical feedback, and for all the support on the way. Also, I like to thank Dr. Jan Rürger for all his advice, for the time invested and support with Raman data analysis. I want to thank Dr. Clara Stiebing as well for all her feedback and advice, Dr. Claudia Beleites, Dr. Shuxia Guo and Dr. Roman Kiselev for all his useful comments, feedback and interesting discussions.

I like to thank Florian Knorr and Abdullah Saif Mondol for their support with the technical implementations of the developed devices and for sharing their knowledge and skills. I also

want to thank my work colleagues to create a nice and constructive work environment, they helped to keep motivation up and was fun to work together.

The presented work was mainly done at Leibniz Institute of Photonic Technologies (IPHT). I want to express my gratitude to IPHT for the excellent work environment provided. I acknowledge support of numerous work colleagues at the institute in different departments of the institute for the fruitful networking and interesting discussions. This research work received funding from the European Union project MIB (Horizon 2020, grant agreement No 667933). I express my deep gratitude to IPHT and MIB for all the financial assistance during my research experience working on this project.

I acknowledge the organizations that support me financially for scientific events, workshops and conferences. First, IPHT and MIB for all the financial support to attend professional development workshops and conferences. I thank the Graduierten Akademie (GA) for the Intudoc scholarship to serve as a tutor of international students, specially to Dr. Alexander Schwarzkopf and the other GA tutors for all the assistance and advice. I thank to SPIE for the opportunity of opening a student chapter in Jena, especially for the support with the travel and activity grants. The experience managing the chapter as a president contribute fruitfully to my career development. I want to express my gratitude to Prof. Dr. Jürgen Popp to support the student chapter as advisor and I acknowledge the unconditional support of Cristina Amaya and Emma Brambila during all the planning, coordination and organization of many of the successful activities done during 2018 and 2019 with the SPIE Jena student chapter.

For the correction of my doctoral thesis I want to thank Prof. Dr. Iwan Schie, Dr. Clara Stiebeing, Dr. Max Nimmer and Dr. Jan Rüger, I fully appreciate their energy, time, feedback, suggestions and comments.

I am very thankful to my Colombian and German close friends for their optimism, trust and for all the fun moments. I deeply thank my loved ones, specially my family and my dear Max who have supported me throughout the entire process, keeping me happy, cheering me up and motivating me more. I will be grateful forever for your love.



Eliana Cordero

Researcher in Biophotonics

- April 15, 1989
- Sonnenhof 1, 07743 Jena
- +49 151 288 64916
- www.linkedin.com/in/e-cordero
- elianacordero@gmx.com

Languages

- Spanish ●●●●●
- English ●●●●●
- German ●●●●●

Key Skills

- Analytical and goal oriented manner to solve problems
- Practical know-how and founded knowledge in semiconductor and optics technologies
- Statistical modeling, computational chemistry and multivariate data analysis
- Effective technical communication, both written and verbal

IT Skills

- Data Analysis ●●●●●
 - Matlab
 - R
 - Labview
- Office and Design ●●●●●
 - Office
 - LaTeX
 - Inkscape
 - InDesign
- CAD Optics & Mechatronics ●●●●●
 - Zemax
 - ANSYS
 - CATIA
 - Quartus
 - Eagle
 - Proteus

Soft Skills

- Self-management
- Leadership
- Networking
- Coordination

Sport and Lifestyle

- Capoeira, Hiking, Calistenics, Dancing, Traveling, Playing Drums

Working Experience

- 2016 – Today **PhD Researcher** Leibniz Institute of Photonic Technology, Jena
Development of Raman fiber optic probes for endoscopic applications.
 - Optical design of microoptical probe tips and optimization of the optical system of the Raman spectroscopy setup.
 - Design, test and implementation of automatic measuring systems for scanning and Raman signal acquisition.
 - Chemometric analysis of Raman spectra, data processing and algorithm development.
 - Research in current topics of technical optics and linear spectroscopy in laser scanning and fiber-based applications.
- 2015 – 2016 **Product Test Engineer Working Student** Texas Instruments, Freising
Design and development of a method to demagnetize a magnetically shielded IC test base for production test of fluxgate sensors.
 - Characterization/calibration of magnetic sensors and signal processing of data.
- 2014 – 2015 **Quality Engineer Intern** Texas Instruments, Freising
 - Physical analysis via scanning electron microscopy and reactive ion etching for failure analysis on semiconductor samples.
- 2010 – 2013 **Technical Trainer** Cerrejon, Albania, Colombia
 - Preparation, conduction and evaluation of technical training courses and writing technical literature. Assessment of training needs and certification requirements.

Education

- 2013 – 2016 **M.Sc. Scientific Instrumentation (1.5)** Ernst Abbe Hochschule Jena
Focus: Optical instrumentation, microsystem technology and advanced material research.
Master Thesis (1.0) Leibniz Institute of Photonic Technology
"Development and Characterization of Silicon Nanostructures for Water Splitting Hydrogen Generation"
- 2006 – 2011 **Diploma in Mechatronics Engineering (1.3)** University of Pamplona
Focus: Robotics, automation, programming, mechanical and electronic design.
Bachelor Thesis (1.0) Cerrejon
"Automation Engineering of the Process of Backwashing and Washing of Filters at the Water Plant"

Extra-Curricular Activities

- Management **President of SPIE student chapter:** Coordinating the student chapter and organizing chapter activities and workshops.
- Organizational **International tutoring service (Intudoc):** Planning, organizing social events, supporting international researchers with organizational issues.
- Education **Student assistant in the clean room of the Ernst Abbe Hochschule Jena:** Hands-on photolithography, sputtering and etching.
- Education **Student assistant in the Robotics laboratory of the University of Pamplona.**

Publications

- 2017 **Evaluation of Shifted Excitation Raman Difference Spectroscopy and Comparison to Computational Background Correction Methods Applied to Biochemical Raman Spectra**
E. Cordero, F. Korinth, C. Stiebing, C. Krafft, I. W. Schie and J. Popp
Sensors
- 2018 **In-vivo Raman spectroscopy: from basics to applications**
E. Cordero, I. Latka, C. Matthäus, I. W. Schie and J. Popp
Journal of Biomedical Optics